

Modeling Nonlocal and Nonlinear Response Phenomena of Plasmonic and Biological Systems

Author: Alexander J. Shvonski

Persistent link: <http://hdl.handle.net/2345/bc-ir:108209>

This work is posted on [eScholarship@BC](#),
Boston College University Libraries.

Boston College Electronic Thesis or Dissertation, 2018

Copyright is held by the author, with all rights reserved, unless otherwise noted.

Modeling Nonlocal and Nonlinear Response Phenomena of Plasmonic and Biological Systems

Alexander J. Shvonski

A dissertation
submitted to the Faculty of
the department of Physics
in partial fulfillment
of the requirements for the degree of
Doctor of Philosophy

Boston College
Morrissey College of Arts and Sciences
Graduate School

September 2018

Modeling Nonlocal and Nonlinear Response Phenomena of Plasmonic and Biological Systems

Alexander J. Shvonski

Advisor: Professor Krzysztof Kempa, Ph.D.

ABSTRACT

In this work, we first examine nonlocal behavior in plasmonic systems and develop or expand upon models that enable calculation of higher-order, nonlocal responses for systems with novel geometries. The effects of nonlocality, i.e., spatial dispersion, are prominent in nanostructures with small feature sizes, and accurate calculations of the nonlocal response of nanostructures are increasingly important for the study of novel physics at the nanoscale. Next, we consider a specific biological system, double-stranded DNA, and investigate the nonlocal and nonlinear model that describes its dynamics. We consider the regime of strong driving with THz radiation and study the parameter-space where molecular damage occurs, motivated by the prospect of using selective damage for potential novel therapies. In a related study, we also consider the possibility of generating THz radiation through the nonlinear, difference-frequency response of a plasmonic system. Plasmonic difference-frequency generation could enable deep penetration of THz signals into the body and, therefore, these projects are intimately connected. Ultimately, these two regimes of behavior, nonlocality and nonlinearity, represent rich areas for applicable research.

ACKNOWLEDGEMENTS

I would like to first thank my wife Allie for her unending support. There were many times when her positivity and confidence inspired me to work harder. My pursuit of a PhD in physics began years before I even came to BC, and Allie has been by my side throughout the entire journey.

Next, I am thankful to the BC Physics Department, which has afforded me many significant opportunities for personal and professional growth. It has been a pleasure to know and to work with Jane, Sile, Nancy, and Scott, who have always been so friendly, helpful, and responsive. Additionally, Professor Graf was always supportive of my teaching interests and available to entertain my questions about class instruction and pedagogy. Yun also put time and effort into training me and ensuring that I was well-prepared to act as Lab Manager. I could not have excelled without the support of the Department.

I am also indebted to Professor Herczyński for entrusting me with many responsibilities, including the job of Lab Manager. Over the years, we developed an extremely effective working relationship and I've learned a lot from serving as his TA. From serious circumstances related to classes, to jovial (and often loud) conversation, he always listened thoughtfully and truly treated me as a colleague. However, he did always point out that I should be giving him half of my paycheck for the experience.

Of course, Professor Kempa was singularly impactful on my trajectory as a physicist. I have appreciated his advising style, which allowed me great leeway to explore different avenues of inquiry, many of which were fruitful, and some of which led to dead-ends—"that's physics," he would say. There were also many memorable times when we would frenetically work on problems together and discuss equations scrawled on the whiteboard. Ultimately, I am grateful for his mentorship and for allowing me to maintain an enjoyable work-life balance.

Finally, I am happy to have made many friends at BC, some of which have growing families like my own. There are too many instances to recall, but in general I will think fondly of our debates about physics, discussions about life, and commiseration regarding the plight of being a graduate student.

TABLE OF CONTENTS

Acknowledgements	iv
Table of Contents	vi
List of Figures	viii
1. Introduction	1
1.1 Plasmonic Systems	2
1.2 Response Functions	3
1.3 Nonlocality and Nonlinearity	6
1.4 Motivation and Overview	13
<u>PART I: NONLOCAL RESPONSE PHENOMENA</u>	16
2. Nonlocal Physics of Plasmonic Systems	17
2.1 Electronic Response: Drude, RPA, & LDA	17
2.2 The Hydrodynamic Approximation	26
2.3 The d-Function Formalism	29
2.4 Charge Centroid Model of the d-Function	38
3. Extended d-function Formalism	42
3.1 Dynamic Charge Centroid Model	43
3.2 Full <i>ab initio</i> Nonlocal Response of Metallic Slabs	54
3.3 HDA-extended d-function Formalism	60
3.4 Effective Medium Scaling Properties	62
3.5 Self-Energy Extension of Dielectric Response	64
4. Effective Thin-Film Method	67
4.1 Geometric Mapping of d-Function Formalism	68
4.2 Identification of Physically Valid Response	74
4.3 Nonlocal Mie Resonance of Metallic Spheres	82
<u>PART II: NONLINEAR RESPONSE PHENOMENA</u>	92
5. Nonlinear Response of DNA with Strong Driving	93
5.1 Motivation & General Characteristics of DNA	94
5.2 Nonlinear Model of Double-Stranded DNA	97
5.3 Model Simulations	105
5.4 Behavior of Homogeneous AT and GC Sequences	111
5.5 Behavior of Single Base-Pairs in Heterogeneous Sequences	123
5.6 Comparison of Different Heterogeneous Sequences	133
5.7 Discussion and Caveats	140

6. Difference Frequency Generation for Biological Applications	142
6.1 Enhanced Penetration Depth via DFG	143
6.2 Derivation of Classical Miller's Rule for DFG	149
6.3 Simulation of DFG from Classical Anharmonic Oscillator	155
7. Effective Miller's Rule for Plasmonic DFG	174
7.1 Modal Model of Plasmonic Response	174
7.2 Optimization of Difference Frequency Generation	183
7.3 Driven DNA Damage with Plasmonic DFG	202
8. Conclusion	209
8.1 Summary of Work	209
8.2 Outlook and Future Work	211
Bibliography	214
Appendices	223
A. List of Physical Constants	224
B. Maxwell and Auxiliary Equations	225
C. Derivation of Surface Plasmon Condition	227
D. Derivation of Reflection from Two Layers	229
E. Simulations of mPBD Model at T=310 K	232
F. Derivation of DFG from Frequency Modulated Signal	235

LIST OF FIGURES

<u>Figure</u>		
1.1	Gaussian spatial response	8
1.2	Fourier transform of gaussian spatial response	8
1.3	Delta-function spatial response	9
1.4	Fourier transform of delta-function spatial response	9
1.5	Linear harmonic oscillator response	12
1.6	Anharmonic oscillator response	12
2.1	Drude model fit to Al	19
2.2	SP disperion of Al for small- q	22
2.3	Nonlocal SP disperion of Al	23
2.4	Comparison of HDA dispersion with LDA & exp. (for potassium) . . .	28
2.5	The d-function of potassium from literature	31
2.6	Model fit to the d-function of potassium	33
2.7	Comparison of d-function dispersion with LDA & exp. (for potassium)	35
2.8	Comparison of extended dispersion with LDA & exp. (for potassium)	37
2.9	Tsuei model of SP dispersion	40
3.1	Dynamic charge centroid model fit to RPA calculation (1)	47
3.2	Dynamic charge centroid model fit to RPA calculation (2)	48
3.3	Dynamic charge centroid model fit to RPA calculation (3)	49
3.4	Dynamic charge centroid model fit to RPA calculation (4)	50
3.5	Dynamic charge centroid model fit to RPA calculation (5)	51
3.6	Dynamic charge centroid model fit to RPA calculation (6)	52
3.7	Lang-Kohn potential of metallic slab	56
3.8	Eigenfunctions calculated within the Lang-Kohn potential	57
3.9	RPA calculations of metallic jellium	59

3.10	SP dispersions for metallic jellium slabs	61
4.1	Schematic of effective thin-film method	69
4.2	Reflection geometry for p-polarized light	71
4.3	Thin-film dielectric function (1)	75
4.4	Thin-film dielectric function (2)	76
4.5	Thin-film reflection coefficient (1)	78
4.6	Thin-film reflection coefficient (2)	79
4.7	Absorption cross-section: fixed R_c	84
4.8	Absorption cross-section: fixed Δd	86
4.9	Absorption cross-section: fixed R	87
4.10	Mie frequency vs. particle size	89
5.1	DNA geometry	95
5.2	PBD schematic diagram	98
5.3	Total potential energy of AT and GC pairs at equilibrium	100
5.4	Contributions to potential energy of nth AT pair (1)	102
5.5	Contributions to potential energy of nth AT pair (2)	103
5.6	Contributions to potential energy of nth AT pair (3)	104
5.7	Average energy vs. simulation time	107
5.8	Average energy and melting transition	108
5.9	Time-series: GC sequence at A=200 pN and f=1.5 THz	110
5.10	Average base-pair separation for homogeneous AT sequence	112
5.11	Average base-pair separation for homogeneous GC sequence	113
5.12	Continuous driving at A=100 pN and f=1.5 THz	115
5.13	Continuous driving at A=150 pN and f=1.5 THz	116
5.14	Continuous driving at A=150 pN and f=1 THz	117
5.15	Continuous driving at A=100 pN and f=1 THz	118

5.16	10ps pulse at A=100 pN and f=1.5 THz	120
5.17	50ps pulse at A=100 pN and f=1.5 THz	121
5.18	10ps pulse at A=150 pN and f=1.5 THz	122
5.19	Damage threshold for homogeneous AT & GC sequences	124
5.20	Homogeneous sequences with one BP substitution: A=400 pN and f=1.5 THz	126
5.21	Homogeneous sequences with one BP substitution: A=400 pN and f=2.8 THz	127
5.22	Homogeneous sequences with one BP substitution: A=200 pN and f=1.5 THz	128
5.23	Homogeneous sequences with one BP substitution: A=200 pN and f=2.8 THz	129
5.24	Heterogeneous vs. homogeneous sequences: A=400 pN	131
5.25	Heterogeneous vs. homogeneous sequences: A=200 pN	132
5.26	Heterogeneous sequence with evenly ordered BP substitution: A=400 pN and f=1.5 THz	135
5.27	Heterogeneous-even vs. homogeneous sequences: A=400 pN	136
5.28	Heterogeneous sequence with randomly ordered BP substitution: A=400 pN and f=1.5 THz	137
5.29	Heterogeneous-random vs. homogeneous sequences: A=400 pN	138
5.30	Heterogeneous-random vs. heterogeneous-even: A=400 pN	139
5.31	Absorption spectrum of water	141
6.1	Absorption spectrum of human body	143
6.2	Penetration depths schematic	146
6.3	DFG parameter space (1)	147
6.4	DFG parameter space (2)	148

6.5	Time series and Fourier transform of anharmonic oscillator	157
6.6	Full response of anharmonic oscillator to two driving frequencies . . .	159
6.7	Second-order response of anharmonic oscillator (1)	161
6.8	Second-order response of anharmonic oscillator (2)	162
6.9	Analytic vs. simulated linear response of anharmonic oscillator	164
6.10	Comparison of simulated first-order response with analytic formula (1)	165
6.11	Comparison of simulated first-order response with analytic formula (2)	166
6.12	Comparison of simulated DFG response and Miller's rule (1)	167
6.13	Comparison of simulated DFG response and Miller's rule (2)	168
6.14	3D parameter space of ω_1 , ω_2 and Fourier spectra	170
6.15	DFG response for $\omega_2 \geq \omega_1$ and $\omega_0 = 4$ rad/s	172
6.16	DFG response for $\omega_2 \geq \omega_1$ and $\omega_0 = 6$ rad/s	173
7.1	DFG from PNP model with three resonances (1)	185
7.2	DFG from PNP model with three resonances (2)	188
7.3	DFG from PNP model with three resonances (3)	189
7.4	DFG from PNP model with three resonances (4)	190
7.5	DFG from PNP model with three resonances (5)	191
7.6	DFG from PNP model with three resonances (6)	192
7.7	DFG from PNP model with three resonances (7)	193
7.8	DFG from PNP model with three resonances (8)	194
7.9	DFG from PNP model with three resonances (9)	195
7.10	DFG from PNP model with three resonances (10)	196
7.11	DFG from PNP model with three resonances (11)	197
7.12	DFG from PNP model with three resonances (12)	198
7.13	DFG from PNP model with three resonances (13)	199
7.14	DFG from PNP model with three resonances (14)	200

7.15	DFG from PNP model with three resonances (15)	201
7.16	Homogeneous AT sequence at high frequencies	204
7.17	Homogeneous GC sequence at high frequencies	204
7.18	Homogeneous sequence with one BP substitution: driving with no DFG	206
7.19	Homogeneous sequence with one BP substitution: driving with DFG	207
E.1	Average energy vs. simulation time: T=310 K vs. T=290 K	233
E.2	Average base-pair separation for homogeneous AT sequence (T=310 K)	234

CHAPTER 1

Introduction

This thesis is an examination of second-order response phenomena of plasmonic systems. By second-order phenomena, we mean physics that is generally neglected in leading-order models because the contributions of such effects are small in magnitude compared to leading-order effects, in typical regimes of interest. For instance, the nonlocal (q -dependent) response of plasmonic systems is usually neglected in regimes of small q , such that $\chi(q, \omega) \approx \chi(0, \omega)$. Similarly, higher-order responses introduced by nonlinearities in plasmonic systems are typically not considered, such that $\chi(t) = \chi^{(1)}(t) + \chi^{(2)}(t) + \chi^{(3)}(t) + \dots \approx \chi^{(1)}(t)$. In this work, we investigate response models, $\chi(q, \omega)$, in the moderate to large- q range, and second-order effects introduced by nonlinearities, $\chi^{(2)}(t)$, for plasmonic systems with nontrivial geometries and structures. In this chapter, we define the terminology introduced above, develop a general picture of response theory, and explain how nonlocality and nonlinearity are manifested in generic systems. We conclude by summarizing the material to be presented in the remaining chapters.



1.1 Plasmonic Systems

At a most basic level, a *plasmonic* system is metallic. It has free carriers (i.e., electrons in its conduction band) that behave, to first order, like a free electron gas. Metallic systems range from alkali metals to noble metals with electron densities on the order of $n \sim 10^{28} \text{ m}^{-3}$. Other systems, e.g., doped semiconductors, also exhibit metallic behavior. The collective properties of these free carriers are defined as *plasmonic* properties and include plasma waves of various types. For instance, bulk plasmon waves called “plasmons” propagate through metals above a characteristic plasma frequency, $\omega_p^2 = ne^2/m_{eff}\epsilon_0$, that depends on the density of the charge carriers, n , their effective mass, m_{eff} , their charge e , and the permittivity, ϵ_0 [1] (we include a list of physical constants in Appendix A). Plasma waves cannot propagate below this frequency [1] and, therefore, metals are reflective below ω_p , from visible frequencies and below, but they can be transparent for frequencies above the ω_p , e.g., in the UV range [1].

Additionally, in the next chapter we discuss surface plasmons (SPs), which propagate at the interfaces of a metallic systems. The coupling between surface plasmons and light generates surface-plasmon-polaritons (SPPs), which manifest themselves, e.g., in the reflective properties of a system [1]. Plasmons also interact with phonons [2] and single electrons [3] and, therefore, they augment thermal and transport properties. Plasmonic systems host a huge variety of phenomena.

Finally, structured metallic systems can also exhibit plasmonic dynamics as a result of their effective medium behavior [1], i.e., subwavelength structures induce collective effects that make the system behave as if it were imbued with the properties of a completely different medium [4]. Thus, the sensitivity of plasmonic modes to material and structural degrees of freedom obviously permits a large design space for the realization of novel phenomena including cloaking [5], perfect absorption [6],

epsilon near-zero materials [7, 8], etc. For a rich and thorough review of plasmonic properties see [1]. We will elaborate on some of the above material in the next chapter.

In this thesis, we argue that nonlocal and nonlinear properties of plasmonic systems offer yet additional degrees that may be tuned to affect the response phenomena of these systems. In the next section, we expand upon this concept.

1.2 Response Functions

By “response phenomena,” we refer to the behavior of a system when acted upon by external forces. Response functions of plasmonic systems, e.g., the dielectric function, $\epsilon(q, \omega)$, or electric susceptibility, $\chi(q, \omega)$, can be used to calculate observable properties like reflectance, where the reflection coefficient at normal incidence on a flat interface between vacuum and a material is related to $\epsilon(q, \omega)$ through $r = (\epsilon(q, \omega) - 1)/(\epsilon(q, \omega) + 1)$, in the non-retarded limit, or scattering rates, which involve terms that depend on $\text{Im}\{\epsilon^{-1}(q, \omega)\}$. Largely, this thesis is a study of response functions, which take into account the microscopic properties of a system.

To illustrate the simplest possible example of a response function, and to introduce a model that we will subsequently return to in this work, we briefly consider the polarization of a system composed of bound charges in response to an oscillating electric field. Eq. (1.1) gives the local, time-dependent polarization of a medium in response to an applied field $\vec{E}(t)$ (for now, we drop the spatial dependence \vec{r}), where $\vec{\chi}(t - t')$ is the retarded electric susceptibility:

$$\vec{P}(t) = \epsilon_0 \int \vec{\chi}(t - t') \vec{E}(t') dt' \quad (1.1)$$

For a geometry in three spatial dimensions, the response function $\vec{\chi}(t - t')$ is a tensor. Thus the i^{th} component of the polarization would be written as $P_i(t) = \varepsilon_0 \int \chi_{ij}(t - t') E_j(t') dt'$, for an incident field $E_j(t)$. For simplicity, we drop the vector notation and just refer to the scalar response. Also, it is often useful to work with the frequency response of the system, rather than the time-dependent response. This is obtained through the Fourier transform of the time-dependent response, using the convolution theorem, and is given as:

$$P(\omega) = \varepsilon_0 \chi(\omega) E(\omega) \quad (1.2)$$

To obtain $\chi(\omega)$, which is our objective, we consider the microscopic physics. Each bound charge (i.e., electron coupled to a large, fixed ion) can be modeled as a mass in a harmonic potential, driven by a sinusoidal electric field, $E(t) = E(\omega) \exp[-i\omega t]$. The equation of motion is:

$$m\ddot{x}(t) + \gamma m\dot{x}(t) + m\omega_0^2 x(t) = -eE(t) \quad (1.3)$$

where m and e are the mass and charge of the particle, γ is the phenomenological damping parameter, and ω_0 is the resonant frequency of the system. The dynamical variable $x(t)$ is the position of the electron.

Assuming that the system exhibits a harmonic, time-dependent response, $x(t) = x(\omega) \exp[-i\omega t]$, we can rewrite the equation of motion in the frequency domain:

$$-\omega^2 x(\omega) - i\omega\gamma x(\omega) + \omega_0^2 x(\omega) = -\frac{e}{m} E(\omega) \quad (1.4)$$

Solving for the electron's frequency-dependent amplitude, we get:

$$x(\omega) = -\frac{e}{m} \frac{E(\omega)}{(\omega_0^2 - \omega^2 - i\gamma\omega)} \quad (1.5)$$

The polarization is related to the amplitude of the system via $P(\omega) = \epsilon_0\chi(\omega)E(\omega) = -nex(\omega)$, leading to:

$$\chi(\omega) = \frac{\omega_p^2}{(\omega_0^2 - \omega_j^2 - i\gamma\omega_j)} \quad (1.6)$$

where n is the number density of bound charges and we have used the definition of the plasma frequency, $\omega_p^2 = ne^2/m\epsilon_0$.

In this simple example, we have illustrated how a response function, in this case the electric susceptibility, convolves an external force to produce a response of the system. The response function is “built” from knowledge of the underlying, microscopic properties of the system. In chapter 2, we will discuss response theory as it relates to electron systems, and this theory will take into account the proper, quantum mechanical details of electron-electron interactions. However, one conclusion from the above analysis is quite general. That is, once the response function of a system is known, whether it is derived from first principles or a phenomenological model, the behavior of a system in response to external forces can be fully described. The models of plasmonic response functions that we investigate will enable us to describe physical observables (e.g., reflection coefficients, scattering amplitudes, etc.) of systems under investigation.

1.3 Nonlocality and Nonlinearity

Continuing with the general example of polarization, we now discuss nonlocality and nonlinearity. Locality refers to a response that occurs at the same space-time coordinates as an external perturbation. The form of the electric susceptibility introduced in the previous section, Eq. (1.6), is *temporally nonlocal* (i.e., retarded) because it generates polarization at time t that depends on the electric field at all previous times t' . A *temporally local* response (i.e., non-retarded) occurs instantaneously in time. Now, referring to the spatial dependence of response phenomena, a *spatially local* response only occurs where a force is applied, whereas a *spatially nonlocal* response occurs at many spatial locations. Again, considering the electric susceptibility response function, nonlocality must be incorporated as follows (here we work in the frequency domain):

$$P(\vec{r}; \omega) = \varepsilon_0 \int \chi(\vec{r} - \vec{r}'; \omega) E(\vec{r}'; \omega) d\vec{r}' \quad (1.7)$$

As done in the previous section, we can express the Fourier transform of Eq. (1.7) using the convolution theorem, where the conjugate variable of \vec{r} is the wave-vector, \vec{q} :

$$P(\vec{q}, \omega) = \varepsilon_0 \chi(\vec{q}, \omega) E(\vec{q}, \omega) \quad (1.8)$$

We will often be working with the conjugate variable \vec{q} , so it is important to emphasize the meaning of locality and nonlocality in terms of the q -dependence of a response function. Clearly, if a response function is *spatially nonlocal*, then it will be q -dependent, as shown by Eq. (1.8). On the other hand, a *local* response function will not depend on q . To see this by way of example, we consider a fictitious nonlocal response function, a Gaussian in one spatial dimension. The response function and

its Fourier transform are given below:

$$\chi(x - x'; \omega) = \chi_0(\omega) \exp\{-a^2(x - x')^2\} \quad (1.9)$$

$$\chi(q, \omega) = \chi_0(\omega) \left(\frac{\pi}{a}\right)^{3/2} \exp\left\{-\left(\frac{\pi}{2a}\right)^2 q^2\right\} \quad (1.10)$$

Now, we consider a fictitious local response function, a delta-function in one spatial dimension. Again, the response function and its Fourier transform are given below:

$$\chi(x - x'; \omega) = \chi_0(\omega) \delta(x - x') \quad (1.11)$$

$$\chi(q, \omega) = \chi_0(\omega) \quad (1.12)$$

These functions are plotted in Fig. 1.1 - 1.4. The Fourier transform of a spatially nonlocal response is q -dependent, whereas the Fourier transform of a spatially local response (e.g., a delta-function) is q -independent.

We mentioned that nonlocal effects become pronounced in small systems and, therefore, must be considered in response models of plasmonic systems. The simplistic reasoning is that, in a large system, the response in one spatial part of the system does not necessarily need be considered when calculating the response at another part of the system. However, for spatially confined systems, part of the system may greatly affect nearby parts, and therefore, spatial dependence is more pronounced.

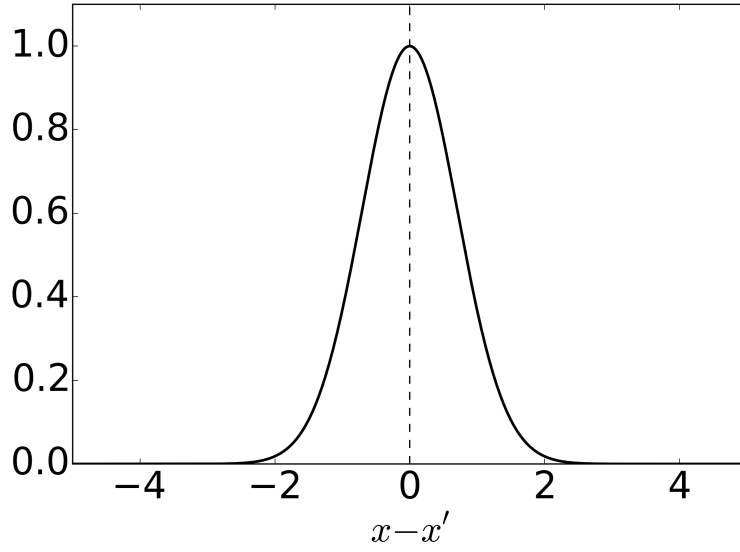


Figure 1.1: *Gaussian spatial response:* based on Eq. (1.9)

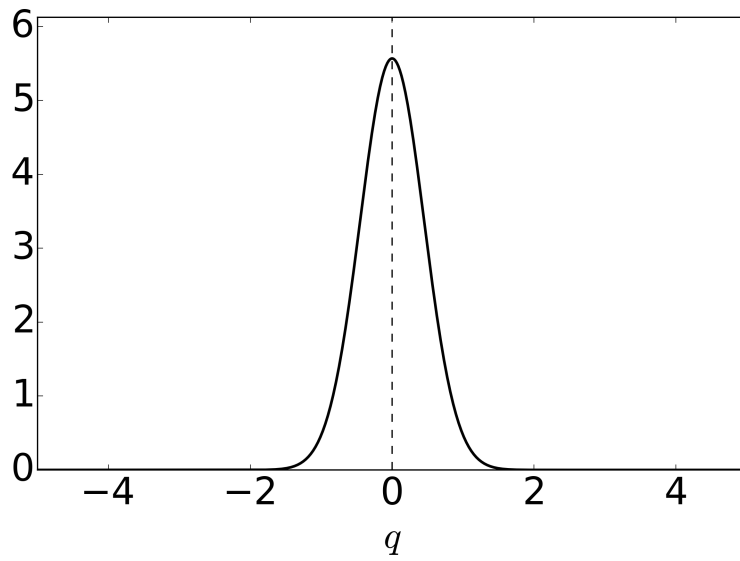


Figure 1.2: *Fourier transform of gaussian spatial response:* based on Eq. (1.10)

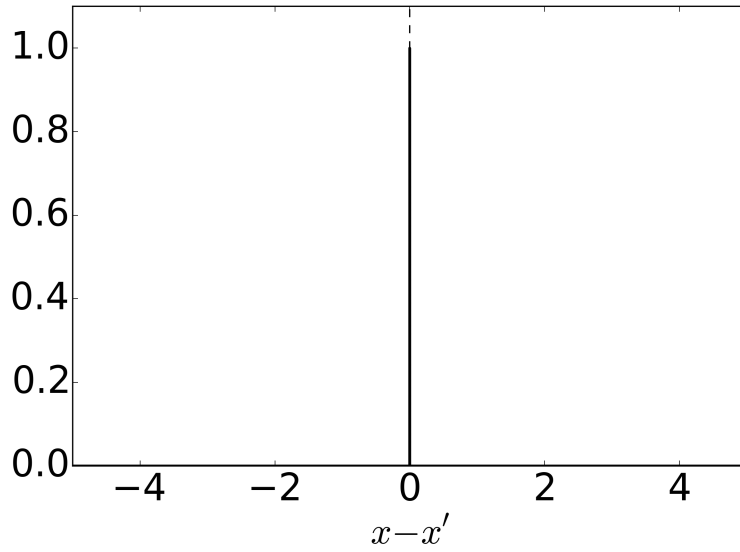


Figure 1.3: *Delta-function spatial response:* based on Eq. (1.11)

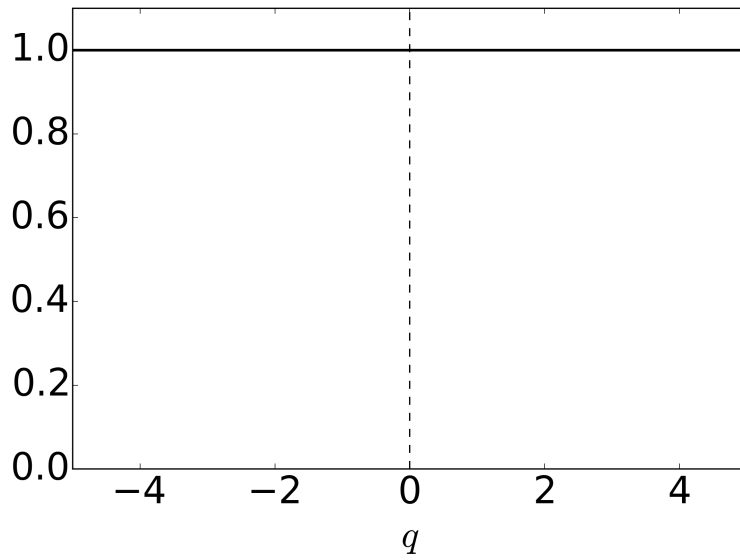


Figure 1.4: *Fourier transform of delta-function spatial response:* based on Eq. (1.12)

Another aspect of systems that we are studying in this thesis is the production of higher-order response phenomena caused by nonlinearity. To examine this characteristic, we again refer to the situation where a local system is driven by a harmonic electric field:

$$P(t) = \varepsilon_0 \int \chi(t - t') E(t') dt' \quad (1.13)$$

Now, we will make a perturbative expansion of the response, thus introducing higher order terms, like $\chi^{(2)}$, $\chi^{(3)}$, etc.

$$P(t) = \varepsilon_0 \left[\int \chi^{(1)}(t - t') E(t') dt' + \int \int \chi^{(2)}(t - t', t' - t'') E(t') E(t'') dt' dt'' + \dots \right] \quad (1.14)$$

Again, system is most readily analyzed in Fourier space. If we assume that the driving signal has the form $E(t) = E(\omega) \cos(\omega t)$, then the Fourier transform of Eq. (1.14) is:

$$P(\omega) = \varepsilon_0 \left[\underbrace{\chi^{(1)}(\omega) E(\omega)}_{\text{1st order}} + \underbrace{\chi^{(2)}(0) E^2(0) + \chi^{(2)}(2\omega) E^2(2\omega)}_{\text{2nd order}} + \dots \right] \quad (1.15)$$

Thus, the first order response of the system is the harmonic response, and there exist two contributors to the second-order response, for the specific example of a harmonic driving signal. These two contributions are the so-called DC response and the second-harmonic response. In other words, in a simple linear system, the “output” signal has the same frequency components as the “input” signal. However, the existence of nonlinearity in a system will cause additional harmonics to appear in the output signal. We note that a nonlinear system can generate many different frequency combinations in its second-order response depending on the har-

monic characteristics of the driving input. For instance, the second-order response for a driving electric field with two frequency components will contain signals at the sum-frequency and difference-frequency of the inputs, in addition to the DC and second-harmonic responses.

The responses of two realistic systems to harmonic driving forces are shown in the following figures, one shows a simple, linear harmonic oscillator and the other shows a nonlinear, anharmonic oscillator. The equation of motion for the linear system is given by Eq. (1.3), and the equation for the nonlinear system is:

$$m\ddot{x}(t) + \gamma m\dot{x}(t) + m\omega_0^2 x(t) + max^2(t) = -eE(t) \quad (1.16)$$

where a is the strength of the nonlinearity of the system. The response is shown in both the time domain and frequency domain. In the frequency domain, we can observe that the nonlinear oscillator indeed exhibits a second-order response, seen as an additional frequency characteristic at $\omega = 2\omega_0$.

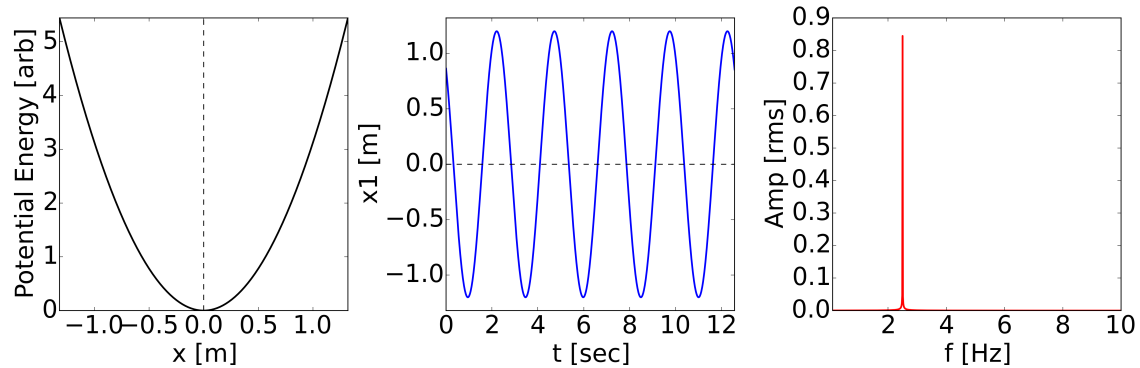


Figure 1.5: *Linear harmonic oscillator response.* Left: the symmetric, harmonic potential. Center: the time series response of the oscillator. Right: the Fourier transform of the time series. There is a single feature in the frequency domain, at the driving frequency.

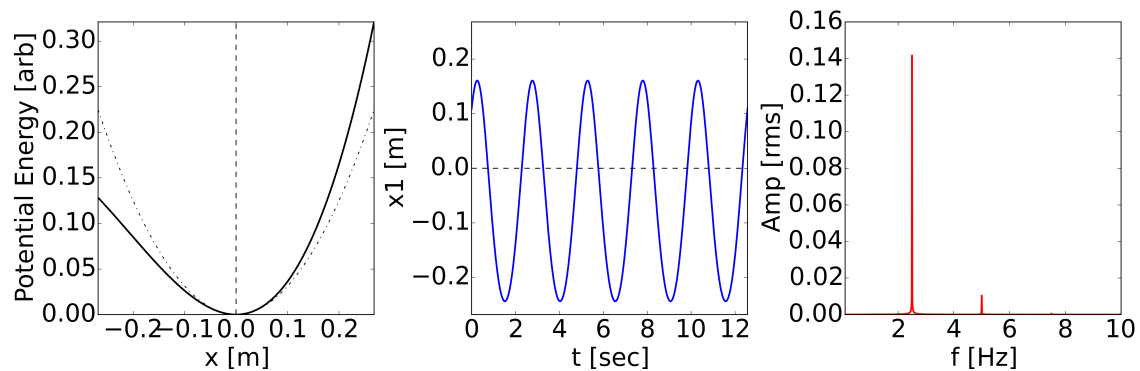


Figure 1.6: *Anharmonic oscillator response.* Same format as above. The nonlinearity makes the potential non-symmetric and introduces a feature in the frequency domain at the second harmonic of the driving frequency.

1.4 Motivation and Overview

In *Part I* of this work, we discuss nonlocal extensions to the canonical, local Drude response theory of metallic systems [9]. We explore q -dependent models of plasmonic response functions that are applicable to structured surfaces and non-trivial geometries ranging from the nanoscale to mesoscale. Existing nonlocal models of electronic response include the phenomenological hydrodynamic approximation (HDA) [10] and the *ab initio* d-function formalism [11, 12]. In §2, we discuss these formalisms and lay the groundwork for understanding the models presented in subsequent chapters.

In §3, we discuss how to combine the aforementioned d-function formalism and HDA to produce an “extended d-function formalism,” which is capable of qualitatively describing nonlocal properties of plasmonic systems to higher order in q . We demonstrate that this model describes the nonlocal dispersion of surface plasmons at the interface of a metallic slab, through comparison with *ab initio* calculations, and argue how it can be applied to structured surfaces with effective medium parameters (e.g., metamaterials). The work in this chapter was published by the author in Ref. [13].

Finally, in §4, we investigate methods to incorporate the nonlocal characteristics of real metals into local FDTD calculations using the d-function formalism. This is done via mapping nonlocal properties onto a local, fictitious film, which can be explicitly included in local calculation schemes. It is the permittivity of the added film that imbues the system with nonlocal properties, thus the proper choice of permittivity is required. The non-uniqueness of the mapping relation leads to several possible choices of permittivity, which are discussed. Several mappings are physically valid, but we argue that one solution best reflects the nonlocal physics. Finally, we discuss how the incorporation of this film affects the nonlocal Mie resonance of spherical nanoparticles and compare with literature. The work in this chapter is

related to our publication, Ref. [14].

In *Part II*, we focus on one project, with several interconnected areas of investigation, related to the realization of damaging double-stranded DNA via THz radiation, and supported by the National Science Foundation, grant No. PHY1725118. This study comprises the nonlocal and nonlinear behavior of both biological and plasmonic phenomena and is thus an extension of the theme of this thesis, which is the examination of higher-order response phenomena.

In §5, we study the behavior of double-stranded DNA in the regime of strong driving, where the system is highly nonlinear. We discuss destructive behavior, where the system is driven towards “breaking” in certain regions of parameter-space. The objective of this investigation was to find the regions of parameter-space where damage occurs (i.e., for different driving amplitudes and frequencies), such that DNA is effectively destroyed. This investigation is motivated by an ongoing effort to demonstrate selective molecular damage at THz frequencies for potential therapies, and at the date of publication of this thesis, we are preparing these results for publication.

A major complication of using THz radiation to selectively damage biological constituents *in vivo* is that the body is opaque to THz frequencies. Thus, it is desirable to use higher frequencies to deeply penetrate the body, then locally convert this power into a THz signal. This frequency conversion—specifically, the demodulation of two high frequencies into a lower frequency that is equal to their difference—is a nonlinear phenomenon called difference-frequency generation (DFG), that could be promoted by local plasmonic constituents. Therefore, in the remaining two chapters, we examine nonlinear models of plasmonic response, primarily utilizing the anharmonic oscillator model as a classical analogy, with the objective of promoting DFG in plasmonic systems.

In §6, we first present a thorough derivation and analysis of the response of a

simple anharmonic oscillator. We derive the classical “Miller’s rule” [15], which perturbatively relates the second-order response function of a system to a product of first-order response functions. We numerically integrate the equation of motion of this simple system to calculate the full nonlinear response and demonstrate that the numerically simulated properties adhere to Miller’s rule, in a perturbative limit. We seek to utilize a Miller-like relation for complex plasmonic systems, where simulation of first-order properties can be readily performed.

Finally, in §7, we explore the nonlinear response of plasmonic oscillators (e.g., metallic nanoparticles). Specifically, we examine a modal model of plasmonic response and propose an “effective” Miller’s rule, which describes the second-order polarizability of the plasmonic system in terms of its first-order polarizability. We discuss the potential use of this model for understanding and optimizing difference-frequency generation (DFG) from plasmonic nanoparticles, with the objective of utilizing plasmonic-DFG to generate strong THz fields within the body to target DNA.

PART I:

NONLOCAL RESPONSE PHENOMENA

CHAPTER 2

Nonlocal Physics of Plasmonic Systems

In the introduction, we discussed some salient properties of response functions, very generally, and introduced the definition of nonlocality, but in this chapter we will specifically discuss these properties as they relate to plasmonic systems. First, we examine the local Drude model and discuss regimes where it is accurate, as well as where it fails. Then we introduce first-principles calculations of the nonlocal electronic response and examine two formalisms: the phenomenological hydrodynamic approximation (HDA) and the d-function formalism. In the subsequent two chapters, we expand upon these approaches.



2.1 Electronic Response: Drude, RPA, & LDA

Starting from the forced, damped, simple harmonic oscillator model of a charge from the previous chapter, it is straightforward to derive the Drude model response of a metal [1,2]. The Drude model response is equivalent to the assumption that the electron experiences no restoring force, therefore the susceptibility is:

$$\chi(\omega) = -\frac{\omega_p^2}{\omega(\omega + i\gamma)} \tag{2.1}$$

and the dielectric function is related to the susceptibility through $\epsilon(\omega) = 1 + \chi(\omega)$, such that:

$$\epsilon(\omega) = 1 - \frac{\omega_p^2}{\omega(\omega + i\gamma)} \quad (2.2)$$

Eq. (2.2) is a rudimentary, classical model of electronic response, but it goes quite far in accurately describing real systems. For instance, the Drude model fit to the dielectric function of aluminum (Al) is shown in Fig. 2.1 on a log-scale, where Drude model parameters are from [16] and dielectric function data are from [17]. The Drude response has high fidelity at high frequencies, and captures the low frequency features qualitatively.

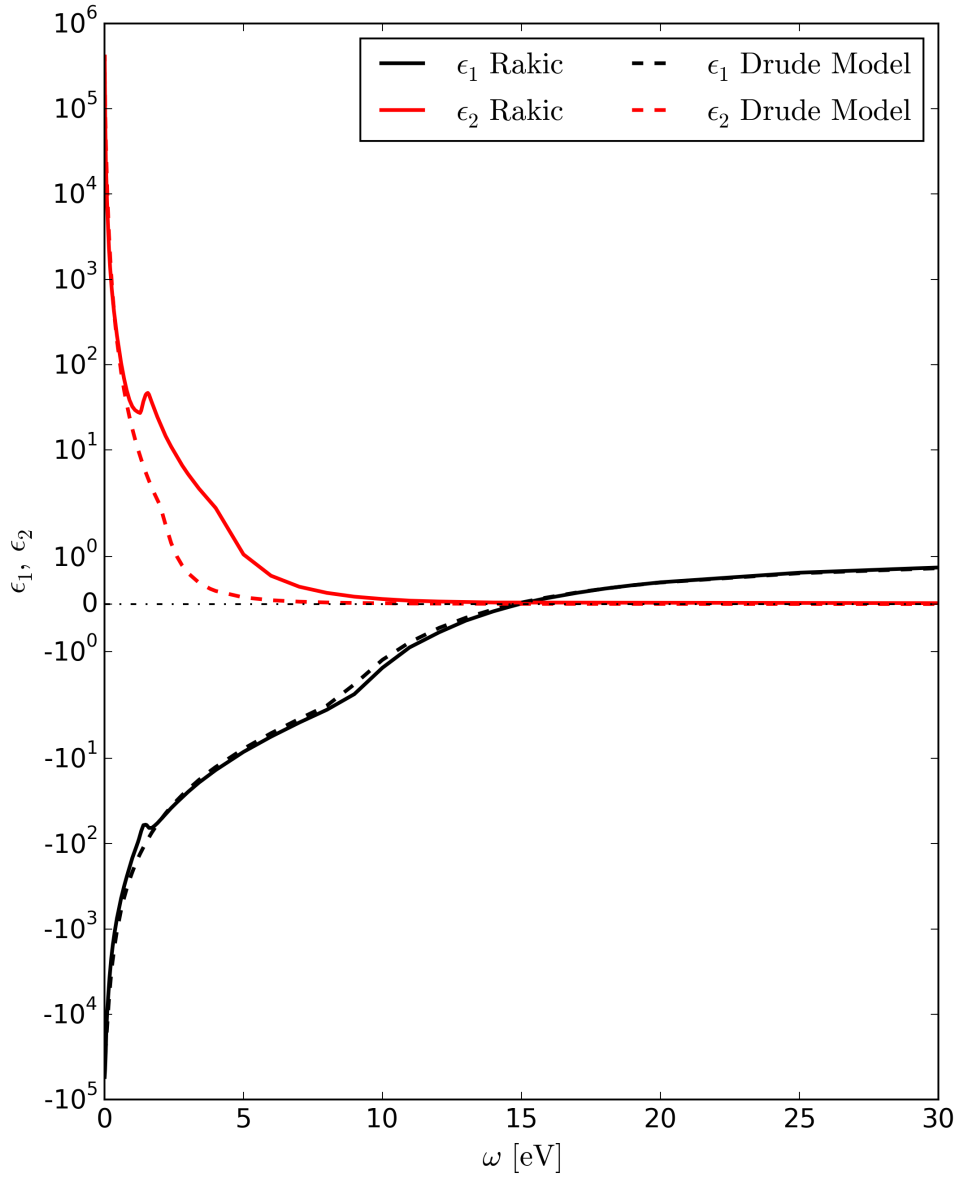


Figure 2.1: *Drude model fit to Al.* Drude model parameters are from [16] (dashed lines) and dielectric function data are from [17] (solid lines). The black and red colors correspond to real and imaginary parts of ϵ , respectively.

Additionally, the Drude model response yields an accurate prediction for the SP dispersion in the small- q regime, as measured experimentally from reflection spectra. Below, we derive the SP dispersion relation and afterwards compare with data from literature. For a plane wave incident on the planar interface of a nonmagnetic medium, the boundary conditions for the fields lead to the following relation for the wavevector [1] (see Appendix B for Maxwell's equations and Appendix C for a full derivation, based on reflection geometry of Fig. 4.2):

$$q = \frac{\omega}{c} \sqrt{\frac{\epsilon(\omega)}{\epsilon(\omega) + 1}} \quad (2.3)$$

Inserting the Drude model into the above equation and solving for $\omega(q)$, we obtain the surface plasmon dispersion. In the equation below, we have used $\gamma = 0$ to simplify the expression (when $\gamma \neq 0$, the dispersion is cumbersome to express analytically, but still straightforward to compute numerically).

$$\omega(q) = \left[\frac{\omega_p^2}{2} + (cq)^2 \pm \left[\left(\frac{\omega_p^2}{2} \right)^2 + (cq)^4 \right]^{1/2} \right]^{1/2} \quad (2.4)$$

From Eq. (2.4), we see that the surface plasmon mode has an upper branch and lower branch, which fall above and below the light-line, $\omega = cq$, respectively. The upper surface plasmon branch is radiative and, therefore, dissipates quickly [1]. The lower surface plasmon branch follows the light-line for small wavevectors and reaches a plateau at the surface plasma frequency $\omega_{sp} = \omega_p/\sqrt{2}$, in the $\omega/c \ll q$ limit. The SP frequency can also be derived from the roots of the reflection coefficient for light normally incident on a planar surface, $r = (\epsilon(\omega) - 1) / (\epsilon(\omega) + 1)$, which yields the relation $\epsilon(\omega) = -1$, for which ω_{sp} is a solution.

In Fig. 2.2, we show the SP dispersion for aluminum in the small- q , retarded

regime, with experimental data shown in the figure inset [18]. The two branches of Eq. (2.4) are shown as black lines, ω_p is shown as a magenta line, ω_{sp} is shown as a cyan line, and the red-dashed line shows the solution to Eq. (2.3) for $\gamma \neq 0$. Note, the upper and lower modes are connected in a characteristic s-shape. The light-line, $\omega = cq$, is also shown as a black-dashed line.

The Drude model is accurate in the retarded limit, $\omega/c \sim q$, which is why it is so predictive for the SP dispersion near the light-line. However, the model begins to break down in the non-retarded limit, where $\omega/c \ll q$. For instance, at higher wavevectors, $q \sim 10^{-1} \text{\AA}^{-1}$, the Drude model no longer captures observed behavior. We show this highly nonlocal regime in the second figure, Fig. 2.3, with data of the SP mode at high-q obtained from electron energy-loss spectroscopy (EELS) [19]. The EELS data for the SP mode are slightly *less than* the classical SP frequency for moderate q-values ($q \sim 10^{-1} \text{\AA}^{-1}$), and then become *greater than* ω_{sp} for higher-q.

The high-q dispersive behavior can be described by *ab initio* quantum formalisms, which we detail next. We plot the results from one formalism, the local density approximation (LDA) [19], in Fig. 2.3 to illustrate the nonlocal behavior and we will discuss the details of this formalism later. However, we emphasize that *ab initio* quantum formalisms are cumbersome if not intractable when applied to complex, structured systems. Thus it is the objective of this work to extend existing nonlocal formalisms using an effective medium perspective, without the need for intractable, first-principles calculations. We will expand more on this point in the next two chapters.

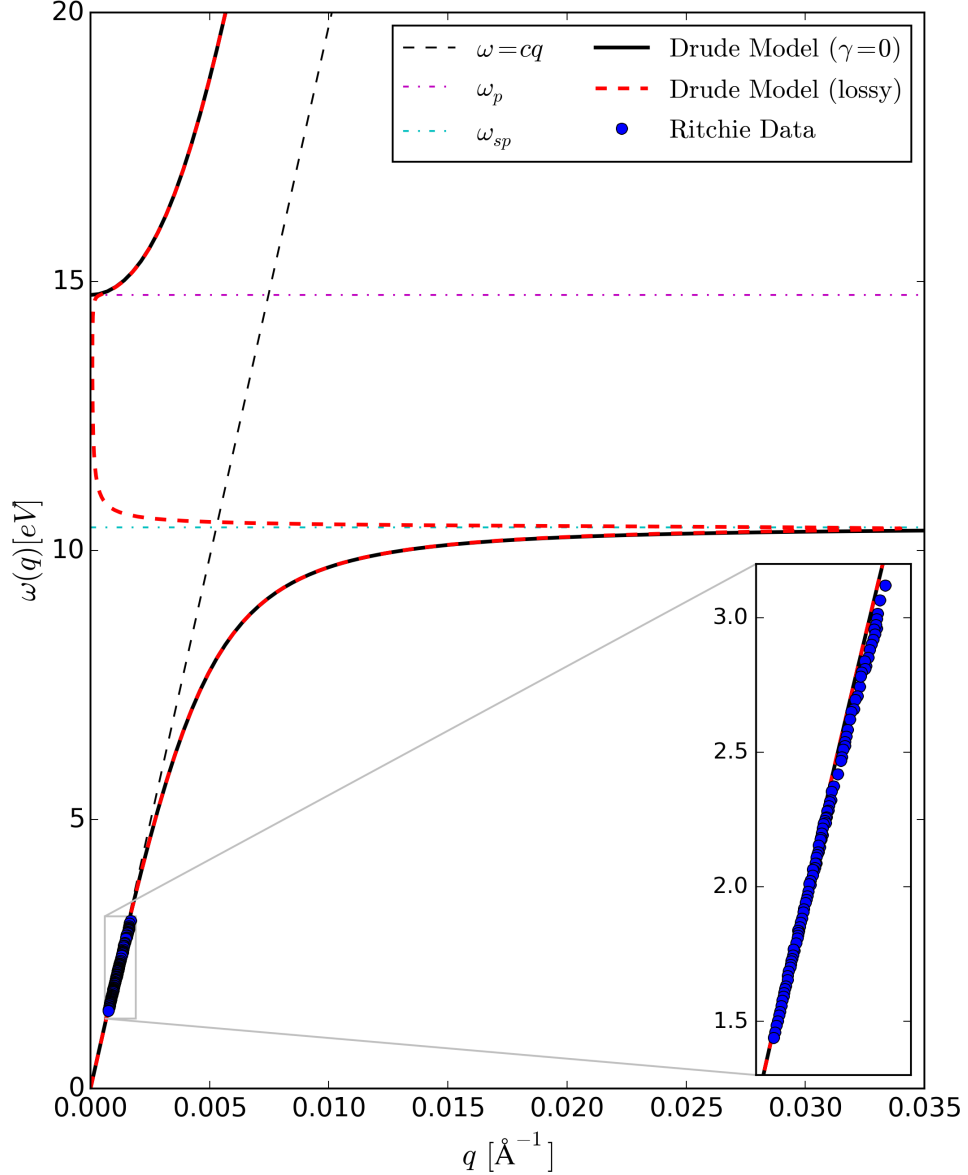


Figure 2.2: *SP dispersion of Al for small- q .* Dispersion based on the Drude model parameters of [16]. The dispersion is plotted for $\gamma = 0$ (black solid line) and $\gamma \neq 0$ (red dashed line), showing that the lossy Drude model yields a characteristic s-shaped dispersion. Shown are the light-line, $\omega = cq$ (black dashed line), the plasma frequency, ω_p (magenta dash-dotted line), and the SP frequency, $\omega_{sp} = \omega_p/\sqrt{2}$ (green dash-dotted line). The inset shows measured SP dispersion with data from [18].

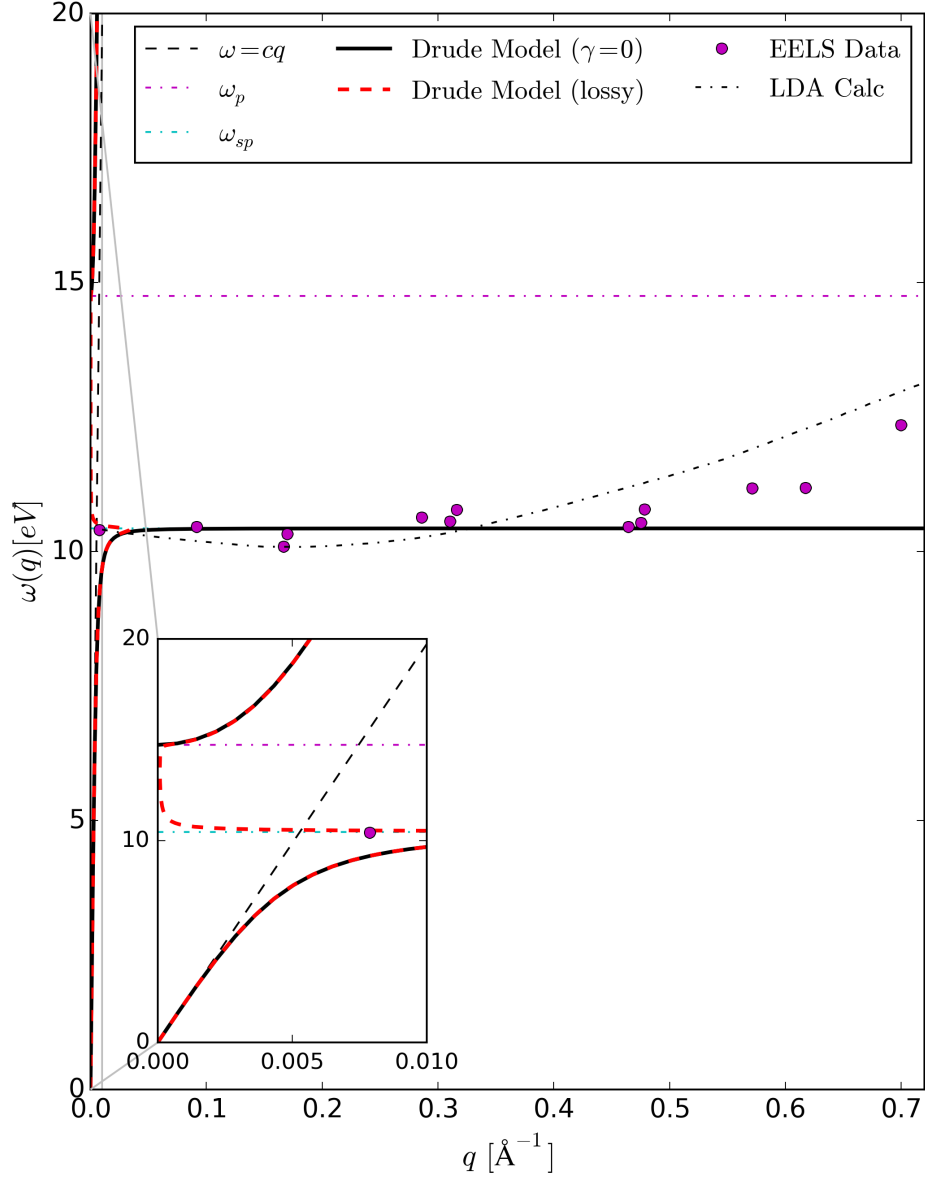


Figure 2.3: *Nonlocal SP dispersion of Al.* The lines are identical to Fig. 2.2 and the inset shows part of the range of Fig. 2.2, for reference. Data points from [19] (magenta) show the nonlocal dispersion measured by EELS. The black dash-dotted line is the nonlocal SP dispersion calculated by LDA [19].

Higher-order formalisms, beyond the Drude model, essentially entail calculating $\epsilon(q, \omega)$ based on approximations of the screening potential felt by electronic charges in a system [1, 2]. The dielectric function, $\epsilon(q, \omega)$, “measures” the response of a system to an external potential, $V_i(q, \omega)$, through the ratio:

$$\epsilon(\vec{q}, \omega) = \frac{V_i(\vec{q}, \omega)}{V(\vec{q}, \omega)} \quad (2.5)$$

where $V(q, \vec{\omega})$ is the “dressed” potential of the system due to charges which screen the external potential. Thus,

$$V(q, \vec{\omega}) = V_i(q, \vec{\omega}) + V_s(q, \vec{\omega}) \quad (2.6)$$

and different formalisms amount to calculating $V_s(q, \vec{\omega})$ using different models and approximations (for full review, see Ref. [2]). For instance, in the simplest nonlocal scheme, the semi-classical Thomas-Fermi model, the screening potential and dressed potential are related by

$$V_s(\vec{q}) = - \left(\frac{q_{TF}}{q} \right)^2 V(\vec{q}) \quad (2.7)$$

where q_{TF}^2 is the Thomas-Fermi wavevector. Inserting into Eq. (2.6) leads to $\frac{V_i(\vec{q})}{V(\vec{q})} = 1 + \left(\frac{q_{TF}}{q} \right)^2$, where immediately the dielectric function can be identified as

$$\epsilon(\vec{q}) = 1 + \left(\frac{q_{TF}}{q} \right)^2 \quad (2.8)$$

In the RPA, the screening potential is again related to the dressed potential, such that

$$V_s(\vec{q}) = v_q P^{(1)}(\vec{q}) V(\vec{q}) \quad (2.9)$$

where v_q is the Coulomb potential and $P^{(1)}(\vec{q})$ is the single-particle polarizability. Again, inserting into Eq. (2.6) leads to $\frac{V_i(\vec{q})}{V(\vec{q})} = 1 - v_q P^{(1)}(\vec{q})$, so

$$\epsilon_{RPA}(\vec{q}) = 1 - v_q P^{(1)}(\vec{q}) \quad (2.10)$$

Obviously, the form of Eq. (2.10) is reminiscent of the local response formalism, $\epsilon = 1 + \chi_e$, where χ_e is the electric susceptibility. The single-particle polarizability, $P^{(1)}(\vec{q})$, is quantum mechanical in origin and can be calculated from either a density-operator approach or a diagrammatic approach [2, 20]. In the RPA, the result for a free electron gas (i.e., no lattice or impurities) is [2]:

$$P^{(1)}(\vec{q}) = \frac{1}{V} \sum_k \frac{f_k - f_{k+q}}{\epsilon_k - \epsilon_{k+q} + \omega + i\delta} \quad (2.11)$$

where f_k terms are the Fermi-Dirac distribution functions and ϵ_k terms are the eigenenergies of the system.

Calculating $\epsilon_{RPA}(\vec{q})$ requires calculating the quantum mechanical eigenstates of the system, which are simply plane waves for a 3D isotropic, free electron gas. However, these eigenstates are different for a system that contains an interface, i.e., a half-space. Unlike the isotropic system, a half-space exhibits a potential that varies at the surface, which must be accounted for in the electronic ground states. This surface potential was self-consistently calculated by Lang and Kohn [21] for metals of various electron densities, and we perform RPA calculations for a planar slab using this potential in the next chapter. One could also calculate the electronic ground states and, consequently, $\epsilon(q, \omega)$, for any complex geometry based on this *ab initio* procedure, but such an approach is wildly impractical for more complicated systems due to computational load.

Finally, the LDA is yet another approximation to calculate the screening poten-

tial, by including electron exchange and correlation energies. Again, this requires calculation of the complete quantum ground states of the system and, therefore, is similarly impractical for non-trivial systems. It should now be clear why *ab initio* formalisms like the RPA and LDA are cumbersome for complex structures. Calculation of eigenstates, etc., is inordinately difficult for large-scale, non-symmetric systems, whereas it is relatively straightforward for highly symmetric geometries and small systems. To circumvent this difficulty, we wish to use an effective response formalism that captures the relevant detail without requiring *ab initio* calculations. Next, we show two approximate, small- q models that are derived from the above formalisms.

2.2 The Hydrodynamic Approximation

The RPA dielectric function for a bulk, 3D electron gas is called the Linhard function, and it reduces to the HDA in the small- q limit [1]. The real part of the Lindhard function yields [2]:

$$\begin{aligned} \lim_{q \rightarrow 0} \text{Re} \{ \epsilon_{RPA}(q, \omega) \} &= 1 - \frac{\omega_p^2}{\omega^2} \left\{ 1 + \frac{1}{\omega^2} \left[\frac{3}{5} v_F^2 q^2 + \epsilon_q^2 \right] + \mathcal{O}(\omega^{-4}) \right\} \\ &\approx 1 - \frac{\omega_p^2}{\omega^2} \left[1 + \frac{\beta q^2}{\omega^2} \right] \end{aligned} \quad (2.12)$$

where the so-called hydrodynamic term, $\beta = \frac{3}{5} v_F^2$, is identified, and v_F is the Fermi velocity. Furthermore, in this limit, one may express the dielectric function as [10, 22]

$$\epsilon(q, \omega) = 1 - \frac{\omega_p^2}{\omega(\omega + i\gamma) - \beta q^2}, \quad (2.13)$$

where γ is the loss parameter (rate of electron scattering with phonons and defects). The hydrodynamic term is effectively an extension of the Drude model, such that $\epsilon(q, \omega) = 1 - \omega_p^2/\tilde{\omega}^2$, where $\tilde{\omega}^2 = \omega(\omega + i\gamma) - \beta q^2$. Note, Eq. (2.13), reduces to the Drude model for high frequency, $\omega^2 \gg \beta q^2$, and the Thomas-Fermi model for

vanishing frequency, $\epsilon(q, 0) = 1 + q_{TF}^2/q^2$, showing that the Thomas-Fermi wavevector is given by $q_{TF} = \omega_p/\sqrt{\beta}$. Finally, the SP dispersion for the HDA can be derived from the condition $\epsilon(q, \omega) = -1$, and is:

$$\omega(q) = \omega_{sp} \left[1 + \frac{\beta}{2\omega_{sp}^2} q^2 \right] \quad (2.14)$$

In Fig. 2.4, we plot the SP dispersion of the alkali metal potassium using the HDA model (blue-line), compared to the full LDA calculation (black dashed line) and experimental data (squares) [19]. For potassium ($r_s = 4.86$) the quadratic term in the HDA is equal to $\beta/2\omega_{sp}^2 \approx 1.00\text{\AA}$. Ultimately, the SP dispersion calculated using the HDA fails to match the negative dispersion exhibited by alkali metals [23, 24]. Additionally, it cannot account for the upper plasmonic branch, which we will discuss in the next section.

Before moving on, we emphasize that the definition of β from the HDA is purely a *bulk* definition and, therefore, it may not accurately capture the behavior of surface modes. Presumably there is an equivalence for surface problems, where $\beta_{\text{surface}} \propto v_F^2$. Thus, the HDA is useful in a phenomenological way, but β is not really representative of first-principles information pertaining to metal surfaces.

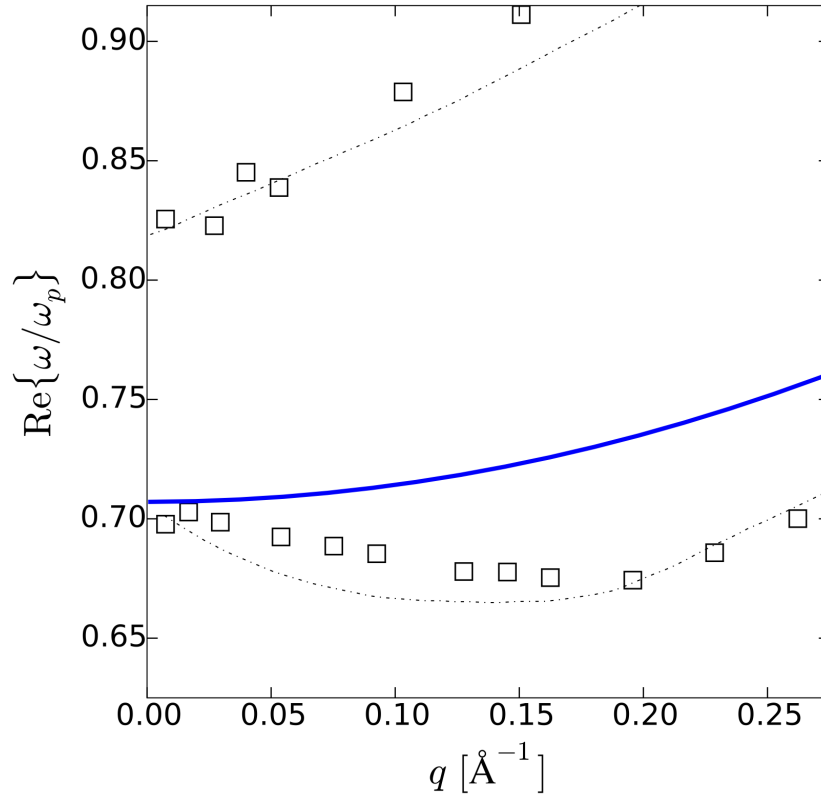


Figure 2.4: Comparison of HDA dispersion with LDA & exp. (for potassium) The pure HDA result, Eq. (2.14), is shown as blue line. LDA calculations (black dashed line) and experimental data (squares) are shown from literature [19]

2.3 The d-Function Formalism

The issue with the HDA, as previously mentioned, is that it is an approximation related to the bulk response and does not explicitly take the surface into account. Therefore, it is inadequate in some regimes, as shown in the previous section. In contrast, the d-function formalism of Feibelman explicitly takes surface states into account and may be calculated from the RPA or LDA [11, 12]. The d -function formalism has been thoroughly confirmed by electron energy loss spectroscopy (EELS) experiments [19, 25] and provides deep insight into the SP dynamics at small q . Therefore, any first-order calculation of non-local surface physics should incorporate the d -function.

The d-function is a complex surface response function, calculated from *ab initio* quantum states, which naturally augments the standard Fresnel formulas for reflection from a metallic half-space in the following way [12]:

$$r_p = \frac{\varepsilon(\omega) - \varepsilon_0 \frac{k_2}{k_1} + i \frac{[\varepsilon(\omega) - \varepsilon_0]}{k_1} q^2 d(\omega)}{\varepsilon(\omega) + \varepsilon_0 \frac{k_2}{k_1} - i \frac{[\varepsilon(\omega) - \varepsilon_0]}{k_1} q^2 d(\omega)} \quad (2.15)$$

where r_p is the p-polarized reflection coefficient, $\varepsilon(\omega)$ is the Drude model dielectric function of the metal half-space, ε_0 is the dielectric function of the outer half-space, the wavevectors are $\vec{k}_j = (q, -k_j)$, where $k_j = \sqrt{(\omega/c)^2 \varepsilon_j - q^2}$ is the z-component and q is the in-plane component, and indices refer to the half-spaces of the outer dielectric ($j = 1$) and metal ($j = 2$). Feibelman showed that this nonlocal Fresnel formula is exact to linear order in q , and may be readily calculated for simple (alkali) metal surfaces [12].

The d-function is given by

$$d(\omega) = \frac{\int_{-\infty}^{\infty} dz z \delta \rho(z, q = 0, \omega)}{\int_{-\infty}^{\infty} dz \delta \rho(z, q = 0, \omega)} \quad (2.16)$$

where $\delta\rho(z, \omega)$ is the in-plane charge density induced by a long-wavelength field at frequency ω , and integration is over the entire domain perpendicular to the surface [1]. Physically, $d(\omega)$ is a response function, like $\epsilon(\omega)$, but localized at the surface of a system. It is a complex function that obeys Kramers-Kronig relations and has the high-frequency behavior $\lim_{\omega \rightarrow \infty} d(\omega) = 0$. We expand upon the notion of $d(\omega)$ as a surface response function in Chapter 4, where we consider response models that use thin, surface films with properties related to $d(\omega)$.

In addition to being a type of response function, $d(\omega)$ represents the physical location of the induced charge density. For alkali metals, this centroid of induced charge is located *outside* of the surface, in the long-wavelength limit ($q = 0$). The induced charge density, calculated in the RPA, is [26]:

$$\delta\rho(z; \omega) = \int dz' \chi_0(z, z'; \omega) \left[V_{ext} + \int dz'' V_c(z', z'') \delta\rho(z''; \omega) \right] \quad (2.17)$$

where $V_c(z, z') = e^2/|z - z'|$ is the Coulomb potential, and $\chi_0(z, z'; \omega)$ is the single particle susceptibility given by:

$$\chi_0(z, z'; \omega) = \sum_k \sum_{k'} \frac{f_k - f_{k'}}{\epsilon_k - \epsilon_{k'} + \hbar\omega} \psi_k^*(z) \psi_{k'}(z) \psi_{k'}^*(z') \psi_k(z') \quad (2.18)$$

where f_k terms are Fermi-distribution functions and ϵ_k and ψ_k are eigen-energies and eigenstates of the system.

The d-functions have been calculated for various simple (alkali) and complex (noble) metals, using both RPA and LDA formalisms [23, 27, 28, 29, 30]. For instance, the d-function of potassium is shown in Fig. 2.5, where the data have been taken from [23]. Note, data are only available for $\omega/\omega_p < 0.95$. The d-function exhibits two pole-structures: one at $\omega/\omega_p \approx 0.82$, which is the so-called “multipole” feature, and one at $\omega/\omega_p \approx 1$, which we will discuss below.

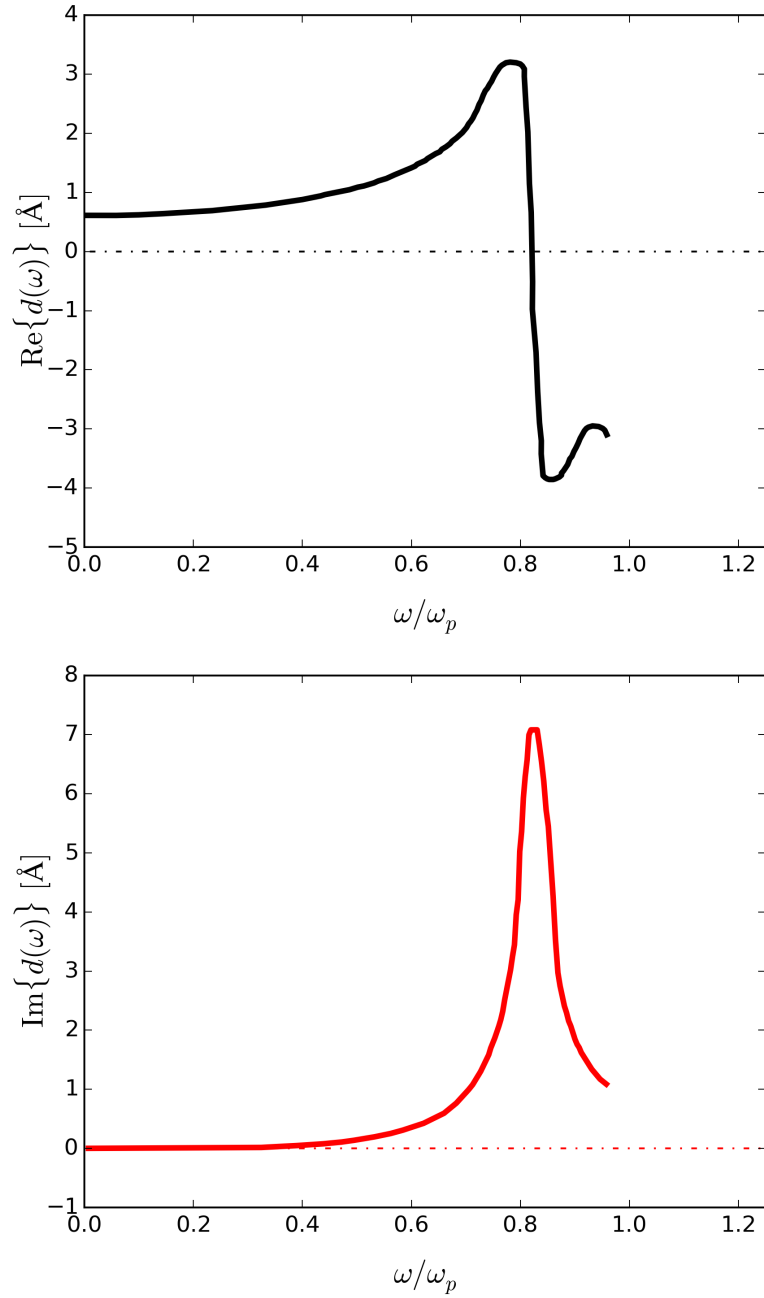


Figure 2.5: *The d-function of potassium from literature [23]. Real and imaginary parts are shown (black and red, respectively).*

The pole structure of the d-function at ω_p can be seen from the alternate form of Eq. (2.16), where integration of the charge centroid is carried out over the *outside* region only ($z > 0$), which leads to [23]:

$$d(\omega) = \frac{\epsilon(\omega) - 1}{\epsilon(\omega)} f(\omega) \quad (2.19)$$

where

$$f(\omega) = \frac{\int_0^\infty dz z \delta\rho(z, q = 0, \omega)}{\int_{-\infty}^\infty dz \delta\rho(z, q = 0, \omega)} \quad (2.20)$$

as in [23]. The so-called dynamic force sum rule enables the d-function to be expressed in this way [23]. The function $f(\omega)$ only has two resonant features, one at the multipole frequency, and one at a lower frequency that is related to the work function [23]. Therefore, the pole structure of $d(\omega)$ at $\omega/\omega_p \approx 1$ is solely due to the condition $\epsilon(\omega) = 0$ in Eq. (2.19).

Motivated by this discussion, we propose a simple Lorentzian-like model for the d-function, which will enable us to perform numerical calculations more easily in later work. Our model simply treats $f(\omega)$ as the sum of two Lorentzian contributions and a bulk contribution, f_∞ , such that:

$$f(\omega) = f_\infty + \frac{A_1}{\omega_1^2 - \omega(\omega + i\gamma_1)} + \frac{A_2}{\omega_2^2 - \omega(\omega + i\gamma_2)} \quad (2.21)$$

where ω_1 is approximately equal to the threshold frequency of the work function, and ω_2 is the multipole resonance. Using this model and the definition of Eq. (2.19), we explored parameter fits for the d-function of potassium and found the following: $f_\infty \approx 0.372 \text{ \AA}$, $A_1/\omega_p^2 \approx 0.054 \text{ \AA}$, $\omega_1/\omega_p \approx 0.75$, $\gamma_1/\omega_p \approx 0.25$, $A_2/\omega_p^2 \approx 0.126 \text{ \AA}$, $\omega_2/\omega_p \approx 0.825$, and $\gamma_2/\omega_p \approx 0.065$. Our model fit is shown in the following figure.

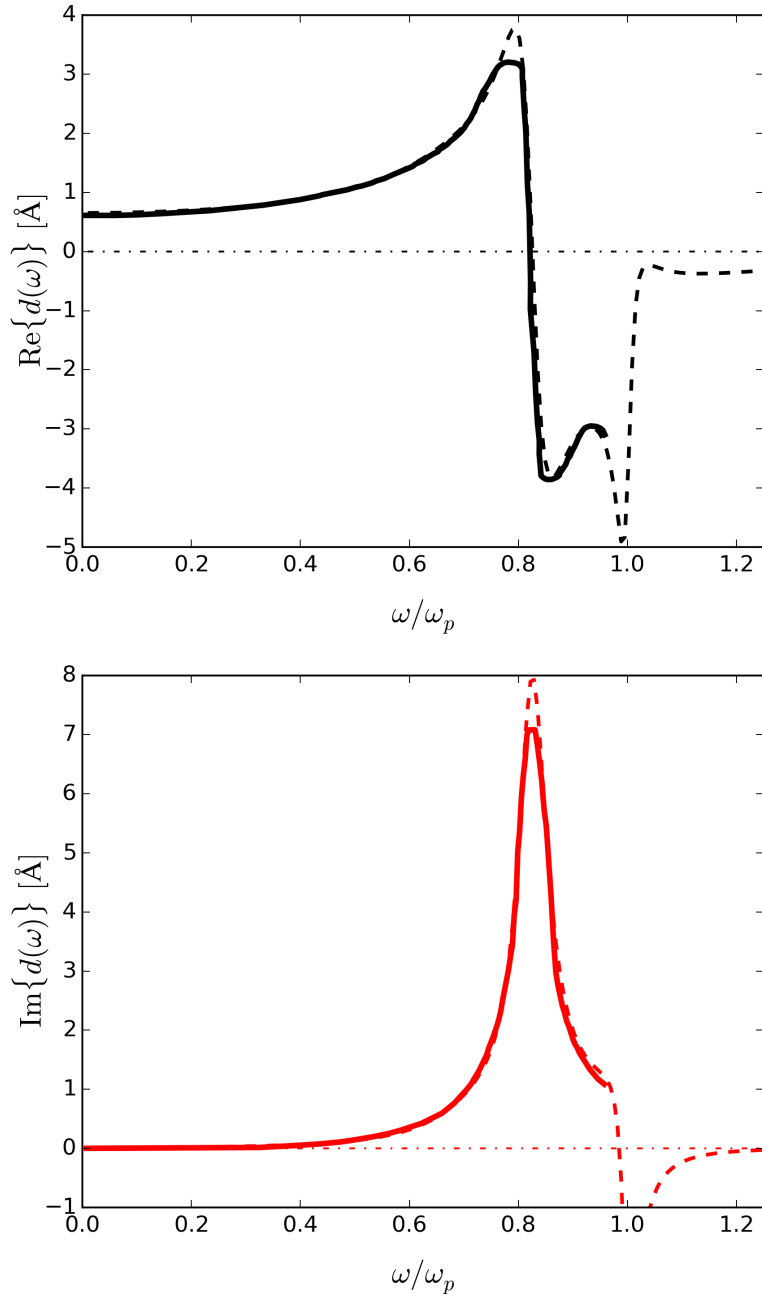


Figure 2.6: *Model fit to the d-function of potassium.* The model of Eqs. (2.19) & (2.21) is fit to the d-function from literature [23]. Real and imaginary parts are shown (black and red, respectively).

We also note that our model exhibits expected behavior for $\omega/\omega_p > 1$, for which $\text{Re}[d(\omega)] < 0$ and $\text{Im}[d(\omega)] < 0$. This behavior was confirmed by [29]. It also has the necessary high-frequency behavior, $\lim_{\omega \rightarrow \infty} d(\omega) = 0$.

Now we briefly discuss the dispersive properties. Using the d-function formalism, a very simple, non-local expression for the SP dispersion of metals can be obtained by solving for the roots of Eq. (2.15). In the non-retarded limit, where $k_1 = k_2 = iq$, Eq. (2.15) becomes

$$r_p = \frac{(\epsilon_m - \epsilon_0) + (\epsilon_m - \epsilon_0) qd(\omega)}{(\epsilon_m + \epsilon_0) - (\epsilon_m - \epsilon_0) qd(\omega)} \quad (2.22)$$

which yields the well know result [12]

$$\omega(q) = \omega_{sp} \left[1 - \frac{1}{2} d(\omega) q \right], \quad (2.23)$$

Since $d(\omega) > 0$ for all alkali metals [24], Eq. (2.23) demonstrates that the initial slope of the dispersion, for small q , is negative for these metals. Another feature of this dispersion is the existence of a second SP branch, which arises from the pole structure of the d-function. We exemplify these features in Fig. 2.7, where we again plot the SP dispersion of the alkali metal potassium, this time using Eq. (2.23) with $d(\omega)$ from our fit function, and compare to the full LDA calculation (solid black line) and experimental data (squares) [19], as in Fig. 2.4.

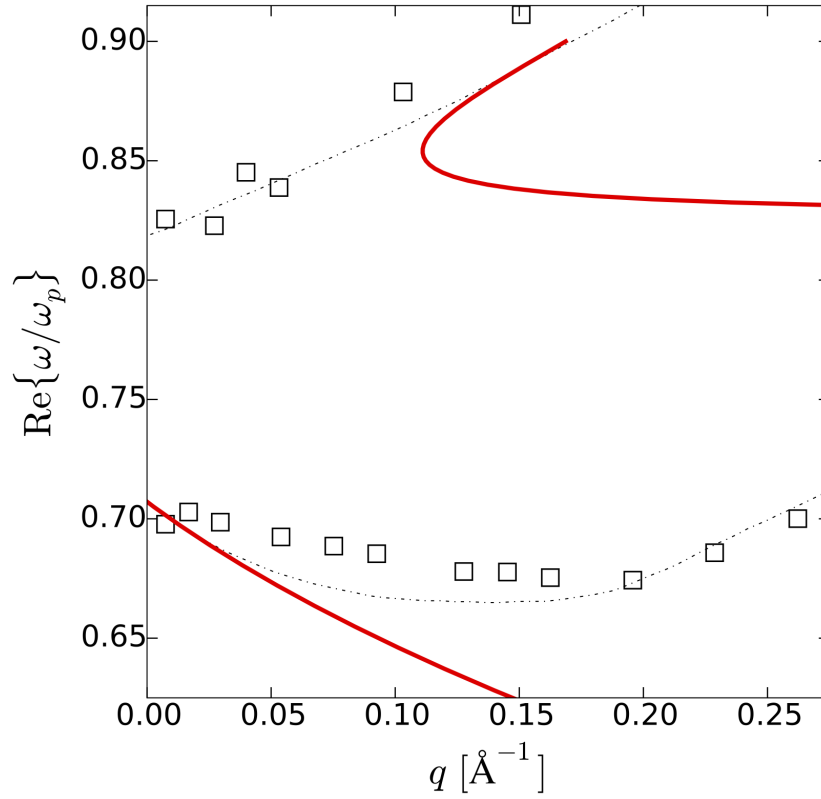


Figure 2.7: Comparison of *d*-function dispersion with LDA & exp. (for potassium) The *d*-function result, Eq. (2.23), is shown as red line. LDA calculations (black dashed line) and experimental data (squares) are shown from literature [19].

Fig. 2.7 shows that there are two plasmon branches, the lower branch is the monopole SP and the upper branch is the multipole SP, and these branches are connected in a characteristic s-shape due to the lossiness of the d-function. The d-function formalism captures both the initial negative dispersion and the multipole feature, as opposed to the HDA, which only has the correct qualitative behavior at high-q.

From Fig. 2.4 and Fig. 2.7, we note that both the d-function formalism and the HDA fail to describe the SP dispersion in its entirety. In particular, the d-function formalism does not capture the positivity of the dispersion for intermediate to high-q values, and the HDA does not capture the initial negative slope of the dispersion. Thus, a formalism is required which includes both linear and quadratic orders.

The most naive way to achieve a higher-order model would be to combine the Feibelman formalism, $\mathcal{O}(q)$, with the HDA, $\mathcal{O}(q^2)$:

$$\omega(q) = \omega_{sp} \left[1 - \frac{1}{2}d(\omega)q + \frac{\beta}{2\omega_{sp}^2}q^2 \right]. \quad (2.24)$$

As we show in the following, Fig. 2.8, this simple combination does *not* reflect what is observed from experiment or first-principles calculations. In fact, the HDA parameter, $\beta = \frac{3}{5}v_F^2$, significantly underestimates the observed positive dispersion. In the next chapter, we examine if either the d-function formalism or the HDA can provide insight into the full, nonlocal dispersion.

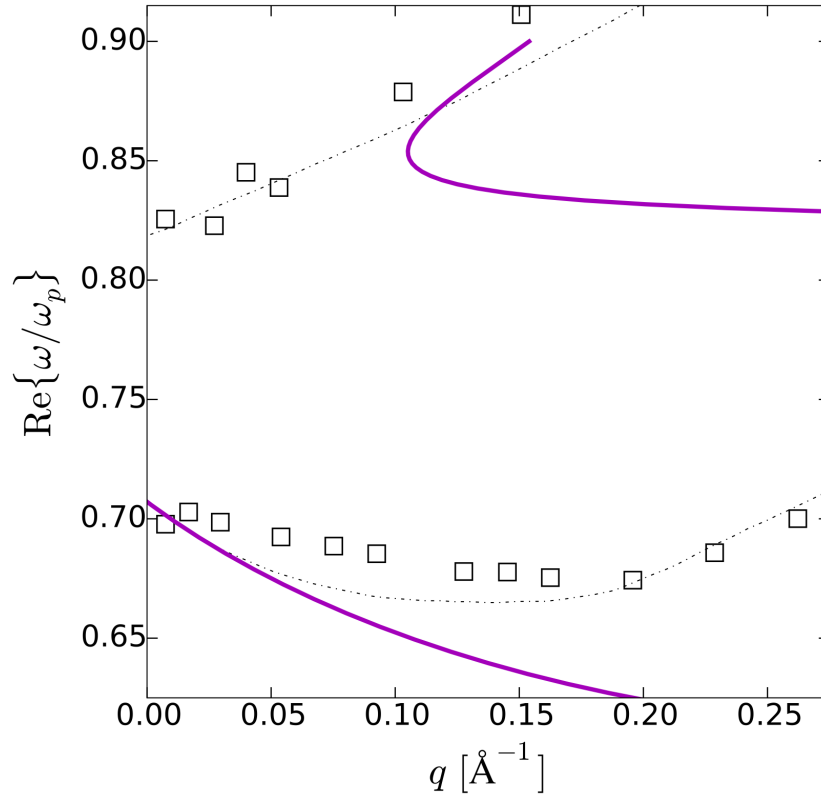


Figure 2.8: Comparison of extended dispersion with LDA & exp. (for potassium) The extended dispersion of Eq. (2.24) is shown as magenta line. LDA calculations (black dashed line) and experimental data (squares) are shown from literature [19].

2.4 Charge Centroid Model of the d-Function

Finally, we conclude with a more in-depth discussion the d-function, which we will expand upon in the following chapter. We previously mentioned that the d-function is the location of the induced charge centroid. This identification also explains the small- q dispersion behavior, as explained by Tsuei [31], which we summarize here.

The SP frequency is related to the average charge density at the location of the induced charge centroid by:

$$\omega(q) = \sqrt{n_{avg}(q)e^2/m\epsilon_0} \quad (2.25)$$

which is the typical definition of the plasma frequency, but renormalized by an effective electron density, $n_{avg}(q)$. In Ref. [31], Tsuei argued that the average electron density experienced by the induced charge at a metal surface would decrease with increasing q , leading to a *negative* surface plasmon dispersion, if the induced charge was located *outside* of the surface. The argument follows from the following definition of the average charge density:

$$n_{avg}(q) = \frac{\int dz n(z)\phi(z, q)}{\int dz \phi(z, q)} \quad (2.26)$$

where,

$$\phi(z, q) = \int dz' \delta n(z') \exp(-q|z - z'|) \quad (2.27)$$

where $\delta n(z)$ is the induced density, i.e., $\delta n(z) = \delta\rho(z)/e$, and $n(z)$ is the background jellium density. Thus, $\phi(z, q)$ is a quantity that decreases with increasing q , which means that the average charge density, $n_{avg}(q)$, samples *less* of the jellium charge distribution $n(z)$ when $\delta n(z)$ is located *outside* of the jellium background, and *more*

of $n(z)$ when $\delta n(z)$ is located *inside*. See the following Fig. 2.9, reprinted from Ref. [31]. Note, the convention of our axis is flipped from this picture, where we use $n(z) > 0$ for $z > 0$ in our analysis. The behavior of the induced charge centroid and the interpretation of $d(\omega)$ is the same, however.

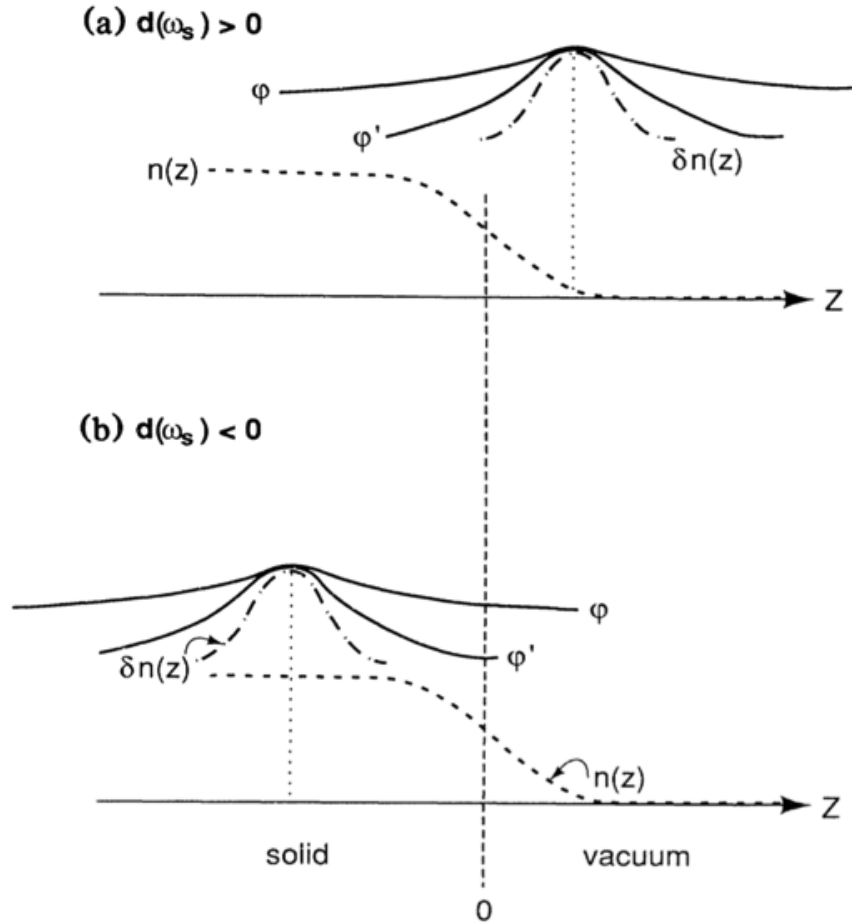


Figure 2.9: *Tsuei model of SP dispersion* Figure taken from [31]. In (a) the induced charge centroid, $\delta n(z)$, lies outside the jellium background. As q increases, the charge centroid experiences *less* of the background, leading to a reduced effective plasma frequency and negative dispersion. In (b), the induced charge centroid lies inside the jellium background. As q increases, the charge centroid experiences *more* of the background, leading to a increased effective plasma frequency and positive dispersion.

To understand this model, mathematically, we consider the following. Beginning from Eq. (2.26), we treat the background static charge density as a simple step function, such that $n(z) = n_0 H[z]$, where n_0 is the background density and $H[z]$ is the Heaviside step function. In the most simplified terms, we consider the induced charge to be a delta-function located at the centroid position, such that $\delta n(z) \rightarrow \Delta n \delta(z - z_0)$, where z_0 represents the position of the centroid. Then, using Eq. (2.27), the coulomb potential of the induced charge is simply given by,

$$\phi(z, q) \approx \Delta n \exp(-q|z - z_0|) \quad (2.28)$$

Eq. (2.28), inserted into Eq. (2.26), leads to the following expression for the average background charge density experienced by the induced charge:

$$n_{avg} = n_0 \left[1 - \frac{1}{2} \exp(-qz_0) \right] \quad (2.29)$$

Now we expand Eq. (2.29) in the long-wavelength limit:

$$n_{avg} \approx n_0 \left[1 - \frac{1}{2} (1 - z_0 q) \right] \approx n_0 \frac{1}{2} [1 + z_0 q] \quad (2.30)$$

Finally, the dispersion is obtained using Eq. (2.25):

$$\omega(q) = \omega_{sp} \left[1 + \frac{1}{2} z_0 q \right] \quad (2.31)$$

Thus, it is clear from the above derivation that $z_0 = -d(\omega)$ in the $q = 0$ limit.

In the next chapter, we investigate the possibility of “combining” the HDA and d-function formalism to create a higher-q model. Then in the final chapter of *Part I*, we present a new method of incorporating the d-function into FDTD calculations of complex systems.

CHAPTER 3

Extended d-function Formalism

In this chapter, we explore the higher-order nonlocal behavior of plasmonic surfaces, with the aim of extending existing formalisms. The d-function formalism, introduced in the previous chapter, is explicitly applicable to surfaces, but only exact to order q . On the other hand, the HDA is a higher-order model, $\mathcal{O}(q^2)$, but it has limited applicability to problems involving surface plasmons since it is an approximation related to bulk properties. We propose extending the d-function formalism to order q^2 , first by considering an extension of the Tsuei model, and then by considering an extension using the HDA. We demonstrate the viability of the latter model by comparing with published *ab initio* calculations and experiments, as well as by performing our own RPA calculations (valid for all q) of the surface plasmon dispersions for simple metals with various electron gas densities. We argue that this model can be applied to arbitrary plasmonic/metamaterial structures, as long as the non-flat interfaces can be modeled as effective media films. This work was published in Ref. [13].



3.1 Dynamic Charge Centroid Model

Generically, a quadratic extension of the surface plasmon dispersion will have the following form:

$$\omega(q) = \omega_{sp} [1 - aq + bq^2] \quad (3.1)$$

We first examine extending the d-function formalism to $\mathcal{O}(q^2)$ by augmenting the Tsuei model [31], rather than by simply adding a hydrodynamic-like term. Ultimately, we discuss the limitations of this strategy, but we demonstrate that this extended model is capable of describing qualitative features of the surface plasmon dispersion to higher order in q and has a natural physical interpretation.

We developed the extended Tsuei model by expanding the d-function to linear order in q , as such:

$$d(\omega, q) \approx d(\omega, q)|_{q=0} + \left(\frac{d}{dq} d(\omega, q)|_{q=0} \right) q \quad (3.2)$$

where $d(\omega, q)|_{q=0} = d(\omega)$ is the definition of the Feibelman d-function. Thus, the SP dispersion of Eq. (2.23), from the previous chapter, is extended to order q^2 :

$$\omega(q) \approx \omega_{sp} \left[1 - \frac{1}{2} d(\omega) q - \frac{1}{2} \left(\frac{d}{dq} d(\omega, q)|_{q=0} \right) q^2 \right] \quad (3.3)$$

This model has the following physical implication. In order to match the observed SP dispersion at high- q , it is required that $\frac{d}{dq} d(\omega, q)|_{q=0} < 0$, such that the quadratic dispersion is positive. This means that the charge centroid must move *towards* the jellium surface background of the metal as q increases.

Using this extended model of the d-function, we calculate the SP dispersion within the Tsuei model and show how a “dynamic charge centroid” captures the qualitative

features of the nonlocal dispersion, as calculated in the RPA. Specifically, we use Eq. (2.31) of the previous chapter with $z_0 \rightarrow z(q)$, where $z(q)$ now has the following, phenomenological form:

$$z(q) = -a' + b'q \quad (3.4)$$

The variable a' represents the location of the charge centroid outside of the jellium background at $q = 0$. Nominally, $a' = d(\omega)$, but here we consider it to be a parameter in our analysis. The variable b' represents the rate at which the charge centroid changes its position, as a function of q . In the small- q limit, we can calculate the SP dispersion based on the approximations of the previous chapter to obtain:

$$\omega(q) = \omega_{sp} \left[1 - \frac{1}{2}a'q + \frac{1}{2}b'q^2 \right] \quad (3.5)$$

Thus, this form of the d -function generates the desired quadratic extension to the SP dispersion and, based on Eq. (3.1), we can identify $a = \frac{1}{2}a'$ and $b = \frac{1}{2}b'$.

In the following analysis, we show that the parameters a' and b' in Eq. (3.5) may be chosen such that the model dispersion is in excellent agreement with the *ab initio* dispersion calculated in the RPA for a semi-infinite slab. Specifically, we calculate $\omega(q)/\omega_{sp}$, which, based on the definition of Eq. (2.25) in the previous chapter, is $\omega(q)/\omega_{sp} = \sqrt{2n_{avg}(q)/n_0}$. We numerically calculate $n_{avg}(q)$ based on Eq. (2.26), for an idealized system. We consider a static background charge density that is smoothly varying at the surface with the following functional form:

$$n(z) = \frac{1}{2} [\tanh(cz) + 1] \quad (3.6)$$

Eq. (3.6) was chosen for ease of numerical calculation, but the true self-consistent

charge density, which has a similar qualitative shape, should be used for quantitative comparisons—here, we are merely trying to demonstrate that the model works.

In the following plots, we show how different parameter choices for a' and b' affect the SP dispersion. The bars below all figures permit a' , b' , and q to be changed, and their values are stated in each figure. In each figure, the **top plot** depicts the location of the charge centroid as given by Eq. (3.4) (solid-black line). The dotted-red line and red-point are meant to aide the eye as q is varied. The dotted-black line represents the location of the metal surface ($z = 0$). The **middle plot** shows the background charge density (Eq. (3.6); blue line), Coulomb potential of the induced charge (Eq. (2.27); green line), and normalized background charge experienced by the charge centroid (grey-shaded region). The latter quantity is the integrand of Eq. (2.26) and, therefore, the integrated area of the grey-shaded region yields $n_{avg}(q)$. As in the first plot, the dotted-red line shows the location of the charge centroid and the dotted-black line represents the location of the metal surface ($z = 0$). Finally, the **bottom plot** shows $\omega(q)/\omega_{sp}$ (proportional to the integrated area of the grey-shaded region) as a green-solid line and $\omega(q)/\omega_{sp}$ as calculated in the RPA for a semi-infinite slab (blue-points) [19]. Again, the red-point references the same point in the right-most plot, and is meant to guide the eye as parameters are varied.

Here we describe the salient observations for each figure:

- Fig. 3.1 & 3.2 show the “best fit” model for $z(q)$ at different q points. For $z(q) < 0$, the charge centroid is *outside* of the jellium background and the dispersion is negative. The dispersion becomes positive as q increases and, ultimately, the charge centroid lies *inside* the jellium background for large q .
- When the intercept a' is varied, the portion of the curve that has negative dispersion changes—with increasing a' (i.e., the charge centroid “starts” farther away from the jellium edge at low q), the negative portion of the surface plas-

mon dispersion persists until a turning point at higher q (Fig. 3.3). For lower a' , the dispersion is more positive (Fig. 3.4).

- When the slope b' is varied, the steepness of the surface plasmon dispersion changes—increasing the parameter b' leads to a steeper dispersion (Fig. 3.5), whereas the limit of $b' \rightarrow 0$ causes the dispersion to be negative (Fig. 3.6). This is the regime of the original Feibelman formalism.

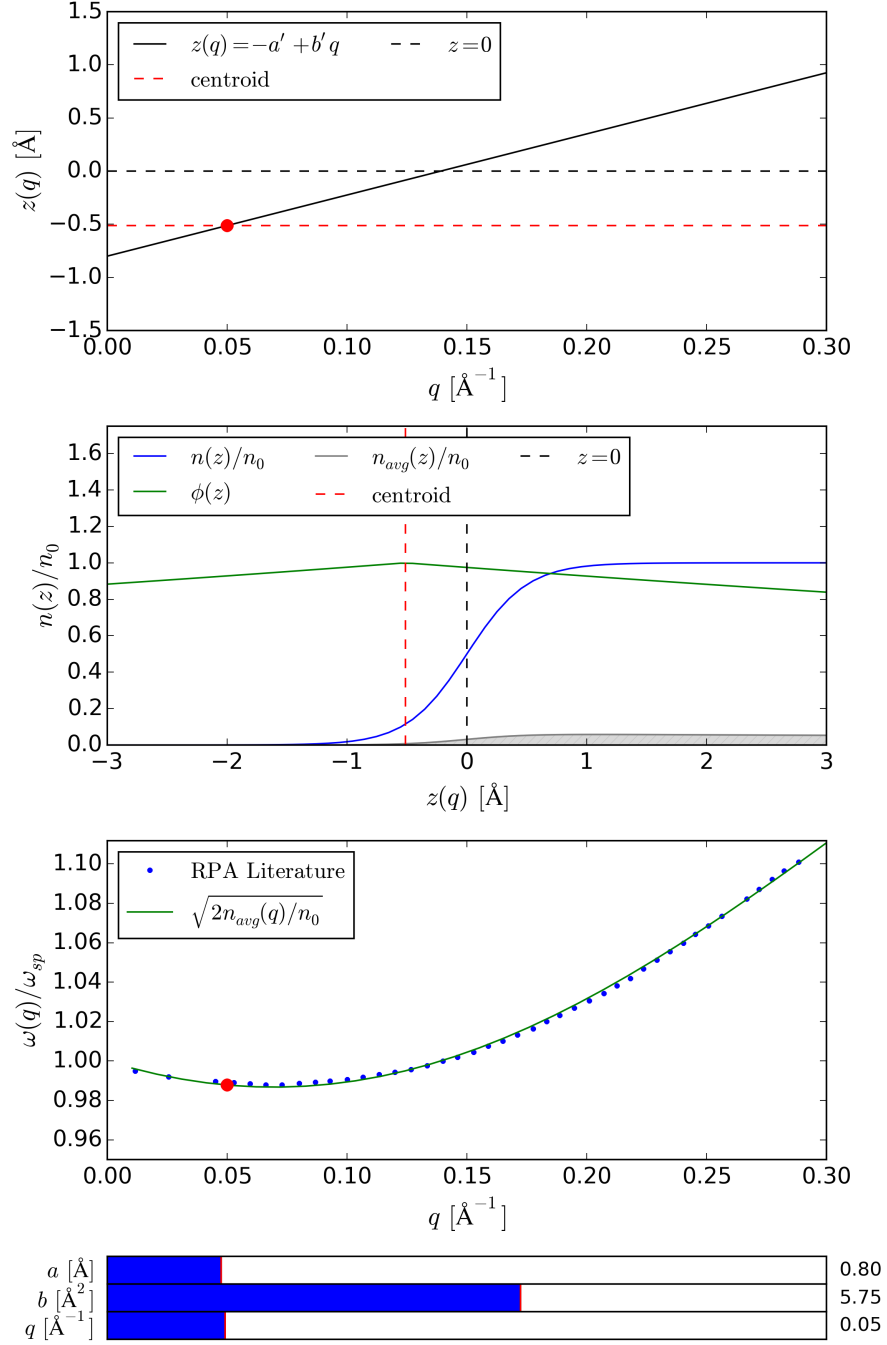


Figure 3.1: *Dynamic charge centroid model fit to RPA calculation (1).* Fit parameters given in figure. For $q = 0.05 \text{ \AA}^{-1}$, the charge centroid (red dashed line) is outside of the jellium bulk. The dispersion is negative in this regime.

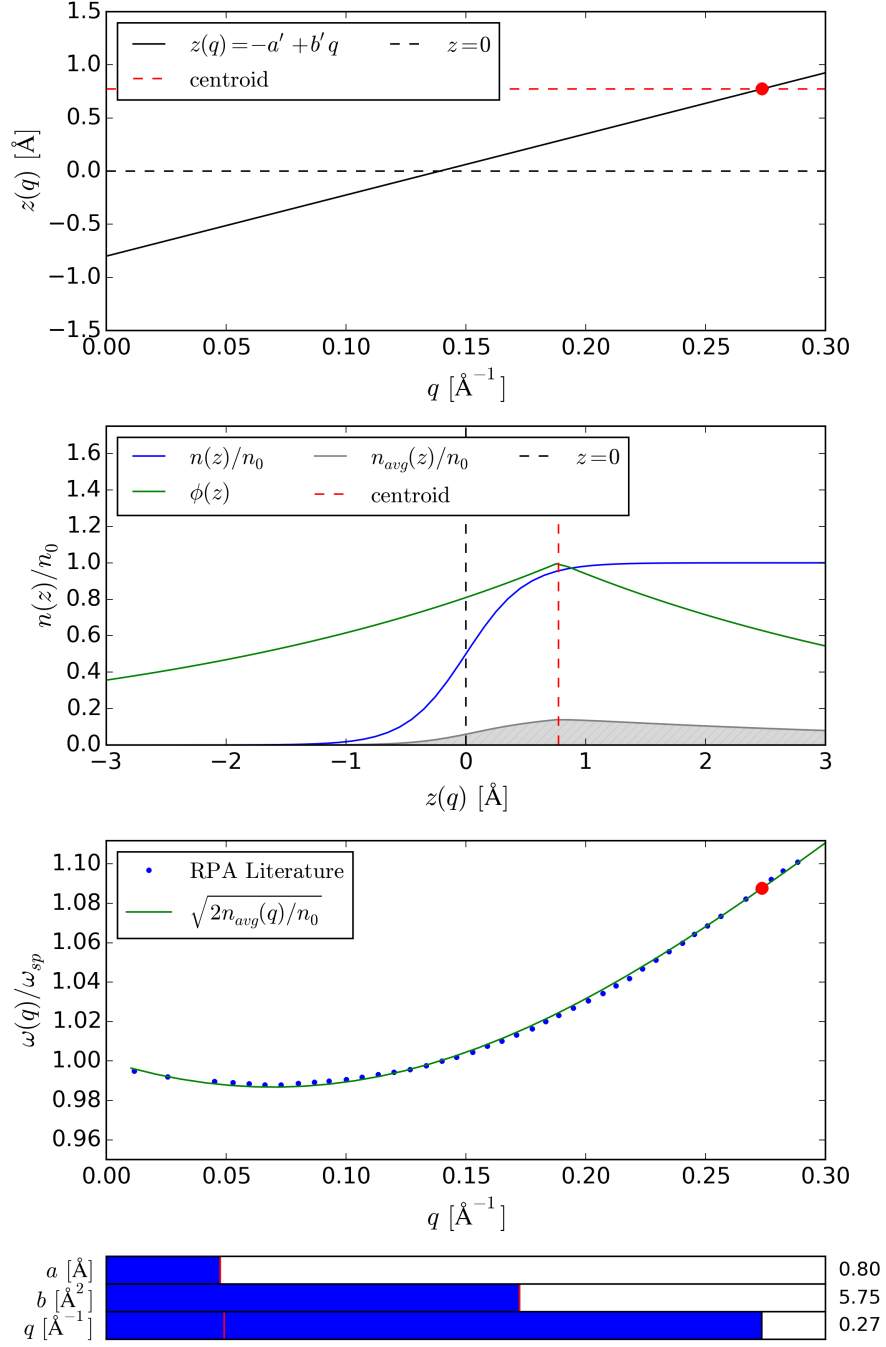


Figure 3.2: *Dynamic charge centroid model fit to RPA calculation (2).* Fit parameters given in figure. For $q = 0.27 \text{\AA}^{-1}$, the charge centroid (red dashed line) is inside of the jellium bulk. The dispersion is positive in this regime.

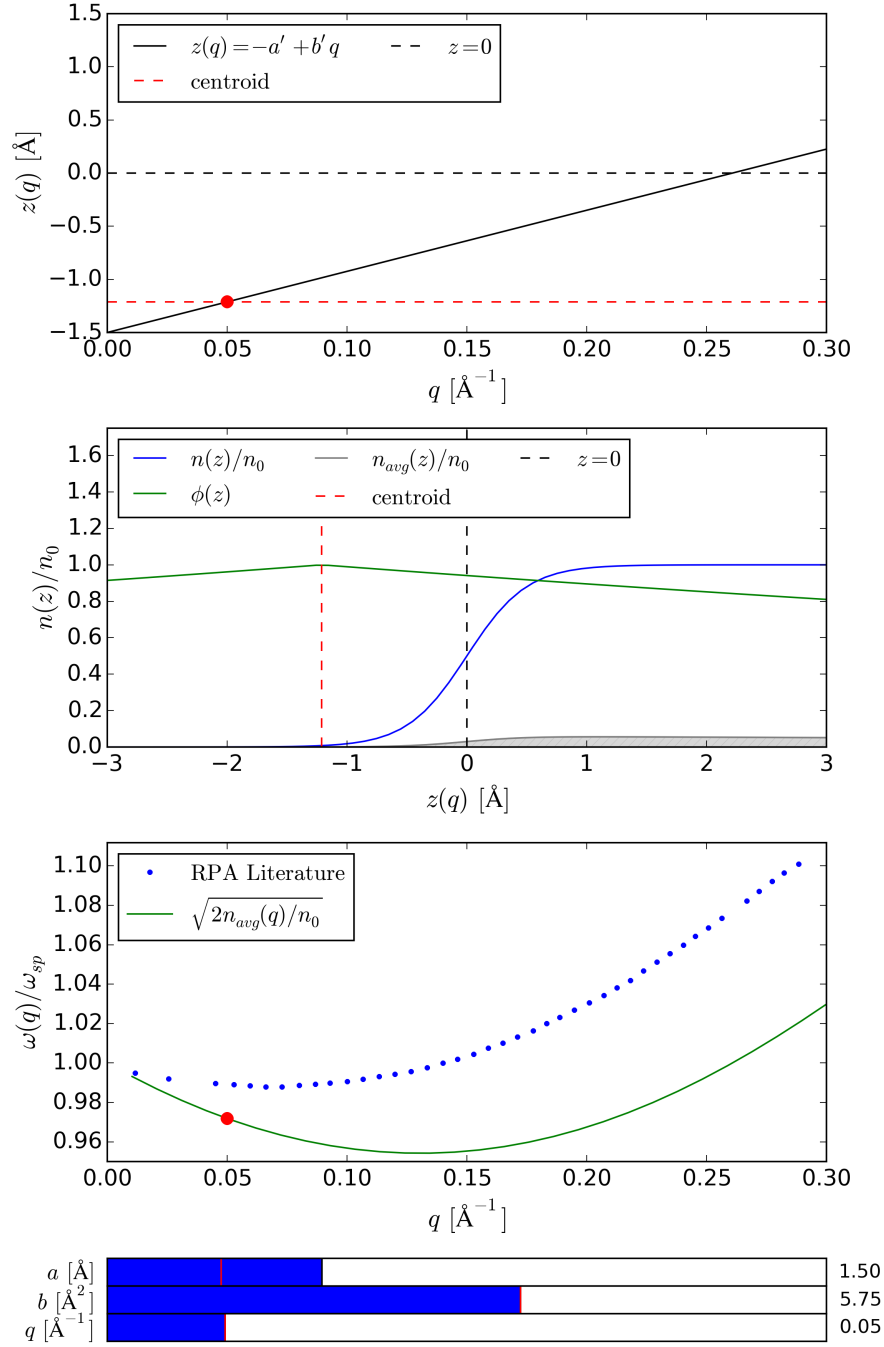


Figure 3.3: *Dynamic charge centroid model fit to RPA calculation (3).* Fit parameters given in figure. When the parameter a' is large, the dispersion is more negative.

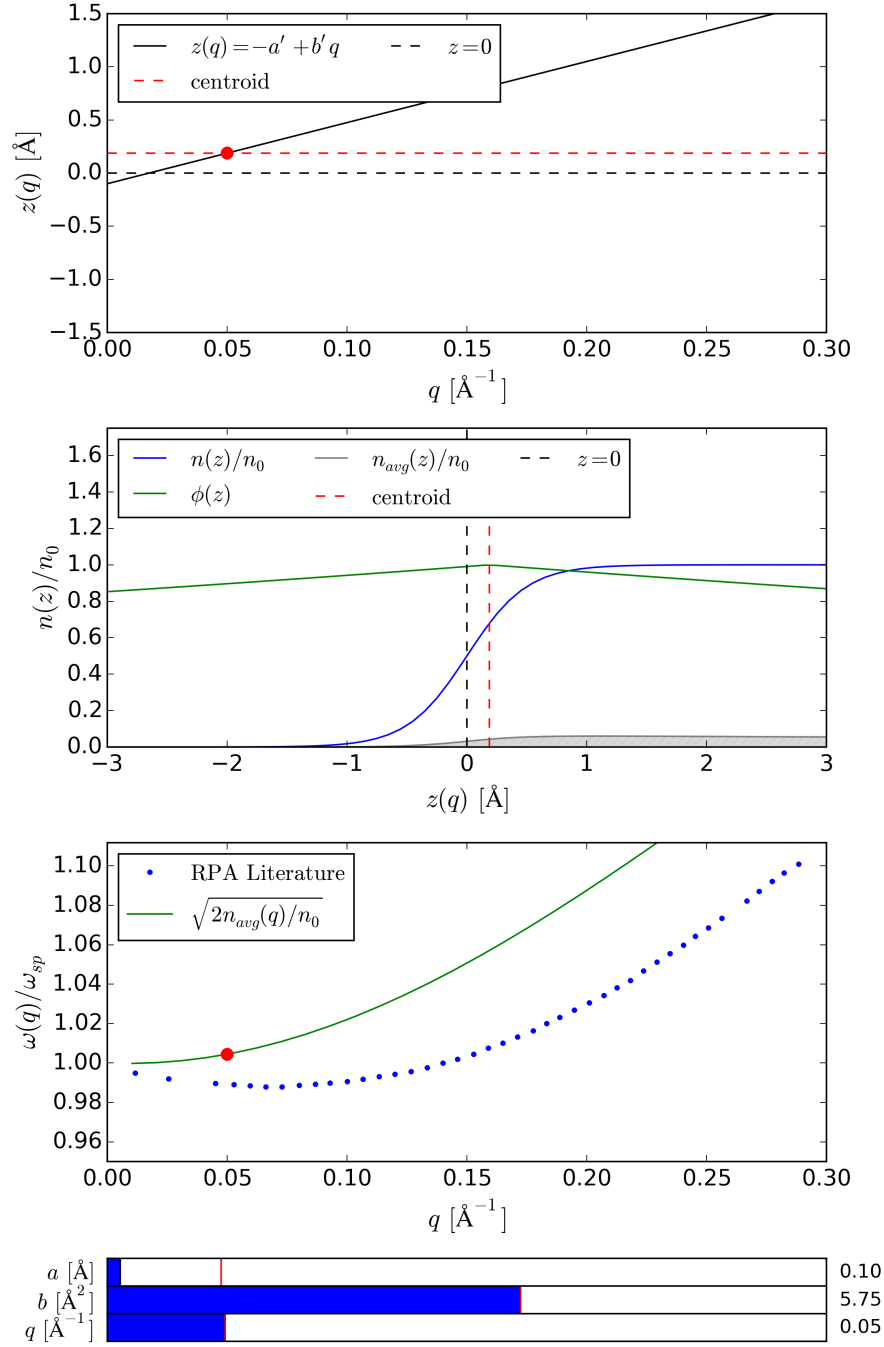


Figure 3.4: Dynamic charge centroid model fit to RPA calculation (4). Fit parameters given in figure. When the parameter a' is small, the dispersion approaches the HDA result.

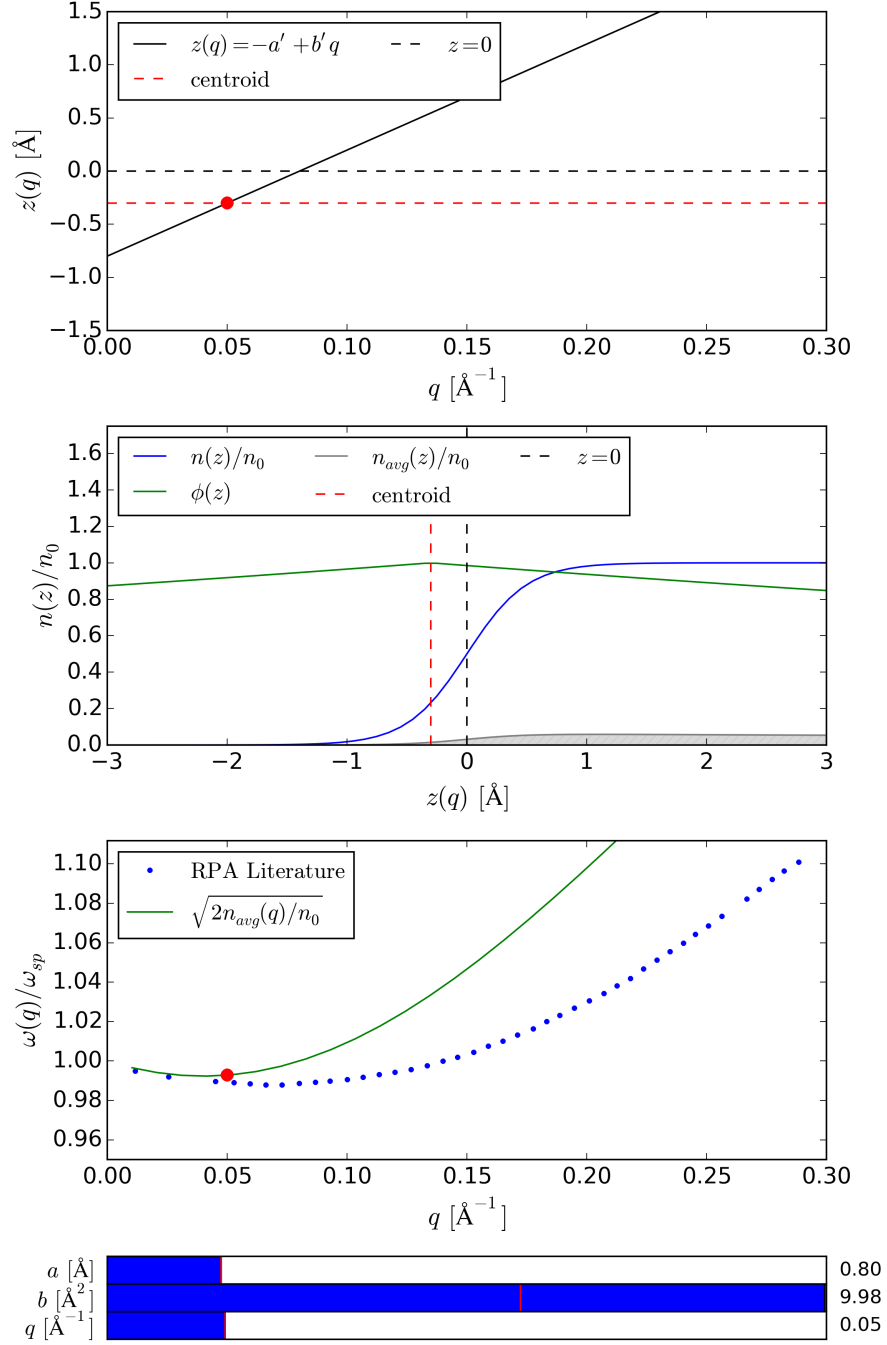


Figure 3.5: *Dynamic charge centroid model fit to RPA calculation (5).* Fit parameters given in figure. When the slope of $z(q)$ is large (i.e., large b'), the dispersion also has a steeper slope.

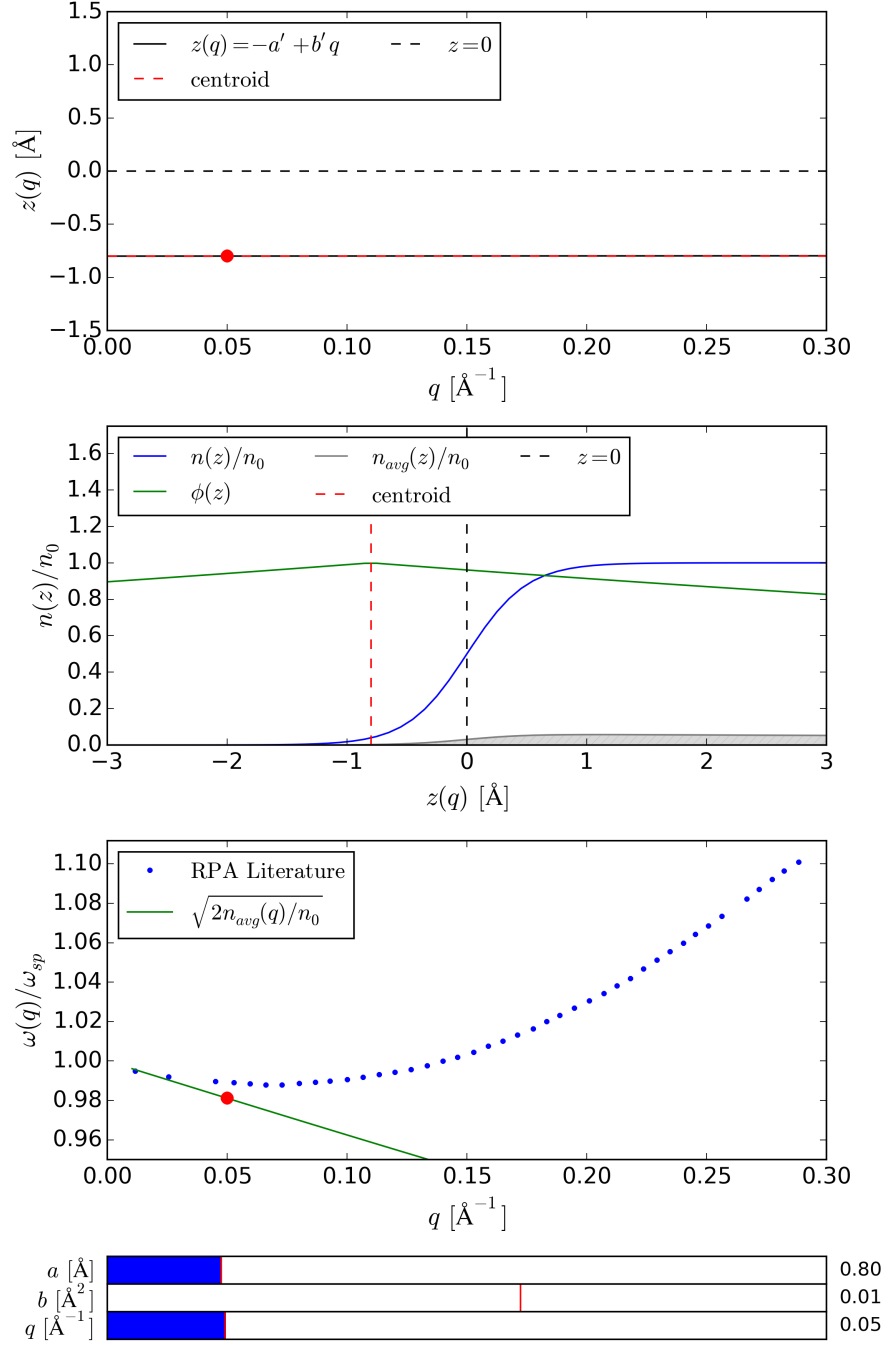


Figure 3.6: *Dynamic charge centroid model fit to RPA calculation (6).* Fit parameters given in figure. When the slope of $z(q)$ is small (i.e., small b'), the dispersion approximates the d-function prediction, Eq. (2.23).

The physical picture that emerges can be easily understood. Firstly, when the centroid is outside of the slab, the induced charge initially “sees” less of the static background as q increases. This leads to an initial *decrease* in the surface plasma frequency, as noted by Tsuei. If the centroid begins farther outside of the surface, the negative part of the dispersion should be enhanced (see Fig. 3.3). As q increases further, the centroid moves inward and, consequently, the induced charge will begin to experience a region of higher static charge density. This will lead to an *increase* in the surface plasma frequency and a positive dispersion. If $z(q)$ rapidly increases with q , the charge centroid will experience more of the background charge at smaller values of q , and the dispersion will increase more quickly (see Fig. 3.5). On the other hand, when the rate of increase of the charge centroid is less steep (Fig. 3.6), it will take longer for the induced charge to experience an increased background charge density as q is increased and, thus, the dispersion should be shallower.

The Tsuei model has not previously been extended to interpret the positive dispersion in this manner. This extension is admittedly heuristic. For instance, it assumes that both the background static charge density and the induced charge density are q -independent. These assumptions may not be entirely valid, and should perhaps be considered more carefully moving forward. Nonetheless, this model is attractive because it only relies upon two free parameters (a' & b') and provides physical insight.

Ultimately, the limitation of the dynamic charge centroid model is that it does not provide a way to readily calculate the quadratic term b' . The d -function formalism is based on the first-principles, local calculation of $d(\omega)$, i.e., at $q = 0$. A way to calculate $b' = \frac{d}{dq}d(\omega, q)|_{q=0}$ must, similarly, be established based on first-principles. However, this is not our objective, since we wish to approximate the linear and quadratic terms of the dispersion *without* the need for additional *ab initio* calculations. Thus, in the next sections, we focus our investigation on the behavior of the

leading terms of the SP dispersion from a phenomenological perspective, and seek to uncover scaling relations of these terms with physical parameters of the system, like r_s , m , and e .

3.2 Full *ab initio* Nonlocal Response of Metallic Slabs

In this section, we calculate the nonlocal SP dispersion of a thick metallic slab exactly in the RPA, for various electron densities, in order to examine how the dispersion depends the parameter r_s . We also compare our calculations to other *ab initio* calculations and experimental data of the SP dispersion for simple metallic surfaces, as reported in the literature. Our objective is to fit Eq. (3.1) to our calculated dispersions and elucidate the functional dependence of the parameters $a \equiv a(r_s)$ and $b \equiv b(r_s)$ on this system property. Ultimately, we demonstrate that the HDA can be used to estimate the parameters $a(r_s)$ and $b(r_s)$, and, in the following sections, we argue that this model can also be applied to arbitrary plasmonic/metamaterial structures, as long as the non-flat interfaces can be modeled as effective media films. This work was published in Ref. [13].

Our RPA calculations use a proprietary Fortran code and are based on the formalism of Ref. [32] applied to a metallic slab of finite thickness [19, 33]. The SP dispersion was calculated from the roots of the reflection coefficient, $r(q, \omega)$, which depends on the the induced density, $\delta\rho(z, \omega)$, in the following way:

$$r(q, \omega) = \int dz e^{qz} \delta\rho(z; \omega) \quad (3.7)$$

The induced density, $\delta\rho(z, \omega)$, was introduced previously as Eq. (2.17), and it is related to the single-particle susceptibility, given previously as Eq. (2.18). The single-

particle susceptibility depends on the eigen-energies and eigenstates of the system, ε_k and $\psi_k(z)$, respectively. Thus, in order to calculate $r(q, \omega)$, it was first necessary to calculate ε_k and $\psi_k(z)$ for our slab geometry. To do this, the single-particle energies and eigenstates were determined from the Hamiltonian of the system, using the self-consistent Lang-Kohn potential V_{eff} [21].

$$\left[-\frac{\hbar^2}{2m_e} \nabla^2 + V_{eff} \right] \psi_k = \varepsilon_k \psi_k \quad (3.8)$$

V_{eff} , which we show in Fig. 3.7, represents the energy profile of the jellium background, which has the form of a smooth, step-like function. In the slab geometry that we chose, this profile is symmetric about its center. This symmetric slab was bounded by an infinite potential, followed by a plateau region of fixed width, smoothly connected to the Lang-Kohn (LK) potential [21].

Eigenfunctions of the system were calculated using numerical integration and a cutoff number (~ 50 eigenstates) was chosen based on the mesh resolution of the potential (i.e. the wavelength of the highest eigenfunction was still resolved within the spacing of points). The choice of total number of eigenstates used in the calculation did not seem to change the results, as long as there were a sufficient number of states above the maximum of the LK potential and the eigenfunctions themselves were spatially resolved. Below, we show the LK potential (Fig. 3.7) and the calculated eigenfunctions (Fig. 3.8). Eigenstates with energies below the plateau of the LK potential decay exponentially at the boundaries, while eigenstates with energies above this value are oscillatory outside of the LK potential.

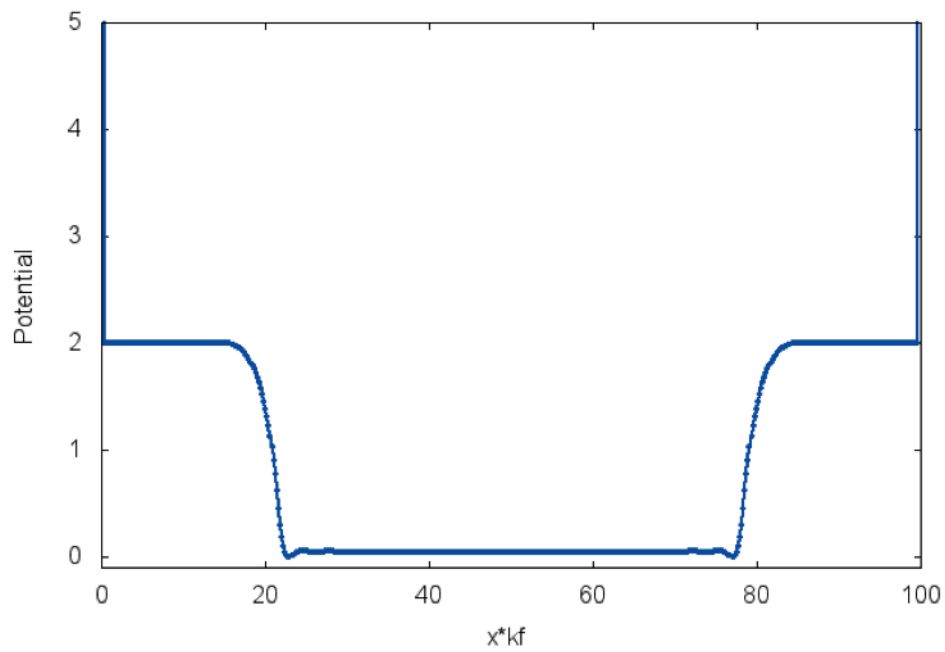


Figure 3.7: *Lang-Kohn potential of metallic slab.* The self-consistent potential [21] is symmetric about the center of the slab. There is a plateau region outside of the slab, bounded by infinite potentials.

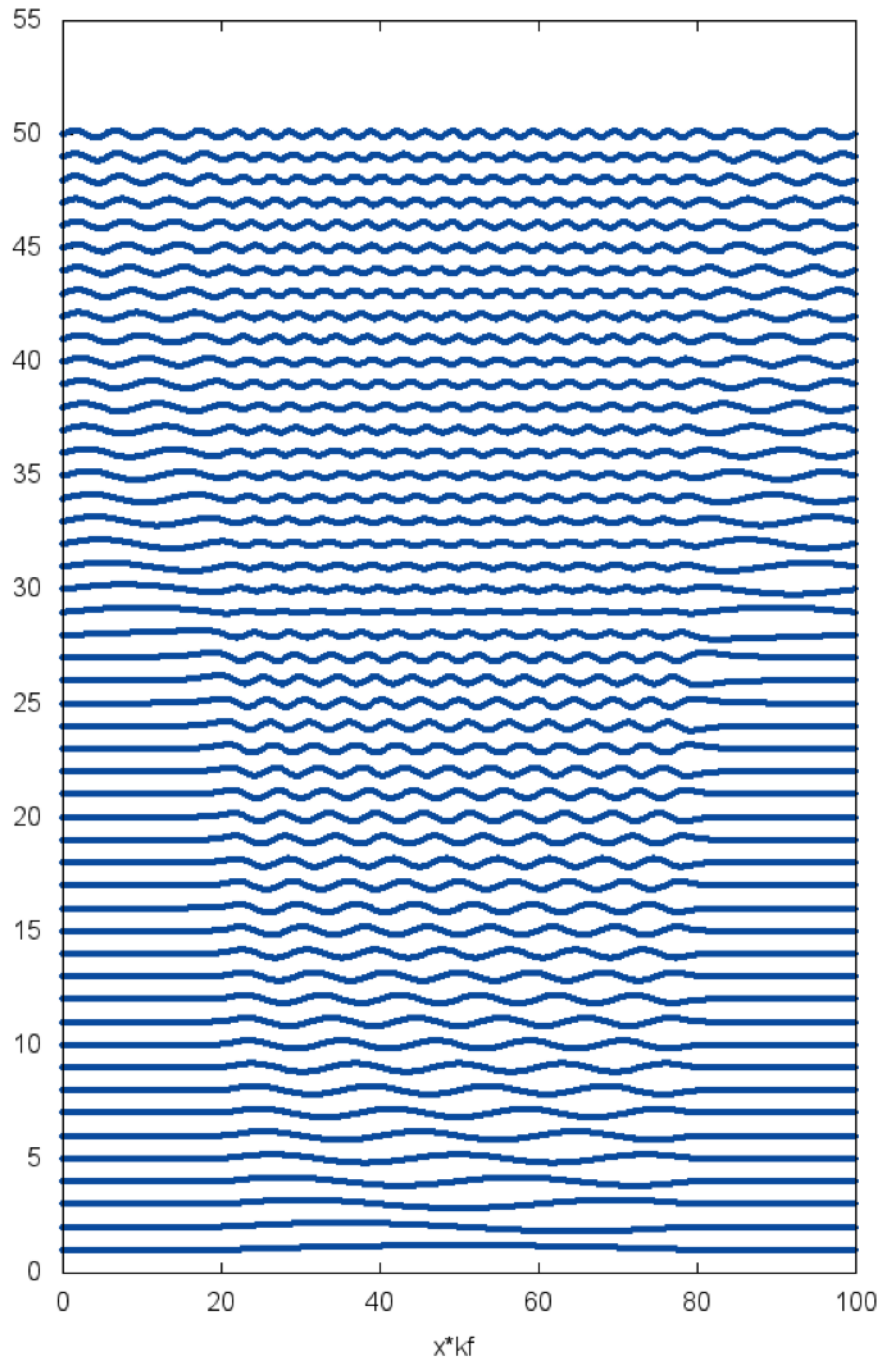


Figure 3.8: *Eigenfunctions calculated within the Lang-Kohn potential.* The eigenfunctions are normalized and offset vertically for readability. A total of 50 eigenstates are computed.

As stated, the electron density, $\delta\rho(z;\omega)$, and reflection coefficient, $r(q,\omega)$, were calculated following Ref. [32]. We computed $r(q,\omega)$ for four different electron densities, parametrized by Wigner-Seitz radii $r_s = 2, 3, 4$, and 5. These values were chosen because they match available data in the literature and approximately correspond to the following real elemental values: Al ($r_s = 2.07$), Li ($r_s = 3.25$), Na ($r_s = 3.93$), and K ($r_s = 4.86$). Fig. 3.9 shows color maps of $\log[\text{Im}\{r(q,\omega)\}]$ plotted vs. ω/ω_p and wavevector q , for each r_s value. Maxima of $\text{Im}\{r(q,\omega)\}$ occur at the surface plasmon condition, and those maxima are marked as open circles on these maps.

Due to the finite thickness of the slab and the resulting coupling between SPs on opposite sides, there is a well-known split of the dispersion at small momenta (here for $q < 0.05 \text{ \AA}^{-1}$), with the upper and lower branches representing the anti-symmetric and symmetric coupled SP modes, respectively. The maxima corresponding to these split-modes have not been marked, but are visible due to color-coding. For larger q (of interest here) a single branch exists, representing the SP mode of a single surface. The thin-solid lines represent the results of RPA calculations for semi-infinite metallic systems, available in the literature [19, 25], calculated for similar electron densities, and squares are experimental data [19].

There is an excellent agreement between our slab and the semi-infinite calculations for $q > 0.1 \text{ \AA}^{-1}$, demonstrating the usefulness of the slab scheme. We note, however, that there was a very small, constant shift of the calculated dispersion for a given density resulting from the finite thickness employed in our calculations. This spurious shift was removed by enforcing all dispersions to start at $0.707\omega_p$. The previously calculated dispersions and experimental data are in qualitative agreement with our calculations in the $q > 0.1 \text{ \AA}^{-1}$ range, in particular at higher electron densities. Note, that no simulation or experimental data exist in the literature for $r_s = 3$.

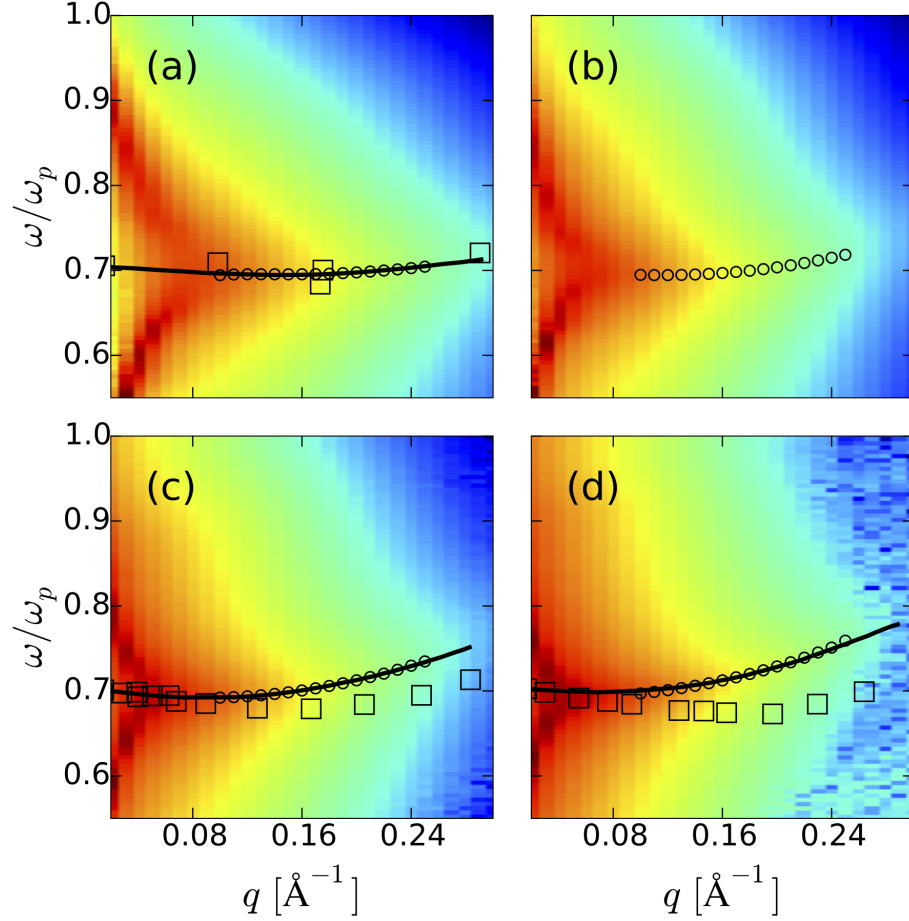


Figure 3.9: *RPA calculations of metallic jellium.* Color maps of $\log[\text{Im}\{r(q, \omega)\}]$ from RPA calculations of metallic jellium slabs for: (a) $r_s = 2$, (b) $r_s = 3$, (c) $r_s = 4$, and (d) $r_s = 5$. Circles represent maxima of $r(q, \omega)$, which occur at the SP dispersion condition. Solid lines represent the RPA calculated results for semi-infinite jellium [19] and squares are experimental results [19] for: (a) $r_s = 2.07$, (c) $r_s = 3.93$, and (d) $r_s = 4.86$. No simulation or experimental data are available in literature for $r_s = 3$.

3.3 HDA-extended d -function Formalism

We then investigated the density scaling properties in detail by fitting Eq. (3.1) to the calculated dispersions of Fig. 3.9 using the least-squares method. Fig. 3.10(a) shows that this fit is excellent, again confirming that our extended d -function formalism is well-motivated. Fig. 3.10(b) shows the fit-extracted parameters a (black triangles) and b (red squares) plotted as a function of r_s .

Clearly, b scales linearly with r_s , with the red-dashed line a guide to the eye. This linear scaling is consistent with the behavior of β in the HDA, implying that the HDA is a good model for b . As shown in the previous chapter, the HDA dispersion has the form $\frac{\omega}{\omega_{sp}} = \left[1 + \frac{\beta}{2\omega_{sp}^2} q^2\right]$, thus b can be identified:

$$b = \beta/2\omega_{sp}^2 \propto r_s. \quad (3.9)$$

Similarly, the dependence of a on r_s can be understood by assuming the HDA-form of the d -function. This result was derived by [22, 12]:

$$d_{HDA}(\omega) = \sqrt{\beta / [\omega_p^2/\varepsilon_b - \omega(\omega + i\gamma)]}, \quad (3.10)$$

Thus, the parameter a has the following functional dependence:

$$a = \sqrt{\beta}/2\omega_{sp} \propto \sqrt{r_s}. \quad (3.11)$$

The black-dashed line in Fig. 3.10(b) represents the scaling given by Eq. (3.11). This demonstrates that the HDA can be used to estimate the electron density scaling of both the a and b parameters of our extended d -function formalism. We note, however, that although the functional dependencies of parameters a and b are described by the HDA, the constants of proportionality in Eq. (3.9) and Eq. (3.11) are not.

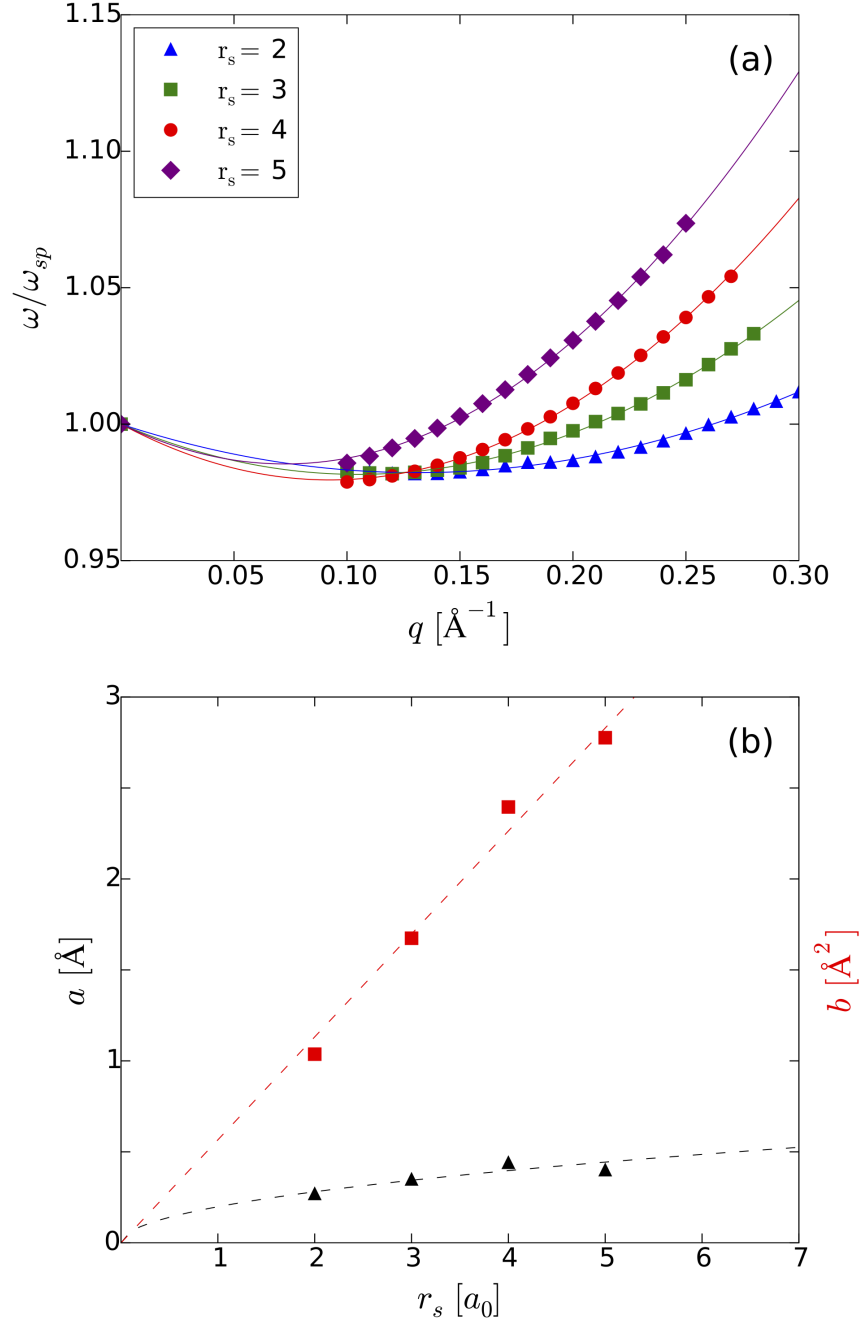


Figure 3.10: *SP dispersions for metallic jellium slabs.* In (a), we plot RPA-calculations (symbols), least-square fits to these calculations using Eq. (3.1) (solid lines), for the densities $r_s = 2, 3, 4$ and 5 . In (b), we plot fit-extracted parameters a (black triangles) and b (red squares) plotted as a function of r_s . The red and black colored lines correspond to Eqs. (3.9) & (3.11), respectively.

In the next section, we examine other possible scaling relations of the parameters a and b . Ultimately, we argue that one can create a useful nonlocal extension of the material response, i.e., $\epsilon(\omega) \rightarrow \epsilon(q, \omega)$, for structured systems using effective medium scaling arguments.

3.4 Effective Medium Scaling Properties

In the previous section, we explicitly examined r_s scaling, and here we comment on other scaling behavior, motivated by the notion that simple scalings are expected to hold for structures with non-flat interfaces, treated as flat effective media films. This idea is supported by Pendry et al. [4] in their important paper, which pioneered the metamaterial concept. They showed that the effective dielectric function of a 3D cubic metallic wire array in the long-wavelength limit is given by the Drude form, but with the plasma frequency renormalized by the effectively reduced density (electrons are confined to wires, and thus occupy smaller volume of the array), which is an r_s -scaling property. Also, the plasma frequency incorporates an increased effective mass, which is an inductive effect, and in what follows we parameterize the effective mass by η , such that $m = \eta m_0$. As a result of both renormalizations, the wire medium was shown to have its plasma frequency dramatically shifted down from the UV to the radio range, with both scaling factors of the same order ($\sim 10^5$). The same phenomenon is expected for other metamaterial structures, e.g for those with non-flat surface morphology.

Now we examine the effective mass scaling, where $m = \eta m_0$. Relations Eq. (3.9) and Eq. (3.11) from the previous section suggest that for systems with the effective

electron mass changed, $m = \eta m_0$, at constant r_s , the following scalings hold:

$$b \propto 1/\eta \tag{3.12}$$

and

$$a \propto 1/\sqrt{\eta}. \tag{3.13}$$

Finally, for completeness, we consider a case where the entire dispersion scales by a common factor, such that $\underline{\omega}(q) = \omega(q)/\eta$, where $\underline{\omega}(q)$ represents the scaled plasma frequency. To make this possible, we require $\underline{m} = \eta m_0$ and $\underline{V}_{eff} = V_{eff}/\eta$, where η now parameterizes *both* the magnitude of the effective electron mass and the screening of electronic interactions. We argue that such a scaling is possible, since the presence of plasmonic structures will inductively increase the mass of electrons in a system and simultaneously screen the electronic charge. For simplicity, we require that these properties scale by the same amount, thereby reducing the scaling of the response to one effective parameter, η .

We determine the behavior of the dispersion by starting with the Hamiltonian equation:

$$\left[-\frac{\hbar^2}{2\underline{m}} \nabla^2 + \underline{V}_{eff} \right] \underline{\psi}_k = \underline{\varepsilon}_k \underline{\psi}_k \tag{3.14}$$

The above scaling ansatz leads to renormalization of the electron energies of the system, while the eigenstates are unaffected; i.e. Eq. (3.14) may be written as:

$$\left[-\frac{\hbar^2}{2m_e} \nabla^2 + V_{eff} \right] \psi_k = \eta \underline{\varepsilon}_k \psi_k \tag{3.15}$$

where $\underline{\varepsilon}_k = \varepsilon_k/\eta$. The response of the scaled system is then related to the response

of the bare system in the following way:

$$\begin{aligned}
\chi_0(z, z'; \underline{\omega}) &= \sum_k \sum_{k'} \frac{f_k - f_{k'}}{\varepsilon_k - \varepsilon_{k'} + \hbar \underline{\omega}} \psi_k^*(z) \psi_{k'}(z) \psi_{k'}^*(z') \psi_k(z') \\
&= \eta \sum_k \sum_{k'} \frac{f_k - f_{k'}}{\varepsilon_k - \varepsilon_{k'} + \eta \hbar \underline{\omega}} \psi_k^*(z) \psi_{k'}(z) \psi_{k'}^*(z') \psi_k(z') \\
&= \eta \chi_0(z, z'; \omega)
\end{aligned} \tag{3.16}$$

where we define $\underline{\omega} = \omega/\eta$, where ω is the complex frequency of the bare system.

The induced charge density, Eq. (2.15), is given by:

$$\begin{aligned}
\delta \rho(z; \underline{\omega}) &= \int dz' \chi_0(z, z'; \underline{\omega}) \left[V_{ext} + \int dz'' \underline{V}_c(z', z'') \delta \rho(z''; \underline{\omega}) \right] \\
&= \int dz' \eta \chi_0(z, z'; \omega) \left[V_{ext} + \int dz'' \frac{V_c(z', z'')}{\eta} \delta \rho(z''; \omega) \right]
\end{aligned} \tag{3.17}$$

We can immediately identify $\delta \rho(z; \underline{\omega}) = \eta \delta \rho(z; \omega)$, which makes Eq. (3.17) identical to Eq. (2.17). Thus, according to Eq. (3.7), the surface response of the scaled system is related to that of the bare system by, $\underline{r}(q, \underline{\omega}) = \eta r(q, \omega)$.

The above relation implies that the poles of the bare system, $r(q, \omega)$, must be equal to the poles of the scaled system $\underline{r}(q, \underline{\omega})$, and thus the effect of our scaling ansatz is such that the overall surface plasmon dispersion of the bare system is simply scaled by our effective parameter, i.e., $\underline{\omega}(q) = \omega(q)/\eta$. Specifically, the long-wavelength surface plasma frequency is redshifted and dispersion is “flattened” compared to the bare system

3.5 Self-Energy Extension of Dielectric Response

Finally, the nonlocal response $\epsilon(q, \omega)$ can be constructed from knowledge of the SP dispersion, so if this dispersion is known (i.e., based on effective medium scaling properties), then other response phenomena can be calculated. To incorporate knowledge

of the dispersion into $\epsilon(q, \omega)$, we make the ansatz, as in Ref [34]:

$$\epsilon(q, \omega) = \epsilon_b - \frac{\omega_p^2}{\omega(\omega + i\gamma) + \Sigma}, \quad (3.18)$$

and require that the roots of the nonlocal reflection coefficient, $r_p = \frac{\epsilon(q, \omega) - \epsilon_0}{\epsilon(q, \omega) + \epsilon_0}$, yield the dispersion of our extended model, i.e., Eq. (3.1). This leads to the identification:

$$\Sigma = 2\omega_{sp}^2 (aq - bq^2), \quad (3.19)$$

where a and b can be estimated by the HDA.

Therefore, accounting for non-local effects amounts to the following, very simple transformation in the effective dielectric function formula:

$$\omega(\omega + i\gamma) \rightarrow \omega(\omega + i\gamma) + \Sigma. \quad (3.20)$$

The same transformation can be used in the more general Drude-Lorentz form of the effective dielectric function

$$\epsilon(\omega) = \epsilon_b + \sum_m \frac{\omega_{pm}^2}{\omega_{0m}^2 - \omega(\omega + i\gamma)}. \quad (3.21)$$

Thus, the full procedure to implement the nonlocal extensions is as follows. Firstly, a local simulation of a metamaterial structure should be performed, for example by employing FDTD. Secondly, the effective local dielectric function should be extracted, for example, by using the standard procedure developed in [35], and fitted with the Drude-Lorentz form Eq. (3.21). Finally, the transformation Eq. (3.20) provides the desired extension. A similar procedure was applied in the recent study of the electron scattering in the presence of phonons and plasmons, which requires non-local corrections [3], except, in this case, a simple linear model of Σ was used

instead of Eq. (3.19) and a different method was employed to extract the dielectric function.

In this chapter, we proposed a simple q^2 extension of the d -function formalism and demonstrated the usefulness of this scheme in describing SP dispersions for very large q . Ultimately, we showed that the HDA, even though itself incapable of describing SP dispersions, can be used to estimate the parameters of our extension. We supported this HDA-extended d -function formalism with our own *ab initio* RPA calculations for metallic films with flat surfaces, for various electron densities, and we also explored other valid scaling relations. Finally, we have generalized the HDA-extended d -function formalism to arbitrary plasmonic/metamaterial structures, in which non-flat interfaces can be modeled as effective media films. We presented how $\epsilon(q, \omega)$ may be calculated for such structures based on the “self-energy” ansatz.

CHAPTER 4

Effective Thin-Film Method

As emphasized in the Part I of this thesis, nonlocality strongly affects the electromagnetic response of nanostructures with small or sharp features and, therefore, should be taken into account in simulations. However, this is typically *not* done in FDTD calculations because of the inherent local dependence of the algorithms. We demonstrate that nonlocality can be accounted for in such simulations by including a thin-film over structures of interest, where the thin-film has an effective dielectric response related to the d-function. Thus, any local calculations or simulations that include this film become automatically nonlocal to the same order. We propose a form for the effective response that is physically valid, and we show that our formalism correctly yields red-shifts of the Mie resonance for spheres, compared to classical calculations. Moreover, we show that our formalism is identical to known analytic results in the limit of small film-thickness. Aspects of what we present in this chapter were published in Ref. [14], where our effective thin-film method was used in FDTD simulations to calculate absorption and electric field enhancement from metallic nanospheres and these results were consistent with published, first-principles calculations.



4.1 Geometric Mapping of d-Function Formalism

Nonlocal physics greatly affects the electromagnetic response of metallic nanostructures with feature-sizes much smaller than the wavelength of incoming light, for instance, the Mie resonance frequency of nano-spheres, nano-rods, and nano-tips is known to be shifted (red-shifted for alkali metals and blue-shifted for noble metals) compared to classically derived values [36]. A fully self-consistent, quantum mechanical treatment of the single-particle electron response in metals can be used to calculate nonlocal behavior, as addressed in the previous chapters. However, we also established that first-principles calculations of nonlocal effects are not straightforward to carry out for complex plasmonic systems due to numerical complexity. Thus, we seek a simple strategy for incorporating the appropriate nonlocal physics into local calculations involving nontrivial structures.

The strategy that we developed, motivated by Ref. [22, 37], involves the identification of an equivalence between the reflection coefficient for a planar, nonlocal system and the reflection coefficient for a planar, local system whose surface is augmented by an additional material layer. One of our insights was to use the d-function formalism, since the d-function is a surface response function. Before delving into the derivation, we present a schematic that illustrates the proposed equivalence. On the one hand, the nonlocal physics of a metal, system A, is described by the nonlocal response function, $\epsilon(q, \omega)$, which occupies a half-space. Light is incident from an outer half-space, whose dielectric function is ϵ_0 . The local equivalent, system B, consists of an outer dielectric, ϵ_0 , surface layer, $\epsilon_s(\omega)$, and metal, $\epsilon(\omega)$, in the configuration depicted in Fig. 4.1.

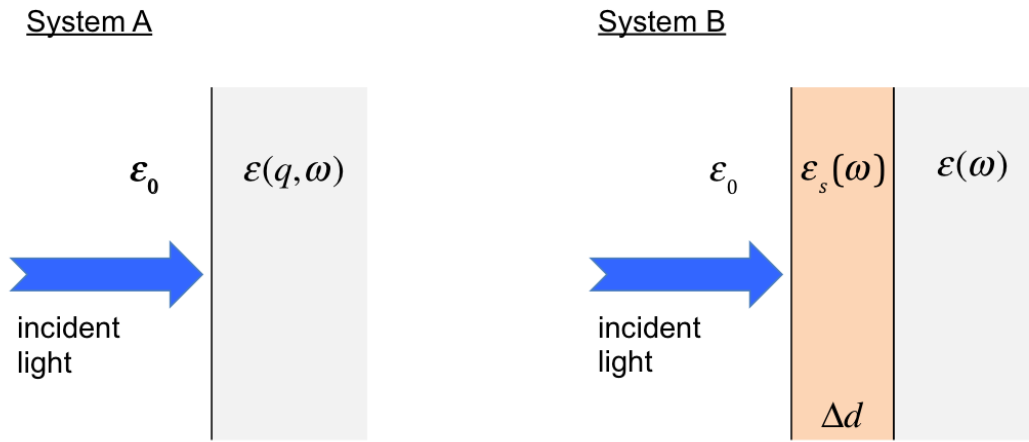


Figure 4.1: *Schematic of effective thin-film method.* The reflection coefficient of a nonlocal system (left) is equivalent to the reflection coefficient of a local system with an intermediate layer of thickness Δd (right). The dielectric function of the layer, ϵ_s , is defined such that the correspondence is preserved.

If there exists a function, $\epsilon_s(\omega)$, that makes the reflection coefficient of system B equal to system A, then the physics of system A may be simulated by system B, where the advantage is that system B only consists of *local* response functions. In other words, the *nonlocal* physics of system A may be conveniently mapped onto the *local* surface dielectric function of a thin, fictitious film (of thickness Δd) placed on top of a *local* metal surface, as depicted for system B, and the calculations for system B may be performed entirely within standard FDTD codes.

To determine the form of $\epsilon_s(\omega)$, we derive the p-polarized reflection coefficient for the geometry of system B, for which we use the superscript *TF* for “thin-film,” and compare to the known, nonlocal reflection coefficient for system A, for which we use the superscript *NL* for “nonlocal.” We partition the system into three regions, shown below, and write the electric field components in each region.

For a monochromatic, transverse wave (p-polarized) incident from the left upon the system described above, the electric field in the three regions can be written as:

$$\vec{E}_1(\vec{r}, t) = \vec{E}_{1+} e^{i(\omega t - qx + k_1 z)} + \vec{E}_{1-} e^{i(\omega t - qx - k_1 z)} \quad (4.1a)$$

$$\vec{E}_s(\vec{r}, t) = \vec{E}_{s+} e^{i(\omega t - qx + k_s z)} + \vec{E}_{s-} e^{i(\omega t - qx - k_s z)} \quad (4.1b)$$

$$\vec{E}_2(\vec{r}, t) = \vec{E}_{2+} e^{i(\omega t - qx + k_2 z)} \quad (4.1c)$$

where $\vec{E}_{j\pm}$ is the electric field vector of the incoming (+) or outgoing (-) wave in the outside dielectric ($j = 1$), surface layer ($j = s$), or metal ($j = 2$). The the respective wavevectors are $\vec{k}_{j\pm} = (q, \mp k_j)$, where $k_j = \sqrt{(\omega/c)^2 \epsilon_j - q^2}$ is the z-component and q is the in-plane component.

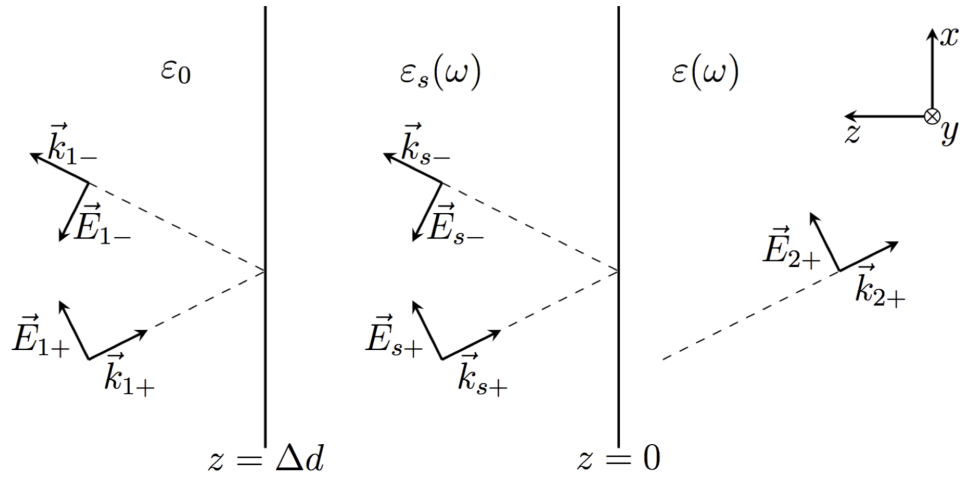


Figure 4.2: *Reflection geometry for p-polarized light.* Light incident on a layered system from the positive z -direction. A slab of thickness Δd and permittivity $\varepsilon_s(\omega)$ acts as an intermediate layer (index s), confined by a dielectric half-space with permittivity ε_0 (index 1) and a metallic half-space with Drude permittivity $\varepsilon(\omega)$ (index 2). The plane of incidence is the xz -plane.

Using the standard boundary conditions across an interface (D_z and E_x continuous), the reflection coefficient is

$$r_p^{TF} \approx \frac{\varepsilon(\omega) - \varepsilon_0 \frac{k_2}{k_1} - i \frac{\varepsilon(\omega)\varepsilon_0}{\varepsilon_s(\omega)k_1} q^2 \Delta d + i \alpha_-(\omega) \Delta d}{\varepsilon(\omega) + \varepsilon_0 \frac{k_2}{k_1} + i \frac{\varepsilon(\omega)\varepsilon_0}{\varepsilon_s(\omega)k_1} q^2 \Delta d - i \alpha_+(\omega) \Delta d} \quad (4.2)$$

where $\alpha_{\pm}(\omega) = \left[\frac{\varepsilon(\omega)\varepsilon_0}{k_1} \left(\frac{\omega}{c} \right)^2 \pm \varepsilon_s(\omega)k_2 \right]$ and an overall phase has been neglected (see Appendix D for a thorough derivation of this formula and additional details).

Now, the non-local reflection coefficient for this geometry, but without the presence of a film, was derived by Feibelman [12] and stated in Chapter 2. We restate it here:

$$r_p^{NL} = \frac{\varepsilon(\omega) - \varepsilon_0 \frac{k_2}{k_1} + i \frac{[\varepsilon(\omega) - \varepsilon_0]}{k_1} q^2 d(\omega)}{\varepsilon(\omega) + \varepsilon_0 \frac{k_2}{k_1} - i \frac{[\varepsilon(\omega) - \varepsilon_0]}{k_1} q^2 d(\omega)}, \quad (4.3)$$

where positive $d(\omega)$ lies above the metal surface. In order to identify the mapping, we require that Eq. (4.2) is identical to Eq. (4.3) in the nonretarded limit, where $\omega/c \ll q$ and $k_1 = k_2 = iq$. In this limit, r_p^{TF} and r_p^{NL} have the following forms:

$$r_p^{TF} = \frac{(\varepsilon_m - \varepsilon_0) + (\varepsilon_s - \varepsilon_m/\varepsilon_s) q \Delta d}{(\varepsilon_m + \varepsilon_0) + (\varepsilon_s + \varepsilon_m/\varepsilon_s) q \Delta d} \quad (4.4)$$

and

$$r_p^{NL} = \frac{(\varepsilon_m - \varepsilon_0) + (\varepsilon_m - \varepsilon_0) q d(\omega)}{(\varepsilon_m + \varepsilon_0) - (\varepsilon_m - \varepsilon_0) q d(\omega)} \quad (4.5)$$

where we make the simplification of notation $\varepsilon_s(\omega) \rightarrow \varepsilon_s$ and $\varepsilon(\omega) \rightarrow \varepsilon_m$. There is more than one solution to the above set of equations and, as we will argue in the next section, only one solution is physically valid.

To continue, one must expand the Eq. (4.4) and Eq. (4.5), assuming that q is

small. The expansion for the thin-film response is:

$$r_p^{TF} = r_p^{CL} \left[1 + 2 \frac{(\epsilon_s^2 - \epsilon_m^2)}{\epsilon_s (\epsilon_m - \epsilon_0) (\epsilon_m + \epsilon_0)} q \Delta d \right] \quad (4.6)$$

where the classical reflection coefficient, $r_p^{CL} = (\epsilon_m - \epsilon_0) / (\epsilon_m + \epsilon_0)$ has been identified. The expansion for the Feibelman response is:

$$r_p^{NL} = r_p^{CL} \left[1 + 2 \frac{\epsilon_m}{(\epsilon_m + \epsilon_0)} q d(\omega) \right] \quad (4.7)$$

We note that each response is a series expansion of the classical response, r_p^{CL} . In fact, it is interesting to note that Eq. (4.7) also has the form:

$$r_p^{NL} = r_p^{CL} [1 + r_p^{CL} 2f(\omega)] \quad (4.8)$$

based on the definition of Eq. (2.19). Therefore, r_p^{NL} is a series expansion in *orders* of r_p^{CL} .

Now we make the following identification between Eqs. (4.6) & (4.7):

$$\frac{(\epsilon_s^2 - \epsilon_m^2)}{\epsilon_s (\epsilon_m - \epsilon_0)} \Delta d = \epsilon_m d(\omega) \quad (4.9)$$

The solutions to this equation are:

$$\epsilon_s = \frac{\epsilon_m}{2} \left[(\epsilon_m - \epsilon_0) \frac{d(\omega)}{\Delta d} \pm \left[(\epsilon_m - \epsilon_0)^2 \left(\frac{d(\omega)}{\Delta d} \right)^2 + 4 \right]^{1/2} \right] \quad (4.10)$$

Immediately, it is clear that the solutions are inversely proportional to Δd , which leads to a compensating effect, i.e., the thin-film strongly affects absorption even though it may be dimensionally negligible. The thin-film response is also directly proportional to $d(\omega)$, which underscores the physical explanation that the d-function

behaves like a surface response function. We also note that the response functions within the thin-film formula, $\epsilon(\omega)$ and $d(\omega)$, are complex. Thus, the appropriate choice of branch-cut must be made when taking the square-root.

4.2 Identification of Physically Valid Response

We now consider the (+) and (-) solutions in the limits of small Δd and large Δd , and scrutinize their validity. For *Case 1*, the positive solution (i.e., $\pm \rightarrow +$), we have the following:

(a) in the limit of $\Delta d \ll d(\omega)$,

$$\epsilon_s \approx \epsilon_m (\epsilon_m - \epsilon_0) \frac{d(\omega)}{\Delta d} \quad (4.11)$$

(b) in the limit of $\Delta d \gg d(\omega)$,

$$\epsilon_s \approx -\epsilon_m \quad (4.12)$$

For *Case 2*, the negative solution (i.e., $\pm \rightarrow -$), we have the following:

(a) in the limit of $\Delta d \ll d(\omega)$,

$$\epsilon_s \approx -\frac{\epsilon_m}{(\epsilon_m - \epsilon_0)} \frac{\Delta d}{d(\omega)} \quad (4.13)$$

(b) in the limit of $\Delta d \gg d(\omega)$,

$$\epsilon_s \approx \epsilon_m \quad (4.14)$$

Plots of $\epsilon_s(\omega)$ for these two solutions, *Case 1* and *Case 2*, are shown in the following figures for varying film thickness, compared to the Drude model.

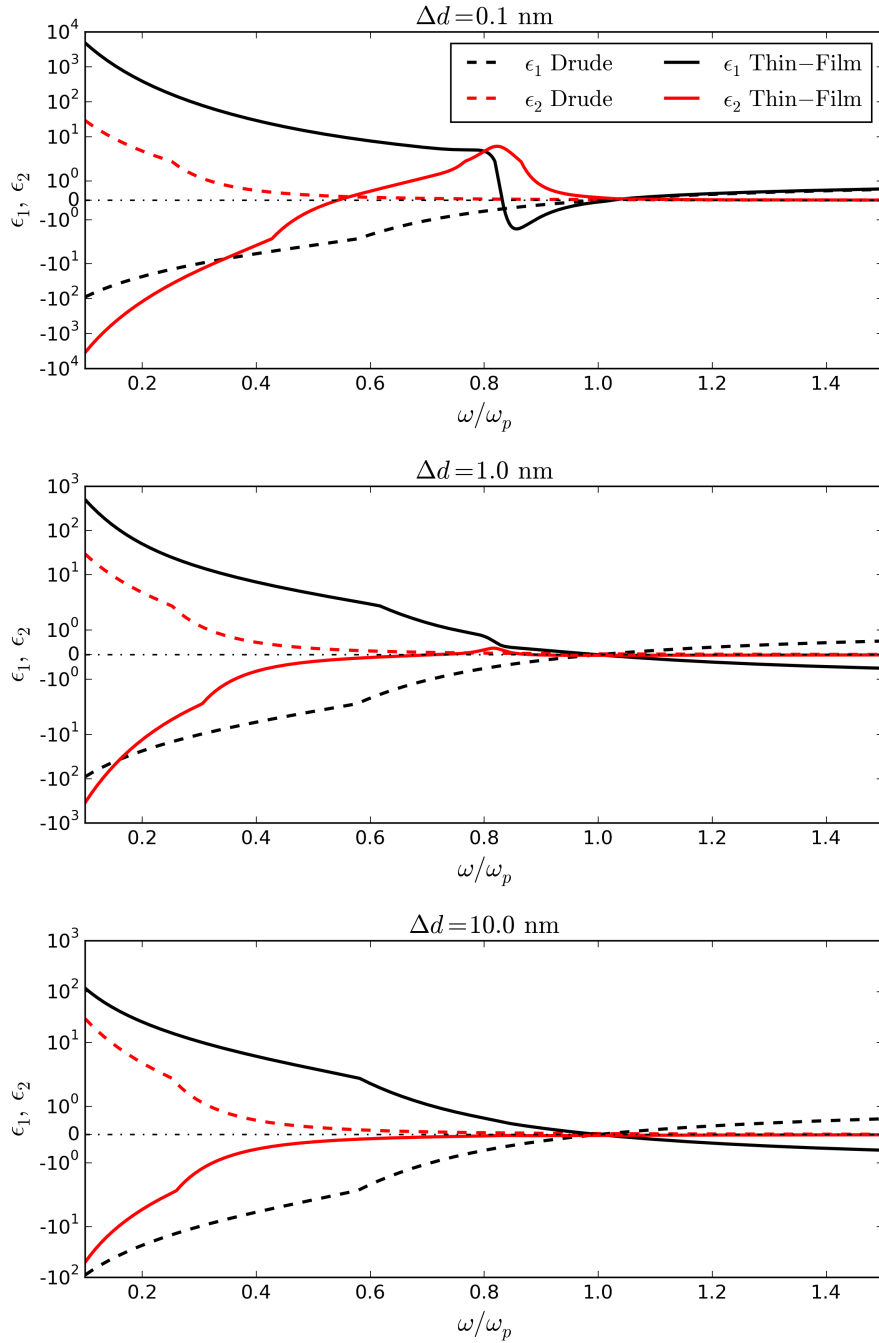


Figure 4.3: *Thin-film dielectric function (1).* Eq. (4.10) is used to calculate the thin-film dielectric function corresponding to *Case 1*, as film-thickness is varied. Also shown is the classical, Drude dielectric function. Real and imaginary parts are shown in black and red, respectively.

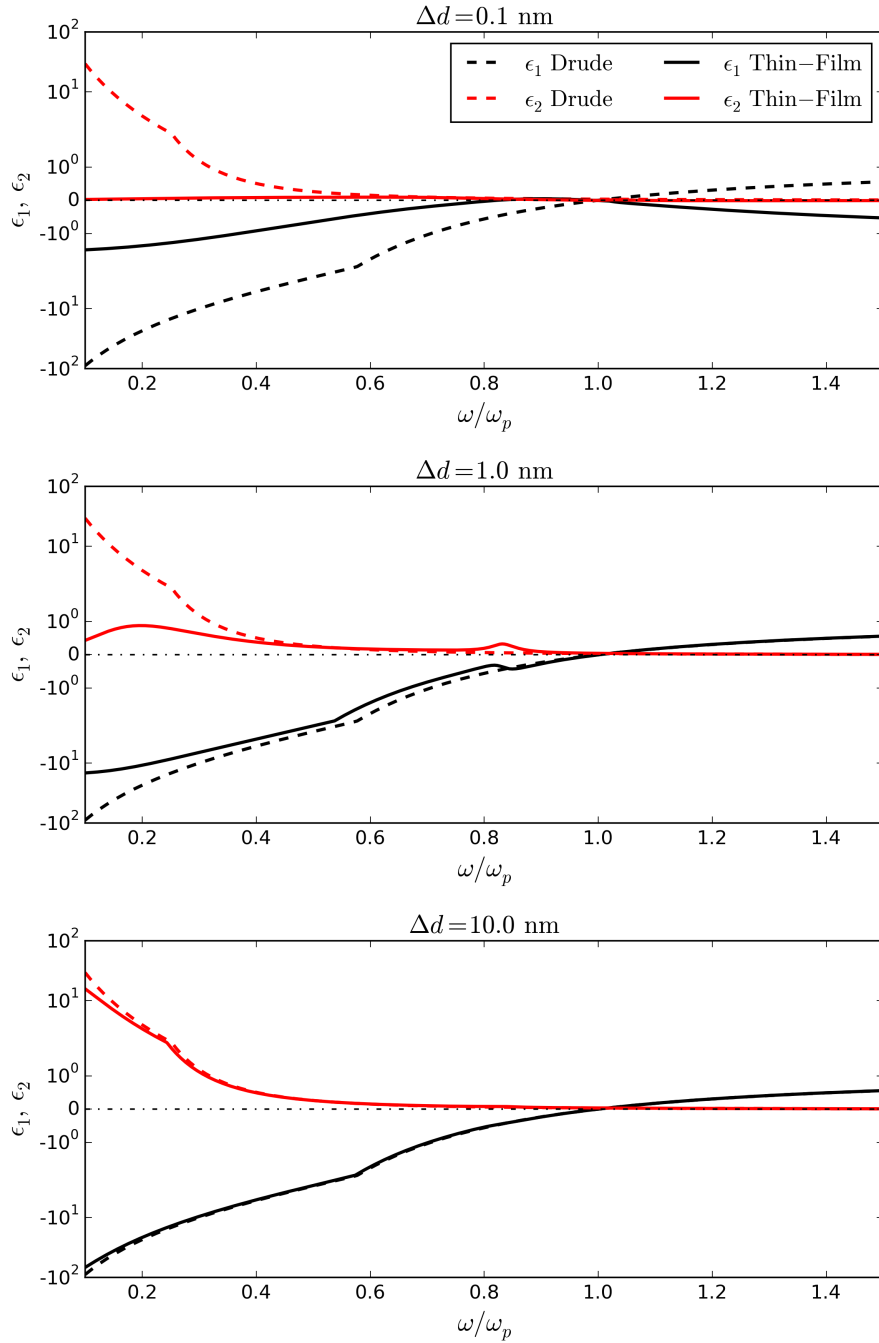


Figure 4.4: *Thin-film dielectric function (1).* Eq. (4.10) is used to calculate the thin-film dielectric function corresponding to *Case 2*, as film-thickness is varied. Also shown is the classical, Drude dielectric function. Real and imaginary parts are shown in black and red, respectively.

Here, we note some salient features of the thin-film response in *Case 1* and *Case 2*. Firstly, it is clear that the dielectric function corresponding to *Case 1* behaves like an “anti-metal” in the regime of small film-thickness and large film-thickness. That is, the real and imaginary parts of $\epsilon_s(\omega)$ are flipped compared to the nominal Drude behavior (see Fig. 4.3). Immediately, this seems strange, particularly because the negative imaginary part implies that $\epsilon_s(\omega)$ acts like a gain medium. In contrast, *Case 2* approaches the metal dielectric function for large film thickness and exhibits metallic behavior, i.e., a negative real permittivity, for small film thickness (see Fig. 4.4). This metallic behavior satisfies our expectation, which is that the thin-film should have the properties of a metal, but with a reduced density of free electrons. This is because the surface region, in actuality, is a region of lower electron density compared to the bulk, where a tail of free electrons diminishes towards the vacuum.

In Fig. 4.5, now we plot the thin-film reflection coefficient, Eq. (4.4) with $\epsilon_s(\omega)$ from Eq. (4.10), for varying film thickness, at fixed q . We compare to the Fiebelman reflection formulae, Eq. (4.5), and the local reflection formula. These reflectance plots also confirm our intuition that *Case 2* is the appropriate choice. The reflectance spectra for *Case 2*, which uses the (-) solution of Eq. (4.10), approaches the nonlocal Fiebelman formula in the small thickness limit, i.e., the first plot of Fig. 4.6. It also approaches and the normal Drude reflectance in the limit of large thickness limit, i.e., the last plot of Fig. 4.6. On the other hand, *Case 1* clearly exhibits incorrect behavior, as shown in Fig. 4.5.

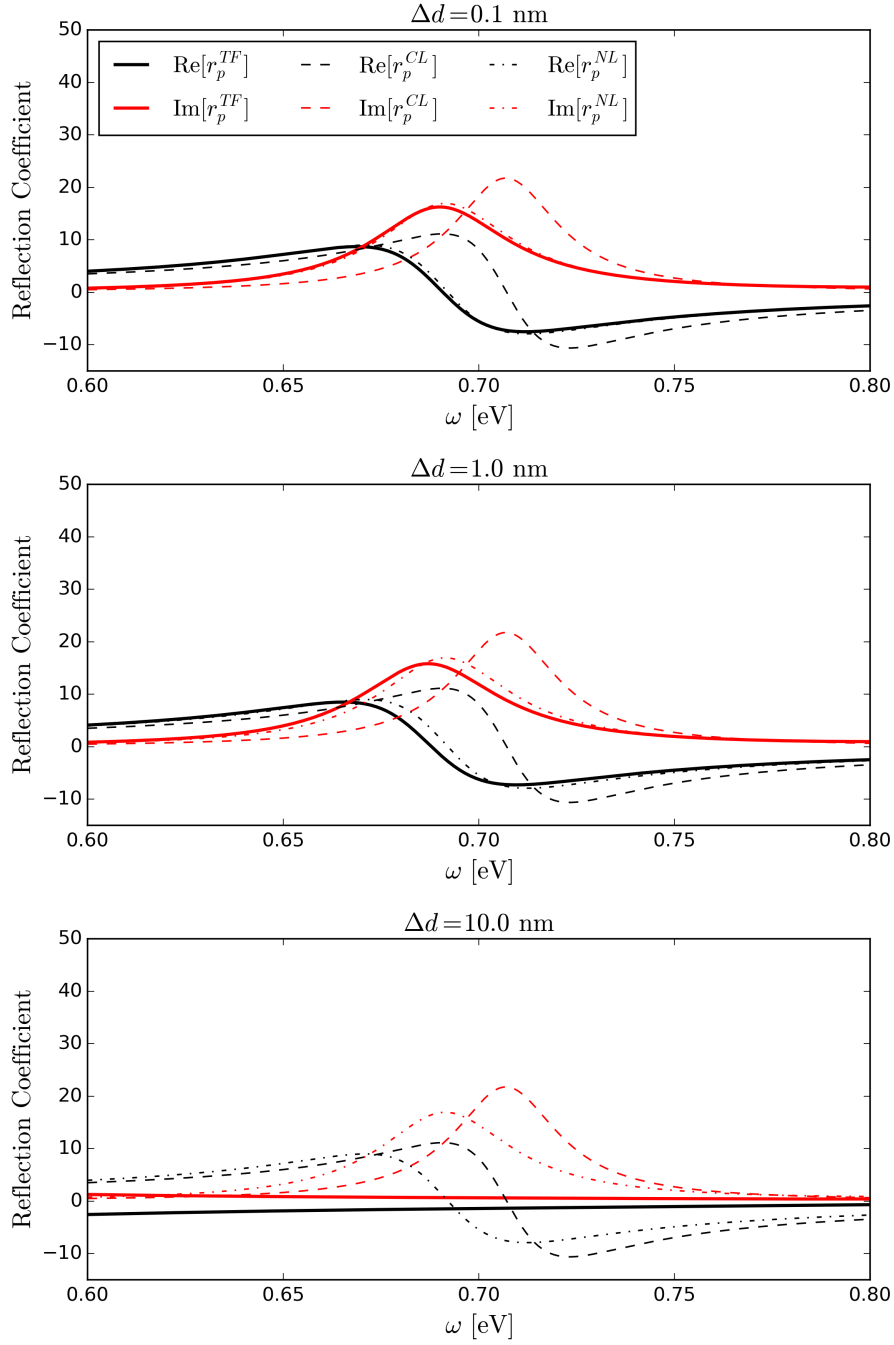


Figure 4.5: *Thin-film reflection coefficient (1).* Eq. (4.4) with $\epsilon_s(\omega)$ from Eq. (4.10) is used to calculate the thin-film reflection coefficient corresponding to *Case 1*, as film-thickness is varied (solid line). This is compared to the local reflection coefficient (dashed line) and the nonlocal reflection coefficient (dash-dotted line).

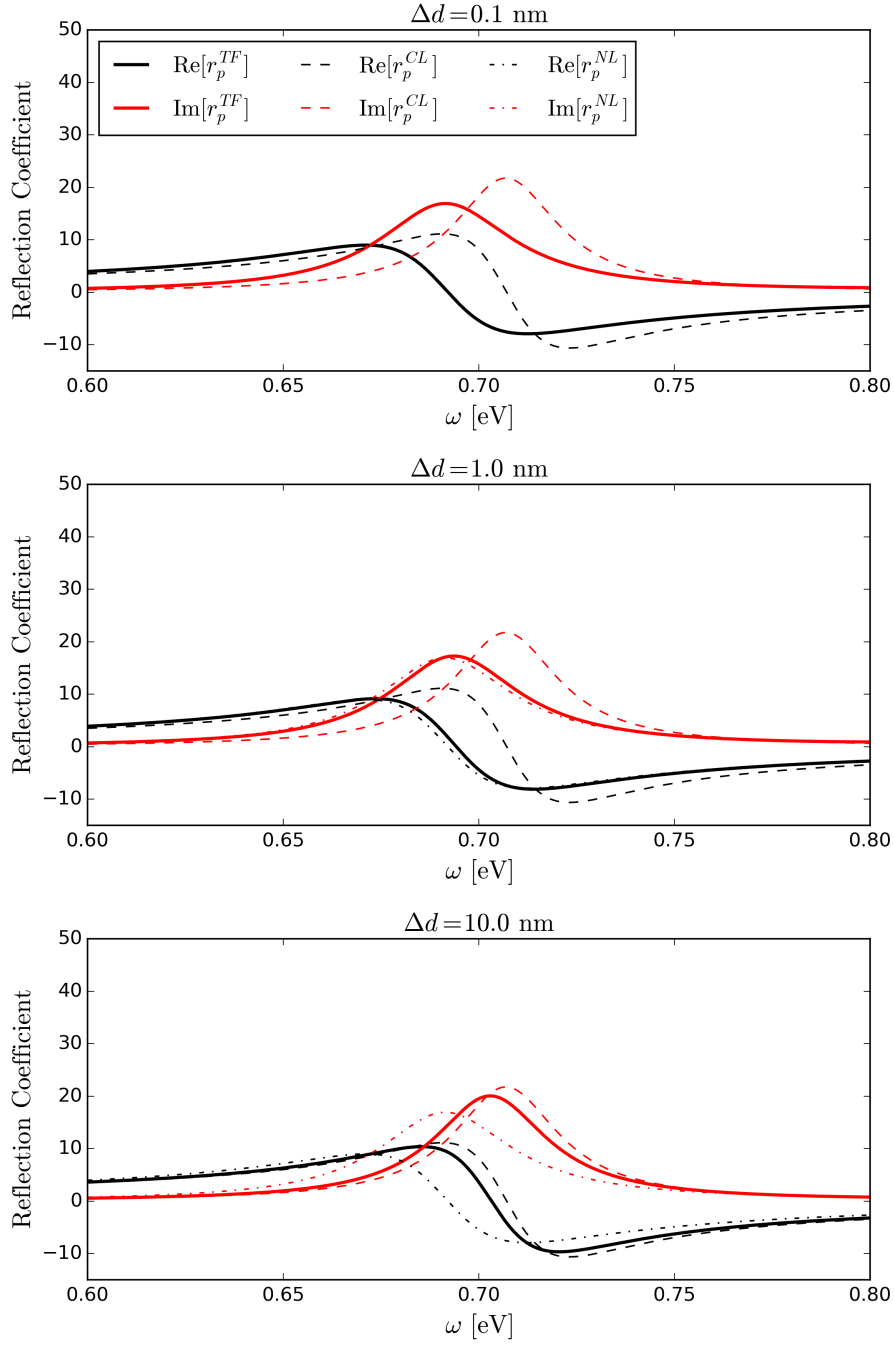


Figure 4.6: *Thin-film reflection coefficient (2).* Eq. (4.4) with $\epsilon_s(\omega)$ from Eq. (4.10) is used to calculate the thin-film reflection coefficient corresponding to *Case 2*, as film-thickness is varied (solid line). This is compared to the local reflection coefficient (dashed line) and the nonlocal reflection coefficient (dash-dotted line).

Ultimately, we propose that *Case 2*, which uses the (-) solution of Eq. (4.10), is a physically valid choice for the thin-film response. To support this claim, we could also show that this formula satisfies Kramers-Kronig relations,

$$\text{Re} [\epsilon_s(\omega)] = 1 + \frac{2}{\pi} \text{P} \int_0^\infty \frac{\omega' \text{Im} [\epsilon_s(\omega')] - \omega \text{Im} [\epsilon_s(\omega)]}{(\omega'^2 - \omega^2)} d\omega' \quad (4.15a)$$

$$\text{Im} [\epsilon_s(\omega)] = -\frac{2\omega}{\pi} \text{P} \int_0^\infty \frac{\text{Re} [\epsilon_s(\omega')] - \text{Re} [\epsilon_s(\omega)]}{(\omega'^2 - \omega^2)} d\omega' \quad (4.15b)$$

and sum rules [2],

$$\int_0^\infty \omega \text{Im} [\epsilon_s(\omega)] d\omega = \frac{\pi}{2} \bar{\omega}_p^2 \quad (4.16a)$$

$$\int_0^\infty \omega \text{Im} [\epsilon_s^{-1}(\omega)] d\omega = -\frac{\pi}{2} \bar{\omega}_p^2 \quad (4.16b)$$

$$\int_0^\infty \omega^{-1} \text{Im} [\epsilon_s^{-1}(\omega)] d\omega = \frac{\pi}{2} \quad (4.16c)$$

For instance, in our related paper [14], we performed these calculations for a simplified, alternative thin-film formulation. However, we do not present a similar calculation in this thesis because Eq. (4.10) poses significant numerical difficulty. Nonetheless, we believe that it should be possible, using the appropriate numerical scheme and choice of branch-cuts, to demonstrate that Eqns. (4.15) & (4.16) are satisfied.

Now, to conclude this section, we briefly report other incarnations of this thin-film correspondence. Firstly, Kempa & Gerhardtts [22] first examined the ellipsometry ratio (i.e. $\rho = r_p/r_s$) of nonlocal thin-films and concluded that the nonlocal properties of a simple surface could be represented by local optics. Thus, by matching $\rho^{TF}(q, \omega) \rightarrow \rho^{NL}(q, \omega)$, they derived the following thin-film correspondence (with a proper (-) sign for compatibility with our convention, and $\epsilon_0 = 1$):

$$d(\omega) = \frac{(\epsilon_s - \epsilon_m)}{(\epsilon_m - 1)} \left(\frac{1}{\epsilon_m} - 1 \right) \Delta d \quad (4.17)$$

which has the following solution (not presented previously):

$$\epsilon_s = \frac{1}{2} \left[(\epsilon_m + 1) - (\epsilon_m - 1) \frac{d(\omega)}{\Delta d} \right] \pm \frac{1}{2} \left[\left[(\epsilon_m + 1) - (\epsilon_m - 1) \frac{d(\omega)}{\Delta d} \right] - 4\epsilon_m \right]^{1/2} \quad (4.18)$$

For the (-) solution, Eq. (4.18) yields $\epsilon_s \approx -(\epsilon_m - 1) \frac{d(\omega)}{\Delta d}$ in the limit of small film-thickness, and $\epsilon_s \approx 1$ in the limit of large film-thickness. Thus, the thin-film takes on the properties of the vacuum when Δd is very large, as if it is no longer present. For the (+) solution, Eq. (4.18) is identical to our result. In the limit of small film-thickness, it yields $\epsilon_s \approx -\frac{\epsilon_m}{(\epsilon_m - 1)} \frac{\Delta d}{d(\omega)}$, and in the limit of large film-thickness, it yields $\epsilon_s \approx \epsilon_m$. This is nice, since it shows that the additional information incorporated into the ellipsometry ratio does not greatly change the thin-film correspondence.

Finally, the HDA version of this mapping of non-local effects into local films was also recently studied in Ref. [37]. In fact, as we show below, our Eq. (4.10) reduces to the corresponding equation in Ref.[37] after a formula for the d -function, appropriate for the HDA, is used [22, 12]. The derivation of Ref.[37] proceeds from the ansatz that $\epsilon_s(\omega) \propto \Delta d$, which then leads to the following form of Eq. (4.4):

$$r_p^{TF} = \frac{(\epsilon_m - \epsilon_0) - (\epsilon_m/\epsilon_s) q \Delta d}{(\epsilon_m + \epsilon_0) + (\epsilon_m/\epsilon_s) q \Delta d} \quad (4.19)$$

Comparing Eq. (4.19) to Eq. (4.5), we can identify the relation $\epsilon_s = -\frac{\epsilon_m}{(\epsilon_m - \epsilon_0)} \frac{\Delta d}{d(\omega)}$. To get the result of Ref.[37], the HDA form of the d -function should be used. This formula was introduced in the previous chapter, $d_{HDA}(\omega) = \sqrt{\beta / [\omega_p^2/\epsilon_b - \omega(\omega + i\gamma)]}$, but we now note the additional definition which enables the correspondence between our result and that of Ref.[37]:

$$d_{HDA}(\omega) \equiv \frac{1}{iq_{pl}} \quad (4.20)$$

where q_{pl} is the plasmon normal wavevector, obtained from the condition $\varepsilon(q, \omega) = 0$, with $\varepsilon(q, \omega)$ given by the hydrodynamic model. Ultimately, this solution suffers from the *ad hoc* assumption $\epsilon_s(\omega) \propto \Delta d$ and, therefore, it is not complete. Our derivation reduces to this function in the small Δd limit.

4.3 Nonlocal Mie Resonance of Metallic Spheres

We now apply our thin-film formula to calculate the absorption cross-section of metallic nanospheres. We also demonstrate that the scheme which employs our physically valid result also correctly predicts the red-shift of the Mie resonance of metallic nanospheres, compared to the classical Mie frequency.

The absorption cross-section is proportional to the imaginary part of the particle polarizability, which has the following classical form in the long-wavelength limit:

$$\alpha^{CL} = 4\pi R^3 \frac{\epsilon(\omega) - 1}{\epsilon(\omega) + 2} \quad (4.21)$$

where R is the particle radius. For a local metal, the Mie frequency is determined from the poles of Eq. (4.21), which yields $\omega_{Mie}^{CL} = \omega_p/\sqrt{3}$ for a Drude metal. Liebsch derived this Mie frequency using the nonlocal d-function formalism and found [34]:

$$\omega_{Mie}^{NL} = \frac{\omega_p}{\sqrt{3}} \left[1 - \frac{d(\omega)}{R} \right] \quad (4.22)$$

This size-dependent dispersion has been confirmed elsewhere in the literature [38, 31, 1]. Liebsch proposed a nonlocal extension to the Drude dielectric function, $\epsilon(\omega) \rightarrow \epsilon(q, \omega)$, which produces the correct, nonlocal Mie frequency when inserted into Eq. (4.21). The generic form of this extension was presented as Eq. (3.18), i.e., $\epsilon(q, \omega) = 1 - \frac{\omega_p^2}{\omega(\omega+i\gamma)+\Sigma}$. For a spherical particle of radius R , the self-energy should

have the form $\Sigma = d(\omega)(\omega_p^2 - \omega^2)/R$ [34], in order for Eq. (4.21) to yield Eq. (4.22). Next, we compare our thin-film approach to both Liebsch's model and the standard local Drude model.

Our thin-film method uses a core-shell geometry, where we use the standard, local Drude formula for the core of radius R_c , and the effective dielectric function $\epsilon_s(\omega)$ for the shell of thickness Δd . The following analytic form for the core-shell polarizability was used to calculate the nonlocal absorption cross-section:

$$\alpha^{TF} = 4\pi (R_c + \Delta d)^3 \frac{(\epsilon_s - 1)(\epsilon_m + 2\epsilon_s) + \left(\frac{R_c}{R_c + \Delta d}\right)^3 (\epsilon_m - \epsilon_s)(2\epsilon_s + 1)}{(\epsilon_s + 1)(\epsilon_m + 2\epsilon_s) + \left(\frac{R_c}{R_c + \Delta d}\right)^3 (\epsilon_m - \epsilon_s)(2\epsilon_s - 2)} \quad (4.23)$$

In the following figure, we plot $\omega \text{Im}\{\alpha^{TF}\}$ by substituting Eq. (4.10) into Eq. (4.23). We also plot the absorption cross-section calculated using Liebsch's ansatz with $\epsilon(\omega) \rightarrow \epsilon(q, \omega)$ in Eq. (4.21), which we call $\omega \text{Im}\{\alpha^{Liebsch}\}$. Finally, we compare both of these results to the local absorption cross-section, $\omega \text{Im}\{\alpha^{CL}\}$. For the first figure, Fig. 4.7, we fix the core size to $R_c = 5$ nm and vary Δd , enforcing the relation $R = R_c + \Delta d$.

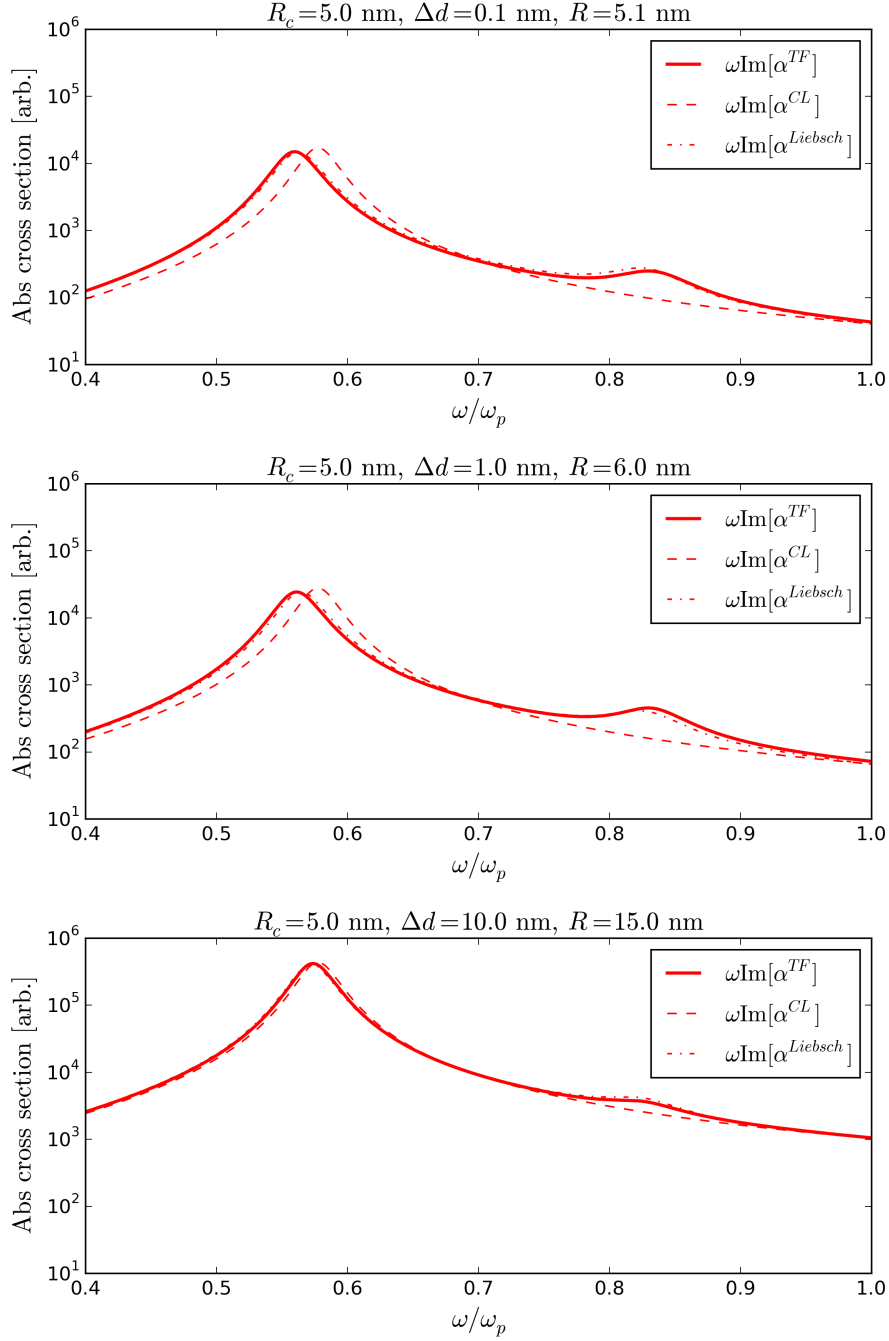


Figure 4.7: *Absorption cross-section: fixed R_c .* The absorption cross-section of the thin-film system, $\omega\text{Im}\{\alpha^{TF}\}$, is plotted compared to Liebisch's ansatz, $\omega\text{Im}\{\alpha^{Liebsch}\}$, and the local absorption cross-section, $\omega\text{Im}\{\alpha^{CL}\}$. The core size is fixed, $R_c = 5$ nm, while Δd is varied. The relation $R = R_c + \Delta d$ is enforced.

We first note the most prominent distinction between the classical absorption cross-section and the nonlocal results, which is the presence of the multipole resonance at $\omega \approx 0.85\omega_p$. Another important result is that the presence of the thin-film produces a redshift of the resonance frequency compared to the classical peak, and this effect is enhanced for smaller particle size, R . In Fig. 4.8, we use a fixed shell-thickness, $\Delta d = 0.1$ nm, and we vary R_c . Similar results are observed.

Finally, in Fig. 4.9, we fix the total particle size, R , and vary both R_c and Δd . The results that we observe indicate that the absorption cross-section is nearly independent of the ratio $\Delta d/R_c$, for fixed R . This is somewhat astonishing, and likely a result that is specific to closed geometries (i.e., particles). Ultimately, it suggests that in both the limit of vanishing film-thickness, $\Delta d \rightarrow 0$ (i.e., when the film is vanishingly small), and the limit where $\Delta d \rightarrow R$ (i.e., when the entire particle is composed of the material ϵ_s), the nonlocal absorption cross-sections are qualitatively equivalent. This is an attractive property, which implies that film-thickness does not strongly effect the underlying results.

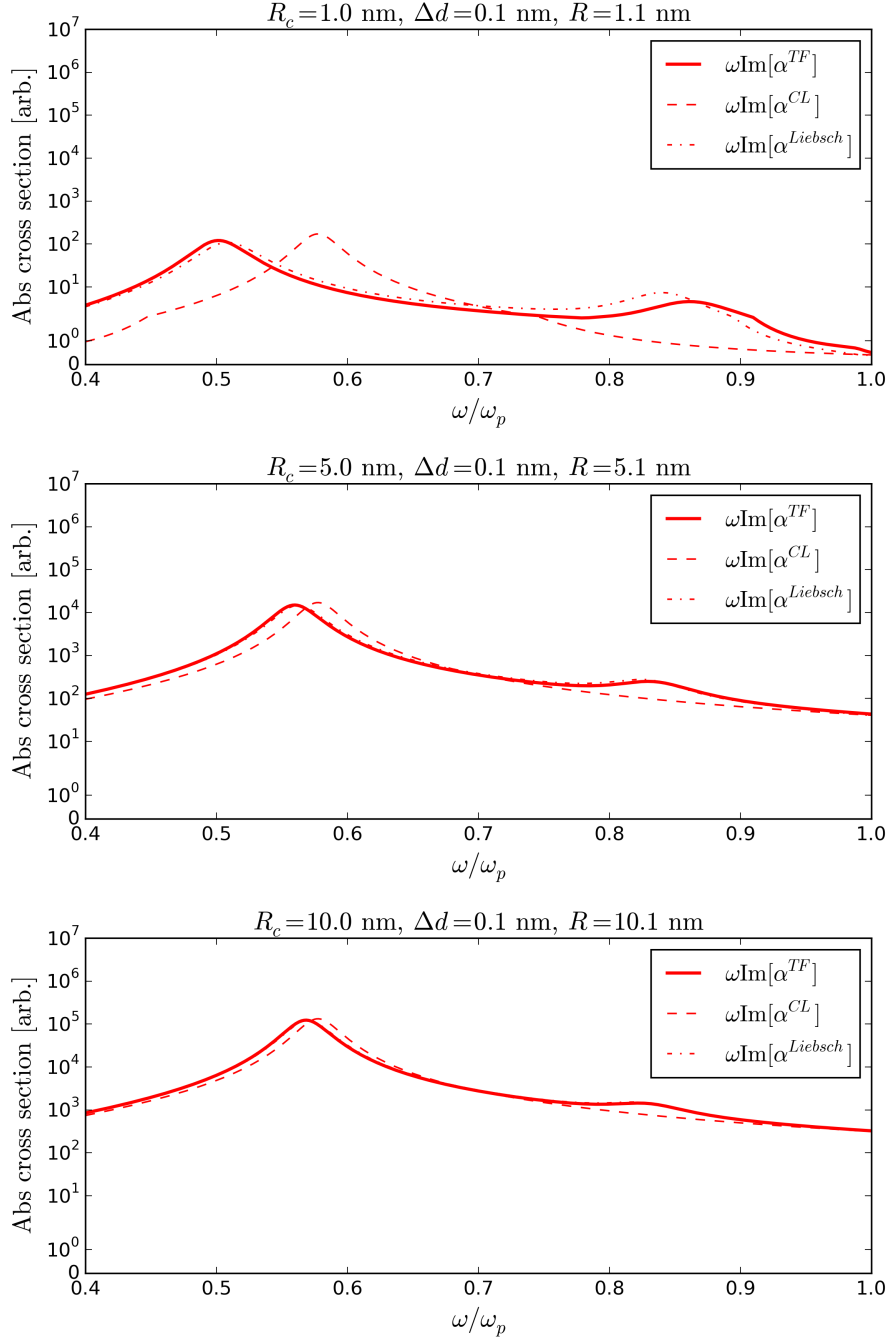


Figure 4.8: *Absorption cross-section: fixed Δd .* The absorption cross-section of the thin-film system, $\omega\text{Im}\{\alpha^{TF}\}$, is plotted compared to Liebsch's ansatz, $\omega\text{Im}\{\alpha^{Liebsch}\}$, and the local absorption cross-section, $\omega\text{Im}\{\alpha^{CL}\}$. The film-thickness, $\Delta d = 0.1 \text{ nm}$, is fixed while the core size, R_c , is varied. The relation $R = R_c + \Delta d$ is enforced.

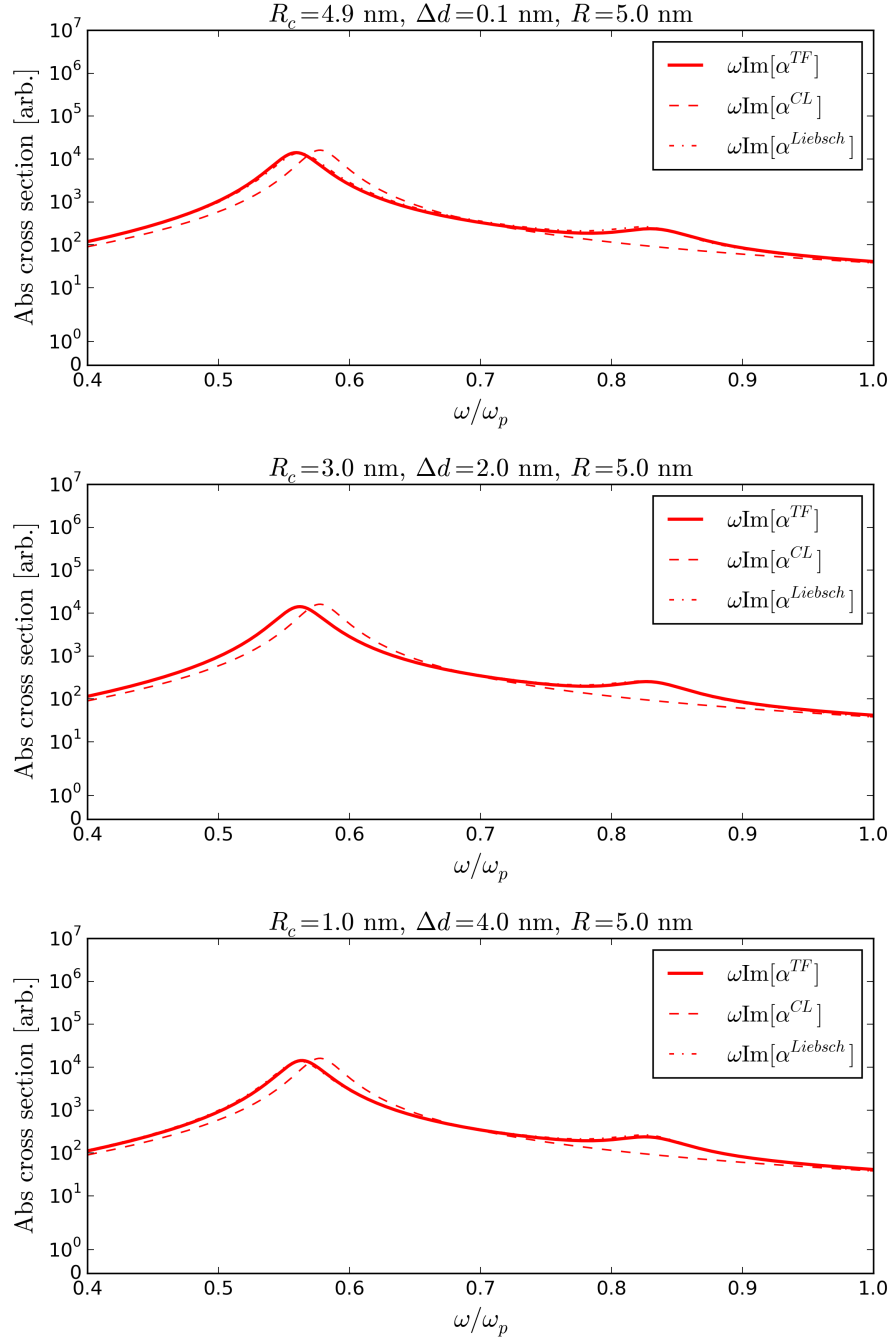


Figure 4.9: *Absorption cross-section: fixed R .* The absorption cross-section of the thin-film system, $\omega\text{Im}\{\alpha^{TF}\}$, is plotted compared to Liebisch's ansatz, $\omega\text{Im}\{\alpha^{Liebsch}\}$, and the local absorption cross-section, $\omega\text{Im}\{\alpha^{CL}\}$. Both the film-thickness, Δd , and the core size, R_c , are varied for fixed particle size, $R = 5$ nm. The relation $R = R_c + \Delta d$ is enforced.

Now we consider the frequency dispersion of metal particles as a function of particle size. Earlier in this section, we reported that the Mie frequency exhibits a redshift that is inversely proportional to the particle radius, i.e., Eq. (4.22). This dispersion can be derived explicitly from our formalism in the limit of small film-thickness, where $\Delta d \ll R_c$ and $R_c \rightarrow R$. Then, the polarizability of Eq. (4.23) reduces to

$$\alpha^{TF} \approx 4\pi R^3 \frac{(\epsilon_m - 1) - \frac{\Delta d}{R} \left[(2\epsilon_m - 1) + \left(\frac{\epsilon_m}{\epsilon_s} - 2\epsilon_s \right) \right]}{(\epsilon_m + 2) - 2\frac{\Delta d}{R} \left[(\epsilon_m + 1) - \left(\frac{\epsilon_m}{\epsilon_s} + \epsilon_s \right) \right]} \quad (4.24)$$

and inserting our thin-film formula in the limit of small Δd , i.e, Eq. (4.13), we have

$$\alpha^{TF} \approx 4\pi R^3 \frac{(\epsilon_m - 1) - 2\frac{d(\omega)}{R} (\epsilon_m - 1)}{(\epsilon_m + 2) - 2\frac{d(\omega)}{R} (\epsilon_m - 1)} \quad (4.25)$$

The roots of Eq. (4.25) determine the dispersion, which is equal to Eq. (4.22). Thus, our thin-film method produces the correct Mie frequency shift, as established by *ab initio* calculations [34] and experiment [38].

In Fig. 4.10, we plot the calculated Mie frequency shift as a function of inverse particle size, using our full thin-film formula, Eq. (4.10), with no approximations. We compare to the analytic dispersion and the classical Mie frequency $\omega/\omega_p = 1/\sqrt{3}$. We plot our dispersion for various ratios of film thickness and core radius, using the definitions $\Delta d = rR$ and $R_c = (1 - r)R$, where R is the total particle size, such that the condition $\Delta d + R_c = R$ is satisfied. Ultimately, we observe that the dispersion *does* depend on the coefficient r , and asymptotes to the expected behavior of Eq. (4.22) in the limit of $r \rightarrow 0$. This subtlety is difficult to see from the full spectrum, Fig. 4.9 and, therefore, represents a near-negligible effect.

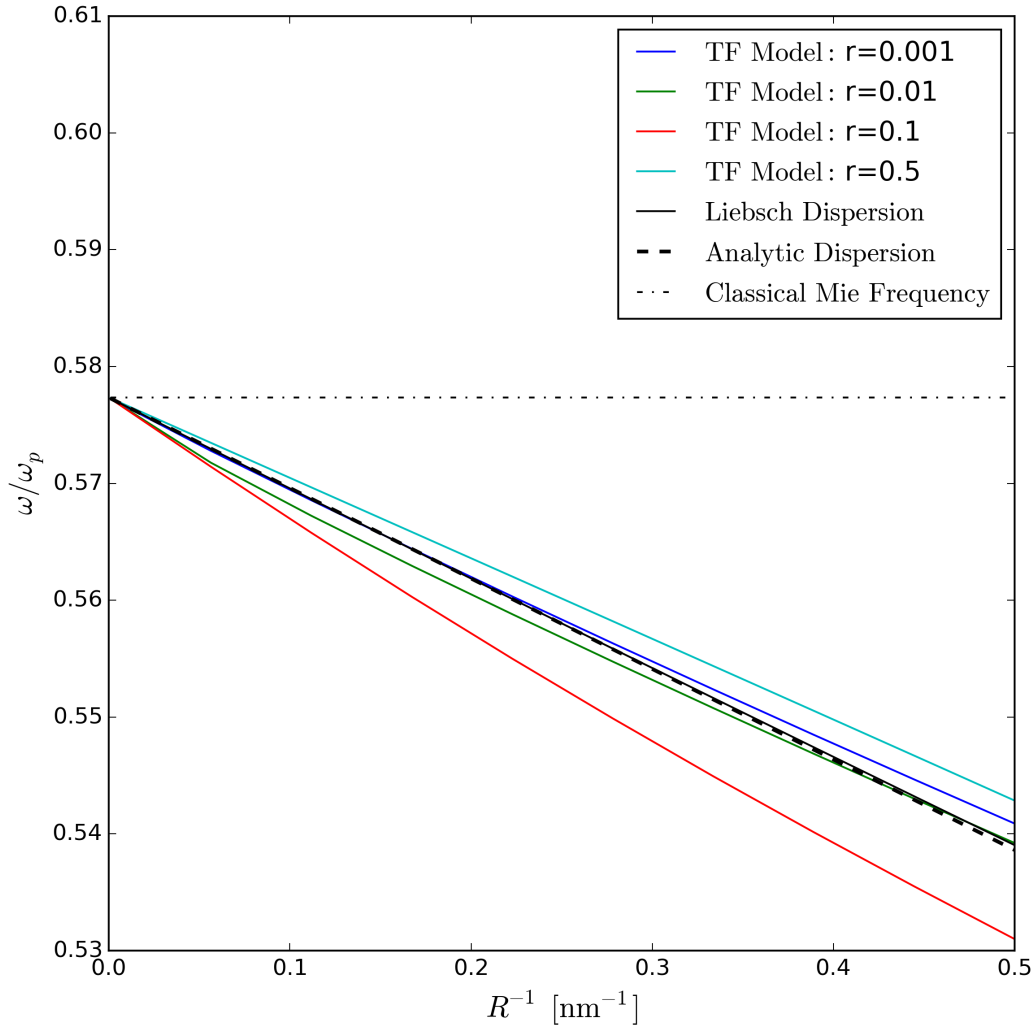


Figure 4.10: *Mie frequency vs. particle size.* The resonance frequency of the thin-film system is compared to both the Liebsch model and the classical Mie frequency as particle size is varied. Different ratios of film-thickness, $\Delta d = rR$, and core size, $R_c = (1 - r)R$, are plotted.

Finally, we note our thin-film calculation of the nonlocal absorption cross-section from nanoparticles is superior to the self-energy approach of Liebsch. This is because Liebsch’s formula requires the geometry of the system to be incorporated into the nonlocal dielectric response through Σ , whereas our formula uses an effective thin-film response that is entirely independent of the geometry of the underlying system. Our method does not require the dispersion of the system to be known *a priori* and, thus, its application to any system will yield valid results in the limit of small film-thickness. Moreover, our method lends itself to the derivation of analytic dispersion relations, like Eq. (4.22), in geometries that have known core-shell expressions. Ultimately, Liebsch’s approach is less general.

Based on our method, one has a simple prescription for extending any local calculation or simulation, such as FDTD, into the small q , non-local domain: before performing a simulation, one must first add a fictitious, dielectric film of finite thickness Δd to any metallic surface of the structure. This film must have the complex, frequency-dependent (but local and non-retarded) dielectric function $\epsilon_s(\omega)$ given by Eq. (4.10). The simulations now include non-local effects, accurate to lowest order in q . The capability of our approach was demonstrated in [14] by implementing the effective thin-film method using COMSOL Multiphysics, albeit for a different form of $\epsilon_s(\omega)$ than presented here. Additionally, in the referenced work, the modified electric field enhancement between the spheres was examined and compared to published DFT calculations. The effective thin-film method proved capable of capturing the qualitative features of *ab initio* calculations, but was more straightforward and simple to apply.

In this chapter, we have introduced a form for the effective response of a thin-film, which mimics the nonlocal effects of a bulk metal when added to its surface. We corroborated the physical validity of this equation by ensuring that it has rea-

sonable limiting behavior. We stated the caveat that this formula should also satisfy Kramers-Kronig relations and sum rules, although we were unable to include these calculations. Finally, using this effective thin-film method, we derived analytic expressions for the Mie frequency-shift induced by nonlocal effects in alkali metal nanospheres, which match known results. Ultimately, nonlocal effects modify the classical electromagnetic response of nanostructures that have extremely subwavelength geometries (e.g. nano-spheres, nano-rods, nano-tips, etc.), and we anticipate that the effective thin-film method will be indispensable for accurate simulations of such structures.

PART II:

NONLINEAR RESPONSE PHENOMENA

CHAPTER 5

Nonlinear Response of DNA with Strong Driving

We shift our focus from *Part I* of this thesis to study nonlinear models of biological and plasmonic systems. Ultimately, we tie this focus back to an investigation of the response function of plasmonic nanoparticles. In this chapter, we study the nonlinear molecular dynamics of double-stranded DNA in the presence of a thermal environment using an established physical model and demonstrate that it is possible to induce damage selectively between base-pair types by driving with pulsed THz radiation. Such selectivity could be useful for targeted therapies, and we briefly discuss potential applications. Specifically, we analyze the amplitude-frequency parameter-space where large DNA base-pair separations occur, which we use as a proxy for “damage,” and we identify regions of the parameter space that distinguish between different base-pair types. In later chapters, we address how plasmonic particles may be used to generate *in vivo* THz fields via nonlinear effects, which is a scheme that is designed to overcome the body’s natural opacity to THz radiation and, thus, allow access to areas deep within the body.



5.1 Motivation & General Characteristics of DNA

This work is exploratory in nature, motivated by the proposed use of electromagnetic (EM) radiation to selectively damage nefarious biological actors, e.g., pathogens or cancer, within the body, and thereby create an effective therapy for disease. We chose to study the effects of THz radiation ($\lambda \sim 100 \mu\text{m} - 1 \text{mm}$) on these constituents, based on previous work showing that biological materials exhibit “finger-print” characteristics in the THz range, which make them identifiable [39, 40]. Specifically, we focus on the dynamical response of DNA to THz radiation, since a possible pathway to inhibiting the spread of biological constituents is through structural damage to their DNA, which may disrupt their ability to replicate [41, 42]. Moreover, previous experimental studies have shown that THz radiation can induce damage in DNA sequences [43]. However, we emphasize that we are not focusing on a particular biological target for our proposed scheme. Rather, we want to understand, very generally, the possible damaging effects that THz radiation can have on DNA and whether these effects are selective between different DNA sequences.

With this caveat in mind, we briefly mention two possible applications in order to provide context and motivation. Firstly, *cancer* is an obvious target, and the scheme that we are proposing could prove superior to harsher, less discriminating therapies like chemotherapy or radiation therapy. Alternatively, other targets might include *infectious agents*, which are rapidly becoming inured to the effects of antibiotics and, therefore, require alternative remediations [44, 45]. We emphasize that any potential application will necessitate that the target DNA is sufficiently distinguishable from “healthy” human DNA and, again, we leave additional details of these applications for future consideration.

Now, we briefly give an overview of the structure of DNA and discuss the many ways in which it is affected by its environment, including radiation across the EM

spectrum. The type of DNA that we are investigating is double-stranded DNA, which has a characteristic double-helix. The helices are composed of phosphate groups, which are bound to nucleobase pairs [41]. These base-pairs (BPs) occur in two realizations, adenine-thymine (AT) and guanine-cytosine (GC), and the properties (e.g., binding energy [46]) of each of these two types of pairs are different. Furthermore, double-stranded DNA can occur in different natural conformational states, for example A-conformation or B-conformation [47]. Our study assumes a B-conformation geometry, which is typical inside the body, so hereafter we refer to this structure when we use the general term “DNA.” Below, in Fig. 5.1, we include a diagram from Ref. [47] illustrating the geometry and scale of a DNA strand.

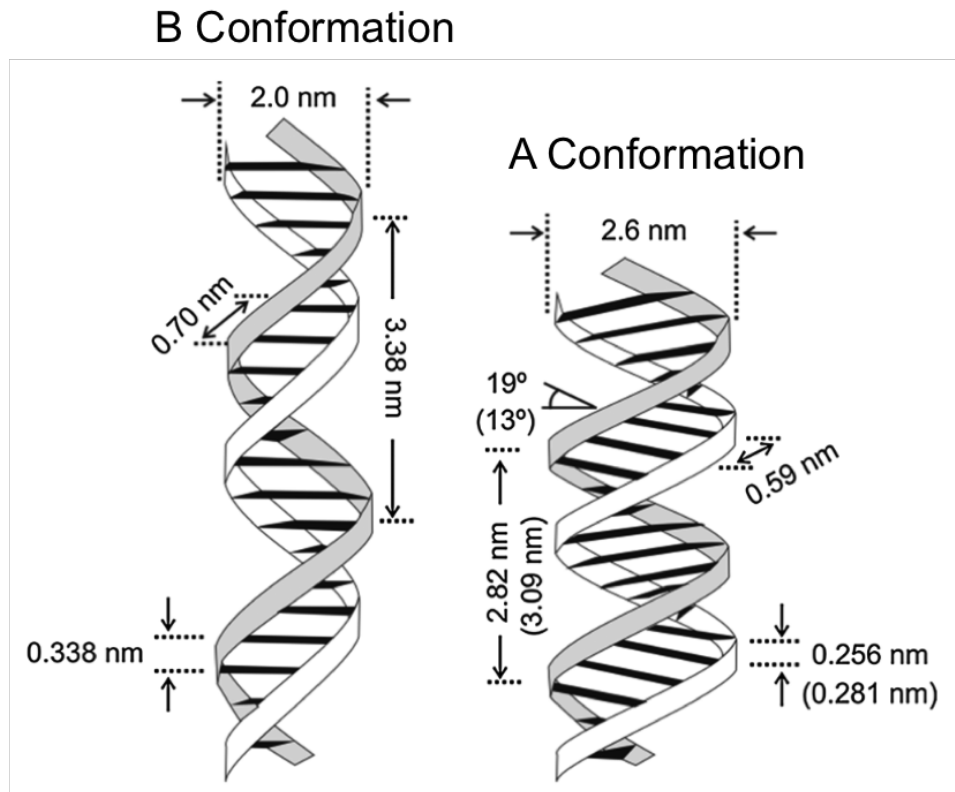


Figure 5.1: *DNA geometry.* Two conformational states of DNA are shown, in a figure from Ref. [47].

DNA exhibits rich dynamics, including twisting, bending, localized openings (i.e., breathing), unzipping, breaking, etc. [41, 48, 49, 50]. Damage to the DNA strand happens when such openings and breaks occur [41]. Although DNA repairs itself through various mechanisms (e.g., see the review by Ref. [51]), persistent damage could disrupt replication and lead to cell “death” [42].

Thermal influences contribute significantly to DNA damage and there is a vast literature focused on the melting properties (i.e., dissociative properties) of DNA as a function of temperature [52, 53, 54, 55, 46]. Thus, in any minimal model of DNA dynamics, the thermal environment must be considered. The response of DNA to EM radiation has also been well studied, for instance UV radiation [56]—though obviously the response of DNA in some regions of the EM spectrum is less understood, as this is the focus of our investigation.

There have been studies of DNA response to THz frequencies, which is our interest. For review, see Ref. [57, 58]. For instance, the authors of Ref. [59] studied the affect of THz radiation on the melting properties of DNA, finding that higher driving amplitudes reduced the melting temperature of all types of DNA strands (i.e, with both homogeneous and heterogeneous BP sequences). The authors only examined driving at certain frequencies. Additionally, in Ref. [60], the authors studied the effect of THz radiation on the unzipping properties of DNA sequences at fixed driving amplitude. Ultimately, some studies found evidence for THz induced damage, e.g., Ref. [61, 62, 63, 64, 65], while other studies did not, e.g., Ref. [66, 67].

Thus far, no study has investigated the complete range of amplitude-frequency parameter-space pertaining to driving with THz radiation, which is what we endeavor to do. We specifically want to find the amplitudes and frequencies at which DNA will be damaged and whether this damage is selective at the single BP level. Thus, we are not investigating the thermalization effects of driving—this was partly

explored by Ref. [59], who explicitly allowed the system to equilibrate with the driving field—rather, our focus is to study the *nonequilibrium* excitation of DNA and examine the parameter space where DNA damage is most likely to occur.

5.2 Nonlinear Model of Double-Stranded DNA

We consider a dynamical model of DNA proposed by Tapia-Rojo et al. [46], which is a modified form of the canonical Peyrard-Bishop-Dauxois (PBD) model [55]. The original PBD model uses minimal assumptions and treats the forces between BPs based on their ladder-like geometry: the interaction within a BP is governed by a Morse-like, intra-base-pair potential, $U(y_n)$, while the outer phosphate strands provide an effective inter-base-pair potential, $W(y_n, y_{n\pm 1})$, which is the so-called “stacking” potential. This stacking potential actually consists of two terms, one for base-pairs either above or below any given BP within a sequence. The dynamics of the BPs are parameterized by the coordinate y_n , which is defined as the normalized separation between the n^{th} BP. The pairs are normalized relative to their equilibrium position (at $T = 0$), which is $y_n = 0$ in the center of mass-frame of the base-pair. The following diagram, Fig. 5.2, depicts these interactions schematically.

Diagram of nth DNA pair

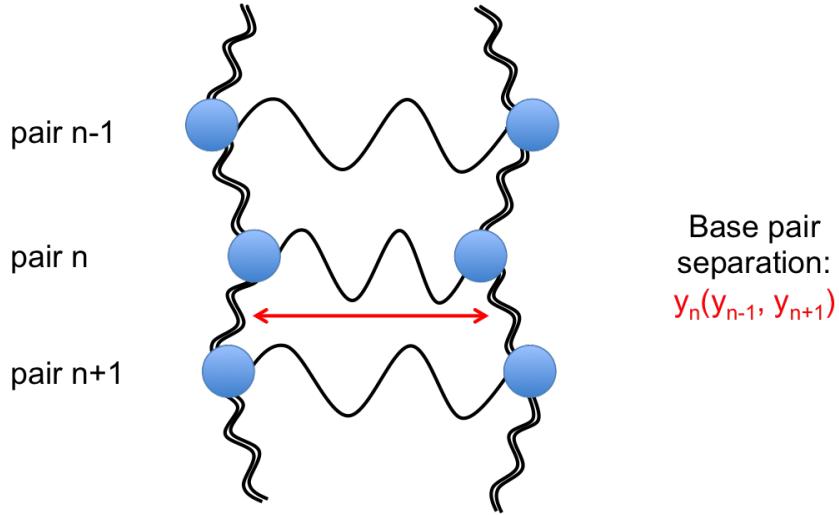


Figure 5.2: *PBD schematic diagram.* Intra-base-pair forces are depicted horizontally and inter-base-pair forces are depicted vertically.

In the absence of external forces, the generalized equation of motion for this system is:

$$m\ddot{y}_n = -U'(y_n) - W'(y_n, y_{n+1}) - W'(y_n, y_{n-1}) - m\gamma\dot{y}_n \quad (5.1)$$

where γ is a phenomenological dissipative term and the primed terms represent spatial derivatives: e.g., $U'(y_n) = \frac{\partial}{\partial y_n}U(y_n)$. In the original PBD model, the hydrogen bond connecting each nucleobase was modeled via a simple Morse potential [55]: $U(y_n) = D_n[\exp(-\alpha_n y_n) - 1]^2$. However, simulations of bubble lifetimes [46] and THz driving [59] demonstrate that this model does not reflect observed behavior accurately. A more realistic model includes a potential barrier to reassociation [46], which reflects the physical propensity of BPs to be slightly repelled from each other after separation. This behavior arises from several sources: a repulsive force between BPs and the phosphate strand, BP's affinity to react with physical solvents

once separated [60], in addition to other possible phenomenological reasons. Thus, a modified Morse potential represents a more physically reasonable model for the intra-base-pair interaction, reflecting the energy barrier to reassociation that occurs during the DNA denaturation process.

In the model of Ref. [46], which we are using in this work, the Morse potential is augmented with a Gaussian barrier, which results in more realistic simulations of bubble lifetimes [46]:

$$U(y_n) = D_n[\exp(-\alpha_n y_n) - 1]^2 + G_n \exp[-(y_n - d_n)^2/b_n] \quad (5.2)$$

The stacking potential is modeled using a position-dependent spring-constant [46], as in the original PBD model:

$$W(y_n, y_{n\pm 1}) = \frac{k}{2}[1 + \rho \exp[-\delta(y_n + y_{n\pm 1})]](y_n - y_{n\pm 1})^2 \quad (5.3)$$

The parameters D_n , α_n , G_n , d_n , and b_n are BP-specific, meaning that they are different for AT vs. GC pairs. Their values are: $D_n[\text{AT}] = 0.05185\text{eV}$, $\alpha_n[\text{AT}] = 4 \text{ \AA}^{-1}$, $D_n[\text{GC}] = 1.5D_n[\text{AT}]$, $\alpha_n[\text{GC}] = 1.5\alpha_n[\text{AT}]$, $G_n = 3D_n$, $d_n = 2/\alpha_n$, and $b_n = 1/(2\alpha_n^2)$. The other parameters are independent of BP type: $k = 0.03\text{eV}\text{\AA}^{-2}$, $\rho = 3$, $\delta = 0.8\text{\AA}^{-1}$, $\gamma = 1\text{ps}^{-1}$, and $m=300$ amu. The total equilibrium potential, Eqs. (5.2) & (5.3), is plotted in Fig. 5.3 for the Tapia-Rojo [46] modified PBD model (mPBD) for both AT pairs (blue) and GC pairs (red). Overall, the GC potential is steeper, representing the stronger intra-pair bonds. Next, we explore some other features of this potential.

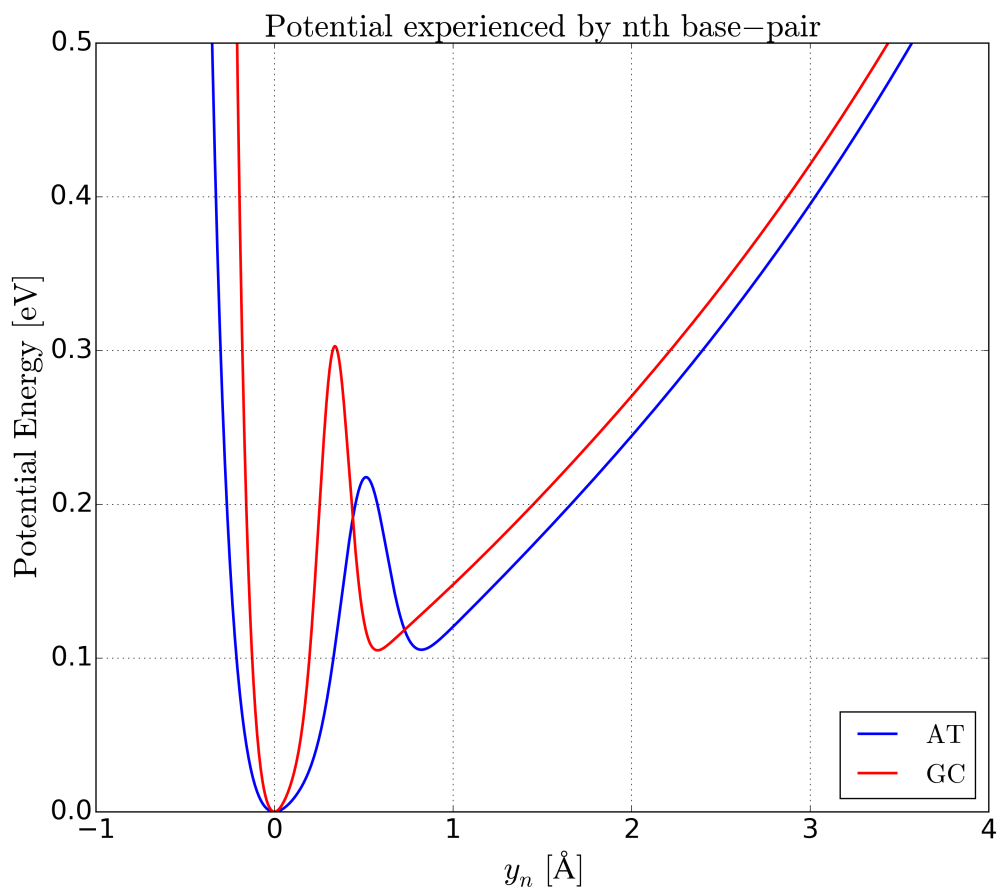


Figure 5.3: Total potential energy of AT and GC pairs at equilibrium. AT pair (blue line) and GC pair (red line).

The mPBD equilibrium potential for the n th base-pair of an AT sequence is again shown in Fig. 5.4, where the Morse potential, stacking potential, and total potential are now delineated. At equilibrium, $y_n = y_{n\pm 1} = 0$. The first diagram depicts the potential when the neighboring BPs are at their equilibrium positions, which is the potential that the n th BP feels due to the $n+1$ and $n-1$ BPs. The horizontal bars at the bottom of the figure show the normalized separation of the $n+1$ and $n-1$ BPs, which are zero in this case. The black-dashed lines represent Taylor expansions about the minima of the potential. The frequency of oscillations about these potential minima can readily be calculated (i.e., $\omega^2 \approx U''(y_{\min})/m$). For an AT pair at equilibrium, these frequencies are $f_a = 1.26$ THz and $f_b = 1.28$ THz. For a GC pair at equilibrium (not shown), these frequencies are $f_a = 2.21$ THz and $f_b = 1.65$ THz. The subscript a refers to the lower potential energy well, and b refers to the higher well.

The movement of the neighboring BPs alters the potential landscape, e.g., as depicted in Fig. 5.5 & 5.6, for the given displacements of the $n+1$ and $n-1$ base-pairs. When the $y_{n\pm 1}$ BPs are both moved to the same large separation, i.e., Fig. 5.5, it becomes energetically favorable for the n th BP to also separate. In a realistic system, when both $y_{n\pm 1}$ BPs are moving continuously, Fig. 5.6 shows that the potential experienced by the n th BP can be quite altered.

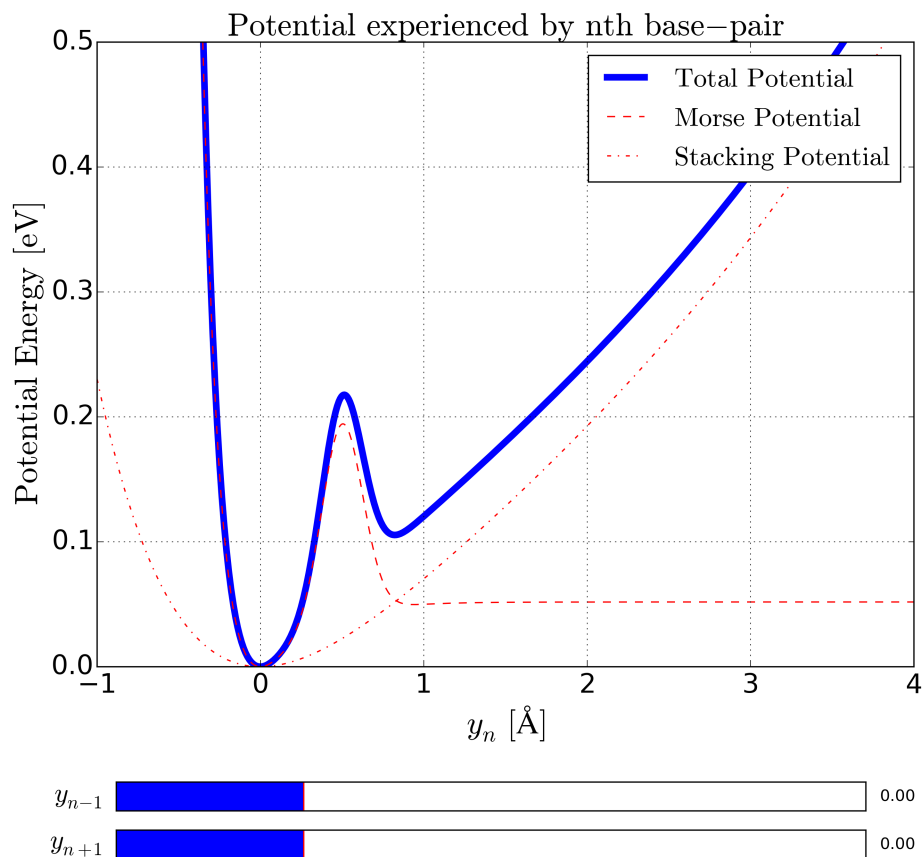


Figure 5.4: Contributions to potential energy of n th AT pair (1). Solid blue line is total potential, red-dashed line is stacking potential, and black-dashed line is Taylor expansion about potential minima. The horizontal bars at the bottom of the figure show the normalized separation of the $n+1$ and $n-1$ BPs.

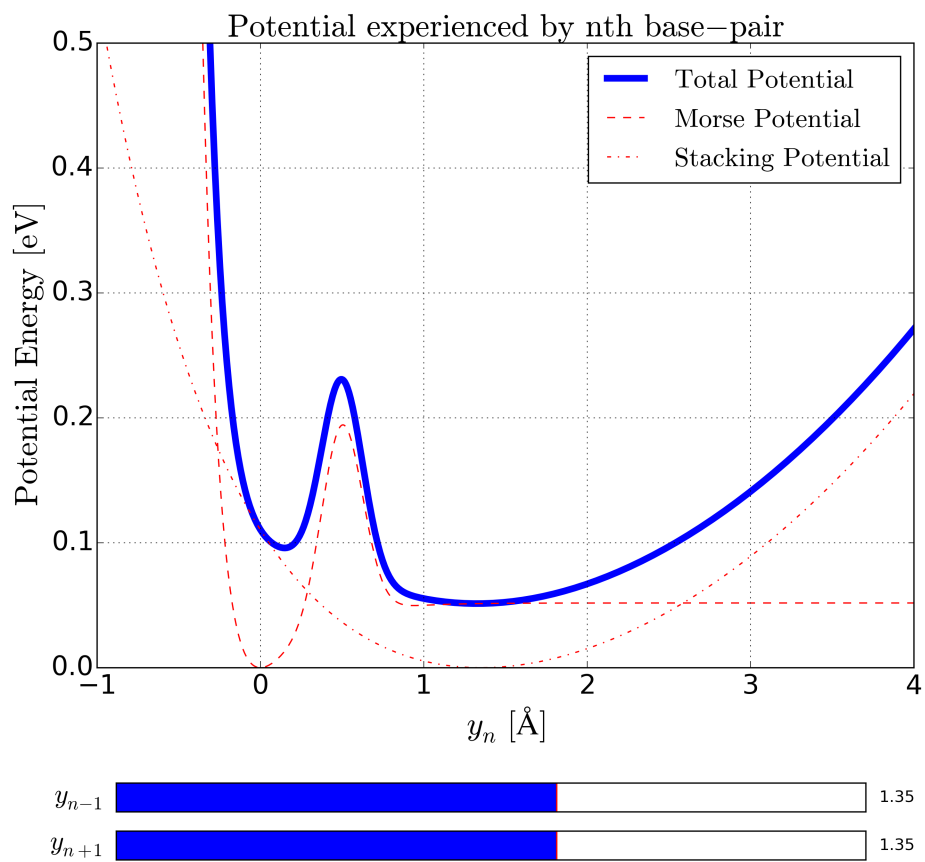


Figure 5.5: Contributions to potential energy of n th AT pair (2). Neighboring pairs, $y_{n\pm 1}$ are at large separations and $y_{n+1} = y_{n-1}$.

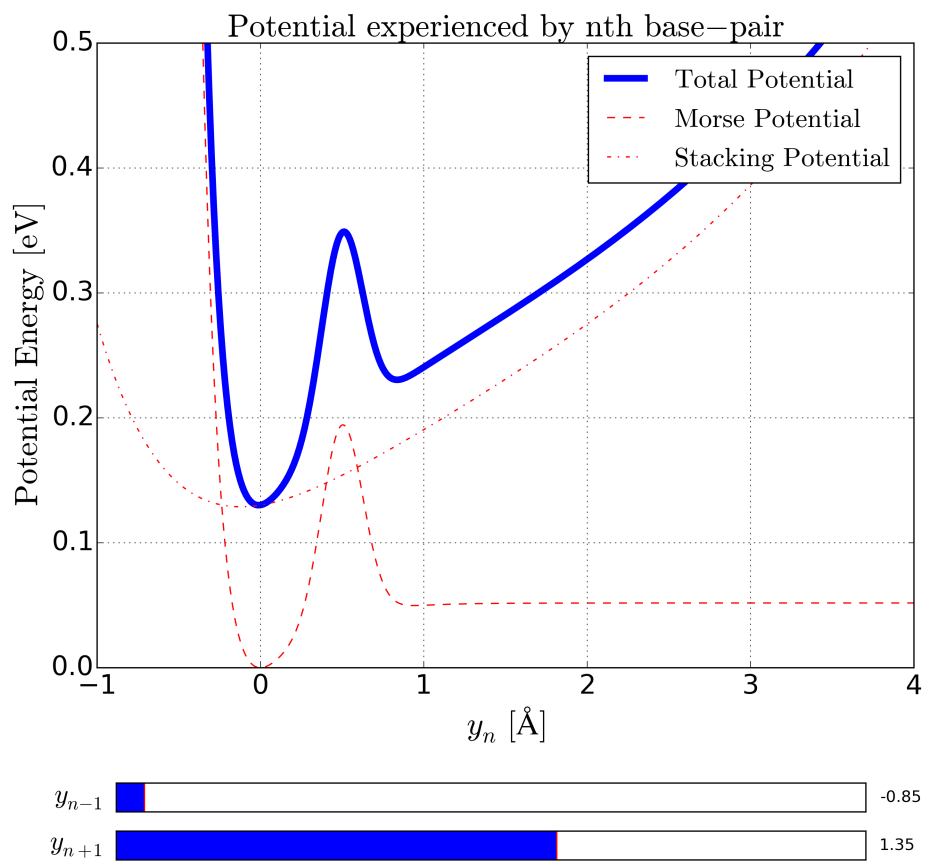


Figure 5.6: Contributions to potential energy of n th AT pair (3). Neighboring pairs, $y_{n\pm 1}$ are at different separations.

5.3 Model Simulations

Within this formalism, we model thermal fluctuations using a Langevin forcing term, $\eta(t)$, and external driving using a sinusoidal field, $F(t) = A \sin(\omega t)$. The Langevin term represents a random force, drawn from a thermal Gaussian distribution with variance $2m\gamma k_B T$, as in [68]. The temperature was set to $T = 290$ K (\sim room temperature) for this study. The reason for this choice, in part, was to compare with previous published numerical studies, specifically Ref. [59], who examined the effect of THz driving on the melting transition of DNA at fixed driving frequency. The authors showed, generally, that THz driving lowers the melting temperature.

Following our study at $T = 290$ K, we performed a limited study at $T = 310$ K (human body temperature). The difficulty of performing simulations at this higher temperature is that it is very close to the melting transition of DNA and, because of this, the system takes longer to thermalize using our simulation scheme. Ultimately, we think that our simulations at $T = 290$ K are generalizable, but we also discuss our results at $T = 310$ K in Appendix E.

The full equation of motion that incorporates thermal fluctuations is shown below:

$$m\ddot{y}_n = -U'(y_n) - W'(y_n, y_{n+1}) - W'(y_n, y_{n-1}) - m\gamma\dot{y}_n - \eta(t) - F(t) \quad (5.4)$$

The dynamics were numerically integrated using a Verlet-type algorithm [68] for a sequence of 64 BPs, with periodic boundary conditions such that the last BP in a sequence is “neighbors” with the first BP. We chose 64 BPs in order to follow a procedure similar to what has been reported in literature (e.g., Ref. [48]), and did not consider the effect of sequence length in our subsequent simulations. We did consider other algorithms, for instance the Euler-Cromer [69], Runge-Kutta [70], BBK methods [71], etc. However, the chosen algorithm requires fewer intermediate calculations

per iteration and is sufficiently accurate—moreover, the Verlet-type algorithms are a frequent choice for molecular dynamics simulations [68].

We tested the algorithm by first calculating the thermodynamic energy of our system at low temperatures, without driving. For low levels of thermal excitation, the mPBD model behaves linearly and, thus, the calculated energy of the system can be approximated by the equipartition theorem for a SHO: i.e, $\frac{1}{2}k_B T = \frac{1}{2}m \langle v^2 \rangle$. We verified that our system was behaving as expected in this limit.

In order to achieve valid results, it was necessary to allow the system to thermally equilibrate before initiating driving. We determined the amount of time needed to reach this equilibrium state by comparing the time-dependent average energy of our system with known results. The average energy per time is defined as $\langle u \rangle_N = \frac{1}{N} \sum_n [U(y_n) + W(y_n, y_{n-1})]$, where the average has been taken over all BPs [46]. For a homogeneous AT sequence, the time-averaged energy over all BPs has been reported as $\langle u \rangle_{NT} \approx 0.019\text{eV}$ for a temperature of 290K [46], where the subscripts N and T represent the number of BPs and time. We calculated $\langle u \rangle_N$ as a function of time for 10 different trials, averaging over all BPs and trials. The following plot, Fig. 5.7, shows the time-series for a given trial, where the BP-index is on the vertical axis and the color intensity represents the magnitude of the energy per BP. The lower plot shows $\langle u \rangle_N$ as a function of time.

From Fig. 5.7, it is clear that $\sim 5000\text{ps}$ is adequate for thermalization, since $\langle u \rangle_N$ plateaus at this timescale. On the next plot, Fig. 5.8, the time-average of the last 2000ps is plotted as a red point alongside the data from literature, showing excellent agreement between our calculations and the reported time-averaged energy, $\langle u \rangle_{NT} \approx 0.019\text{eV}$. It is interesting to note the critical behavior of $\langle u \rangle_{NT}$ as a function of temperature, shown in Fig. 5.8, which represents the so-called “melting transition.” In this study, we remain below this critical limit.

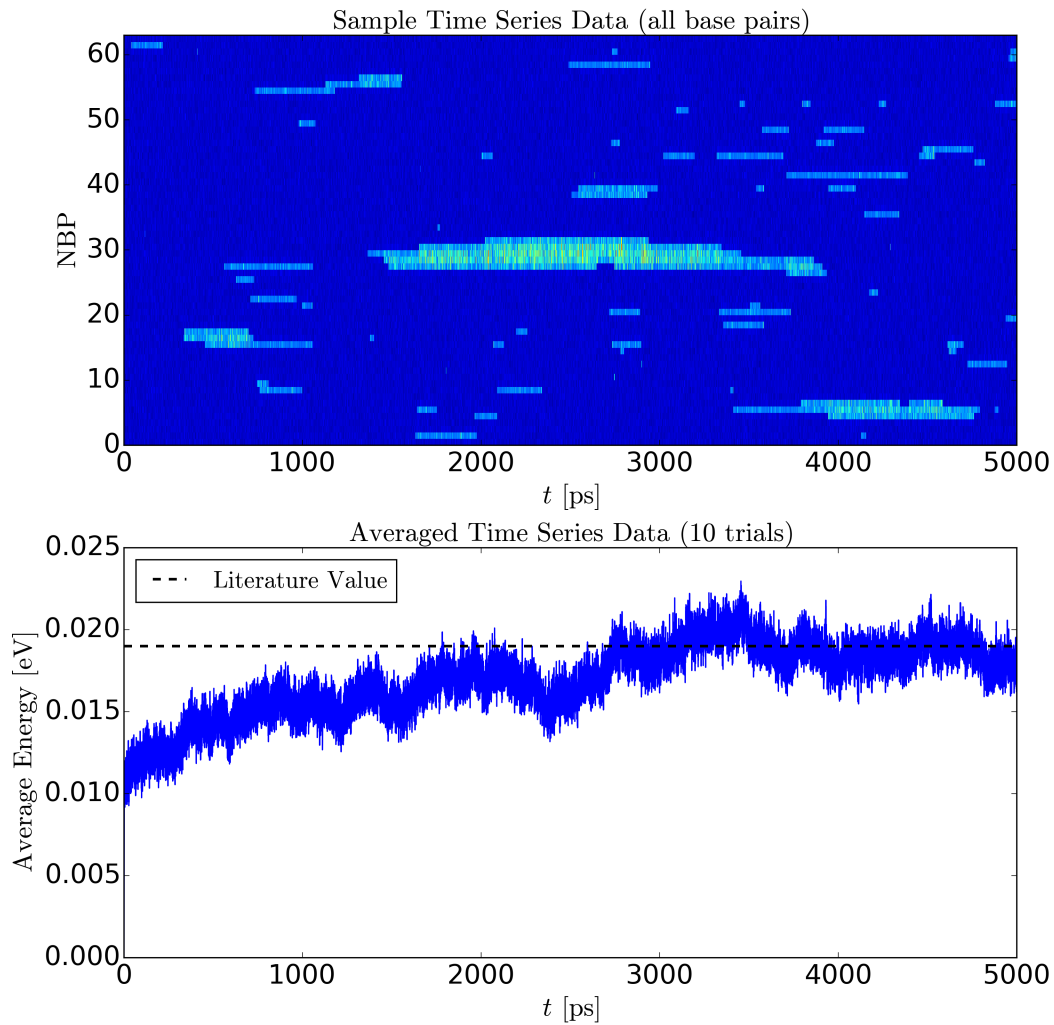


Figure 5.7: *Average energy vs. simulation time.* The simulation is run for 5000 ps and data are taken over 10 independent trials. Top: the time-series data for one trial, where the color intensity is the energy per BP, and the index of the BPs is on the vertical axis. Bottom: the time-series data of the average energy, averaged over all 64 BPs and 10 trials.

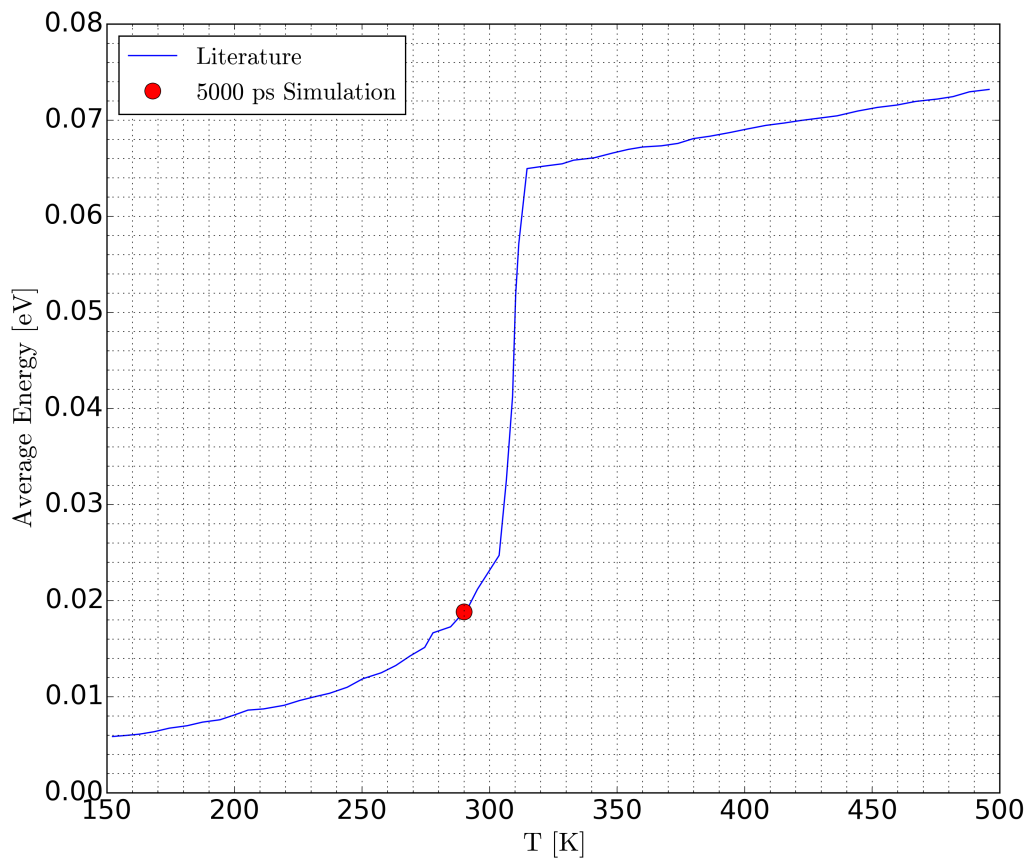


Figure 5.8: *Average energy and melting transition.* The red-dot represents our calculation, averaged over the last 2000 ps of a 5000 ps simulation, and the blue-line is from literature [46].

Before exploring the entire parameter space of interest, we first examine the effects of driving for certain values of amplitude and frequency. Specifically, we want to understand the effects of driving for different durations of time.

We have established that 5000 ps is an adequate amount of time to prepare the system in an equilibrium state, at a temperature of $T = 290$ K and, therefore, in our simulations with driving, we prepare the system by simulating for 5000 ps before driving is initiated. For each combination of driving amplitude and frequency that we explore, we run 10 different trials using 10 different prepared states as initial conditions. We use the same 10 different prepared states for initialization of all points that we simulate with driving. We chose to drive the system for 10 ps and, afterwards, we measured the average separation of BPs and used this as a proxy for damage. The average was taken over the last full period of oscillation, based on the driving frequency, and over all 64 BPs and 10 trials. The simulation duration, 10 ps, is a representative time for pulsed THz radiation, but we also examine the behavior of different pulse times and comment on the compounding effects of pulse duration, amplitude, and frequency.

We discuss all of these results in the next section, but first show a typical simulation run in Fig. 5.9, for a homogeneous AT sequence of 64 BPs, driven with $A=200$ pN and $f=1.5$ THz. The upper plot shows the time series for all BPs, where color intensity represents amplitude of y_n . The lower plot shows the time series for the $n = 0$ BP, only. As time increases, the average amplitude of BPs also increases, seen from the color-intensity. The system also has a characteristic oscillation frequency equal to the driving frequency, seen in the time-series data.

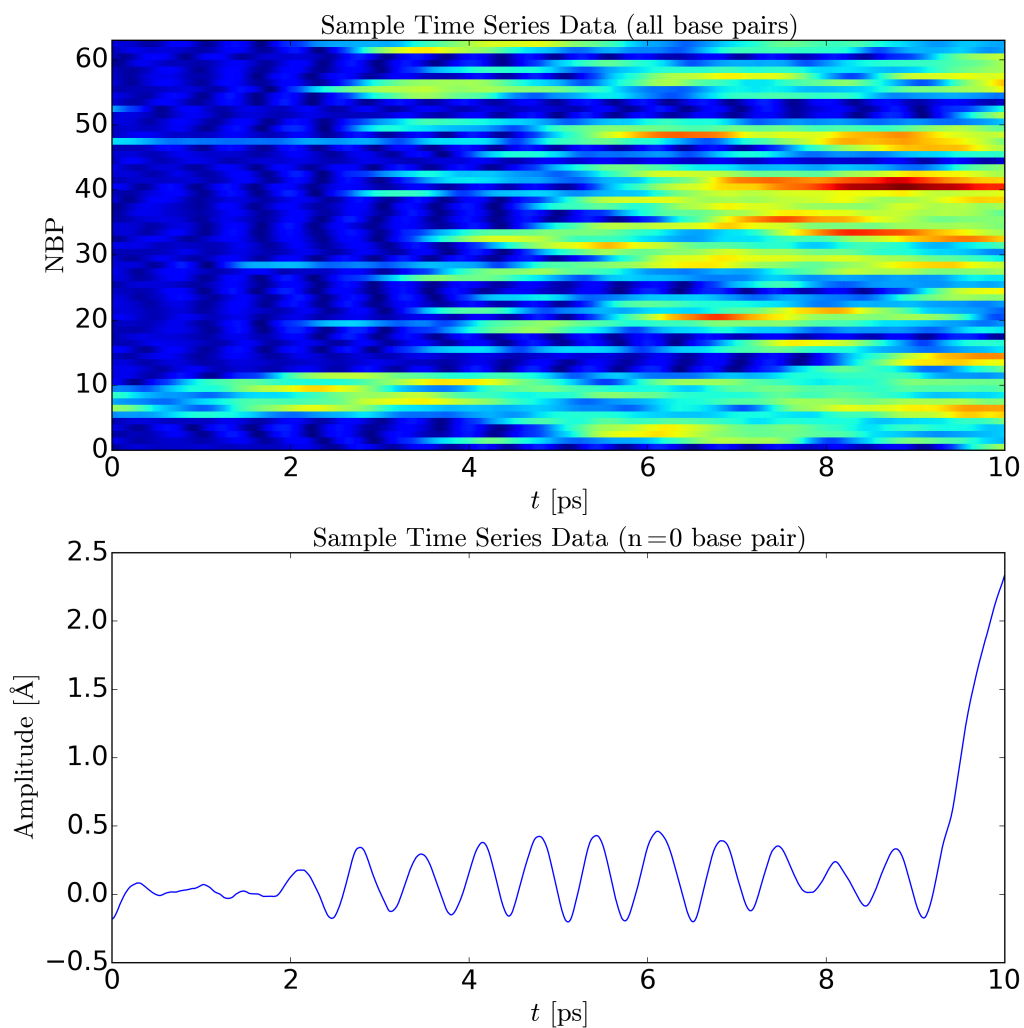


Figure 5.9: *Time-series: GC sequence at $A=200$ pN and $f=1.5$ THz.* Top: the time-series data for one trial, where the color intensity is the separation per BP, and the index of the BPs is on the vertical axis. Bottom: the time-series data for the specific BP with index $n = 0$.

5.4 Behavior of Homogeneous AT and GC Sequences

The objective of this section is to examine the behavior of homogeneous AT and GC sequences for different driving amplitudes and frequencies and to determine where damage occurs within this parameter-space. There are several metrics of “damage” that could be used, for instance the time-averaged separation, the time-averaged energy, or others, and when these quantities exceed a certain value, we can say that the BPs have become damaged. As stated in the previous section, we will use the average separation as a proxy for damage. Specifically, we identify a potentially damaged BP as having a time-averaged separation greater than the separation length associated with the turning point of the modified Morse potential, $\langle y_n \rangle > 0.5125 \text{ \AA}$ for AT pairs and $\langle y_n \rangle > 0.338 \text{ \AA}$ for GC pairs, where the time average is over the last full period of oscillation for a given driving frequency. This is an obvious condition to use, since base-pairs that have a separation greater than these distances will experience an energy penalty for “recombination,” i.e., they will have to overcome a potential barrier to decrease their separation and, thus, are more likely to remain separated. For each sequence, AT vs. GC, we also average over all 64 BPs and 10 trials.

The simulation was run separately on homogeneous AT and CG sequences, for all points in the amplitude-frequency parameter space spanning $A \in [100 \text{ pN}, 400 \text{ pN}]$ and $f \in [1 \text{ THz}, 3.25 \text{ THz}]$. These values were chosen based partly on previous literature, but mostly on exploratory analysis. For the points in this parameter space, the average separation of all BPs within a sequence, over 10 trials, is shown in Fig. 5.10 & 5.11 for AT and CG sequences, respectively. The boundary for damage onset is indicated by a solid white line in each figure.

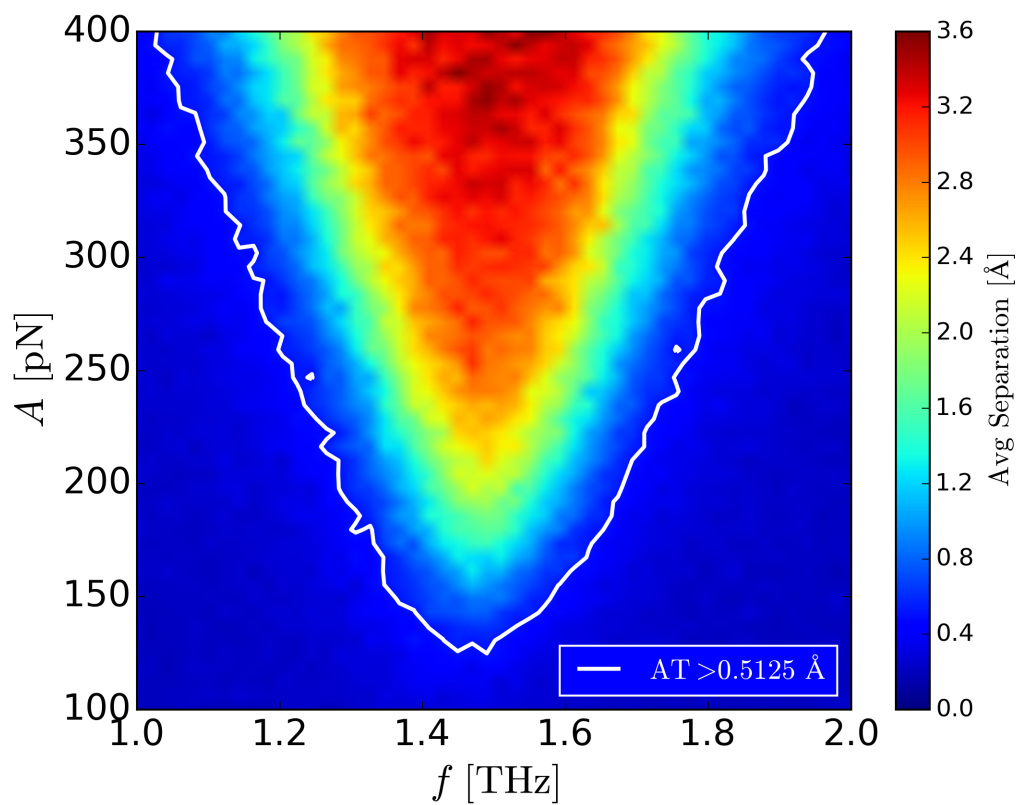


Figure 5.10: Average base-pair separation for homogeneous AT sequence. The intensity scale represents the average base-pair separation and the line indicates the boundary where the onset of damage occurs (average separation $> 0.5125 \text{ \AA}$).

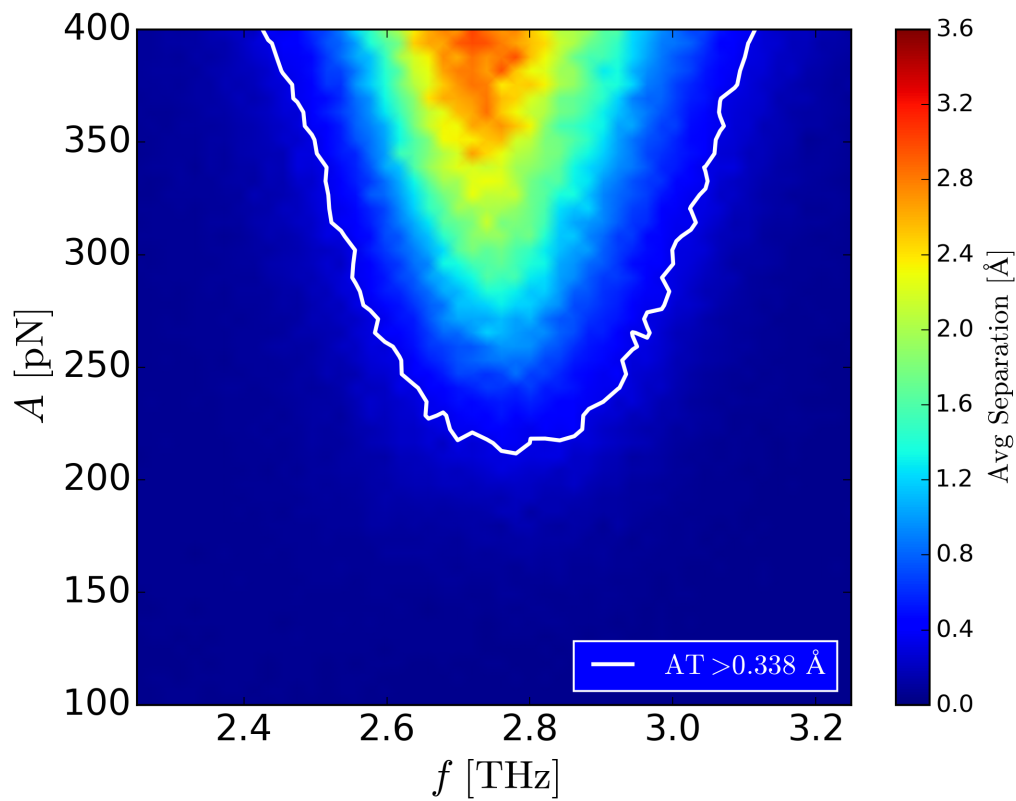


Figure 5.11: *Average base-pair separation for homogeneous GC sequence.* The intensity scale represents the average base-pair separation and the line indicates the boundary where the onset of damage occurs (average separation $> 0.338 \text{ \AA}$).

From the above results, it is clear that the two sequences inhabit different regions of parameter-space, although there is potentially some overlap at higher driving amplitudes (not investigated). Importantly, lower amplitudes result in higher frequency selectivity, as is indicated by the narrowing regions of the diagram for both sequences. For the homogeneous AT sequence, damage may occur at a minimum amplitude of $A \sim 120$ pN, at the frequency $f \sim 1.5$ THz, while for the CG sequence these minimal parameters are $A \sim 210$ pN and $f \sim 2.8$ THz. We note that these frequencies roughly correspond to the resonance frequencies of each system, which are $f_{AT} \approx 1.26$ THz and $f_{CG} \approx 2.21$, as mentioned previously. Apparently, the frequency of damage onset is blue-shifted relative to the natural linear resonance frequency of each system.

Now we consider how pulse duration might affect the above results, by examining 4 points in the parameter-space of Fig. 5.10 (for a homogeneous AT sequence): a) $A=100$ pN, $f=1.5$ THz; b) $A=150$ pN, $f=1.5$ THz; c) $A=150$ pN, $f=1$ THz; and d) $A=100$ pN, $f=1$ THz. For these points, we first initialize the system for 5000 ps without driving, as previously described. Then we examine the effects of a continuous pulse and let the system evolve for an additional 500 ps. For a given amplitude and frequency, in each figure we depict a sample time-series and then the time-dependent average separation over all BPs and 10 trials. The damage threshold is marked by a horizontal red line.

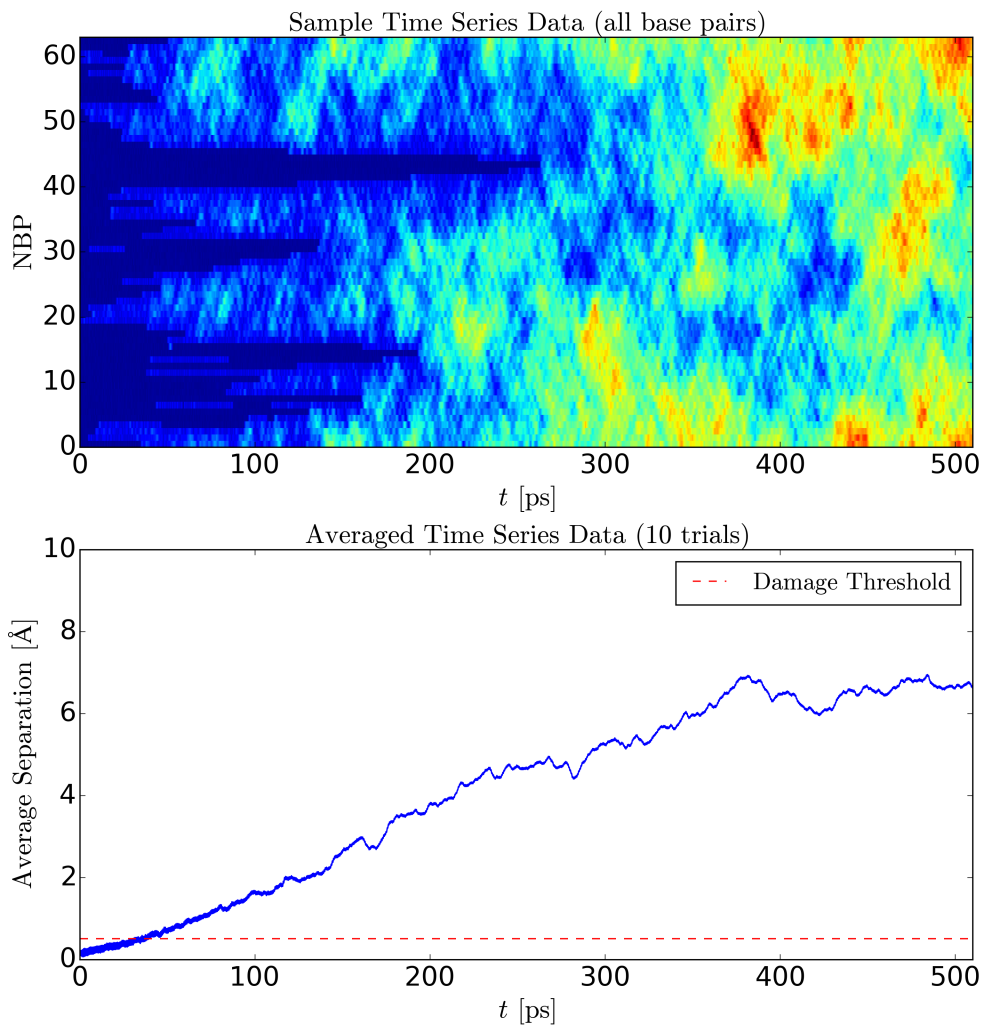


Figure 5.12: *Continuous driving at $A=100$ pN and $f=1.5$ THz.* Data for a homogeneous AT sequence. Top: the time-series data for one trial, where the color intensity is the separation per BP, and the index of the BPs is on the vertical axis. Bottom: the time-series data for the average BP separation, averaged over all 64 BPs and 10 trials. The horizontal red dashed line indicates the damage threshold (average separation > 0.5125 Å).

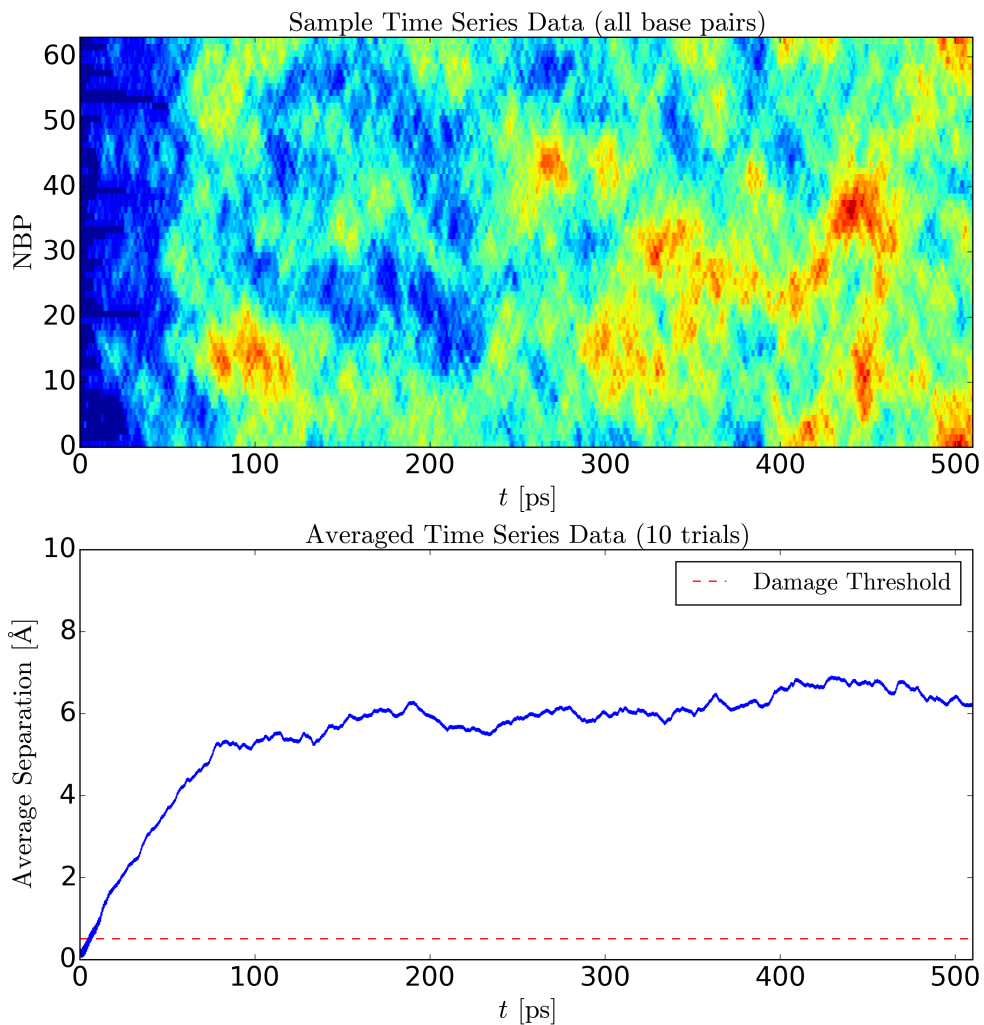


Figure 5.13: *Continuous driving at $A=150$ pN and $f=1.5$ THz.* Data for a homogeneous AT sequence. Top: the time-series data for one trial, where the color intensity is the separation per BP, and the index of the BPs is on the vertical axis. Bottom: the time-series data for the average BP separation, averaged over all 64 BPs and 10 trials. The horizontal red dashed line indicates the damage threshold (average separation > 0.5125 Å).

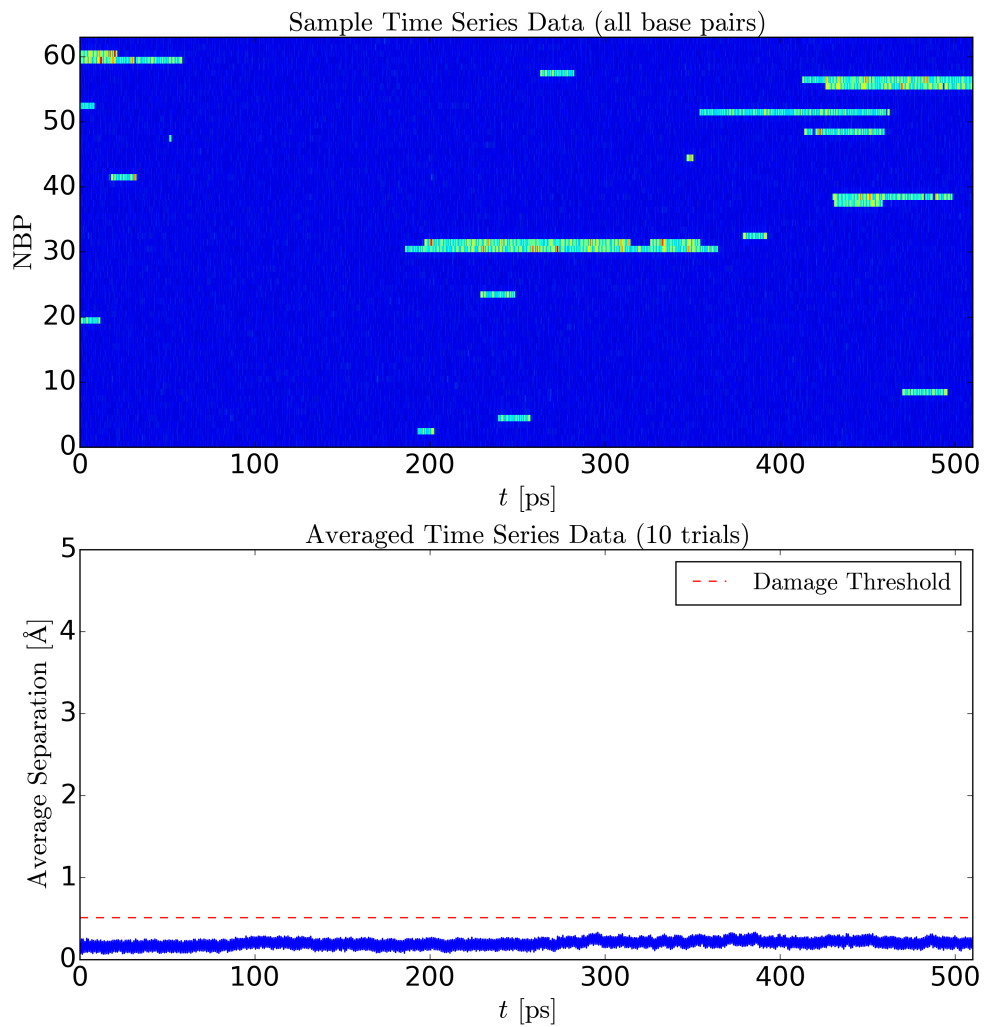


Figure 5.14: *Continuous driving at $A=150$ pN and $f=1$ THz.* Data for a homogeneous AT sequence. Top: the time-series data for one trial, where the color intensity is the separation per BP, and the index of the BPs is on the vertical axis. Bottom: the time-series data for the average BP separation, averaged over all 64 BPs and 10 trials. The horizontal red dashed line indicates the damage threshold (average separation > 0.5125 Å).

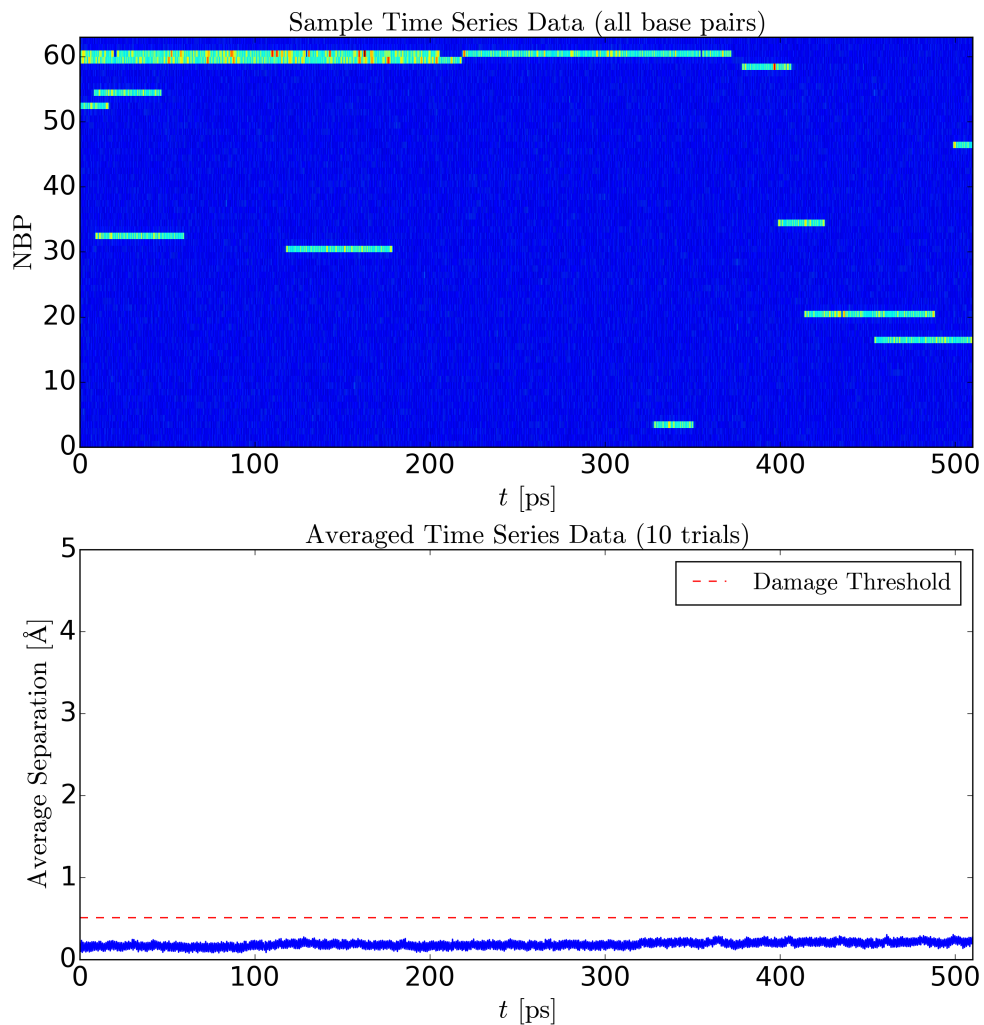


Figure 5.15: *Continuous driving at $A=100$ pN and $f=1$ THz.* Data for a homogeneous AT sequence. Top: the time-series data for one trial, where the color intensity is the separation per BP, and the index of the BPs is on the vertical axis. Bottom: the time-series data for the average BP separation, averaged over all 64 BPs and 10 trials. The horizontal red dashed line indicates the damage threshold (average separation > 0.5125 Å).

The results can be summarized as follows:

1. In the resonant region ($f=1.5$ THz), the average separation tends to increase in time and then plateaus (Fig. 5.12 & 5.13).
2. The onset of the plateau is later for lower driving amplitude.
3. The increase in average separation over time is approximately linear for short times (before the plateau region).
4. The rate of increase in the average separation is greater for higher driving amplitudes (i.e., higher slope).
5. In the off-resonant region ($f=1$ THz), the system does not exceed the damage threshold for either amplitude (Fig. 5.14 & 5.15).

From these observations, we make two conclusions. Firstly, for some values of amplitude and frequency, the slope is approximately zero (e.g., Fig. 5.14 & 5.15), meaning an increase in pulse duration will *not* lead to an increase in average separation. Secondly, at a fixed frequency, the slope appears to increase with increasing amplitude (e.g., Fig. 5.12 & 5.13)—i.e., this means that *longer pulses can be used to achieve damage at lower driving amplitudes*. In the following plots, we show that either increasing pulse duration at fixed amplitude or increasing amplitude at fixed pulse duration can lead to damage within the resonant window. Specifically, for $f = 1.5$ THz, we examine the effects of a 10 ps pulse compared to a pulse of 50 ps, when driving at $A = 100$ pN (Fig. 5.16 & 5.17). The pulse duration is marked by a vertical, black dashed line in these plots. We show that 10 ps is insufficient to cause damage, while 50 ps ultimately achieves this objective. We also compare Fig. 5.16 to a 10 ps pulse at $A = 150$ pN (Fig. 5.18), which shows that the shorter pulse at higher amplitude is also capable of achieving damage.

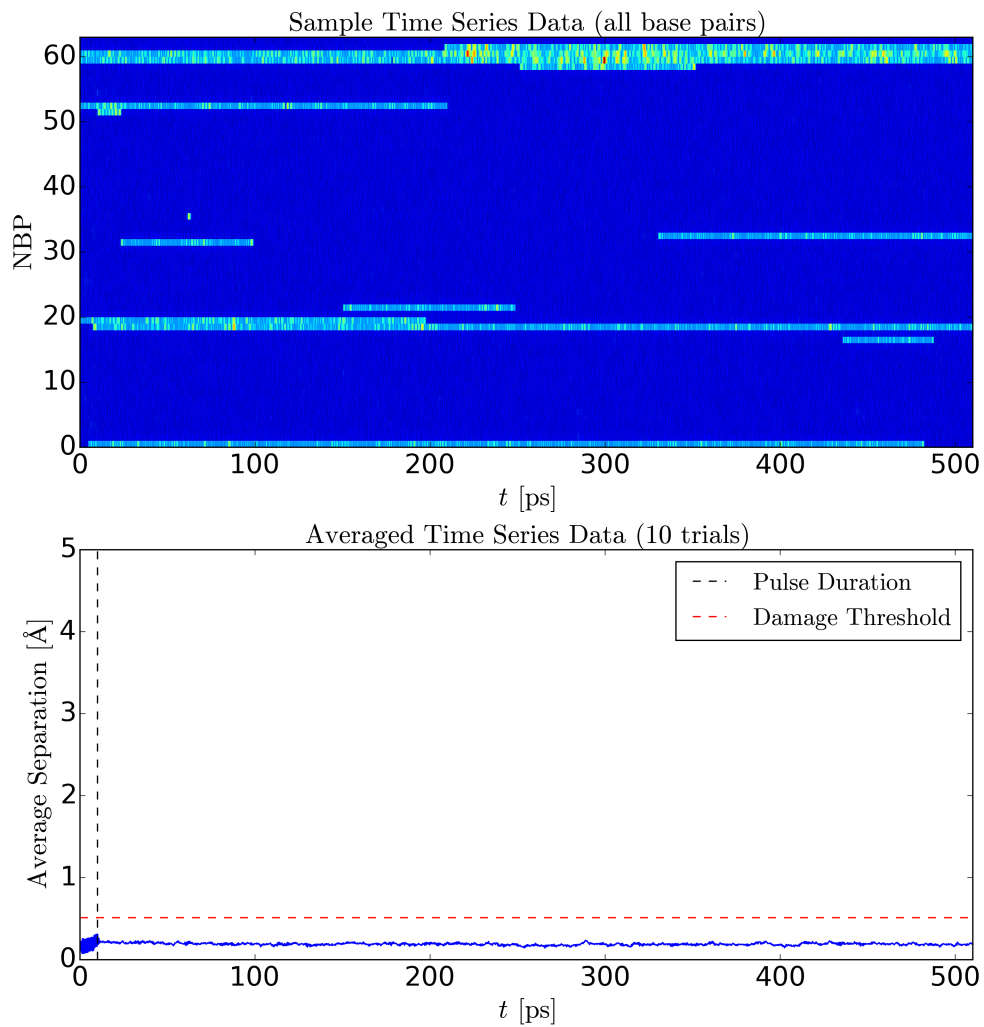


Figure 5.16: *10ps pulse at $A=100$ pN and $f=1.5$ THz.* Top: the time-series data for one trial, where the color intensity is the separation per BP, and the index of the BPs is on the vertical axis. Bottom: the time-series data for the average BP separation, averaged over all 64 BPs and 10 trials. The horizontal red dashed line indicates the damage threshold, and vertical black dashed line indicates the pulse duration.

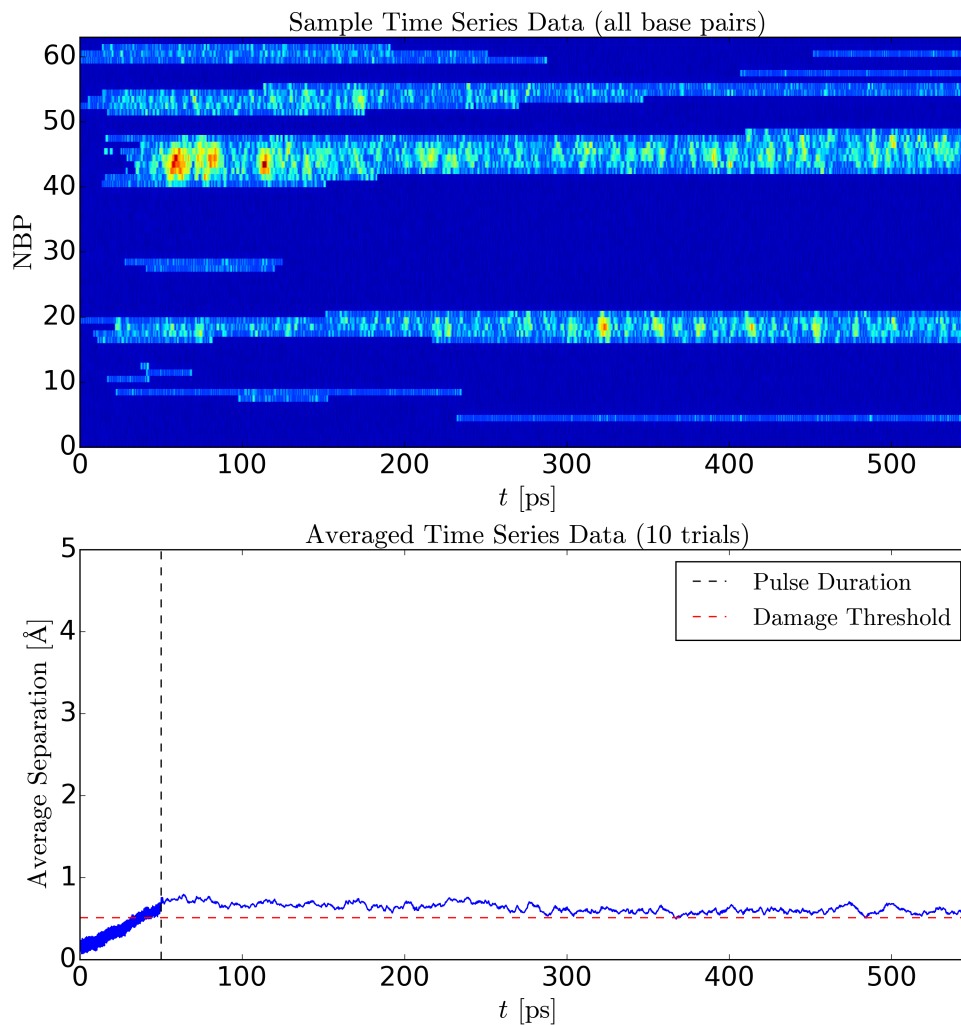


Figure 5.17: *50ps pulse at $A=100$ pN and $f=1.5$ THz.* Top: the time-series data for one trial, where the color intensity is the separation per BP, and the index of the BPs is on the vertical axis. Bottom: the time-series data for the average BP separation, averaged over all 64 BPs and 10 trials. The horizontal red dashed line indicates the damage threshold, and vertical black dashed line indicates the pulse duration.

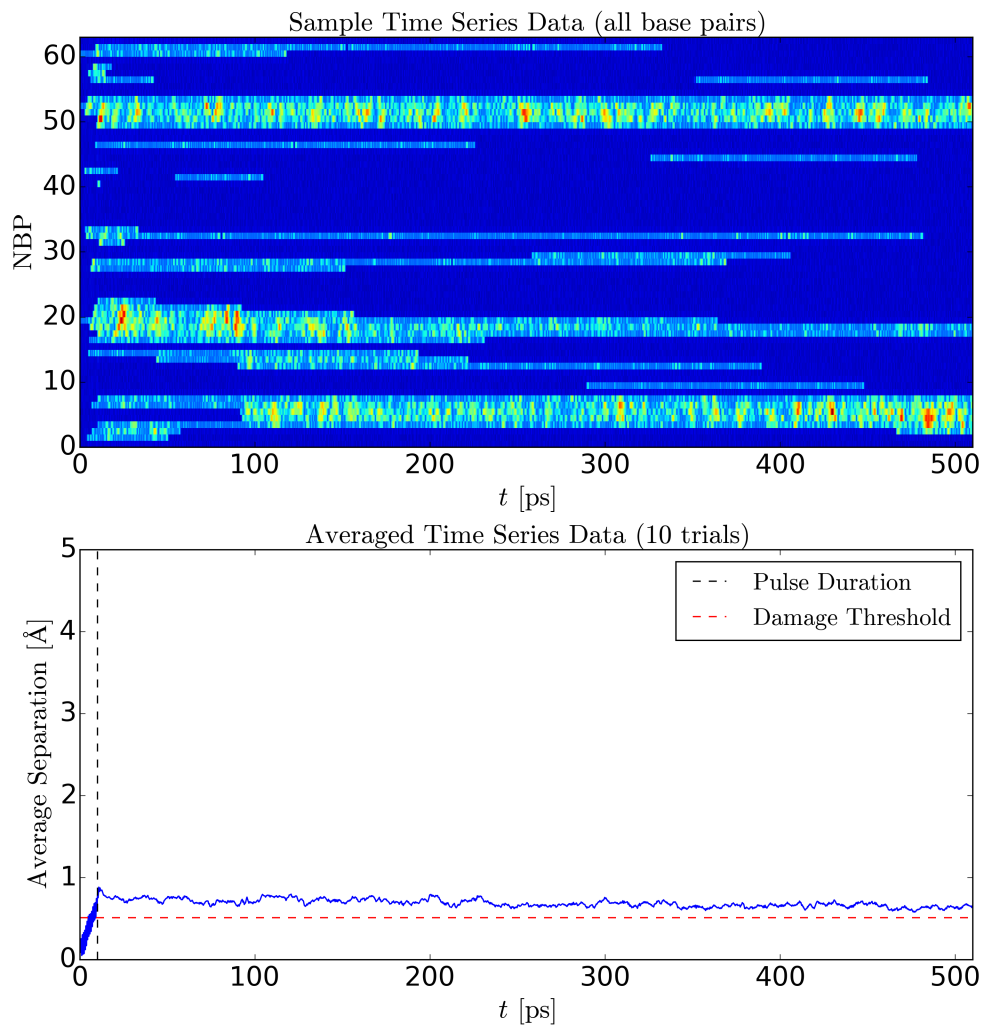


Figure 5.18: *10ps pulse at $A=150$ pN and $f=1.5$ THz.* Top: the time-series data for one trial, where the color intensity is the separation per BP, and the index of the BPs is on the vertical axis. Bottom: the time-series data for the average BP separation, averaged over all 64 BPs and 10 trials. The horizontal red dashed line indicates the damage threshold, and vertical black dashed line indicates the pulse duration.

5.5 Behavior of Single Base-Pairs in Heterogeneous Sequences

Next, we studied the destructive behavior of single BPs of a different type, inserted into otherwise homogeneous sequences. Specifically, we considered cases where one alternate base-pair was substituted into a homogeneous sequence—i.e., one GC pair within an AT sequence, and *visa versa*. We sought to determine whether substituted BPs would exhibit damage within the regions of parameter-space that were identified in the previous section, i.e., Fig. 5.10 & 5.11, and to what extent the presence of surrounding BPs would affect the likelihood of damage to the substituted pair, or themselves be damaged. *Thus, we explored the extent to which individual BPs can be selectively targeted.* Furthermore, we endeavored to quantify whether the occurrence of damage for a substituted BP differed significantly from the occurrence of damage for BPs within a completely homogeneous sequence. In other words, does the likelihood of damage, *vis-à-vis* the parameter-space identified in the previous section, depend significantly on neighboring BPs?

For the following points, depicted in Fig. 5.19, we looked at the behavior of a homogeneous AT sequence with GC substitution, and *visa versa*: a) $A=400$ pN, $f=1.5$ THz; b) $A=400$ pN, $f=2.8$ THz; c) $A=200$ pN, $f=1.5$ THz; and d) $A=200$ pN, $f=2.8$ THz. For each point, we prepared 30 thermal equilibrium trials, and used these for initial states in subsequent runs with driving. When driving the system, we recorded the time-averaged separation per base-pair over 30 independent simulations, after driving for 10ps (as before), and created a normalized histogram of the occurrences when a given base-pair exceeded its damage threshold. Thus, these histograms show the normalized occurrence of damage for each base-pair (i.e., a value of 1 indicates that a base-pair always exceeded its damage threshold for the simulations that were considered).

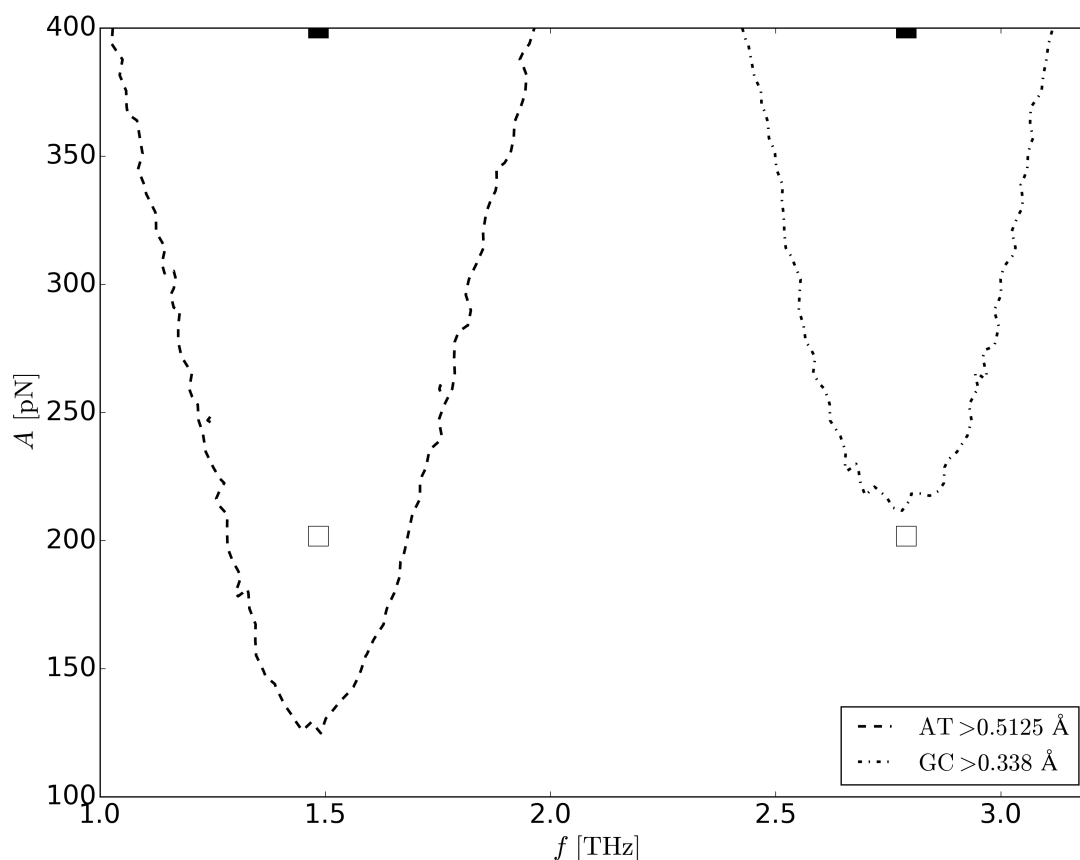


Figure 5.19: *Damage threshold for homogeneous AT & GC sequences* Parameter space with threshold levels are indicated for a homogeneous AT sequence (dashed line) and homogeneous GC sequence (dash-dotted line). Points represent parameter values chosen for following values of frequency and amplitude: $A=400$ pN; $f=1.5$ THz and $f=2.8$ THz (filled squares); $A=200$ pN; $f=1.5$ THz and $f=2.8$ THz (open squares).

The first pair of histograms are shown in Fig. 5.20, below, and they represent the point $A=400$ pN and $f=1.5$ THz. For the homogeneous AT sequence with one GC substitution, the AT base-pairs are unsurprisingly always above threshold. For a homogeneous GC sequence with one AT substitution, the AT base-pair is strongly affected despite the nearest neighbor influences of the GC pairs, which are less affected at this point in parameter space.

The inverse is shown in Fig. 5.21, for the point $A=400$ pN and $f=2.8$ THz. In this set of histograms, it is apparent that the GC base pair within the otherwise homogeneous AT sequence is strongly affected whereas the neighboring AT base pairs are less affected—this is expected, since this point represents driving at the destructive resonance of GC base pairs. Again, the inverted sequence, i.e., GC base-pairs with only one AT pair included, also shows the expected behavior—GC base pairs are excited above threshold, while the AT pair is not. We further this investigation by exploring points for a lower driving amplitude of $A=200$ pN.

The behavior of Fig. 5.22 is very similar to Fig. 5.20, although somewhat attenuated. In other words, AT pairs are selectively driven above threshold relative to GC pairs, but the number of times these base pairs exceed their threshold is less than when they are driven at the amplitude $A=400$ pN. Finally, at the point $A=200$ pN and $f = 2.8$ THz, Fig. 5.23, there appears to be little selectivity between AT and GC pairs. In this region of parameter-space, neither base-pair type exhibits destructive behavior, based on Fig. 5.10 & 5.11, and therefore we do not expect either base-pair type to be strongly selected at this point. This is what is observed. Ultimately, these results show strong selectivity at the single base-pair level, where it appears that the qualitative behavior of single base-pairs under driven conditions depends almost solely on the intrinsic properties of each base-pair type, and perhaps less significantly on nearest neighbor effects.

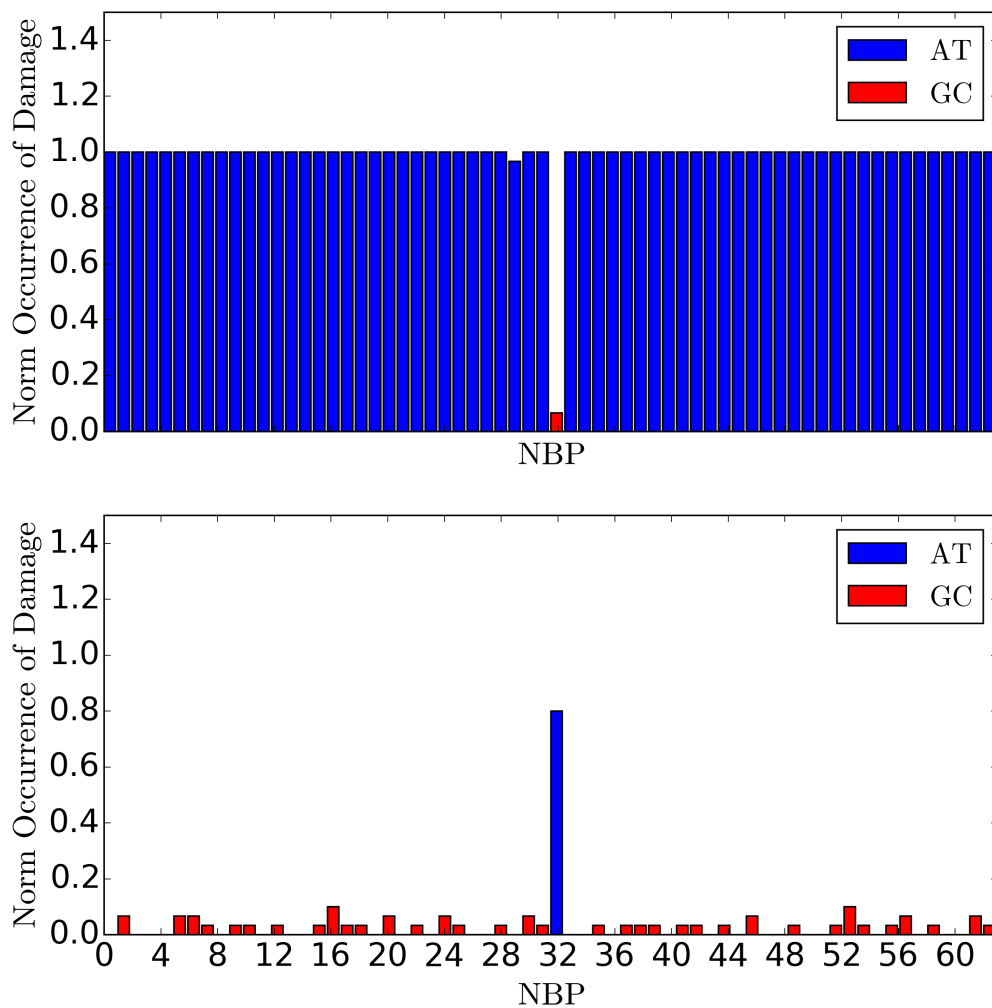


Figure 5.20: *Homogeneous sequences with one BP substitution: $A=400$ pN and $f=1.5$ THz.* The histograms represent the normalized number of occurrences when a given BP exceeds its damage threshold, where BP index is plotted on the horizontal axis. Upper plot: AT sequence with GC substitution at site 32. Lower plot: GC sequence with AT substitution at site 32.

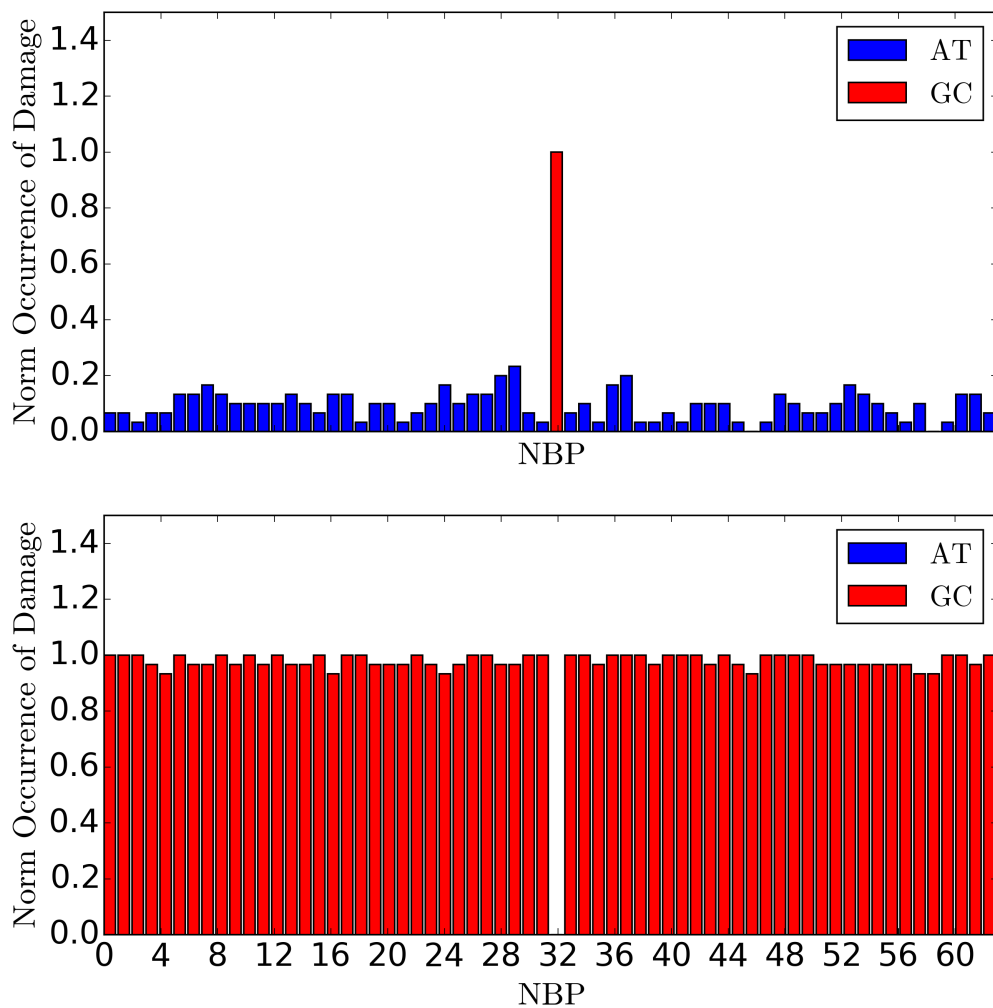


Figure 5.21: *Homogeneous sequences with one BP substitution: $A=400$ pN and $f=2.8$ THz.* The histograms represent the normalized number of occurrences when a given BP exceeds its damage threshold, where BP index is plotted on the horizontal axis. Upper plot: AT sequence with GC substitution at site 32. Lower plot: GC sequence with AT substitution at site 32.

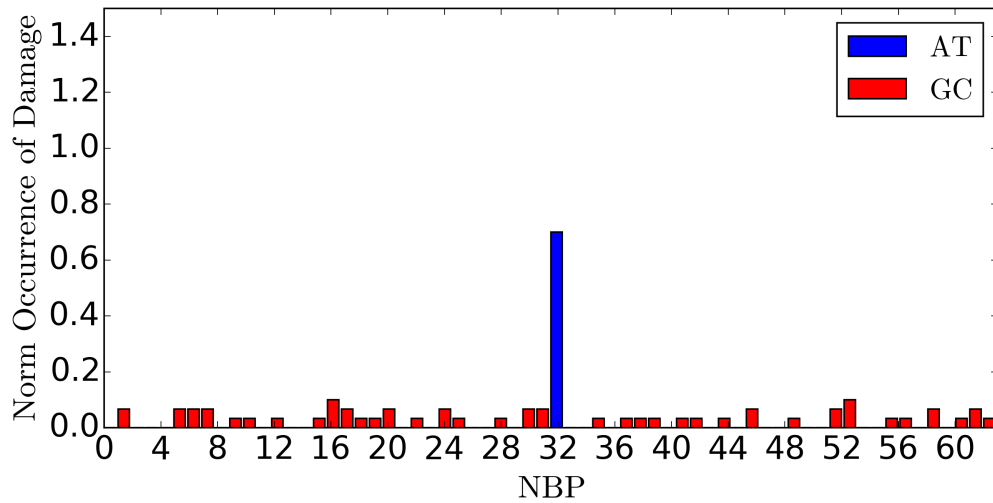
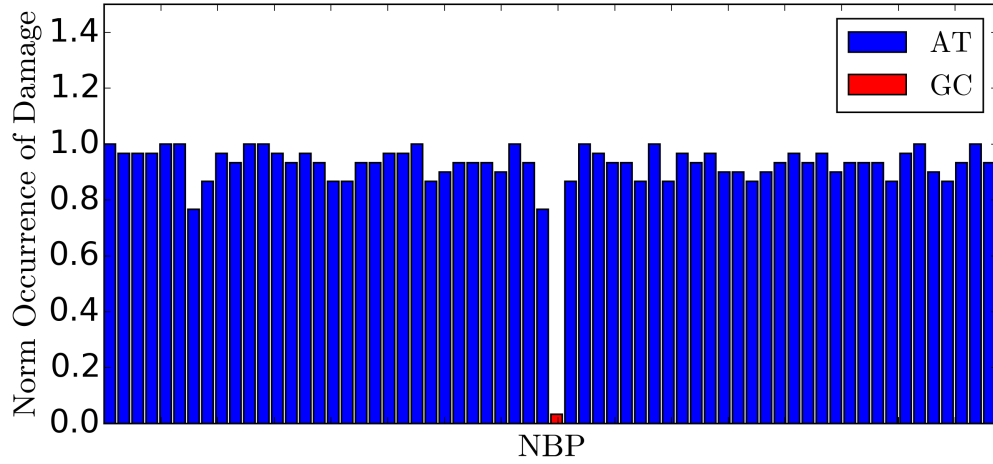


Figure 5.22: *Homogeneous sequences with one BP substitution: $A=200$ pN and $f=1.5$ THz.* The histograms represent the normalized number of occurrences when a given BP exceeds its damage threshold, where BP index is plotted on the horizontal axis. Upper plot: AT sequence with GC substitution at site 32. Lower plot: GC sequence with AT substitution at site 32.

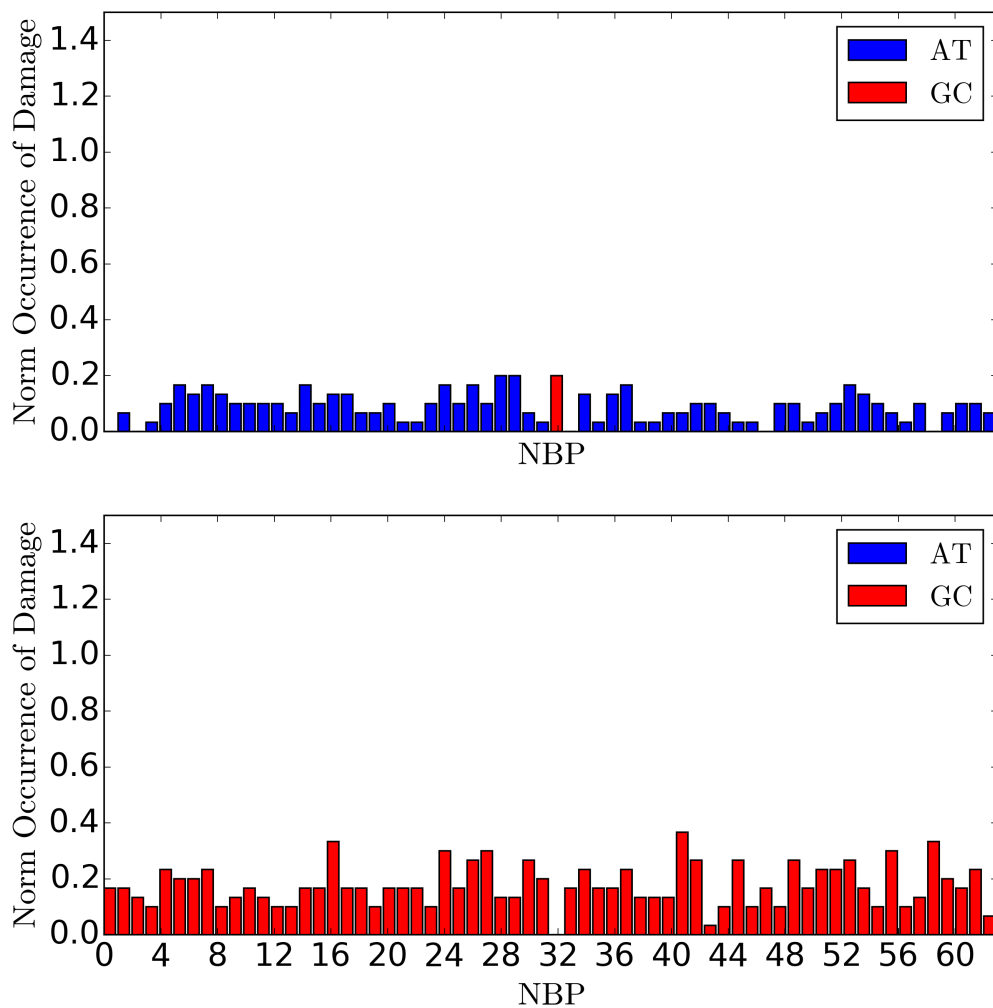


Figure 5.23: *Homogeneous sequences with one BP substitution: $A=200$ pN and $f=2.8$ THz.* The histograms represent the normalized number of occurrences when a given BP exceeds its damage threshold, where BP index is plotted on the horizontal axis. Upper plot: AT sequence with GC substitution at site 32. Lower plot: GC sequence with AT substitution at site 32.

Now we quantify whether the normalized occurrence of damage for substituted BPs is significantly different from that of BPs within a purely homogeneous sequence. In this way, we examine if neighboring BPs of a different type have a statistically significant effect on the occurrence of damage for a single BP. In this analysis, we vary frequency continuously and examine the single-BP response for the amplitudes, $A=400$ pN and $A = 200$ pN (Fig. 5.24 & 5.25). We plot the normalized occurrence of damage for substituted BPs compared to the normalized occurrence of damage for BPs within homogeneous sequences. The normalized occurrence of damage vs. frequency for a GC-substituted BP is shown in red in each figure, and the normalized occurrence of damage vs. frequency for an AT-substituted BP is shown in blue.

For instance, the red solid line in the upper plot of Fig. 5.24 shows the normalized occurrence of damage of a GC pair inserted into an AT sequence at $A=400$ pN, and the specific frequency $f=2.8$ THz in this plot corresponds to the data represented in the upper plot of Fig. 5.21. The blue solid line in the lower plot of Fig. 5.24 shows the normalized occurrence of damage of an AT pair inserted into a GC sequence at $A=400$ pN, and the specific frequency $f=1.5$ THz in this plot corresponds to the data represented in the lower plot of Fig. 5.20. Fig. 5.25 is similarly related to Figs. 5.22 & 5.23. The normalized occurrence of damage for BPs within homogeneous sequences are shown as dashed lines in these figures. Certain points are highlighted with open markers, which we discuss next.

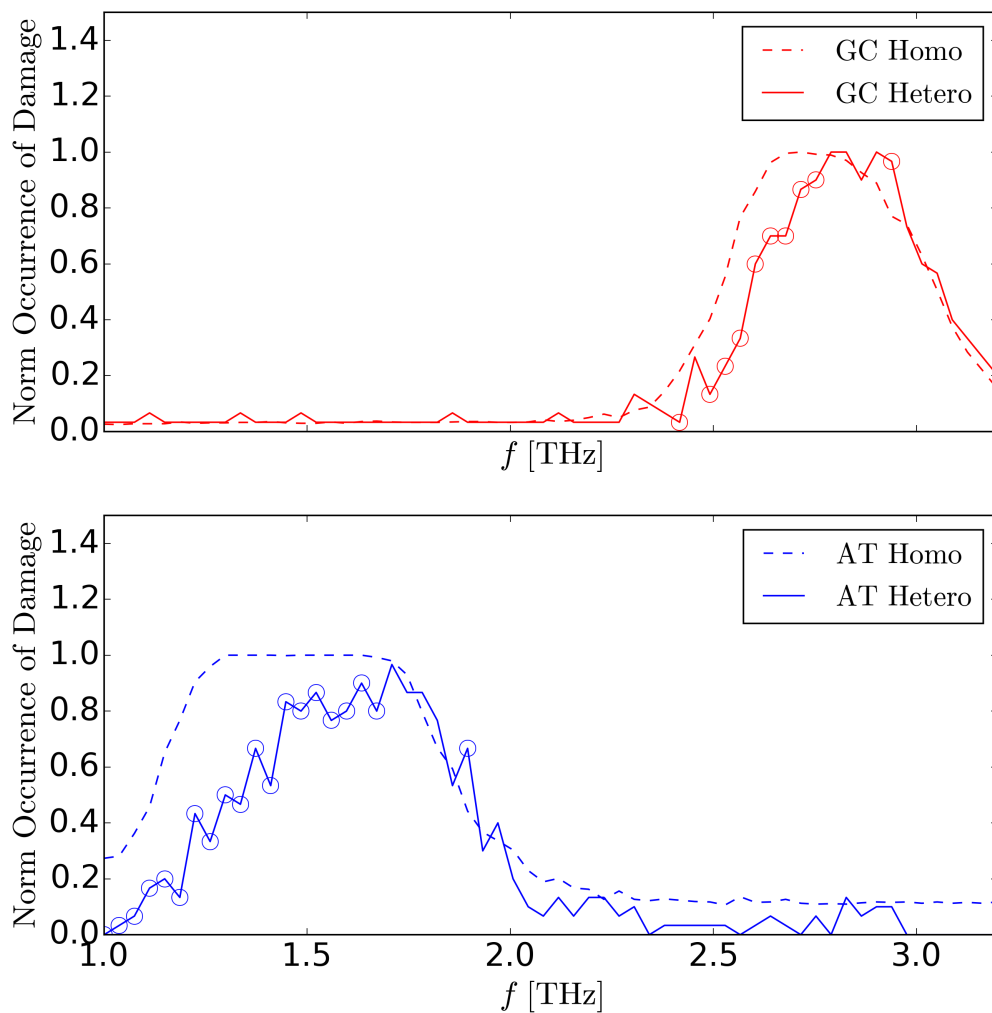


Figure 5.24: *Heterogeneous vs. homogeneous sequences: $A=400$ pN.* For driving at $A = 400$ pN, normalized occurrence of BP damage is compared between homogeneous sequences (dashed line) and heterogeneous sequences with one BP substitution (solid line). Upper plot: AT sequence with one GC substitution. Lower plot: GC sequence with one AT substitution. Open circles represent points where the occurrence of damage for a substituted BP (solid line) is statistically significantly different from the occurrence of damage for a BP of the same type in a homogeneous sequence.

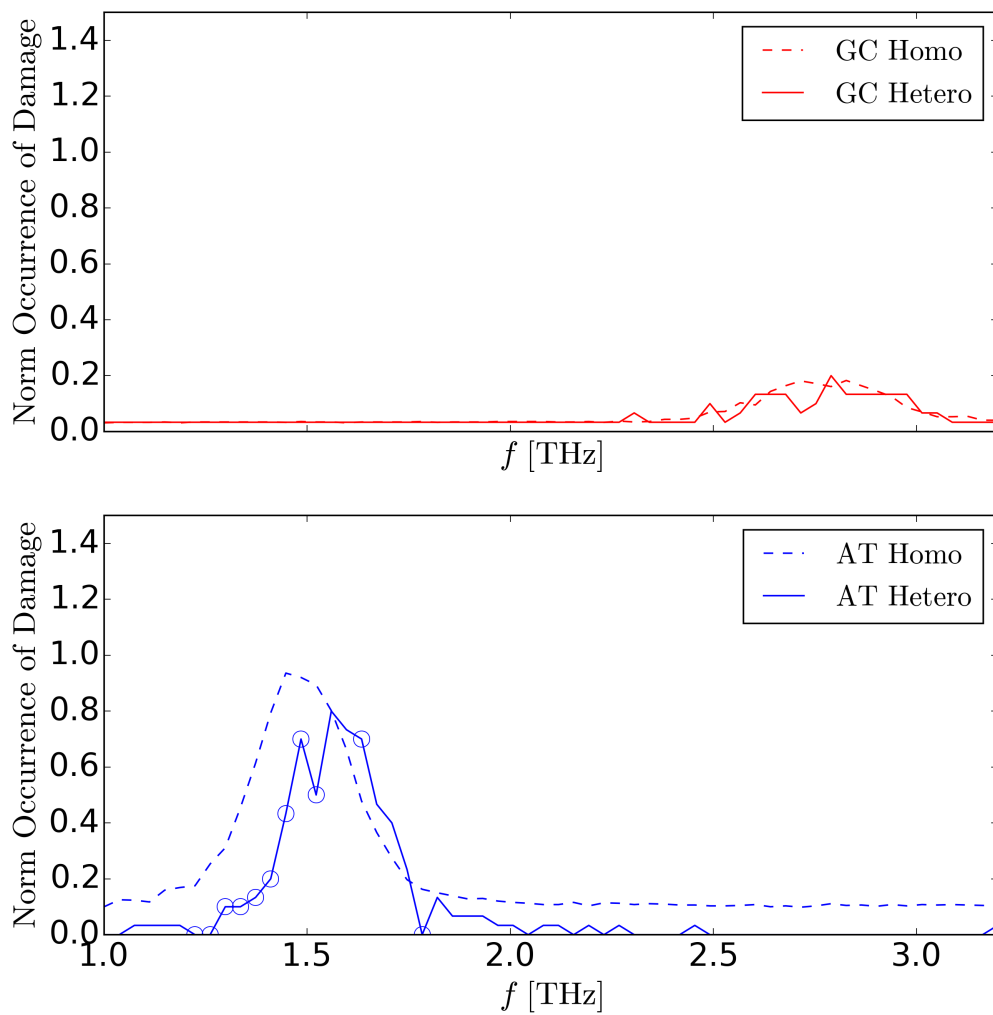


Figure 5.25: *Heterogeneous vs. homogeneous sequences: $A=200$ pN.* For driving at $A = 200$ pN, normalized occurrence of BP damage is compared between homogeneous sequences (dashed line) and heterogeneous sequences with one BP substitution (solid line). Upper plot: AT sequence with one GC substitution. Lower plot: GC sequence with one AT substitution. Open circles represent points where the occurrence of damage for a substituted BP (solid line) is statistically significantly different from the occurrence of damage for a BP of the same type in a homogeneous sequence.

The open circles in these plots indicate points for which the occurrence of damage for a substituted BP is statistically significantly different from the occurrence of damage for a BP within a homogeneous sequence, at the $p < 0.05$ level, based on a two-sample Chi-Square test (using the Python function `scipy.stats.chi2_contingency`). This function measures whether the number of “successes” (in this case, the occurrence of damage) is statistically significantly different between two samples. Ultimately, these open circles show that there are some frequency values for which the normalized occurrence of damage is different for a configuration in which a single BP is surrounded by different BP-types, compared to a configuration of similar BP-types (i.e., a homogeneous sequence).

Additionally, we observe that the damage spectra for substituted BPs appear to be shifted to higher frequency, compared to that of homogeneous BPs. This makes sense physically, since one can imagine that any BPs that are not driven above their breaking threshold would provide a greater restoring force for a substituted BP, thereby increasing the resonance frequency of that pair. Ultimately, since the damage spectra of different sequences are statically significantly different, this suggests that selectivity could be possible at the level of distinct sequences. We investigate this notion further in the next section.

5.6 Comparison of Different Heterogeneous Sequences

In this final study, we examine damage in two different heterogeneous sequences, each containing an equal number of AT and GC pairs. First we consider a sequence in which the BPs are evenly ordered, with AT-GC pairs occurring in an “every-other” sequence. Then we consider a sequence in which BPs are randomly ordered. As in the last section, we plot histograms of normalized damage occurrence for the param-

eters $A=400$ pN and $f = 1.5$ THz (this time performing 10 independent simulations, rather than 30). We then plot the normalized damage occurrence over a range of frequencies and, again, perform a two-sample Chi-Square test to determine whether the occurrence of damage in heterogeneous sequences is statistically significantly different from damage in homogeneous sequences.

The results are shown in the following figures, first for an evenly ordered sequence and then for a randomly ordered sequence. As in the previous section, we observe that substituted BPs are selectively driven in regions of parameter space that roughly correspond to the regions identified in Fig. 5.19. It is also clear, from the open circles in Fig. 5.27 & 5.29, that the frequency-dependence of the occurrence of damage in both heterogeneous sequences is statistically significantly different from the occurrence of damage in homogeneous sequences.

Finally, we directly compare the occurrence of damage for evenly-ordered sequences to that of randomly-ordered sequences, for a range of frequencies. The result, in Fig. 5.30, shows that there is a statistically significant difference between the occurrence of damage in these two sequences, for some frequencies. This very interesting result demonstrates that two sequences with the same number of AT and GC pairs can be distinguished based solely on the *ordering* of BPs.

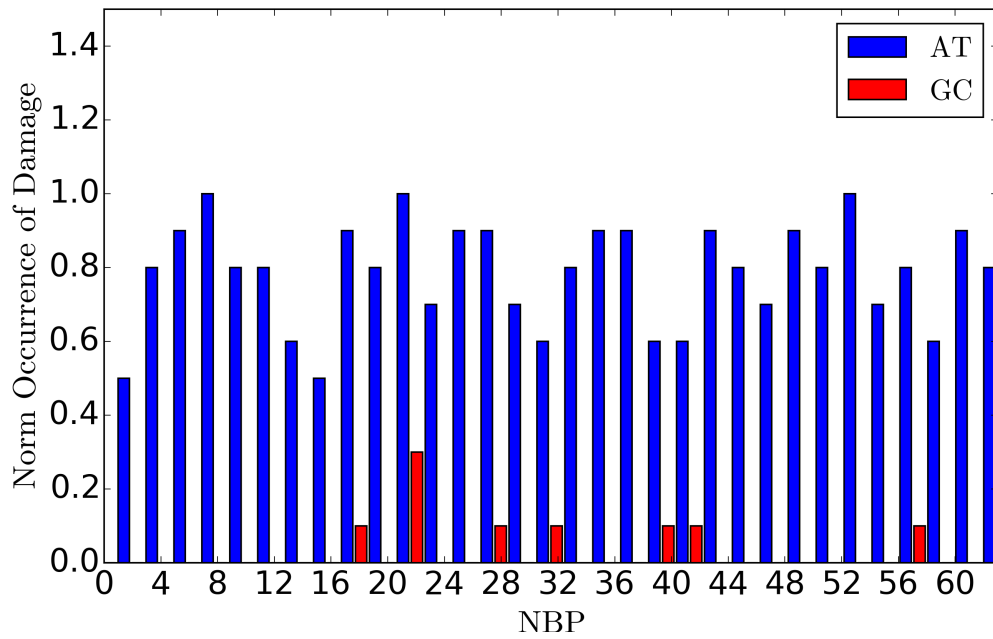


Figure 5.26: *Heterogeneous sequence with evenly ordered BP substitution: $A=400$ pN and $f=1.5$ THz.* The histograms represent the normalized number of occurrences when a given BP exceeds its damage threshold, where BP index is plotted on the horizontal axis. The sequence of 64 BPs contains 32 AT and GC pairs, distributed evenly.

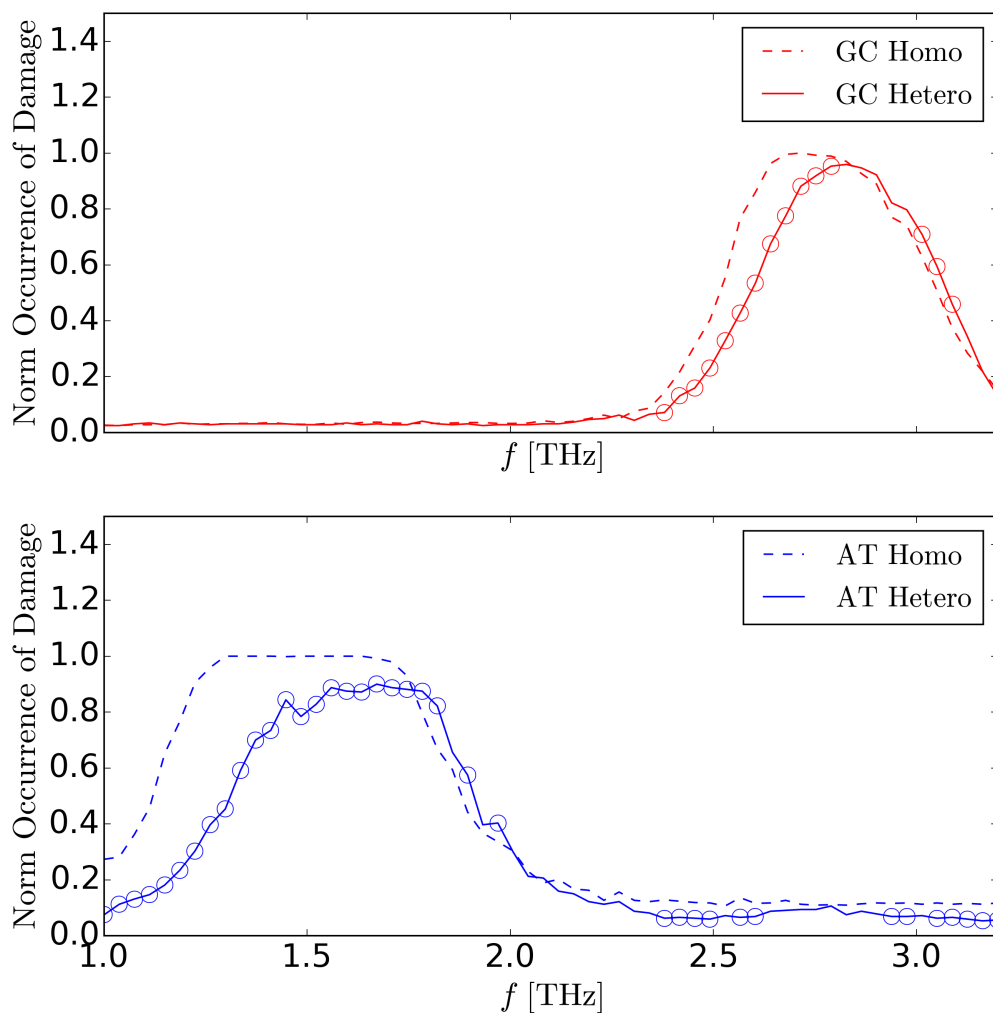


Figure 5.27: *Heterogeneous-even vs. homogeneous sequences: $A=400$ pN.* For driving at $A = 400$ pN, normalized occurrence of BP damage is compared between homogeneous sequences (dashed line) and heterogeneous sequences with evenly ordered, half-and-half BP substitution (solid line). Upper plot: damage of GC pairs. Lower plot: damage of AT pairs. Open circles represent points where the occurrence of damage for BPs in a heterogeneous sequence (solid line) is statistically significantly different from the occurrence of damage for BPs of the same type in a homogeneous sequence.

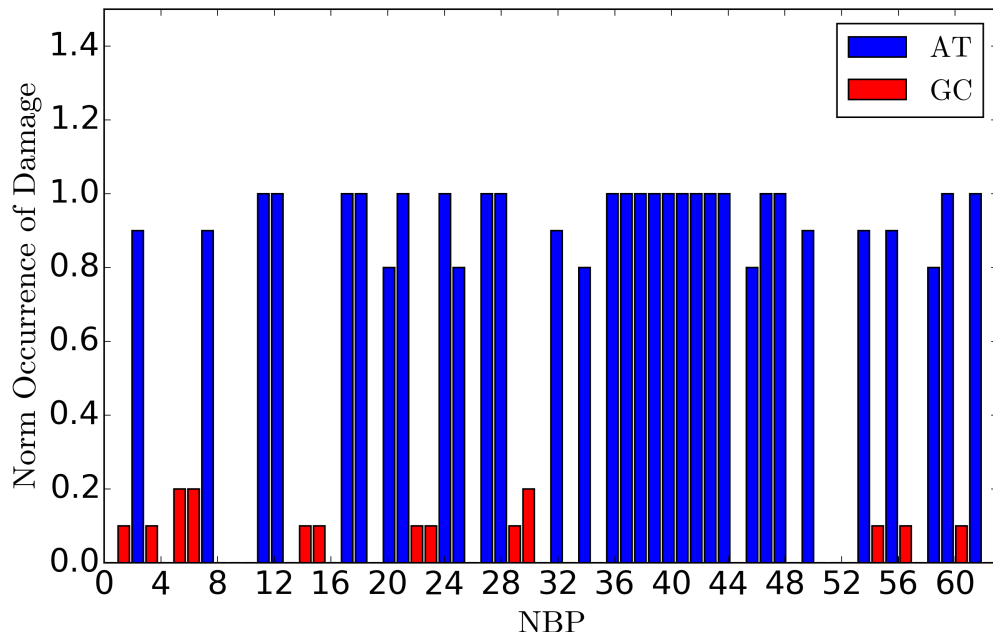


Figure 5.28: *Heterogeneous sequence with randomly ordered BP substitution:* $A=400$ pN and $f=1.5$ THz. The histograms represent the normalized number of occurrences when a given BP exceeds its damage threshold, where BP index is plotted on the horizontal axis. The sequence of 64 BPs contains 32 AT and GC pairs, distributed randomly.

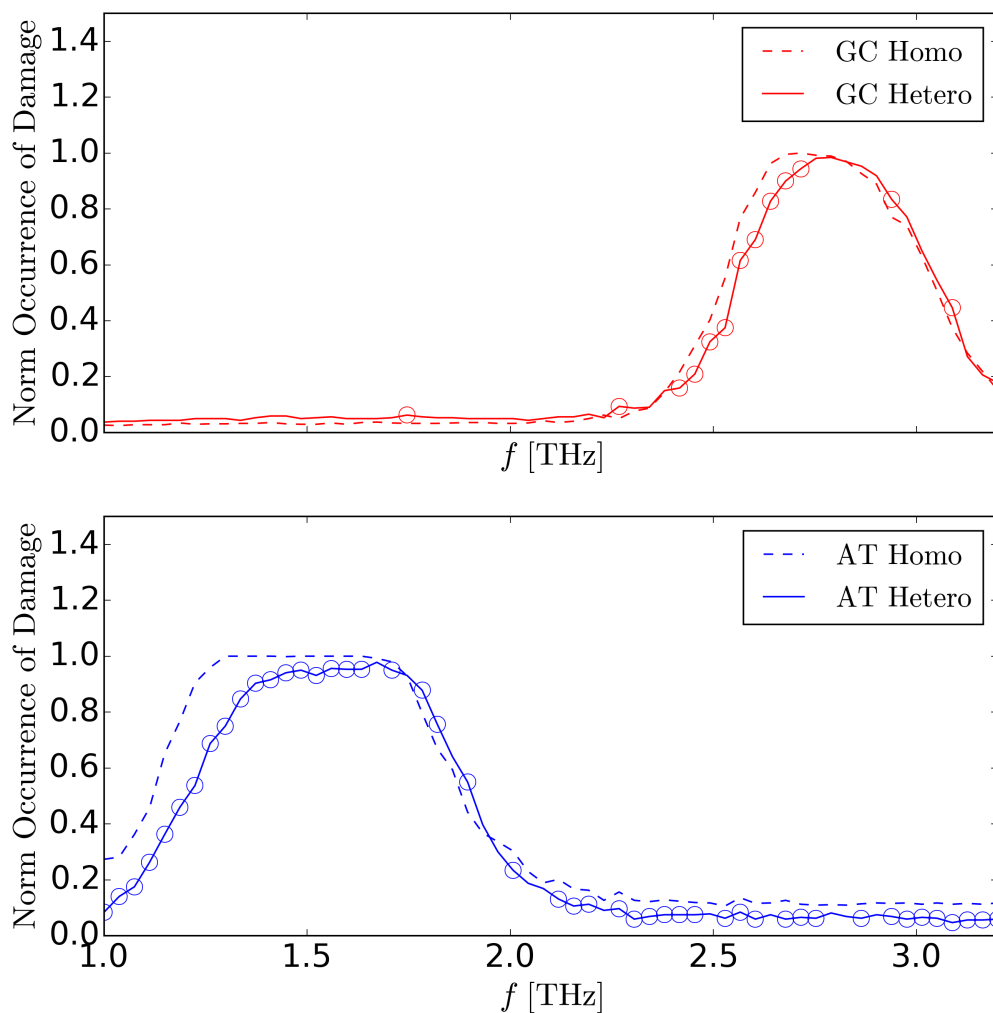


Figure 5.29: *Heterogeneous-random vs. homogeneous sequences: $A=400$ pN.* For driving at $A = 400$ pN, normalized occurrence of BP damage is compared between homogeneous sequences (dashed line) and heterogeneous sequences with randomly ordered, half-and-half BP substitution (solid line). Upper plot: damage of GC pairs. Lower plot: damage of AT pairs. Open circles represent points where the occurrence of damage for BPs in a heterogeneous sequence (solid line) is statistically significantly different from the occurrence of damage for BPs of the same type in a homogeneous sequence.

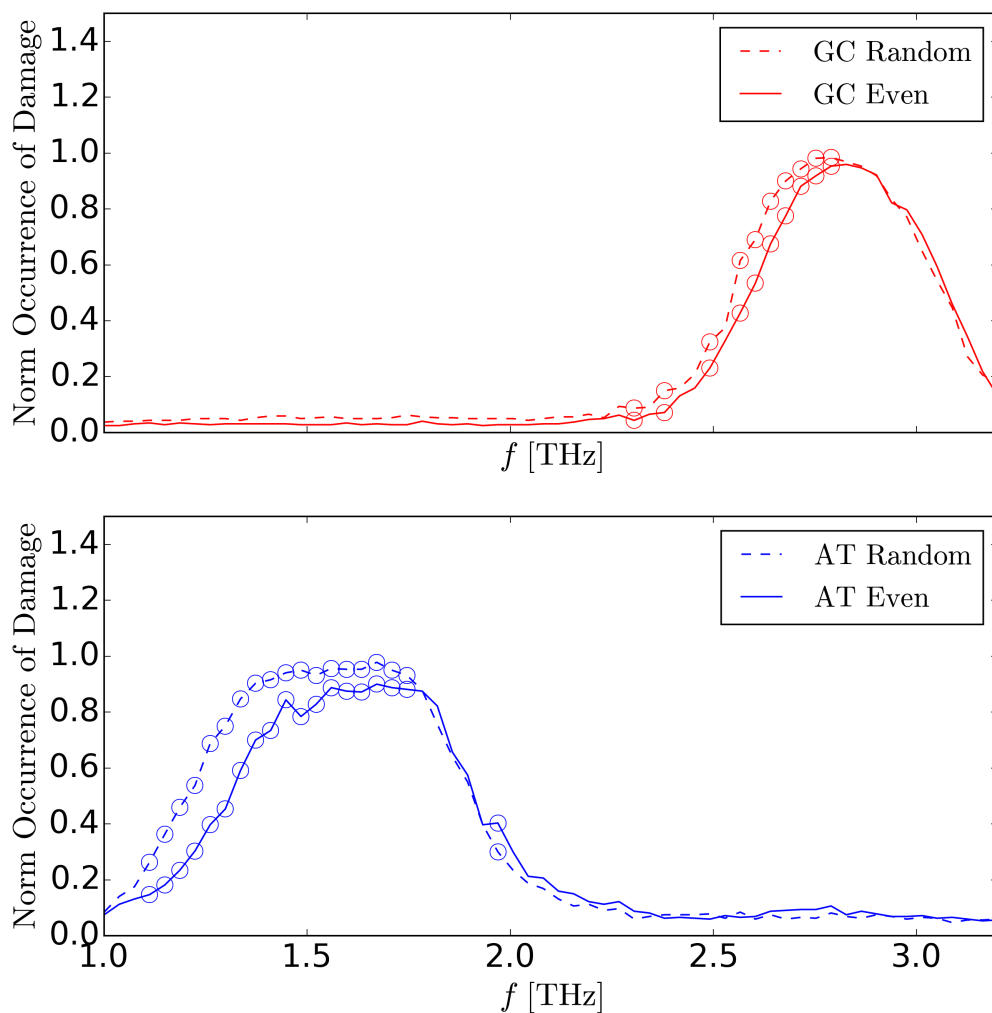


Figure 5.30: *Heterogeneous-random vs. heterogeneous-even: $A=400$ pN.* For driving at $A = 400$ pN, normalized occurrence of BP damage is compared between heterogeneous sequences with randomly ordered, half-and-half BP substitution (dashed line) and heterogeneous sequences with evenly ordered, half-and-half BP substitution (solid line). Upper plot: damage of GC pairs. Lower plot: damage of AT pairs. Open circles represent points where the occurrence of damage for BPs in randomly ordered sequences is statistically significantly different from the occurrence of damage for BPs of the same type in evenly ordered sequences.

5.7 Discussion and Caveats

We have studied the damage of DNA sequences caused by driving with radiation at THz frequencies. We have demonstrated that damage, defined by a threshold of base-pair separation, can be induced for particular amplitudes and frequencies of radiation, and that AT and GC base-pairs exhibit strong responses in entirely different regions of parameter space. Moreover, their distinct responses enable base-pairs of different types to be selectively targeted. Specifically, we demonstrated that BP substitutions within homogeneous sequences can be driven to the point of damage, without the proportionate damage of the rest of the sequence, for certain amplitudes and frequencies. Additionally, we determined that neighboring BPs had statistically significant effects on the occurrence of damage for substituted BPs, in certain regions of parameter-space. Finally, we showed that selectivity is possible at the level of distinct sequences, by examining the effect of BP ordering on damage occurrence in heterogeneous sequences with the same number of AT and GC pairs.

However, there is an underlying problem, which we intend to address, regarding the use of THz radiation for *in vivo* targeting. The penetration depth of THz radiation in the body is on the order of hundreds of microns ($\sim 0.1\text{mm}$) [72], which may only be useful for therapies that are very superficial. This is mainly due to the absorptive properties of water, as depicted in Fig. 5.31 [73, 74], where THz radiation falls within the range $\lambda \sim 100 \mu\text{m} - 1 \text{mm}$, as mentioned previously. Water is very highly absorptive and, consequently, this radiation does not penetrate far. For a more thorough review of the absorptive behavior of *human tissues* in the THz range, see Refs. [72, 75].

We note, however, that although the penetration depth in some human tissues can be greater depending on their content [76], and that deeper penetration depths can be also achieved using pulsed THz radiation [77], ultimately it would be more

desirable to use higher frequencies because they are even more deeply penetrating. We expand upon this point in the next section, where we propose a novel scheme that could enable the local generation of THz radiation within the body using a more penetrative, high-frequency signal, thus circumventing the bodies natural opacity.

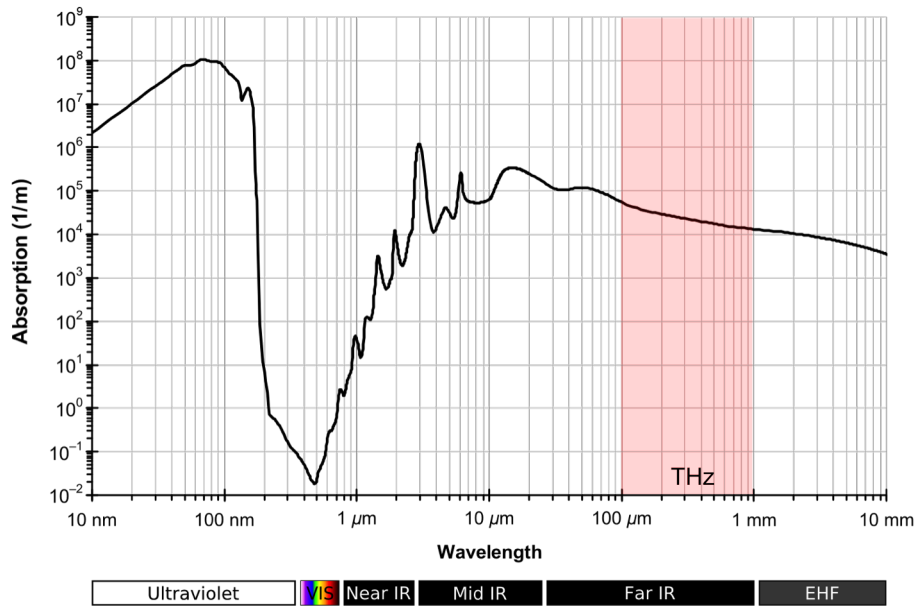


Figure 5.31: *Absorption spectrum of water.* Figure adapted from [73], who used spectral data from [74]. There is significant absorption in the THz range due to the body’s water content.

CHAPTER 6

Difference Frequency Generation for Biological Applications

In the previous chapter, we investigated the strong nonlinear response of DNA to THz radiation and demonstrated that damage can be selectively induced at the individual base-pair level. However, we also emphasized that the body is opaque to THz radiation, thus inhibiting the effectiveness of targeted therapies utilizing this approach. In this chapter, we propose a novel way to allow THz signals to infiltrate the body—through the local generation of THz frequencies at the *difference* of two higher frequencies. These high frequencies (e.g., NIR) could be tailored to the transparent window of the human body, enabling greater penetration depth. Then, a local, microscopic constituent could demodulate the signal, producing radiation at the difference of the two frequencies.

This chapter is dedicated, first, to the detailed exposition of the above scheme, clarifying the underlying concept with supporting calculations. Then, the derivation of difference-frequency generation (DFG) is thoroughly presented. DFG is a nonlinear phenomenon and, thus, is quite relevant to the major investigation of this thesis. Moreover, in the final chapter we propose that plasmonic particles could be used as promoters of DFG. Ultimately, in that chapter, we aim to discuss the phenomenon of DFG by addressing nonlinear response models of plasmonic systems.



6.1 Enhanced Penetration Depth via DFG

As outlined previously, the penetration depth of THz radiation in the body is prohibitively small for useful therapies. Although absorption is significant within the THz range, there exists a NIR window where absorption is very low. Specifically, in a range of NIR wavelengths from about 600nm - 1400nm [78, 79], the penetration depth of radiation significantly increases. For instance, Ref. [80] presents an exhaustive study of penetration depths in the 600nm-800nm range, showing typical values on the order of millimeter length scales. At longer wavelengths the penetration depth increases even more, for instance, see the minimum in the absorbance spectrum of biological constituents, shown in Fig. 6.1 [78]. Thus, NIR frequencies represent an ideal range for “carrier” signals into the human body.

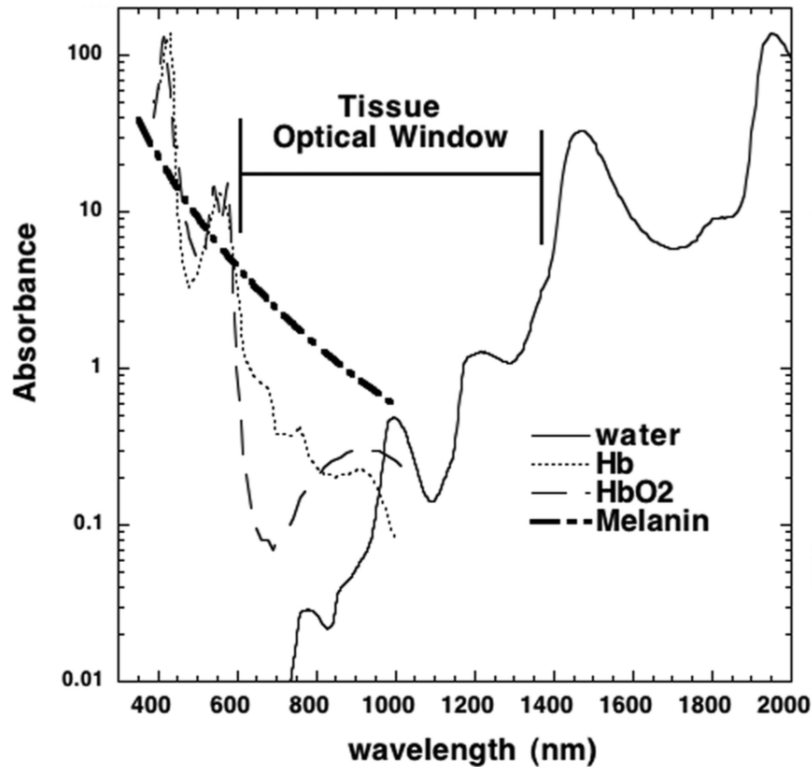


Figure 6.1: *Absorption spectrum of human body.* From Ref. [78]. At short wavelengths, melanin dominates absorbant properties, while at longer wavelengths water dominates.

The objective of our study is to use a local, microscopic constituent to demodulate the signal from a high-frequency “carrier.” Demodulation will occur through the “subtraction” of the carrier frequencies to generate a new signal with the frequency of their difference—thus, if the carrier frequencies are detuned to a THz frequency, the local demodulation will create a THz signal. Again, we will discuss the realization of this demodulation mechanism later.

By “carrier,” we specifically mean an amplitude-modulated (AM) signal:

$$S(t) = A \cos(\omega_m t) \cos(\omega_c t) \quad (6.1)$$

where the high-frequency waveform with frequency ω_c is modulated by a lower frequency, ω_m , such that $\omega_m < \omega_c$. This AM signal can be expressed as the sum of two higher-frequency signals:

$$S(t) = \frac{A}{2} [\cos(\omega_0^+ t) + \cos(\omega_0^- t)] \quad (6.2)$$

where $\omega_0^\pm = \omega_c \pm \omega_m$. These high frequencies could carry information about the low-frequency component into the body, if they occur within the NIR window of low absorption.

The other part of this scheme involves the local “demodulation” of the AM signal to produce a low-frequency (THz) component. The specific “demodulation” to which we are referring is called difference-frequency generation (DFG), wherein a signal is generated at the difference of two input frequencies through a nonlinear process. DFG is produced by the second-order dipole moment of a particle. Recall that the first-order dipole moment is given by $p^{(1)}(t) = \alpha^{(1)} E(t)$, where $\alpha^{(1)}$ is the linear polarizability of the particle and $E(t)$ is the incident field. The second-order dipole moment is given by $p^{(2)}(t) = \alpha^{(2)} E^2(t)$, where $\alpha^{(2)}$ is the second-order, nonlinear

polarizability [15]. Note, the response is proportional to the field squared.

Since DFG is proportional to the square of the incident field, let's see how it arises from our proposed AM signal (a similar derivation is done for an FM signal in the Appendix F). Using the form of Eq. (6.2), the square of the incident signal is:

$$S^2(t) = \left(\frac{A}{2}\right)^2 \left[1 + \frac{1}{2} \cos(2\omega_0^+ t) + \frac{1}{2} \cos(2\omega_0^- t) + \cos([\omega_0^+ + \omega_0^-]t) + \cos([\omega_0^+ - \omega_0^-]t)\right] \quad (6.3)$$

There are 5 terms: 1) the DC term, 2) the second harmonic of ω_0^+ , 3) the second harmonic of ω_0^- , 4) the sum-frequency term, and 5) the difference-frequency term. Note the difference-frequency term occurs at twice the modulation frequency, i.e., $|\omega_0^+ - \omega_0^-| = 2\omega_m$.

Through the appropriate choice of carrier/modulation frequencies in an AM signal, one can generate DFG at any desired frequency. For instance, our desired DFG frequency is ω_{THz} , which means that the modulation frequency should be $\omega_m = \omega_{\text{THz}}/2$. Thus, we can choose ω_c such that the frequencies ω_0^\pm both fall within the NIR window, which would enable maximal penetration of the original AM signal. This is because the absorption from an AM signal can be decomposed into absorption from each frequency component, i.e., $S(t) = S^+(t) + S^-(t)$, where $S^\pm(t) = \frac{A}{2} \cos(\omega^\pm t)$.

The figure below, Fig. 6.2, illustrates this scheme and shows the penetration depth of THz compared to NIR radiation (wavelength and penetration depth not to scale). An AM signal, composed of two high frequency components, will penetrate significantly farther than a lower frequency, THz signal. A local particle can act as a demodulator, creating a second-order signal at the difference frequency of the incident field.

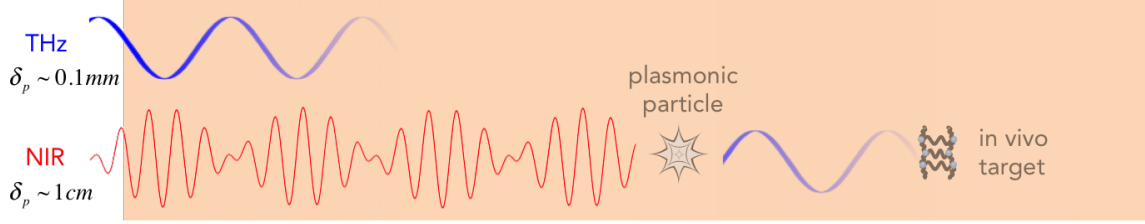


Figure 6.2: *Penetration depth schematic.* A long wavelength, THz signal penetrates less far than a short wavelength, NIR signal. A local plasmonic nanoparticle could demodulate two high frequency signals to produce a long wavelength signal at their difference.

Now we consider the possibility of choosing ω_0^\pm such that $\Delta\omega_0 = \omega_{\text{THz}}$, where $\Delta\omega_0 \equiv |\omega_0^+ - \omega_0^-|$. Specifically, we examine $\Delta\omega_0 = \omega_{\text{AT}}$ and $\Delta\omega_0 = \omega_{\text{GC}}$, where ω_{AT} and ω_{GC} are the destructive resonance frequencies for AT and GC sequences, found in the previous chapter (i.e, $f_{\text{AT}} = 1.5$ THz and $f_{\text{GC}} = 2.8$ THz). The question that we want to answer is “what is the total absorption of a signal composed of two frequencies, f_1 and f_2 within the range of the NIR window, for the cases where $|f_1 - f_2| = f_{\text{AT}}$ and $|f_1 - f_2| = f_{\text{GC}}$?” Thus, we examine the total, relative absorption of this signal in the parameter-space where $f_1, f_2 \in [200 \text{ THz}, 500 \text{ THz}]$.

Fig. 6.3 shows this parameter space, where the two marked lines indicate the conditions when $|f_1 - f_2| = 1.5$ THz and 2.8 THz (squares and circles, respectively). The color intensity map gives the total relative absorbance of the carrier signal (in arbitrary units)—that is, the sum of the absorbance of the NIR carrier signals, $S_1(t) = \frac{A}{2} \cos(2\pi f_1 t)$ and $S_2(t) = \frac{A}{2} \cos(2\pi f_2 t)$, based on the spectral absorbance given by Fig. 6.1. Note, only the half-parameter space is shown, since obviously the plot is symmetric about the line $f_1 = f_2$. The boxed region in Fig. 6.3 indicates the frequency region from $\sim 265 - 285$ THz, and Fig. 6.4 highlights this region.

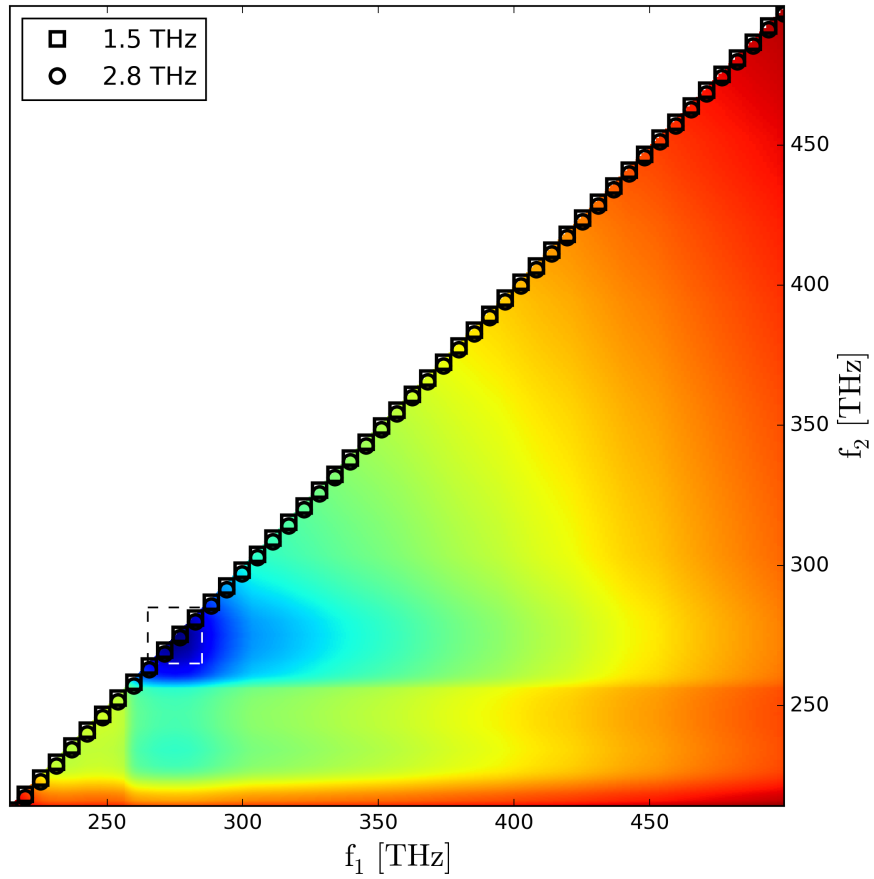


Figure 6.3: *DFG parameter space (1)*. Wavelength pairs are shown, which lead to DFG at 1.5 THz (squares) and 2.8 THz (circles). Color intensity represents the total absorbance of a signal composed of both wavelengths, from Fig. 6.1 [15]. The dashed box represents the range shown in Fig. 6.4.

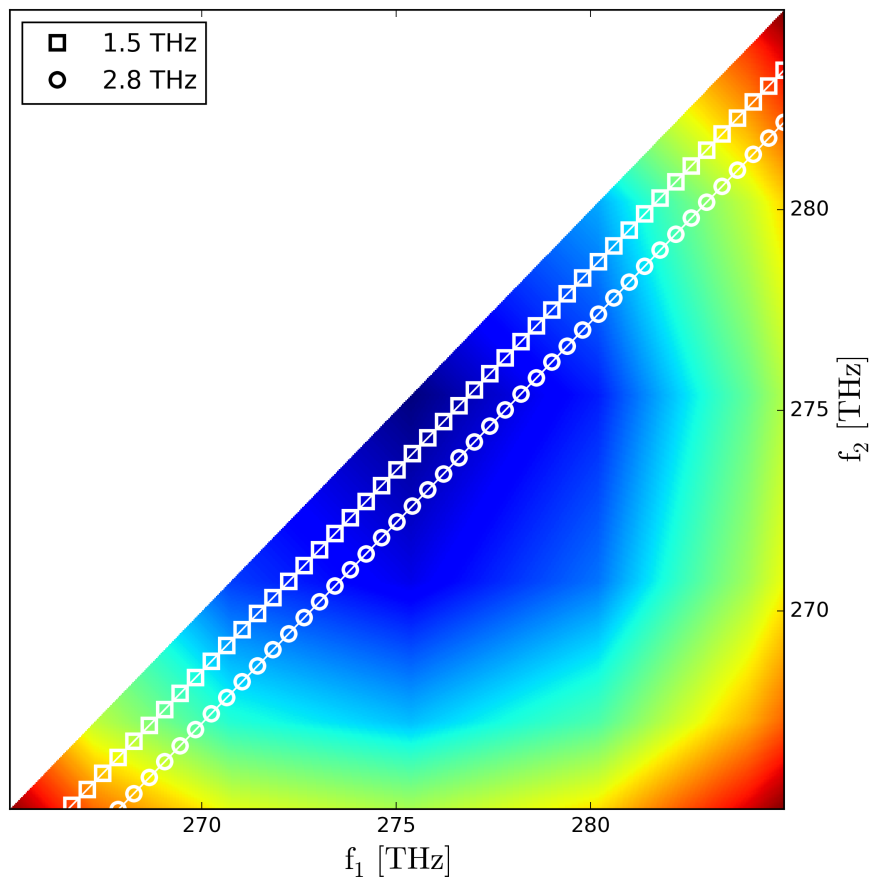


Figure 6.4: *DFG parameter space*(²). A similar plot to Fig. 6.3, with a narrower range of frequencies.

The above figure illustrates that it is possible to achieve DFG at either 1.5 THz or 2.8 THz with minimized absorbance. For instance, a frequency combination of $f_1 = 275$ THz and $f_2 = 272.2$ THz will yield a difference frequency of 2.8 THz. In terms of wavelengths, these correspond to $\lambda_1^{\text{NIR}} \approx 1.090\mu\text{m}$ and $\lambda_2^{\text{NIR}} \approx 1.101\mu\text{m}$. For an AM signal, this requires $\omega_m = 8.8$ THz and $\omega_c = 1719.4$ THz, where $\omega_m = \omega_{\text{THz}}/2$ and $\omega_c = (\omega_1 + \omega_2)/2$. Clearly, it is quite feasible to find combinations of carrier frequencies within the minimum of the NIR window that will yield DFG at the requisite THz frequencies for DNA destruction. Ultimately, we conclude that the scheme, as described thus far, is not prohibited based on the most basic physical analysis.

6.2 Derivation of Classical Miller's Rule for DFG

Moving forward, we want to understand not only how DFG originates, but how to optimize it for maximal efficacy. This requires knowledge of the second-order response of the system, which is the object that we wish to optimize. As stated in the previous section, the source of DFG is the second-order dipole moment, given by:

$$p^{(2)}(\omega_1 - \omega_2) = 2\alpha^{(2)}(\omega_1 - \omega_2)E_0^2(\omega_1, \omega_2) \quad (6.4)$$

where $E_0(\omega_1, \omega_2)$ is the incident field and $\alpha^{(2)}(\omega_1 - \omega_2)$ is the second-order polarizability of the system at the difference-frequency. Therefore, in order to optimize DFG, one should optimize $\alpha_{DFG}^{(2)} \equiv \alpha^{(2)}(\omega_1 - \omega_2)$.

We now proceed to show how $\alpha_{DFG}^{(2)}$ will arise from nonlinearity in a system, using the classical anharmonic oscillator as an example. Moreover, we show how $\alpha_{DFG}^{(2)}$ depends only on the linear response of the system, $\alpha^{(1)}$, in the perturbative

limit. Thus, we suggest that $\alpha_{DFG}^{(2)}$ might be most readily optimized through knowledge of $\alpha^{(1)}$. This strategy is particularly important for our ultimate goal, which is to optimize DFG from a local plasmonic particle. The second-order response of a plasmonic particle may be difficult to simulate in FDTD solvers—moreover, it may be equally difficult to ascertain the origin of the underlying response, and the route to optimization, from simulated results. For instance, having calculated $\alpha_{DFG}^{(2)}$ in an FDTD solver, it is perhaps not clear, *a priori*, how to alter the system to enhance DFG effects. For this reason, it would be beneficial to utilize the relation between a system’s *known linear response* and its *unknown second-order response*, in order to aid in the optimization process. Since it is likely that $\alpha^{(1)}$ is better understood and easier to simulate, only a link between $\alpha^{(1)}$ and $\alpha_{DFG}^{(2)}$ is necessary.

As a model system, we consider a simple, anharmonic oscillator that is driven and damped. The model consists of a charged particle, bound in an anharmonic potential and coupled to the driving electric field. The equation of motion is:

$$m\ddot{x}(t) + \gamma m\dot{x}(t) + m\omega_0^2 x(t) + max^2(t) = -eE(t) \quad (6.5)$$

where m and e are the mass and charge of the particle, γ is a damping parameter, ω_0 is the resonant frequency of the system, and a is the strength of the nonlinearity of the system. The dynamical variable $x(t)$ is the position of the oscillator.

There exists an analytically tractable solution for $x(t)$ when $a = 0$, which is the linear regime of behavior that we initially introduced in Chapter 1. Let’s consider this solution by expressing the driving field as a Fourier series, with driving amplitude $E(\omega_j)$ and frequency ω , where the summation is now over all positive

frequencies:

$$E(t) = \sum_j E(\omega_j) \exp[-i\omega_j t] + \text{c.c.} \quad (6.6)$$

Expressing the solution as a Fourier series, with Fourier amplitudes $x(\omega_j)$, we have:

$$x(t) = \sum_j x(\omega_j) \exp[-i\omega_j t] + \text{c.c.} \quad (6.7)$$

Then the equation of motion takes the following form in Fourier space, where the frequencies are separable since each part of the equation has a common term $\exp[-i\omega_j t]$:

$$-\omega_j^2 x(\omega_j) - i\omega_j \gamma x(\omega_j) + \omega_0^2 x(\omega_j) = -\frac{e}{m} E(\omega_j) \quad (6.8)$$

and the solution is:

$$x(\omega_j) = -\frac{e}{m} \frac{E(\omega_j)}{(\omega_0^2 - \omega_j^2 - i\gamma\omega_j)} \quad (6.9)$$

Dropping the “j” subscripts, we wish to know the response of the system, $\alpha(\omega)$, which is related to $x(\omega)$ through the dipole moment [81]:

$$p(\omega) = \alpha(\omega)E(\omega) = -ex(\omega) \quad (6.10)$$

The above identities, Eq. (6.9) & (6.10), allow us to solve for $\alpha(\omega)$:

$$\alpha(\omega) = \frac{e^2/m}{(\omega_0^2 - \omega^2 - i\gamma\omega)} \quad (6.11)$$

Note, for a system composed of N non-interacting dipoles, the polarization is equal to the dipole moment per volume, times N : i.e., $P(\omega) = np(\omega)$, where $n = N/V$

is the number density. This is related to the susceptibility through the relation $P(\omega) = \epsilon_0 \chi(\omega) E(\omega)$, such that $\chi(\omega) = \omega_p^2 / (\omega_0^2 - \omega_j^2 - i\gamma\omega_j)$, where we have used the definition of the plasma frequency, $\omega_p^2 = ne^2/m\epsilon_0$.

Now that we have established the analytical expression for the linear response, $\alpha^{(1)}(\omega)$ given by Eq. (6.11), we can progress towards deriving the higher-order response. To treat the nonlinearity of the system in the weakly nonlinear regime, we perturbatively expand the equation of motion in orders of the nonlinearity [15]. The driving force and the amplitude response of the system acquire the following forms:

$$E(t) \rightarrow \lambda E(t) \tag{6.12}$$

$$x(t) \rightarrow \lambda x^{(1)}(t) + \lambda^2 x^{(2)}(t) + \dots \tag{6.13}$$

Next, we write corresponding equations of motion to orders of λ . To order $\mathcal{O}(\lambda)$:

$$m\ddot{x}^{(1)}(t) + \gamma m\dot{x}^{(1)}(t) + m\omega_0^2 x^{(1)}(t) = -eE(t) \tag{6.14}$$

To order $\mathcal{O}(\lambda^2)$:

$$m\ddot{x}^{(2)}(t) + \gamma m\dot{x}^{(2)}(t) + m\omega_0^2 x^{(2)}(t) + ma [x^{(1)}(t)]^2 = 0 \tag{6.15}$$

Note, using this perturbative expansion, we can rearrange the previous equation to interpret the first order term as being the “source” of the driving to second-order, i.e., $m\ddot{x}^{(2)}(t) + \gamma m\dot{x}^{(2)}(t) + m\omega_0^2 x^{(2)}(t) = -ma [x^{(1)}(t)]^2$. The first and second order equations are coupled, and $x^{(2)}(t)$ can be solved with knowledge of $x^{(1)}(t)$. Again,

this can be done in Fourier space. Solving for $[x^{(1)}(t)]^2$,

$$\begin{aligned}
[x^{(1)}(t)]^2 &= \left\{ \sum_j x^{(1)}(\omega_j) \exp[-i\omega_j t] + \text{c.c.} \right\} \\
&\quad \times \left\{ \sum_k x^{(1)}(\omega_k) \exp[-i\omega_k t] + \text{c.c.} \right\} \\
&= \sum_j \sum_k [x^{(1)}(\omega_j)x^{(1)}(\omega_k) \exp[-i(\omega_j + \omega_k)t] + \text{c.c.} \\
&\quad + x^{(1)}(\omega_j)x^{(1)}(-\omega_k) \exp[-i(\omega_j - \omega_k)t] + \text{c.c.}]
\end{aligned} \tag{6.16}$$

We split the sum into terms where $j = k$ and $j \neq k$:

$$\begin{aligned}
[x^{(1)}(t)]^2 &= 2 \sum_j x^{(1)}(\omega_j)x^{(1)}(-\omega_j) \\
&\quad + \sum_j [x^{(1)}(\omega_j)]^2 \exp[-i2\omega_j t] + \text{c.c.} \\
&\quad + 2 \sum_j \sum_{k, (j < k)} x^{(1)}(\omega_j)x^{(1)}(\omega_k) \exp[-i(\omega_j + \omega_k)t] + \text{c.c.} \\
&\quad + 2 \sum_j \sum_{k, (j < k)} x^{(1)}(\omega_j)x^{(1)}(-\omega_k) \exp[-i(\omega_j - \omega_k)t] + \text{c.c.}
\end{aligned} \tag{6.17}$$

Now, the second-order response has the following Fourier series expansion:

$$x^{(2)}(t) = \sum_l x^{(2)}(\omega_l) \exp[-i\omega_l t] + \text{c.c.} \tag{6.18}$$

Since there must be a correspondence between the frequency components of $[x^{(1)}(t)]^2$ and $x^{(2)}(t)$, we see from Eq. (6.17) that there are 4 types of second-order response: (1) the DC (zero-frequency) response, $x^{(2)}(0)$; (2) the second-harmonic response, $x^{(2)}(2\omega_j)$; (3) the sum-frequency response, $x^{(2)}(\omega_j + \omega_k)$; and (4) the difference-frequency response, $x^{(2)}(\omega_j - \omega_k)$. It is now straightforward to solve for any of these second-order responses by expressing the coupled equations of motion in Fourier

space. Specifically, the equation of motion for the difference-frequency response is shown below, and subsequently solved for. We require $\omega_l = \omega_j - \omega_k$ in order to match the DFG term in Eq. (6.17). Thus, $x^{(2)}(\omega_l) = x^{(2)}(\omega_j - \omega_k)$. Further, we define $x_{DFG}^{(2)} \equiv x^{(2)}(\omega_j - \omega_k)$ to simplify notation.

$$-(\omega_j - \omega_k)^2 x_{DFG}^{(2)} - i(\omega_j - \omega_k)\gamma x_{DFG}^{(2)} + \omega_0^2 x_{DFG}^{(2)} = -2ax^{(1)}(\omega_j)x^{(1)}(-\omega_k) \quad (6.19)$$

$$x_{DFG}^{(2)} = -\frac{2am}{eE_0}x^{(1)}(\omega_j - \omega_k)x^{(1)}(\omega_j)x^{(1)}(-\omega_k) \quad (6.20)$$

The general form, $x^{(1)}(\omega) = -\frac{e}{m}E(\omega)/(\omega_0^2 - \omega^2 - i\gamma\omega)$, of the first-order response has been used and we assume that the incident field amplitude is frequency independent (i.e., $E(\omega) = E_0$). Using the second-order relations for the polarizability, $p_{DFG}^{(2)} = 2\alpha_{DFG}^{(2)}E_0^2 = -ex_{DFG}^{(2)}$, we can solve for the second-order response:

$$\alpha_{DFG}^{(2)} = a\kappa\alpha^{(1)}(\omega_1 - \omega_2)\alpha^{(1)}(\omega_1)\alpha^{(1)}(-\omega_2) \quad (6.21)$$

where $\kappa = m/e^3$. Note, $\alpha_{DFG}^{(2)}$ and $\chi_{DFG}^{(2)}$ are related by a factor of $(\epsilon_0/n)^2$ such that $\chi_{DFG}^{(2)} = a\kappa'\chi^{(1)}(\omega_1 - \omega_2)\chi^{(1)}(\omega_1)\chi^{(1)}(-\omega_2)$, where $\kappa' = \kappa(\epsilon_0/n)^2 = (e/m)\omega_p^{-4}$.

The relation between the linear response and the nonlinear response is known as Miller's rule [15]. In the most general terms, Miller's rule states that the second order response can be expressed in terms of the first order response and the proportionality is related to the strength of the nonlinearity. Importantly, Miller's rule is also extremely useful when knowledge of the first order response is already available.

In the next section, we further our investigation of the classical anharmonic oscillator by simulating a hypothetical system. We use the simulated linear response of this system to "predict" the second-order response using Miller's rule, and compare with results from full simulation of the second-order response. This serves as the simplest "proof of concept" that first-order simulation results can be used to gain

understanding of second-order phenomena. Moreover, we argue that this is a useful route towards the optimization of real systems.

6.3 Simulation of DFG from Classical Anharmonic Oscillator

For a given system, we suggest that it is possible to make tailored adjustments to the linear response in order to optimize the DFG response, *without* ever having to directly simulate the second order response of the system. To investigate this, we simulate DFG from a classical anharmonic oscillator and retrieve the full response of the system to all orders, without approximations. We then use Miller’s rule, along with the simulated first-order data, to calculate the second-order response of the system and compare with the simulated second-order response. Thus, we demonstrate the possibility of obtaining the second-order response through knowledge of the first-order response only.

Our equation of motion has the same form of Eq. (6.5) of the previous section, namely:

$$\ddot{x}(t) + \gamma\dot{x}(t) + \omega_0^2x(t) + ax^2(t) = F(t) \tag{6.22}$$

We consider a driving field, $F(t) = \frac{B}{2} [\cos(\omega_1t) + \cos(\omega_2t)]$, that explicitly has two frequency components, which can be expressed as an AM signal with amplitude B. We use the following parameter values: $\gamma = 0.1$ rad/s, $\omega_0 = 4$ rad/s, $a = 2\text{m}^3/\text{s}^2$, and $B = 0.2\text{m}/\text{s}^2$. We simulate Eq. (6.22) in the time domain, using the two driving frequencies $\omega_1 = 4$ rad/s and $\omega_2 = 3.5$ rad/s. We again use the Verlet algorithm to numerically integrate the equation of motion, as previously detailed. The potential experienced by the particle, and the time series data, are depicted in Fig. 6.5—the

potential exhibits a subtle nonlinearity. The Fourier transform of the time series is also shown on a log-scale, where the amplitude of the Fourier transform, A_{FT} , is related to the root-mean-square (rms) amplitude of the time series in the following way: $A_{FT} = x_{\text{rms}}^2(\omega)$, where $x_{\text{rms}}(\omega) = \frac{1}{\sqrt{2}}|x(\omega)|$.

There are 6 peaks that can be seen in the FT spectrum of Fig. 6.5, labeled alphabetically: (a) the DFG peak, occurring at $\omega_1 - \omega_2 = 0.5$ rad/s; (b) the linear response of the system at the input driving frequency $\omega_2 = 3.5$ rad/s; (c) the linear response of the system at the input driving frequency $\omega_1 = 4$ rad/s; (d) the second-harmonic frequency of ω_2 , which occurs at $2\omega_2 = 7$ rad/s; (e) the sum-frequency component, occurring at the frequency $\omega_1 + \omega_2 = 7.5$ rad/s; and (f) the second-harmonic frequency of ω_1 , which occurs at $2\omega_1 = 8$ rad/s.

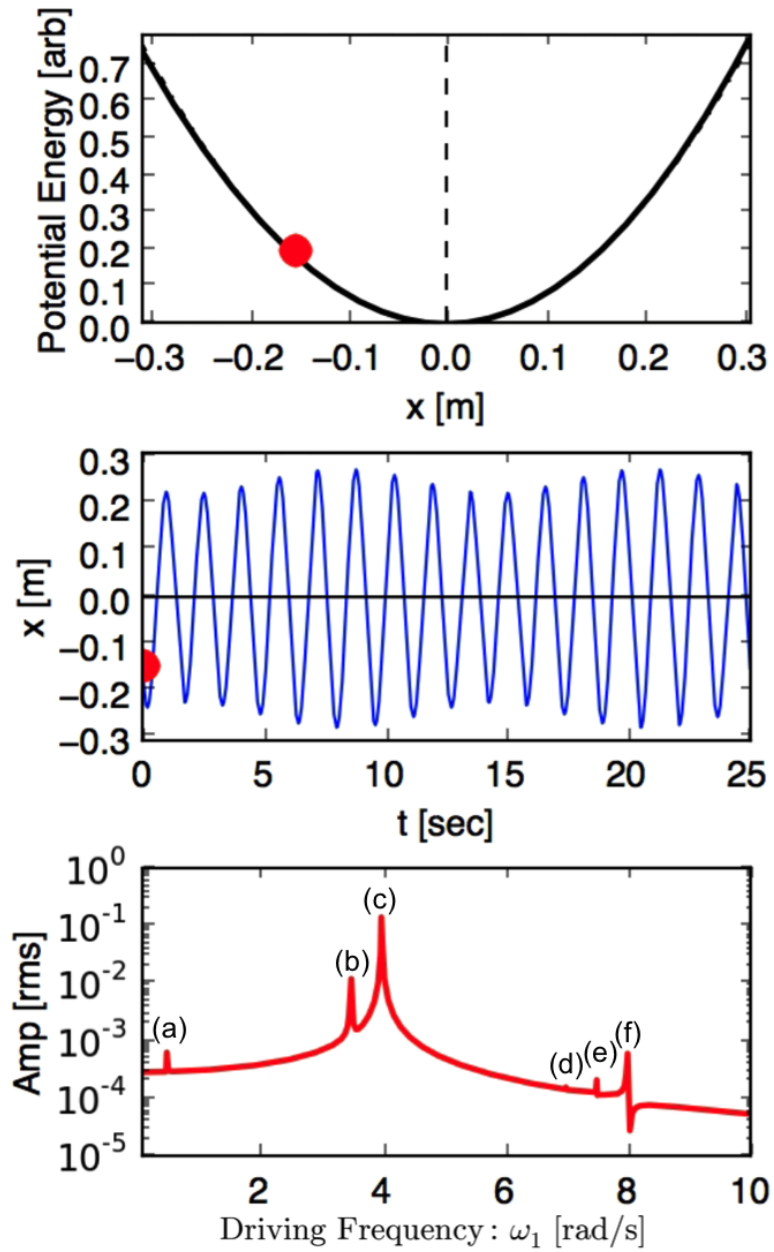


Figure 6.5: *Time series and Fourier transform of anharmonic oscillator.* Upper: anharmonic potential. Middle: time series of system response. Lower: Fourier transform of time series data.

The previous figure, Fig. 6.5, represents the response of the system at two fixed frequencies. We now look at the response when one input frequency is varied. For instance, Fig. 6.6 shows this response for the fixed frequency $\omega_2 = 3.5$ rad/s, while varying ω_1 , where the vertical axis is the Fourier frequency and the color intensity represents the Fourier amplitude. Thus, the Fourier spectrum of Fig. 6.5 is represented as a vertical slice in Fig. 6.6 at $\omega_1 = 4$ rad/s (not shown).

The main diagonal of Fig. 6.6 represents the linear response of the system as the driving frequency ω_1 is swept. There are other first-order response features in this plot, for instance the constant response feature at $\omega = 3.5$ rad/s corresponds to linear response of the system at the fixed driving frequency $\omega_2 = 3.5$ rad/s. Additionally, some artifacts of the simulation process due to the finiteness of the data set are present.

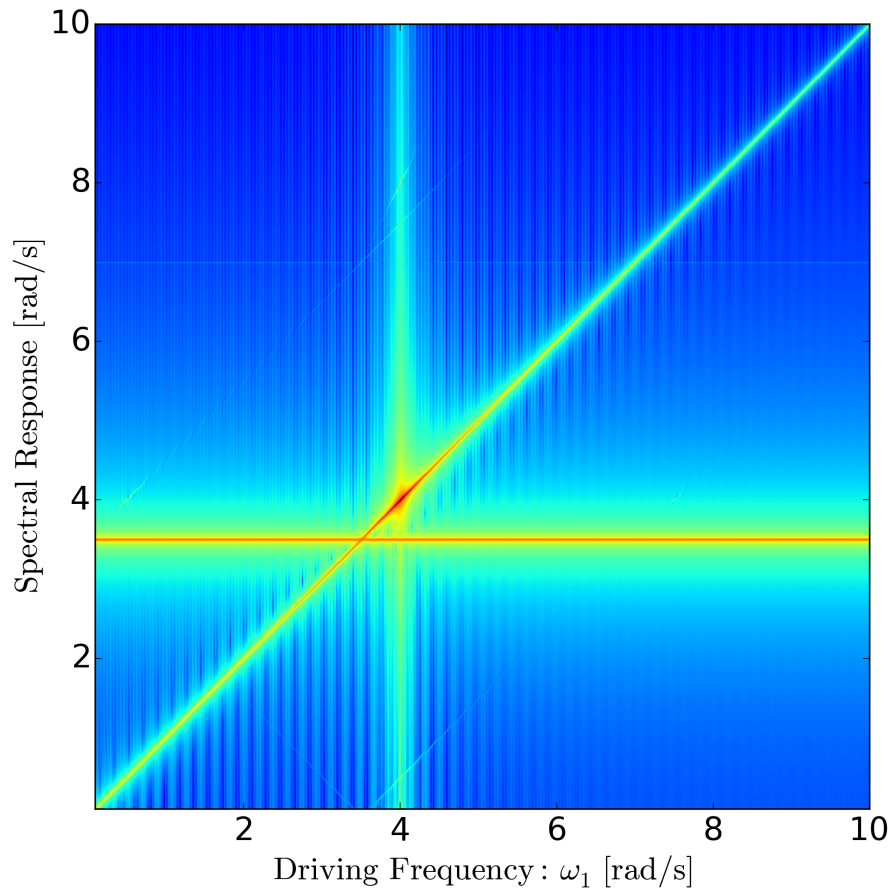


Figure 6.6: *Full response of anharmonic oscillator to two driving frequencies.* For one fixed frequency, $\omega_2 = 3.5$ rad/s, the other driving frequency, ω_1 , is swept. The Fourier transform of the time series data is plotted on the y-axis.

Next, we examine the second-order features of Fig. 6.6. The second-order features can be better visualized when the first order response is subtracted from the plot of the full response. Thus, we simulated the system when the nonlinearity was set to zero and then we subtracted this data from the full nonlinear response, leaving only higher order terms (predominantly second order terms) in Fig. 6.7. The location of several second order features are indicated in Fig. 6.8: the second-harmonic response of ω_1 (blue line), the second-harmonic response of ω_2 (yellow line), the sum-frequency response of ω_1 and ω_2 (green line), and the difference-frequency response of ω_1 and ω_2 (red line). We are interested in the DFG response, so we will examine the amplitude along the red line in what follows:

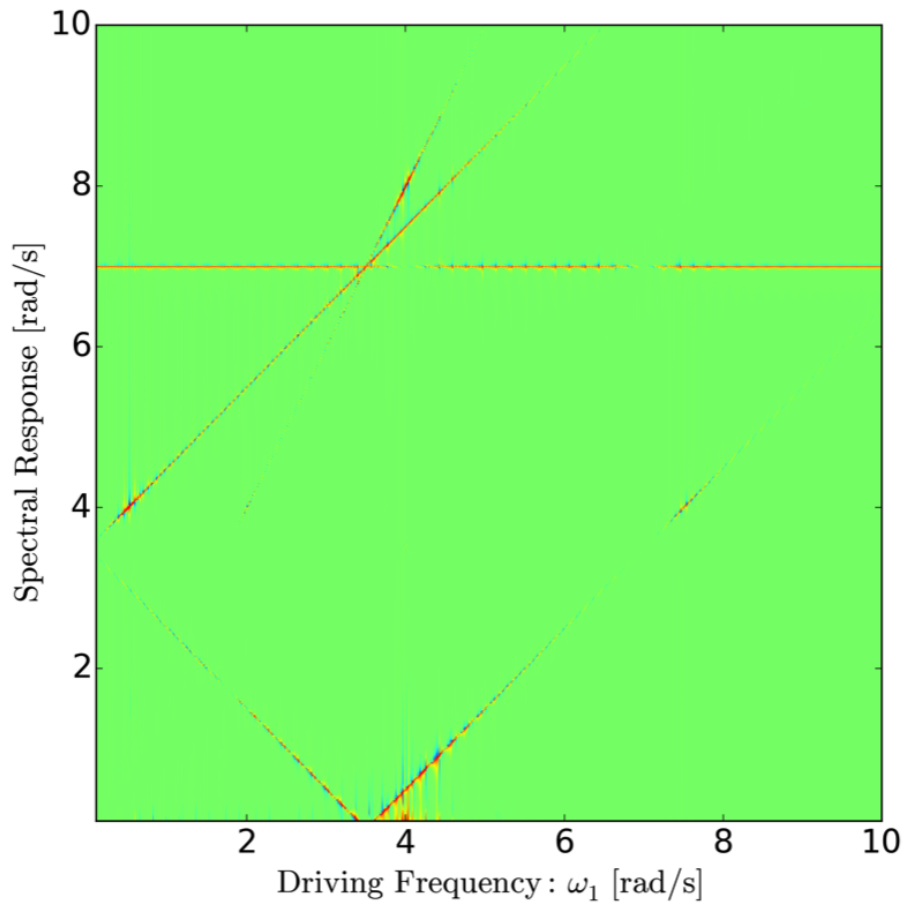


Figure 6.7: *Second-order response of anharmonic oscillator (1).* The data from a simulated harmonic oscillator are subtracted from the nonlinear anharmonic oscillator, to reveal the higher order response only.

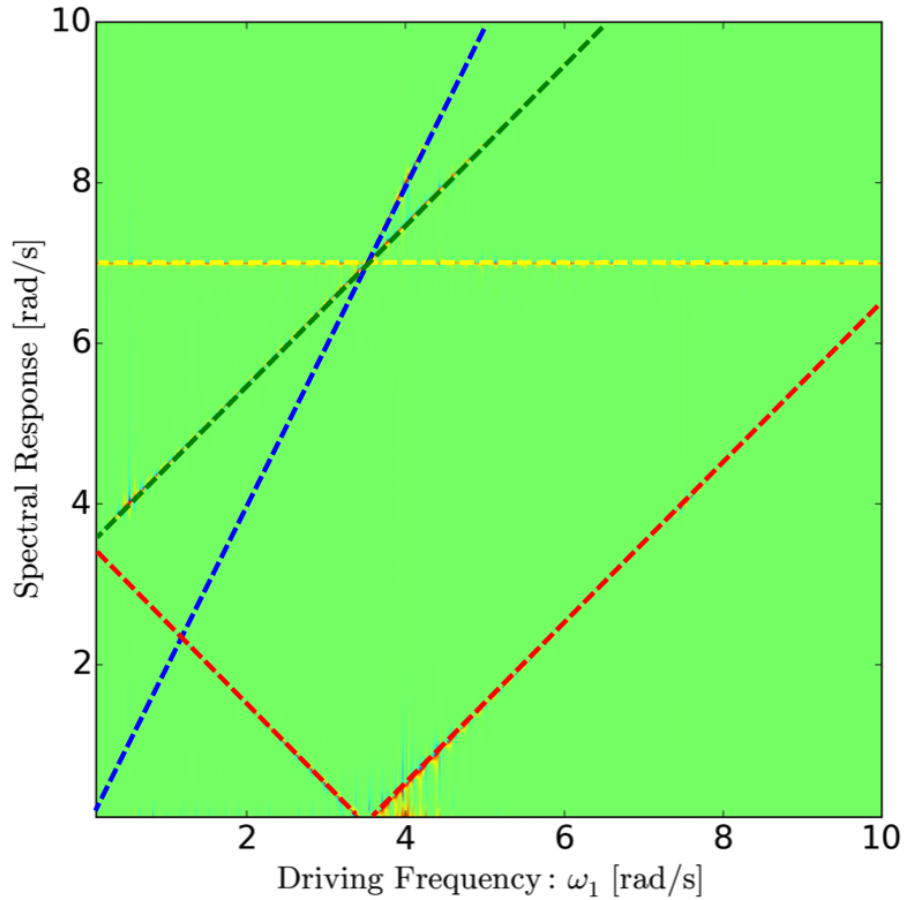


Figure 6.8: *Second-order response of anharmonic oscillator (2).* The data from a simulated harmonic oscillator are subtracted from the nonlinear anharmonic oscillator, to reveal the higher order response only. Colored lines represent different second-order response features: the second-harmonic response of ω_1 (blue line), the second-harmonic response of ω_2 (yellow line), the sum-frequency response of ω_1 and ω_2 (green line), and the difference-frequency response of ω_1 and ω_2 (red line).

Now, we wish to compare the simulated DFG amplitude with the calculation using Miller's rule, Eq. (6.20): $|x_{DFG}^{(2)}| = \frac{2a}{(B/2)} |x^{(1)}(\omega_1 - \omega_2)x^{(1)}(\omega_1)x^{(1)}(-\omega_2)|$. Note that the first-order response in this formula represents the amplitude of the system when driven at a single frequency—i.e., $x^{(1)}(\omega_1)$ is a solution to the equation of motion, Eq. (6.22), for $F(t) = \frac{B}{2} \cos(\omega_1 t)$. Thus, the first order response at frequency ω_1 is:

$$x^{(1)}(\omega_1) = \frac{B/2}{(\omega_0^2 - \omega_1^2 - i\gamma\omega_1)} \quad (6.23)$$

To obtain the first-order response from simulation, we simulate driving for $F(t) = \frac{B}{2} \cos(\omega t)$ and plot the spectral response diagram, as in Fig. 6.6. Then, the diagonal of this diagram, Fig. 6.9, represents the linear response, which we plot in Fig. 6.10 & 6.11, along with the above analytic formula, which matches the simulation, as expected.

We then plot the simulated DFG response from Fig. 6.7 along with the results given by Miller's rule, in both analytic and simulated form. This is shown in Fig. 6.12 & 6.13. The three results—second-order simulation, analytic Miller's rule, and simulated Miller's rule—agree extremely well, as expected.

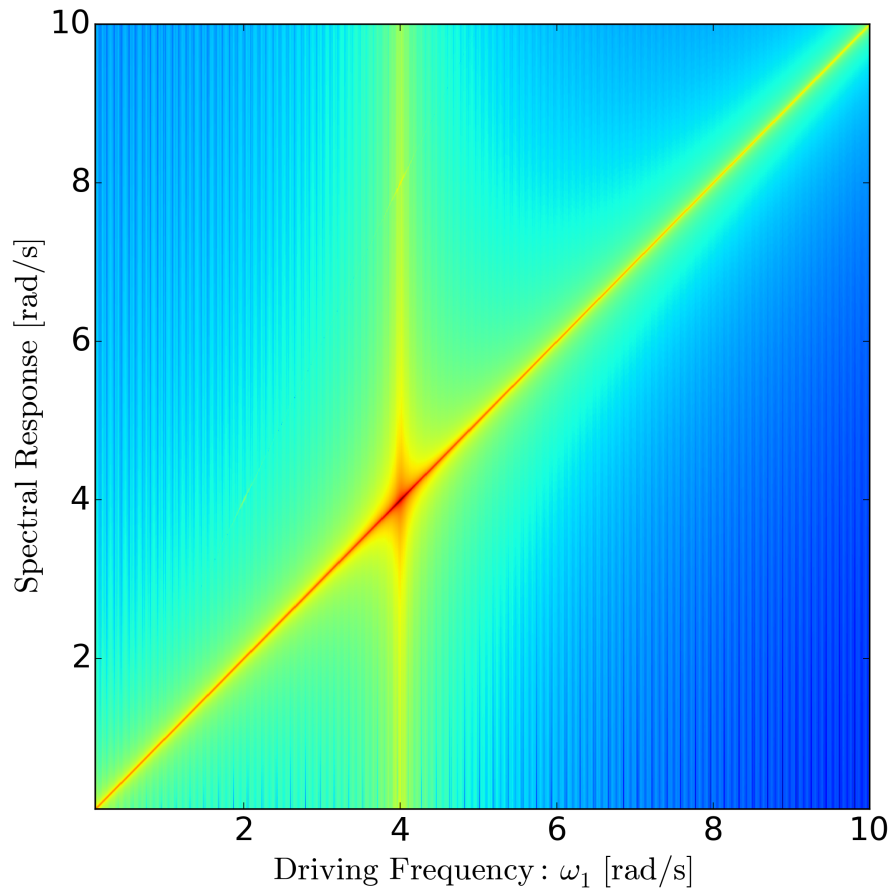


Figure 6.9: *Analytic vs. simulated linear response of anharmonic oscillator.* The blue data points are from simulation, and the black solid line is a fit to those points, based on the analytic formula.

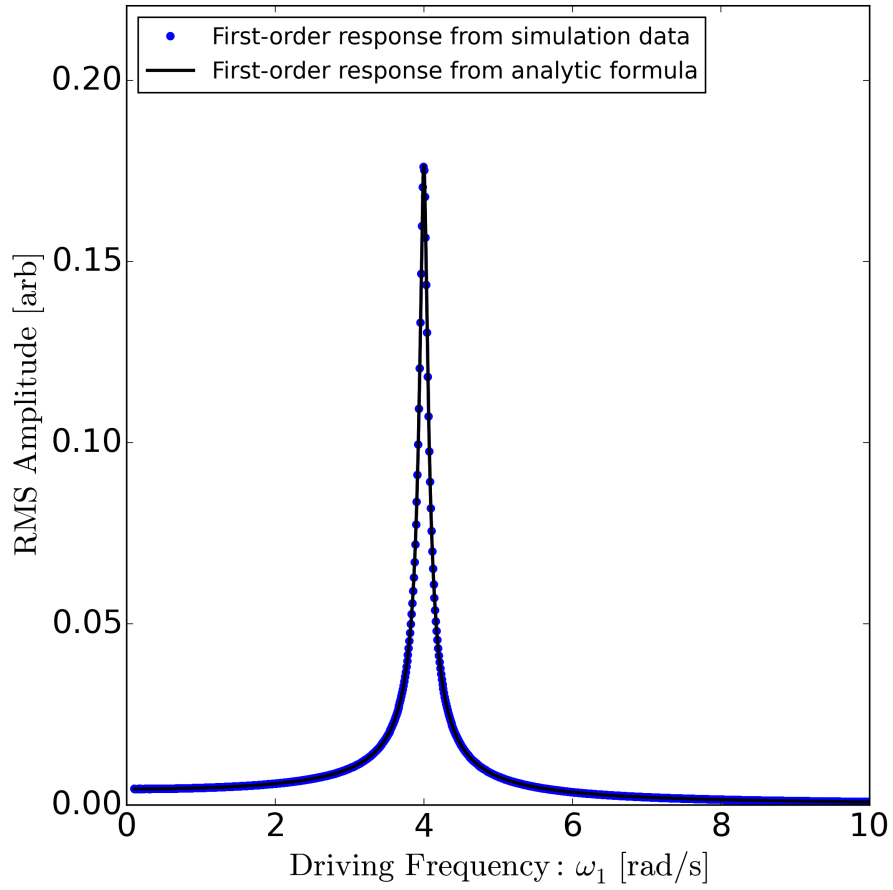


Figure 6.10: Comparison of simulated first-order response with analytic formula (1). The blue data points are from simulation, and the black solid line is a fit to those points, based on the analytic formula related to Eq. (6.23).

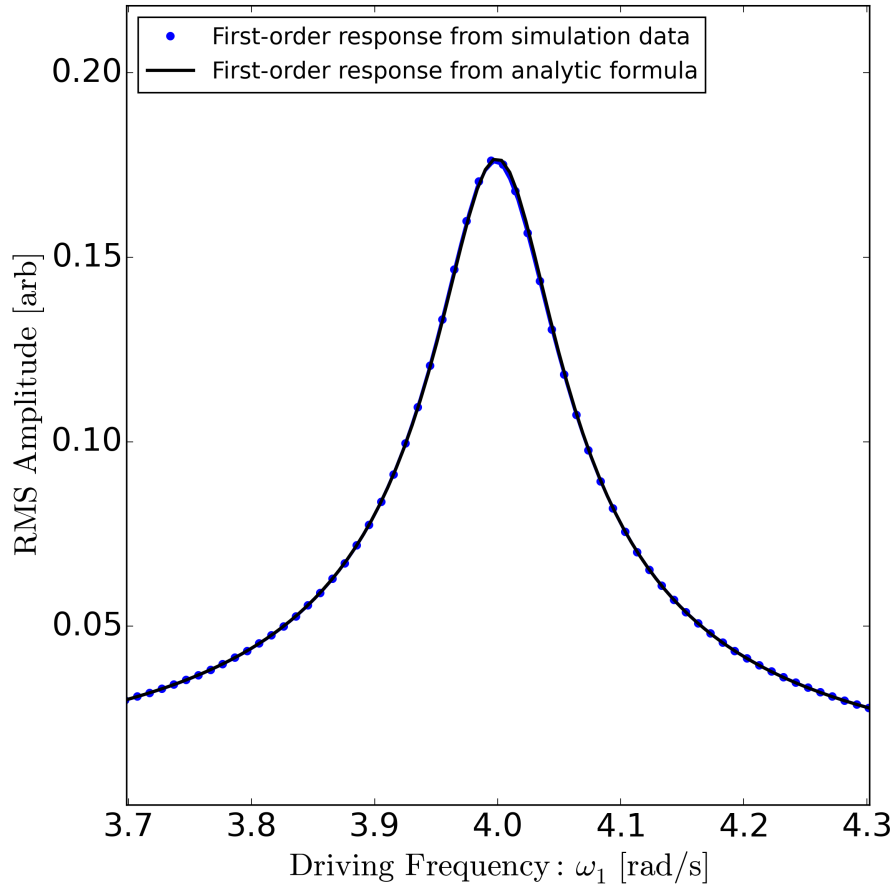


Figure 6.11: Comparison of simulated first-order response with analytic formula (2). The blue data points are from simulation, and the black solid line is a fit to those points, based on the analytic formula related to Eq. (6.23).

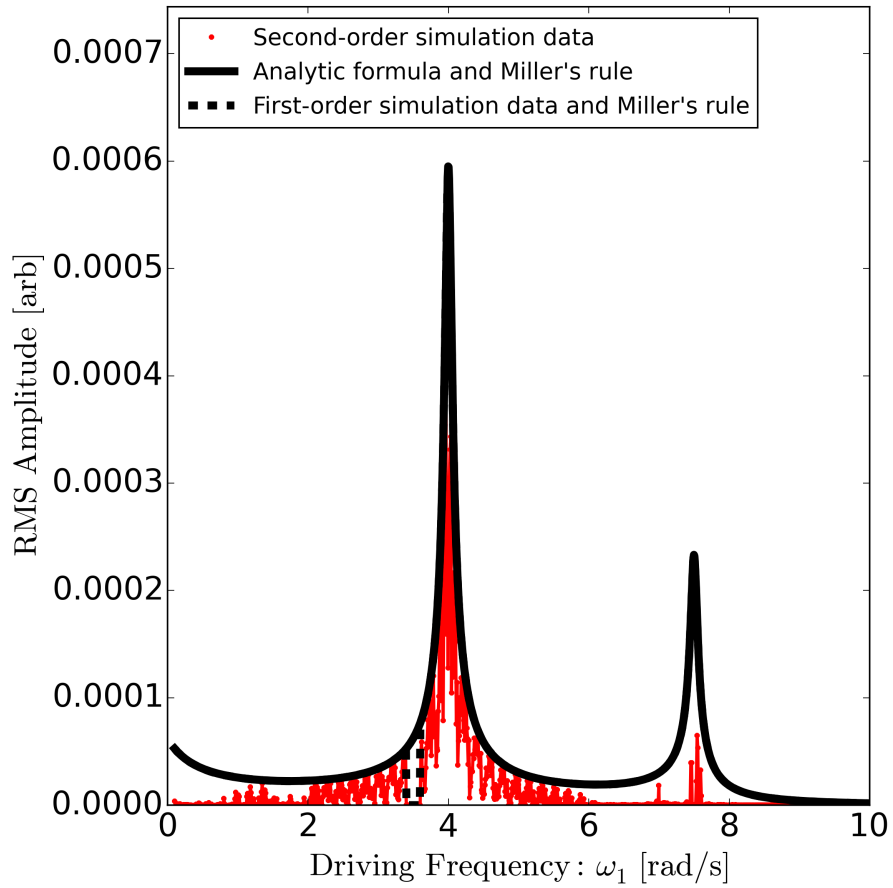


Figure 6.12: Comparison of simulated DFG response and Miller's rule (1). Red line is simulated second-order data (i.e., the red line from Fig. 6.8), black line is Miller's rule using first-order simulated data (i.e., from Fig. 6.10), and black solid line is Miller's rule using analytic formula Eq. (6.23).

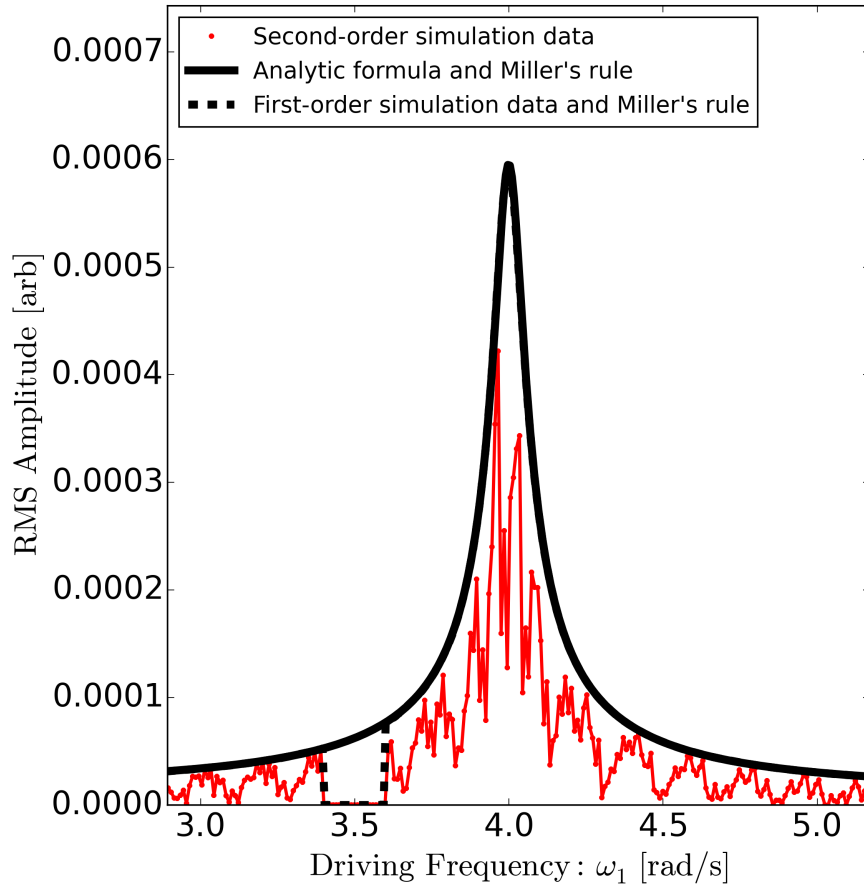


Figure 6.13: Comparison of simulated DFG response and Miller's rule (2). See previous figure for legend information.

There are 2 main features in the DFG response of Fig. 6.12, which can be understood by examining Miller's rule. The most prominent feature occurs when one of the driving frequencies is on-resonance with the system, in this case when $\omega_1 = \omega_0$ (4 rad/s). The second feature occurs when the difference-frequency is on-resonance with the system, in this case when $\omega_1 - \omega_2 = \omega_0$, i.e., when $\omega_1 = 7.5$ rad/s. Miller's rule not only yields the qualitative features of the second-order response, it also gives the amplitude. We note that the DFG amplitudes (simulated vs. Miller's rule) do not match exactly, which we attribute to non-ideality introduced by the Fourier transform of discrete data. The analytic amplitude fits the *envelope* of the simulated data. We emphasize that we have used the actual simulated first-order response data, thus demonstrating that analytic formulae for the dynamical response of the system need not be known, only the Miller relation that connects first- and second-order terms. Assuming $x^{(1)}$ can be measured or calculated, the only term that must be known is "a," the magnitude of the nonlinearity. We note that it is also possible to determine "a" from measurement of the first-order response as driving amplitude is varied (not presented here). This would then represent a *completely* first-order calculation of second-order effects.

We have established that Miller's rule provides a quantitative way to calculate the DFG response and we have compared theory with simulation for one fixed driving frequency, ω_2 . Now we calculate the DFG response for *all* possible values of ω_1 and ω_2 , using the analytical expression for Miller's rule. The purpose of this calculation is to examine the conditions when $|x_{DFG}^{(2)}|$ is maximized. Now, instead of a one-dimensional spectrum, $|x_{DFG}^{(2)}|$ is a surface in the parameter-space of ω_1 and ω_2 . To visualize this surface, consider that $|x_{DFG}^{(2)}|$ is represented in Fig. 6.6 by a line (i.e., the red line in Fig. 6.8). Now, when varying ω_2 , Fig. 6.6 can be represented as a slice in Fig. 6.14, and the line in Fig. 6.8 is now a surface in Fig. 6.14.

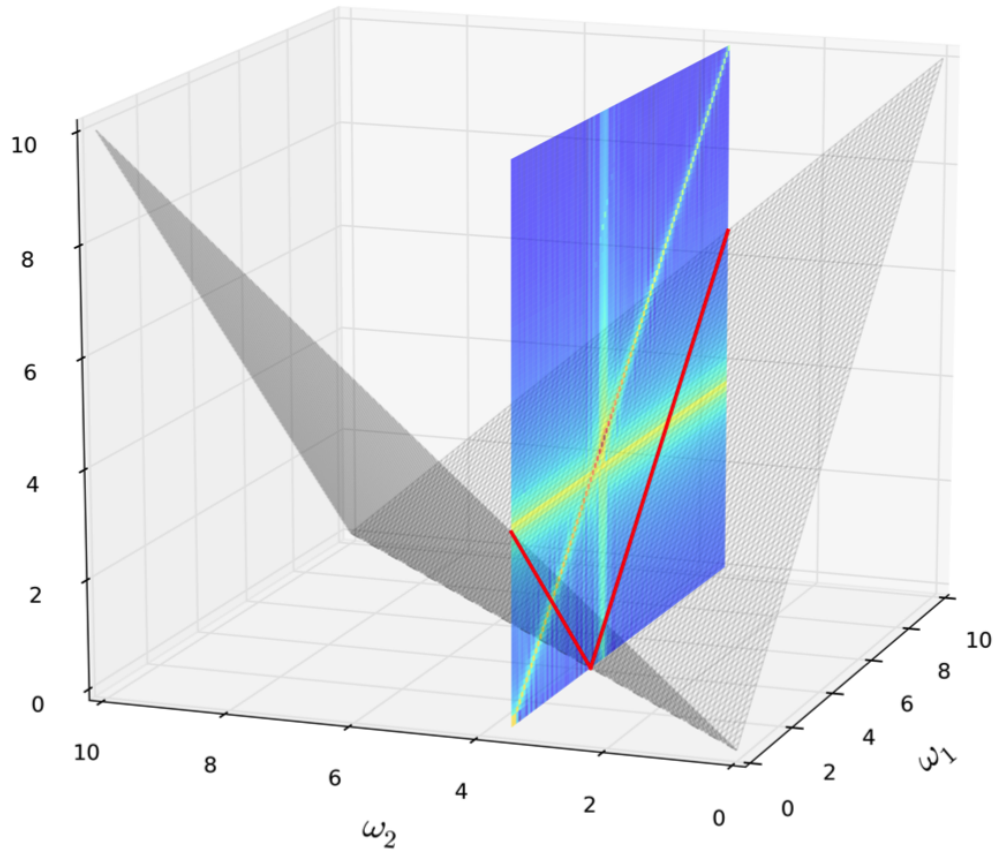


Figure 6.14: *3D parameter space of ω_1 , ω_2 and Fourier spectra.* The vertical slice indicates the simulation space that we have thus far considered, for fixed ω_2 (i.e., Fig. 6.6). The DFG response is represented by a red line on this slice (i.e., the red line in Fig. 6.8). When ω_2 is also varied, the DFG response will occur at the intersection of the vertical slice and the v-shaped plane (grey). The response is symmetric about the line $\omega_1 = \omega_2$.

Finally, Fig. 6.15 shows $|x_{DFG}^{(2)}|$, where the color intensity represents the amplitude of the DFG response in the parameter space of ω_1 and ω_2 , for $\omega_1 \geq \omega_2$. Also shown is the linear response of the system in the subplot, which has a resonance at $\omega_0 = 4$ rad/s, as stated previously. The white-dashed line in this parameter space represents the locus for a desired difference-frequency. For instance, it is set to the value 0.5 rad/s, indicating that frequency combinations falling on this locus will generate a DFG signal of 0.5 rad/s. *The primary finding of this plot is that DFG is maximized on resonance*, since the color intensity along the white dashed line is greatest when either $\omega_1 = \omega_0$ or $\omega_2 = \omega_0$. Intensity is also relatively higher when $\omega_1 - \omega_2 = \omega_0$, but this is far away from the desired difference-frequency. We also plot the response in this parameter space for a different resonance, $\omega_0 = 6$ rad/s in Fig. 6.16. Again, it is clear that *DFG will be maximized when either ω_1 or ω_2 are on resonance*.

We leave this chapter with the following questions, with a look towards generating DFG using a plasmonic particle: Is driving a particle on-resonance a sufficient condition for generating DFG? Is it possible to optimize DFG using multiple resonances? Are the resonant features all that matter, or are there other mechanisms to optimize? Ultimately, what is the theory that will yield answers to these questions?

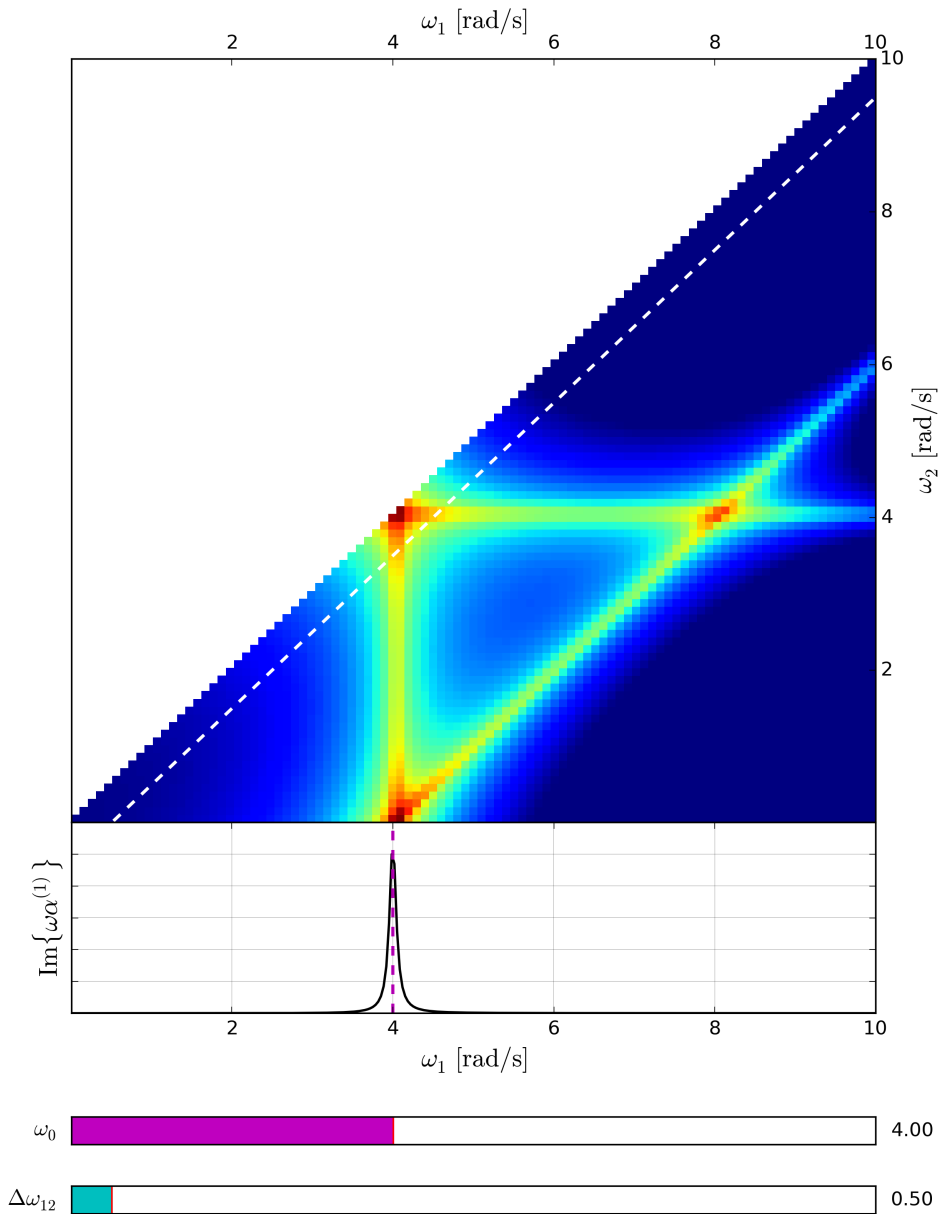


Figure 6.15: *DFG response for $\omega_2 \geq \omega_1$ and $\omega_0 = 4$ rad/s.* Color intensity represents the amplitude of $|x_{DFG}^{(2)}|$. The white-dashed line represents the specific condition $\omega_2 - \omega_1 = 0.5$ rad/s. Thus, the intensity along this line represents the strength of the DFG signal for $\omega_2 - \omega_1 = 0.5$ rad/s. The bottom plot represents the linear response of the system for $\omega_0 = 4$ rad/s.

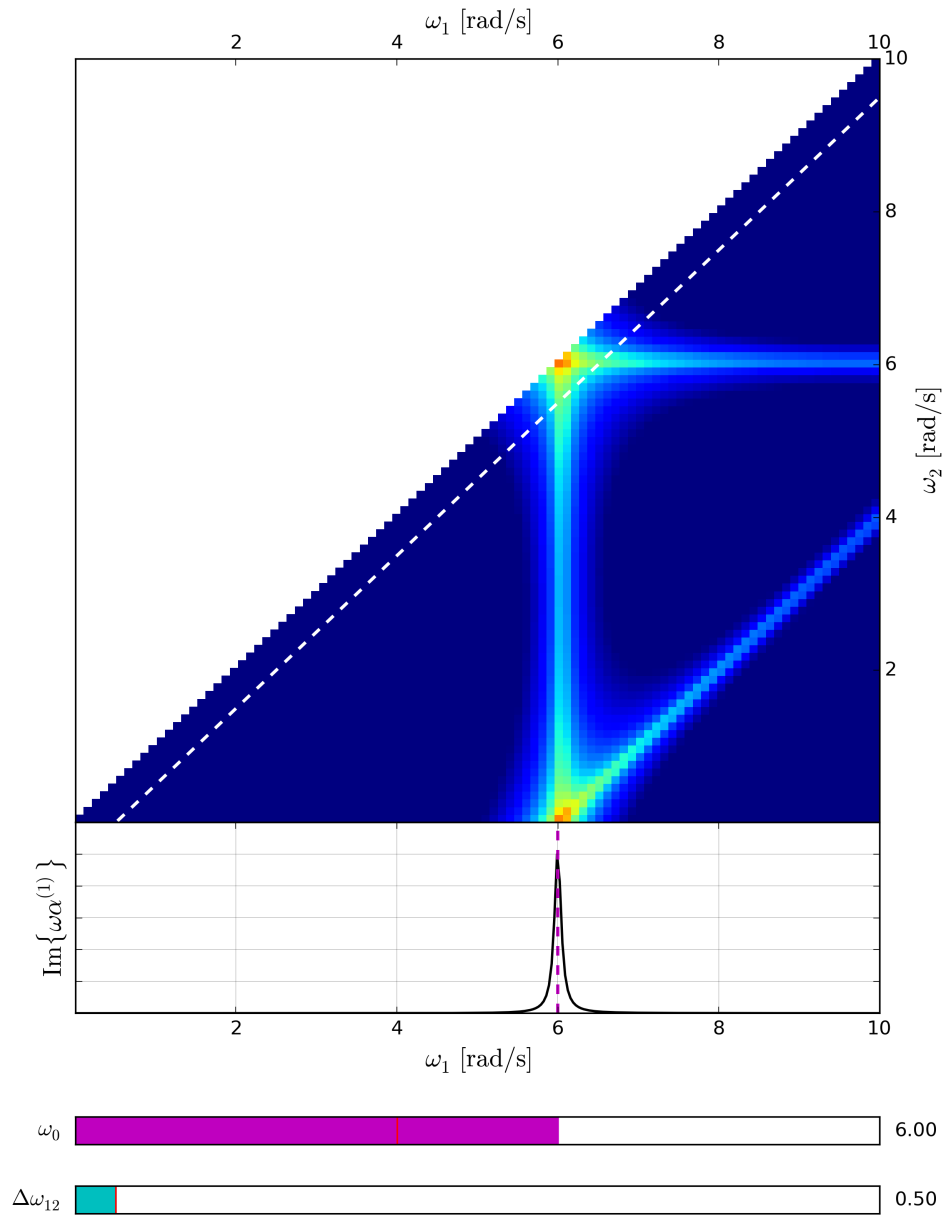


Figure 6.16: *DFG response for $\omega_2 \geq \omega_1$ and $\omega_0 = 6$ rad/s.* Same format as previous figure, but the linear resonance of the system is shifted to $\omega_0 = 6$ rad/s. This indicates that DFG is strongest when either $\omega_2 = \omega_0$ or $\omega_1 = \omega_0$, as expected.

CHAPTER 7

Effective Miller's Rule for Plasmonic DFG

We now consider the nonlinear behavior of plasmonic nanoparticles (PNPs), with the goal of optimizing DFG in such systems. We apply the eigenmode expansion proposed by Ref. [82] to a generic PNP and demonstrate that DFG can be enhanced due to the resonances of the structure. Specifically, when the PNP is resonant at both input frequencies and their difference, significant DFG can be achieved. This resonant coupling effect can be described by an effective Miller's rule for nonlinear plasmonic response, but the rule is modified from the standard formula. Through DFG, PNPs are capable of demodulating an amplitude-modulated signal, paving a new route to the control of light at the nanoscale. In the context of the previous chapters, we argue that plasmonic-DFG could be a useful way to target DNA at THz frequencies, *in vivo*, through the demodulation of high-frequency, more deeply penetrating signals (e.g., NIR).



7.1 Modal Model of Plasmonic Response

There is extensive literature regarding the study of second-order response phenomena in plasmonic systems. For instance, see Ref. [83] for a general review of nonlinear plasmonics. Much of the work has focused on understanding, measuring, and designing

second-harmonic generation (SHG) from plasmonic structures, e.g., see the review by Ref. [84], and generally there has been less focus on other second-order phenomena like difference-frequency generation (DFG). For instance, many fundamental studies of the nonlinearity of metal surfaces explicitly focused on SHG [85, 86, 87, 88, 89, 90]. From a theoretical perspective, there are a variety of approaches for studying SHG from plasmonic structures, including approaches which use a full, nonlinear wave equation [91, 92], those which model nonlinear response through a multipole expansion [93, 94, 95], those which use an eigenmode approach [82, 96], among other theoretical and numerical approaches [97, 98, 99, 100, 101].

It was our objective to find a universal framework for studying DFG in plasmonic nanoparticles (PNPs), in order to draw the most general conclusions. Our first avenue of inquiry was to find a Miller-like relation that describes the nonlinear response of PNPs using knowledge of the first-order response, as in the previous chapter. Modeling the second-order response, $\alpha^{(2)}$, in terms of the linear response, $\alpha^{(1)}$, is advantageous because the linear response of nanoscale plasmonic structures can be calculated straightforwardly via FDTD solvers, whereas the second-order response of such systems may not be calculated as readily. Even in cases where it might be simple to calculate $\alpha^{(2)}$ explicitly, it will still be useful to allow knowledge of $\alpha^{(1)}$ to lead design and optimization efforts, since the physical nature of $\alpha^{(1)}$ is probably better known. Ultimately, the route to optimization requires such a basis in physical understanding.

In the literature, it has been demonstrated that the second-order response of plasmonic nanostructures depends solely on first-order characteristics of the system (e.g., Ref. [102, 103]). But studies have refuted that Miller's rule, in the canonical form of Eq. (6.21), can be applied to the second-order response of plasmonic systems [84]. For instance, an experimental study explicitly showed that SHG from split-ring

resonators did not follow Miller’s rule [103]. Thus, we sought to determine if $\alpha^{(2)}$ could be expressed in terms of $\alpha^{(1)}$ in any possible way, if not in the canonical way.

To begin our investigation, we use the modal analysis framework of Zeng et al. [82] and then expand upon their derivation. The authors of Ref. [82] applied eigenmode analysis to the study of nonlinear plasmonic nanostructures and demonstrated that the nonlinear response could be expressed in terms of linear eigenmodes. They concluded that this formalism could be used to calculate the second-order response from the first-order response of a system, and they stressed that the eigenmodes, therefore, play an important role in optimizing nonlinear effects (specifically, they investigated SHG). Finally, they proposed a way to determine the eigenmodes of a system from Lorentzian fitting to simulation data (in the appendix of Ref. [82]).

We extend the study of Ref. [82] to investigate DFG. Furthermore, we extend their results to express a succinct, Miller-like relation between $\alpha^{(1)}$ and $\alpha^{(2)}$, and underscore a way in which first-order simulations can be used to calculate DFG by modeling $\alpha^{(1)}$ as a Lorentzian series. Our Lorentzian modeling is not borrowed from Ref. [82]—they use Lorentzian fitting to find eigenfrequencies only, and then use this information to find the eigenvectors from subsequent simulation. We *explicitly model* the linear response, $\alpha^{(1)}$, as a Lorentzian series, whose oscillator strengths implicitly depend on the eigenmodes of the system. Finally, we systematically explore how the characteristics of $\alpha^{(1)}$ affect $\alpha^{(2)}$ and thereby determine the constraints on DFG optimization.

To start, following Ref. [82], we make the basic assumption that Maxwell’s equations can be solved for the system under consideration (e.g., via FDTD solvers) and we assume that there exist eigenmodes of the system. The type of system that we are considering is a closed particle. Then the eigenvalue equation that describes the

system, in the absence of external fields, is [82]:

$$\mathcal{L}\mathbf{u} = \omega\mathbf{u} \quad (7.1)$$

where \mathbf{u} is the eigenvector of the system, containing information about the fields, ω is the frequency of the eigenmode (the eigenvalue), and \mathcal{L} is the operator that contains the relations between various field components, i.e., \mathcal{L} encapsulates Maxwell's equations (and auxiliary equations). Again, we refer to Appendix B for the complete set of Maxwell and auxiliary equations, and we refer to Ref. [82] for further details about this eigenvalue equation.

We now study the influence of a driving force on the system. External fields are represented by the vector \mathbf{S} , and the new eigenvalue equation is [82]:

$$\mathcal{L}\mathbf{U} + \mathbf{S} = \omega\mathbf{U} \quad (7.2)$$

where the vector \mathbf{U} now contains information about the *total* field response. At this point, it is useful to use *bra-ket* notation, noting that the spatial dependence can be defined as follows: $\mathbf{u}(\mathbf{r}) = \langle \mathbf{r} | \mathbf{u} \rangle$. Continuing to follow [82], we express the total field as an expansion of eigenstates of the unperturbed system:

$$|\mathbf{U}\rangle = \sum_m \frac{\langle \mathbf{u}_m^\dagger | \mathbf{S} \rangle}{\omega - \omega_m} |\mathbf{u}_m\rangle \quad (7.3)$$

As Ref. [82] describes, the quantity $\langle \mathbf{u}_m^\dagger | \mathbf{S} \rangle$ is the projection of the external excitation onto a given mode, which may be calculated via spatial integration (the closure relation), i.e.:

$$\langle \mathbf{u}_m^\dagger | \mathbf{S} \rangle = \int_{particle} \mathbf{u}_m(\mathbf{r}) \cdot \mathbf{S}(\mathbf{r}) dV \quad (7.4)$$

Let's consider, as in Ref. [82], how to calculate the main object of interest for this study, the electric polarizability. In previous chapters, we have treated the equation $p(t) = \alpha E(t)$ as a scalar relation, but α is really a tensor. Thus,

$$\mathbf{p}(\mathbf{r}) = \tilde{\boldsymbol{\alpha}} \cdot \mathbf{E}(\mathbf{r}) \quad (7.5)$$

and, polarization is related to polarizability by $\mathbf{P} = n\mathbf{p}$. In the new formalism that has been presented, the polarization is simply the “ \mathbf{P} -component” of $|\mathbf{U}\rangle$ [82]:

$$\mathbf{P}(\mathbf{r}) = \langle \mathbf{r} | \mathbf{U}^{\mathbf{P}} \rangle \quad (7.6)$$

Therefore,

$$\mathbf{P}(\mathbf{r}) \equiv \mathbf{U}^{\mathbf{P}}(\mathbf{r}) = \sum_m \frac{\langle \mathbf{u}_m^\dagger | \mathbf{S} \rangle}{\omega - \omega_m} \mathbf{u}_m^{\mathbf{P}}(\mathbf{r}) \quad (7.7)$$

At this point, we expand upon the work of Ref. [82] and go on to derive the explicit form of the polarizability, $\alpha_{ij}(\omega)$. If the source is an electric field, $\mathbf{S} = \mathbf{S}^{\mathbf{E}}$, then the inner product $\langle \mathbf{u}_m^\dagger | \mathbf{S} \rangle$ contains only electric field components, i.e., $\langle \mathbf{u}_m^\dagger | \mathbf{S} \rangle = \int \mathbf{u}_m^{\mathbf{E}\dagger}(\mathbf{r}) \cdot \mathbf{S}^{\mathbf{E}}(\mathbf{r}) dV$, where the integration is over the location of the PNP. Thus,

$$\mathbf{U}^{\mathbf{P}}(\mathbf{r}) = \sum_m \frac{\left[\int \mathbf{u}_m^{\mathbf{E}\dagger}(\mathbf{r}) \cdot \mathbf{S}^{\mathbf{E}}(\mathbf{r}) dV \right]}{\omega - \omega_m} \mathbf{u}_m^{\mathbf{P}}(\mathbf{r}) \quad (7.8)$$

Furthermore, we can suppose that $\mathbf{S}^{\mathbf{E}}(\mathbf{r}) = E_j(\mathbf{r}) \hat{j}$ for a polarized incident field, without loss of generality. Thus,

$$U_i^{\mathbf{P}}(\mathbf{r}) = \sum_m \frac{\left[\int u_{m,j}^{\mathbf{E}\dagger}(\mathbf{r}) E_j(\mathbf{r}) dV \right]}{\omega - \omega_m} u_{m,i}^{\mathbf{P}}(\mathbf{r}) \quad (7.9)$$

Now, we can also make the assumption that the structure is subwavelength, such that $E_j(\mathbf{r}) \approx E_j$ over the volume of the PNP. We explicitly require this condition. Since we have defined the integration to be over the region of the PNP, the equation becomes:

$$U_i^P(\mathbf{r}) = \sum_m \frac{E_j \left[\int u_{m,j}^{E^\dagger}(\mathbf{r}) dV \right]}{\omega - \omega_m} u_{m,i}^P(\mathbf{r}) \quad (7.10)$$

Then, by the definition $P_i = \alpha_{ij} E_j$, we can solve for α_{ij} :

$$\begin{aligned} \alpha_{ij} &= \frac{\int U_i^P(\mathbf{r}) dV}{E_j} \\ &= \sum_m \frac{\left[\int u_{m,j}^{E^\dagger}(\mathbf{r}) dV \right]}{\omega - \omega_m} \left[\int u_{m,i}^P(\mathbf{r}) dV \right] \\ &= \sum_m \alpha_{ij}^m \end{aligned} \quad (7.11)$$

where we have defined,

$$\alpha_{ij}^m \equiv \frac{\left[\int u_{m,j}^{E^\dagger}(\mathbf{r}) dV \right]}{\omega - \omega_m} \left[\int u_{m,i}^P(\mathbf{r}) dV \right] \quad (7.12)$$

Now, to investigate higher order terms in a perturbative expansion, the eigenvalue equation can be expanded to orders of the driving field (as in Ref. [82]):

$$\mathcal{L}\mathbf{U}^{(n)} + \mathbf{S}^{(n)} = \omega\mathbf{U}^{(n)} \quad (7.13)$$

then, the corresponding eigenvector expansion is:

$$|\mathbf{U}^{(n)}\rangle = \sum_m \frac{\langle \mathbf{u}_m^\dagger | \mathbf{S}^{(n)} \rangle}{\omega - \omega_m} |\mathbf{u}_m\rangle \quad (7.14)$$

Zeng et al. [82] used the above expansion to study SHG. We extend their derivation, using our result from Eq. (7.11) to express $\alpha_{SHG}^{(2)}$ in terms of $\alpha^{(1)}$, then we address DFG.

The SHG response is defined as,

$$|\mathbf{U}^{(2)}(2\omega)\rangle = \sum_m \frac{\langle \mathbf{u}_m^\dagger | \mathbf{S}^{(2)}(2\omega) \rangle}{2\omega - \omega_m} |\mathbf{u}_m\rangle \quad (7.15)$$

where Zeng et al. [82] express $|\mathbf{S}^{(2)}(2\omega)\rangle$ in terms of the lower order fields, through the action of the nonlinear operator $\widehat{\beta}$:

$$\begin{aligned} |\mathbf{S}^{(2)}(2\omega)\rangle &= \widehat{\beta} |\mathbf{U}^{(1)}(\omega) \mathbf{U}^{(1)}(\omega)\rangle \\ &= \sum_l \sum_n \frac{\langle \mathbf{u}_l^\dagger | \mathbf{S}^{(1)}(\omega) \rangle}{\omega - \omega_l} \frac{\langle \mathbf{u}_n^\dagger | \mathbf{S}^{(1)}(\omega) \rangle}{\omega - \omega_n} \widehat{\beta} |\mathbf{u}_l \mathbf{u}_n\rangle \end{aligned} \quad (7.16)$$

Zeng et al. [82] define χ as the nonlinear operator, but we use a different variable to avoid confusion with the typical definition of material response. The operator $\widehat{\beta}$ needs to be calculated/simulated explicitly—it is the object which encapsulates nonlinear effects in the system. It is apparent that all second order terms would vanish if $\widehat{\beta} = 0$. Plugging the above expression, Eq. (7.16), into Eq. (7.15) yields:

$$|\mathbf{U}^{(2)}(2\omega)\rangle = \sum_{lmn} \frac{\langle \mathbf{u}_l^\dagger | \mathbf{S}^{(1)}(\omega) \rangle}{\omega - \omega_l} \frac{\langle \mathbf{u}_n^\dagger | \mathbf{S}^{(1)}(\omega) \rangle}{\omega - \omega_n} \frac{\langle \mathbf{u}_m^\dagger | \widehat{\beta} | \mathbf{u}_l \mathbf{u}_n \rangle}{2\omega - \omega_m} |\mathbf{u}_m\rangle \quad (7.17)$$

At this point, again, we diverge from Ref. [82] and go on to derive $\alpha_{SHG}^{(2)}$. Since $P_i^{(2)} = \alpha_{ij}^{(2)} E_j^2$, we first obtain $U_i^{P(2)}$ using the same reasoning as for the derivation of Eq. (7.10):

$$U_i^{P(2)}(\mathbf{r}, 2\omega) = \sum_{lmn} E_j^2 \frac{\left[\int u_{l,j}^{E^\dagger}(\mathbf{r}) dV \right]}{\omega - \omega_l} \frac{\left[\int u_{n,j}^{E^\dagger}(\mathbf{r}) dV \right]}{\omega - \omega_n} \frac{\langle \mathbf{u}_m^\dagger | \widehat{\beta} | \mathbf{u}_l \mathbf{u}_n \rangle}{2\omega - \omega_m} u_{m,i}^P(\mathbf{r}) \quad (7.18)$$

Next, we use the relation $\alpha_{ijj}^{(2)}(2\omega) = [\int U_i^{P(2)}(\mathbf{r}, 2\omega)dV]/E_j^2$ to solve for $\alpha_{ijj}^{(2)}(2\omega)$:

$$\begin{aligned}
\alpha_{ijj}^{(2)}(2\omega) &= \sum_{lmn} \frac{[\int u_{l,j}^{E\dagger}(\mathbf{r})dV]}{(\omega - \omega_l)} \frac{[\int u_{n,j}^{E\dagger}(\mathbf{r})dV]}{(\omega - \omega_n)} \frac{[\int u_{m,i}^P(\mathbf{r})dV]}{(2\omega - \omega_m)} \langle \mathbf{u}_m^\dagger | \widehat{\beta} | \mathbf{u}_l \mathbf{u}_n \rangle \\
&= \sum_{lmn} \alpha_{ij}^{(1),l}(\omega) \alpha_{ij}^{(1),n}(\omega) \alpha_{ij}^{(1),m}(2\omega) \frac{\langle \mathbf{u}_m^\dagger | \widehat{\beta} | \mathbf{u}_l \mathbf{u}_n \rangle}{\Gamma_{l,i}^P \Gamma_{n,i}^P \Gamma_{m,j}^{E\dagger}} \\
&= \sum_{lmn} \alpha_{ij}^{(1),l}(\omega) \alpha_{ij}^{(1),n}(\omega) \alpha_{ij}^{(1),m}(2\omega) \beta_{ij}^{lmn}
\end{aligned} \tag{7.19}$$

where $\alpha^{(1)}$ terms are as defined in Eq. (7.12), and we have created the definitions $\Gamma_{n,i}^P \equiv \int u_{n,i}^P(\mathbf{r})dV$, etc., and $\beta_{ij}^{lmn} \equiv \frac{\langle \mathbf{u}_m^\dagger | \widehat{\beta} | \mathbf{u}_l \mathbf{u}_n \rangle}{\Gamma_{l,i}^P \Gamma_{n,i}^P \Gamma_{m,j}^{E\dagger}}$. Thus, this modal analysis has yielded a relation between first and second-order terms, similar to Miller's rule for second-harmonic generation, which, in its usual form, states $\alpha^{(2)}(2\omega) \propto \alpha^{(1)}(2\omega) [\alpha^{(1)}(\omega)]^2$. However, in the derivation above, we have found that $\alpha_{ijj}^{(2)}(2\omega)$ is equal to a sum over modal contributions with weights given by the modal overlap term, β_{ij}^{lmn} . This is in contrast to Miller's rule, where all weights are equivalent, i.e., $\alpha_{ijj, \text{Miller}}^{(2)}(2\omega) = \beta \alpha_{ij}^{(1)}(2\omega) [\alpha_{ij}^{(1)}(\omega)]^2$.

We can extend this derivation to the DFG second-order term by assuming that, in the presence of two driving frequencies, ω_1 and ω_2 , the second-order source term has the following form:

$$|\mathbf{S}^{(2)}(\omega_1 - \omega_2)\rangle = \widehat{\beta} |\mathbf{U}^{(1)}(\omega_1) \mathbf{U}^{(1)}(-\omega_2)\rangle \tag{7.20}$$

then, the result is:

$$\alpha_{ijk}^{(2)}(\omega_1 - \omega_2) = \sum_{lmn} \alpha_{ij}^{(1),l}(\omega_1) \alpha_{jk}^{(1),n}(-\omega_2) \alpha_{ik}^{(1),m}(\omega_1 - \omega_2) \beta_{ijk}^{lmn} \tag{7.21}$$

where $\beta_{ijk}^{lmn} \equiv \frac{\langle \mathbf{u}_m^\dagger | \widehat{\beta} | \mathbf{u}_l \mathbf{u}_n \rangle}{\Gamma_{l,i}^P \Gamma_{n,j}^P \Gamma_{m,k}^{E\dagger}}$. *This is the main result of this section.* We propose that it is possible to express the DFG response of a PNP in terms of its first-order po-

larizability. However, the relation is not a simple product of polarizabilities, as the classical Miller’s rule might suggest. Rather, the distinct modes of the system contribute an amount that is weighted by the nonlinear, modal-overlap coefficient, β_{ijk}^{lmn} . The authors of Ref. [82] suggested a similar conclusion for SHG, but they did not ultimately relate the second-order polarizability to first-order polarizabilities.

Our form of Zeng’s modal model immediately suggests the following possibility—one may simulate $\alpha_{ij}^{(1)}$ from scattering calculations and, after decomposing it as $\alpha_{ij}^{(1)} = \sum_m \alpha_{ij}^{(1),m}$, quite readily calculate the structure of $\alpha_{ijk}^{(2)}$. However, it is additionally necessary to calculate β_{ijk}^{lmn} terms in such a simulation, which involves explicit modeling of the nonlinearity $\hat{\beta}$. Thus, knowledge of $\alpha_{ij}^{(1)}$ is *not entirely sufficient* for predicting $\alpha_{ijk}^{(2)}$.

Importantly, one may use Eq. (7.21) to guide the design of a PNP with specific DFG properties. For instance, it is apparent that a particle should include 3 resonances in order to have the strongest DFG response: a resonance at each driving frequency and a resonance at the difference frequency. Using this design constraint, one may endeavor to maximize the β_{ijk}^{lmn} terms that contribute to this response. However, it is also possible to have DFG from a bi-resonant structure, but necessarily at lower amplitude. We explore these possibilities in the next section.

Based on the results of this section, we summarize the following findings regarding plasmonic-DFG in the modal-model:

1. Results of first-order simulations, i.e., $\alpha^{(1)}$, are useful for determining the possible behavior of DFG from a subwavelength PNP.
2. In order to maximize DFG, a PNP should exhibit 3 resonances, one at each driving frequency and another at the difference frequency.
3. The magnitude of the DFG response depends on the coupling between the 3 modes that are involved in the process. This coupling (or “modal overlap”)

represents the strength of the nonlinearity. The “modal overlap” is a quantity that can likely be calculated in COMSOL or other FDTD solvers.

7.2 Optimization of Difference Frequency Generation

In this section, we wish to illustrate our findings and explore other possible phenomena resulting from Eq. (7.21) by modeling DFG from a generic plasmonic particle with three resonances. We leave the physical realization of this particle to be determined, so do not specify a geometry—rather, we treat this investigation as a thought experiment. As an idealization, we consider a one-dimensional type model, where our two incident sources and the resultant DFG are all polarized along the same direction. Thus, we can drop the subscripts in Eq. (7.21) and use the form:

$$\alpha^{(2)}(\omega_1 - \omega_2) = \sum_{lmn} \alpha^{(1),l}(\omega_1) \alpha^{(1),n}(\omega_2) \alpha^{(1),m}(\omega_1 - \omega_2) \beta^{lmn} \quad (7.22)$$

We define a triply resonant linear response, $\alpha^{(1)}(\omega) = \sum_{m=a,b,c} \alpha^{(1),m}(\omega)$, where $\alpha^{(1),m}(\omega) = f_m / (\omega_m^2 - \omega^2 - i\gamma_m\omega)$ is a Lorentzian oscillator with resonant frequency ω_m and oscillator strength f_m , where a , b , and c are the modes of the particle—this Drude-Lorentz model, mentioned in Chapter 3, is a common way to describe the response of plasmonic resonators. We allow the oscillator strengths, f_m , and the coupling strengths, β^{lmn} , to range from 0 to a normalized value of 1. In this way, we vary which resonances and coupling terms are “turned on” in the subsequent analysis.

Now we plot, in Fig. 7.1, the difference-frequency response of the system for all values of ω_1 and ω_2 in the half-parameter space below the diagonal. As in the previous chapter, we do not plot the values in the upper diagonal space since the

plot has mirror symmetry across the $\omega_1 = \omega_2$ line. The color intensity represents the amplitude of the DFG response, $|\alpha_{DFG}^{(2)}|$, on a log-scale. We plot the linear response, $\text{Im}\{\omega\alpha^{(1)}\}$, which is proportional to the absorption cross-section, in the middle portion of the figure, as well as values for the resonance frequencies ω_a , ω_b , and ω_c , and their respective oscillator strengths, f_a , f_b , and f_c . Also shown are various parameter settings for the modal interactions, β^{lmn} , indicated in the lower portion of the plot by bars with numeric values.

Two lines and an annulus are drawn on the DFG intensity plot in order to aid the eye. The black-dashed lines represent the driving frequencies, ω_1 and ω_2 , which may be set by the user. The annulus is the intersection of these frequencies, where DFG will occur for the chosen driving frequencies. The DFG frequency, $\Delta\omega_{12} = |\omega_1 - \omega_2|$, is shown in the legend of the figure.

In Fig. 7.1, we initially set the driving frequencies to $\omega_1 = 0.80$ and $\omega_2 = 0.90$ (all units in rad/s). Thus, the DFG frequency is $\Delta\omega_{12} = 0.10$. We set the resonances of the particle to match the driving frequencies and difference frequency: $\omega_a = 0.90$, $\omega_b = 0.80$, and $\omega_c = 0.10$. We set all oscillator strengths to 1 and only keep coupling terms that contribute significantly to DFG.

Fig. 7.1 demonstrates the most significant result from our analysis, that the DFG response is maximized for a system with three resonances when the system is driven at two high-frequency resonances and when the third resonance of the system is tuned to the difference frequency. This is seen from the maximum intensity, which occurs in the annulus, which is the region of parameter-space associated with DFG at 0.1 THz. Thus, we have the following conditions: $\omega_a = \omega_2$, $\omega_b = \omega_1$, and $\omega_c = \Delta\omega_{12}$. Additionally, we can see that only a small number of coupling terms dominate the strength of the response. In this case, all coupling terms are turned off except for the terms responsible for the strong DFG response.

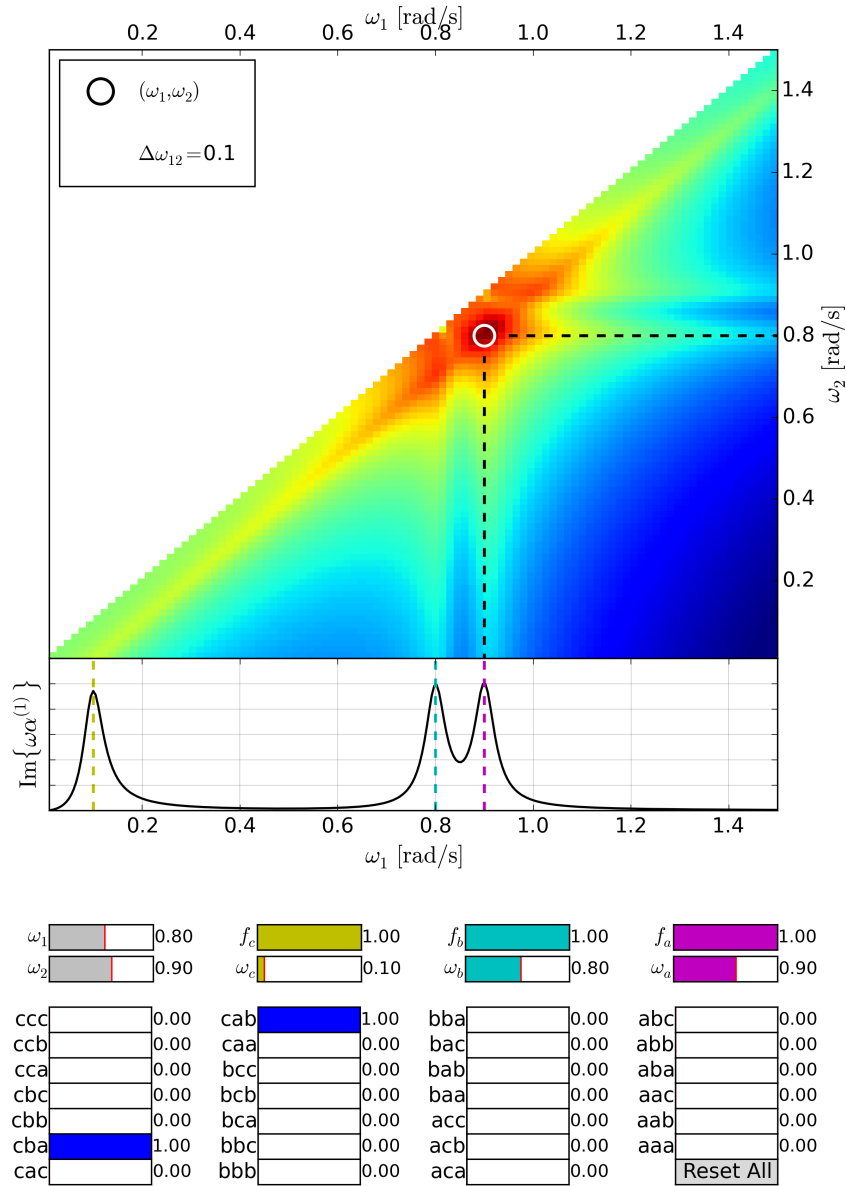


Figure 7.1: DFG from PNP model with three resonances (1). The idealized modal model is shown, where the particle has three resonances and the lowest frequency resonance is at the difference-frequency of the two higher frequency resonances: $\omega_a - \omega_b = \omega_c$. The half-parameter space is shown for the two driving frequencies ω_1 and ω_2 , where the color intensity shows the magnitude of DFG on a log-scale. The lower plot shows the linear response of the system, $\text{Im}\{\omega\alpha^{(1)}\}$. The bars in the lower portion of the figure indicate parameter settings, for instance the coupling parameters that ensure maximal DFG are the “cba” and “cab” terms.

We now vary the parameters and report what happens. The parameter variations and results are as follows:

- Fig. 7.2: Compared to Fig. 7.1, the first driving frequency is changed to $\omega_1 = 1.19$, and DFG will occur at $\Delta\omega_{12} = 0.29$. Since the resonances of the system are at their previous setting, $\omega_a = 0.90$, $\omega_b = 0.80$, and $\omega_c = 0.10$, the DFG amplitude is not maximized within the annulus.
- Fig. 7.3: Compared to Fig. 7.2, the second resonance of the system is changed such that $\omega_b = 1.19$. DFG is enhanced, but not yet maximized.
- Fig. 7.4: Compared to Fig. 7.3, the third resonance of the system is changed such that $\omega_c = 0.29$. DFG is maximized since the system exhibits resonances at the driving frequencies and their difference.
- Fig. 7.5: Compared to Fig. 7.4, the oscillator strength of resonance c is decreased. Consequently, the DFG amplitude also decreases.
- Fig. 7.6: Compared to Fig. 7.5, the oscillator strength of resonance c is set to zero. The DFG response is now only possible when other coupling terms are active. Specifically, the terms aba and bba lead to enhanced DFG.
- Fig. 7.7: Compared to Fig. 7.6, the oscillator strength of resonance b is decreased. Consequently, the DFG amplitude also decreases.
- Fig. 7.8: Compared to Fig. 7.7, the oscillator strength of resonance b is set to zero. The DFG response is now only possible when the coupling term aaa is active.
- Fig. 7.9: Compared to Fig. 7.1, the third resonance of the system is changed such that $\omega_c = 0.50$. The DFG amplitude is no longer maximized, since $\omega_c \neq \Delta\omega_{12}$.

- Fig. 7.10: Compared to Fig. 7.1, the second resonance of the system is changed such that $\omega_b = 0.51$. The DFG amplitude is no longer maximized, since both resonances of the system do not coincide with both driving frequencies, i.e., $(\omega_a, \omega_b) \neq (\omega_1, \omega_2)$.
- Fig. 7.11: Compared to Fig. 7.10, the first driving frequency is changed such that $\omega_1 = 0.51$. Now two resonances of the system coincide with the driving frequencies, i.e., $(\omega_a, \omega_b) = (\omega_1, \omega_2)$, but DFG is still not maximized since $\omega_c \neq \Delta\omega_{12}$.
- Fig. 7.12: Compared to Fig. 7.1, the first resonance of the system is changed such that $\omega_a = 1.26$. The DFG amplitude is no longer maximized, since both resonances of the system do not coincide with both driving frequencies, i.e., $(\omega_a, \omega_b) \neq (\omega_1, \omega_2)$.
- Fig. 7.13: Compared to Fig. 7.12, the second driving frequency is changed such that $\omega_2 = 1.25$. Now two resonances of the system coincide (approximately) with the driving frequencies, i.e., $(\omega_a, \omega_b) = (\omega_1, \omega_2)$, but DFG is still not maximized since $\omega_c \neq \Delta\omega_{12}$.
- Fig. 7.14: Compared to Fig. 7.1, all coupling terms are now active. When all coupling parameters are equal, the modal model reduces to the classical Miller's rule.
- Fig. 7.15: Compared to Fig. 7.14, the coupling terms cba and cab are deactivated. The DFG response decreases, indicating that these terms are responsible for significant DFG amplitude.

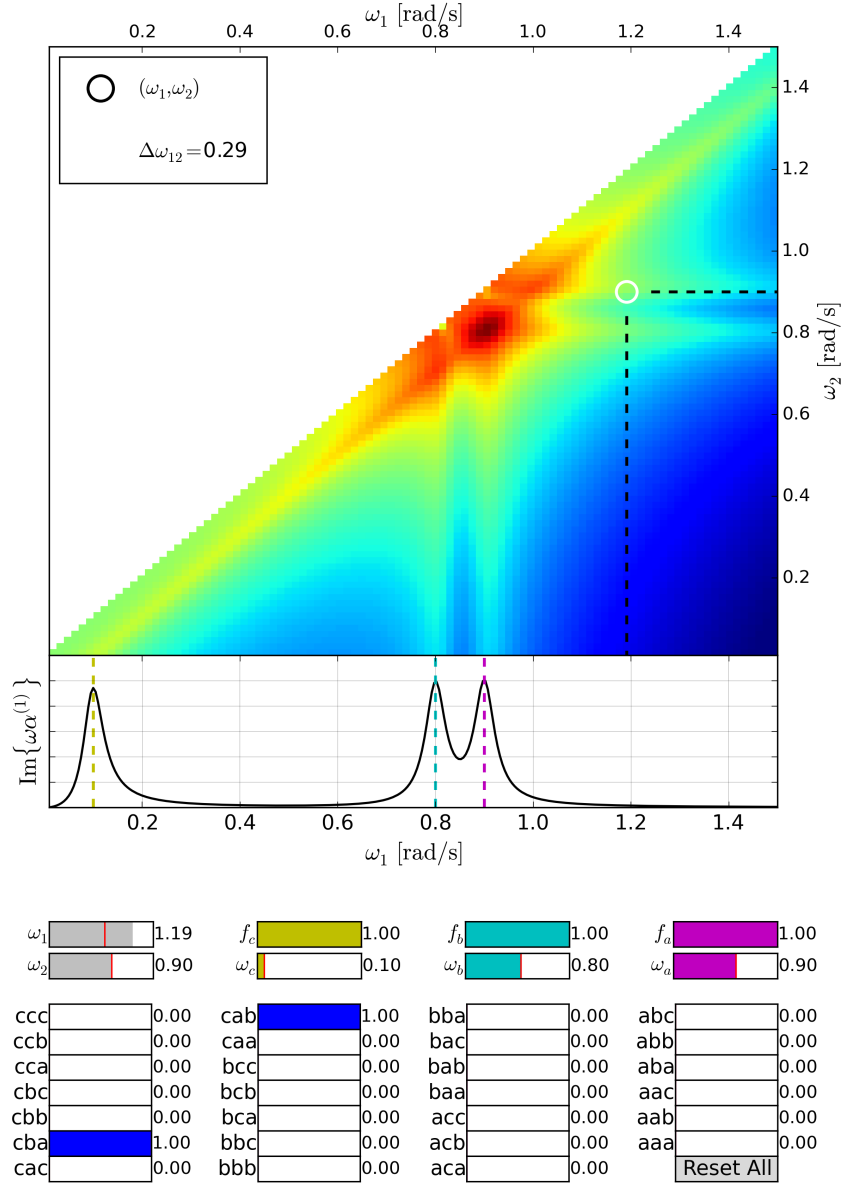


Figure 7.2: DFG from PNP model with three resonances (2). Compared to Fig. 7.1, the first driving frequency is changed to $\omega_1 = 1.19$, and DFG will occur at $\Delta\omega_{12} = 0.29$. Since the resonances of the system are at their previous setting, $\omega_a = 0.90$, $\omega_b = 0.80$, and $\omega_c = 0.10$, the DFG amplitude is not maximized.

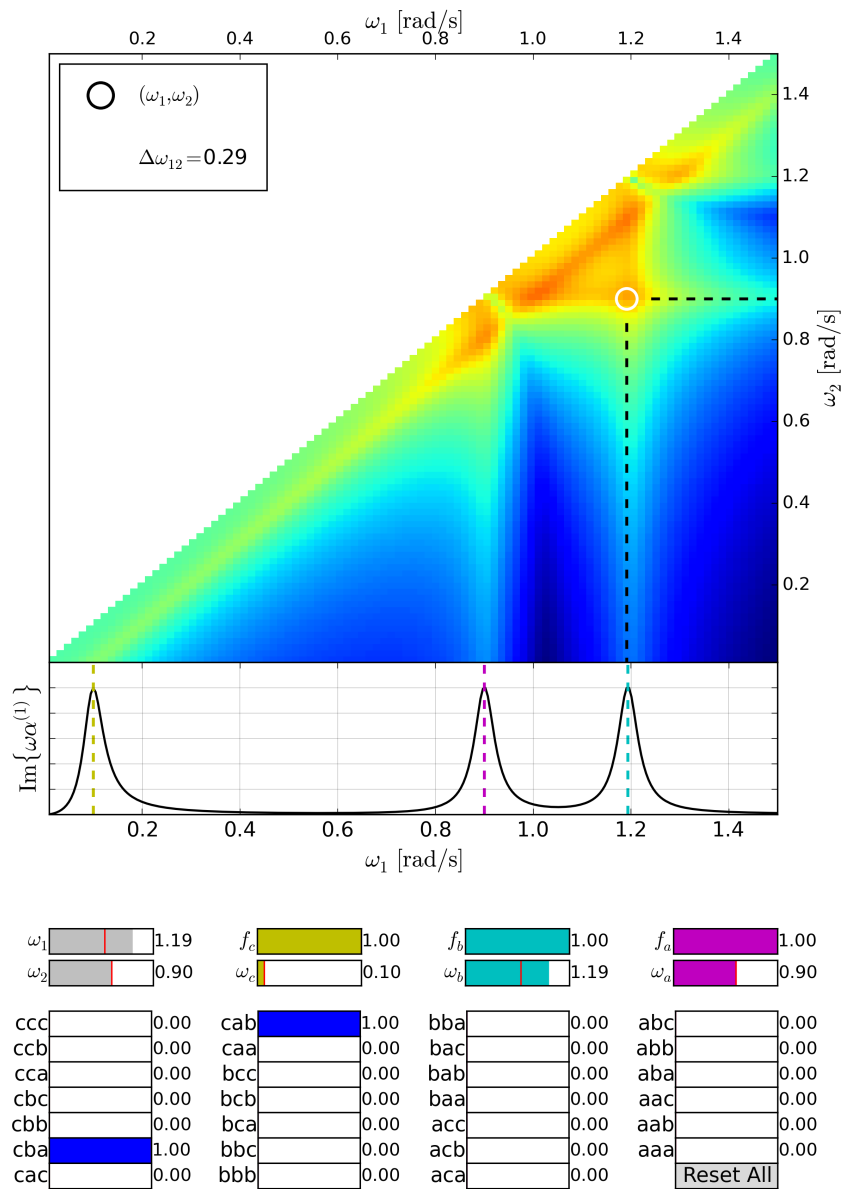


Figure 7.3: DFG from PNP model with three resonances (3). Compared to Fig. 7.2, the second resonance of the system is changed such that $\omega_b = 1.19$. DFG is enhanced, but not yet maximized.

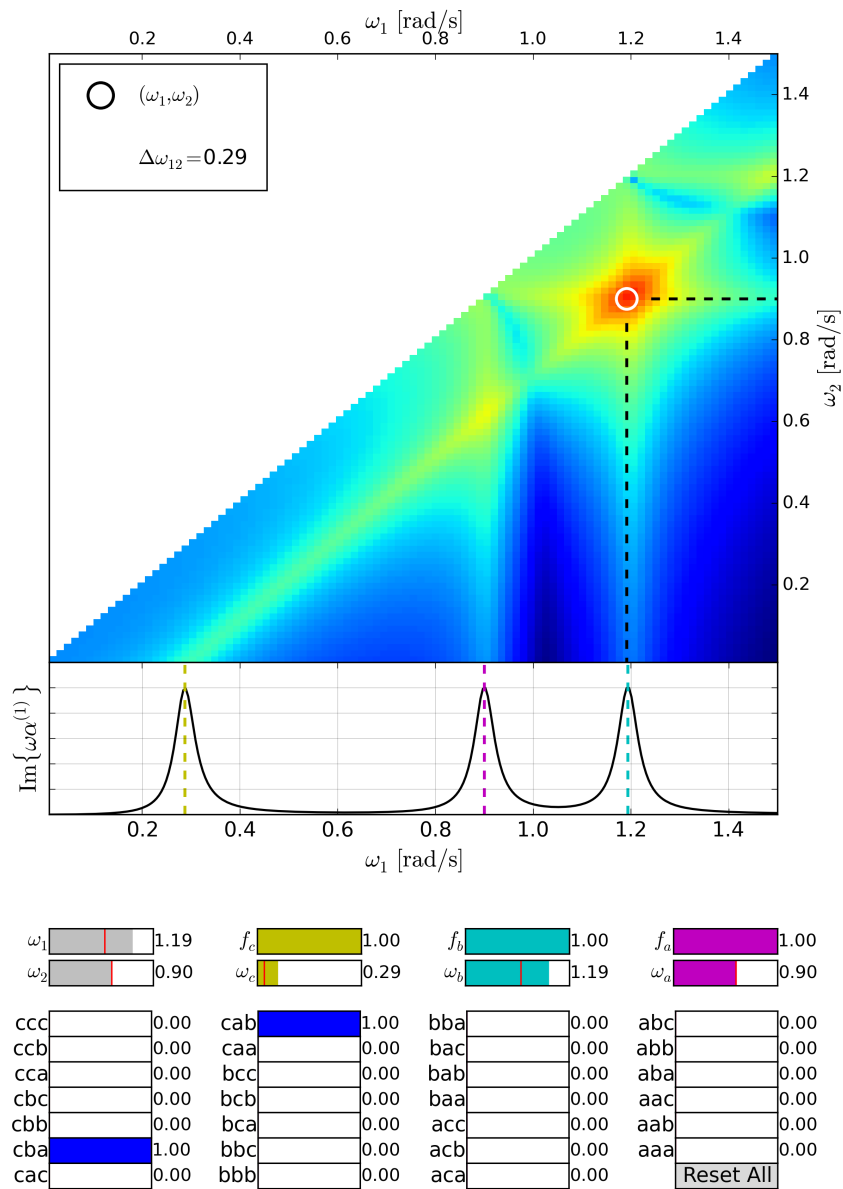


Figure 7.4: DFG from PNP model with three resonances (4). Compared to Fig. 7.3, the third resonance of the system is changed such that $\omega_c = 0.29$. DFG is maximized since the system exhibits resonances at the driving frequencies and their difference.

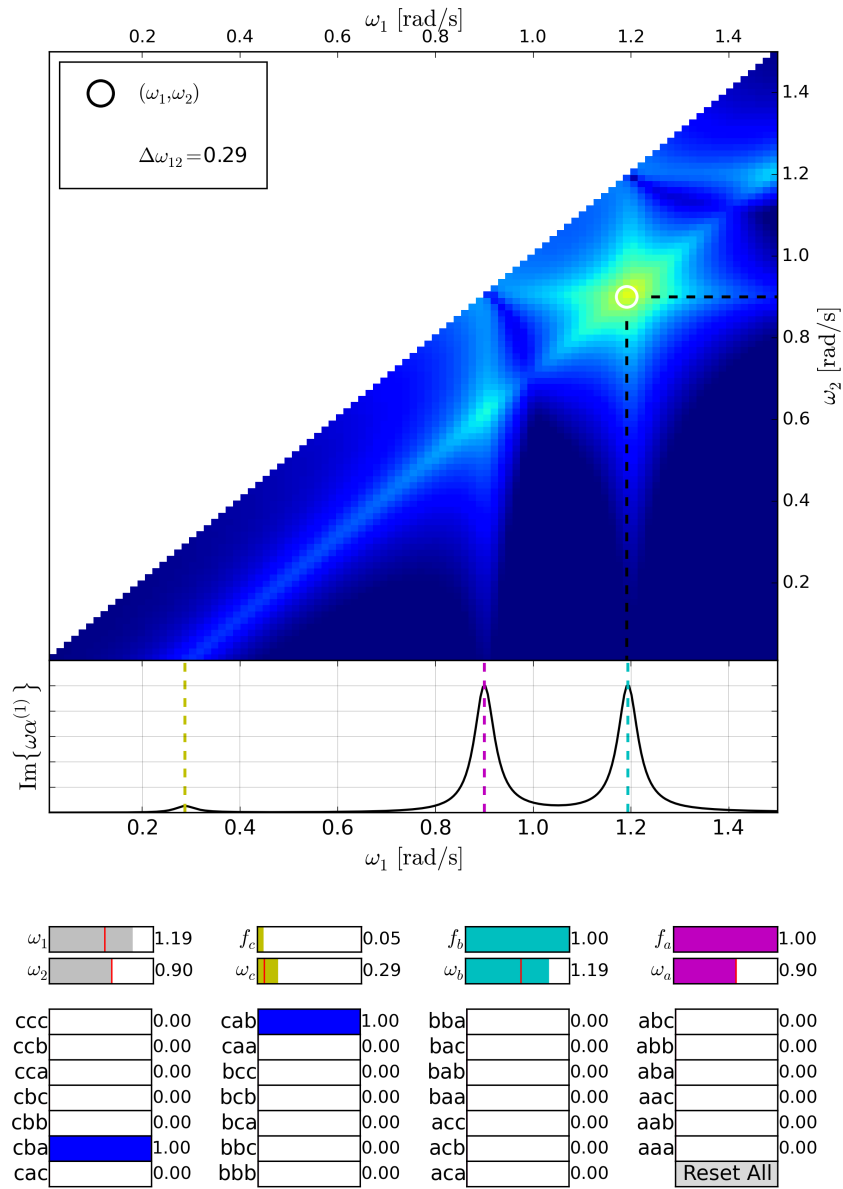


Figure 7.5: DFG from PNP model with three resonances (5). Compared to Fig. 7.4, the oscillator strength of resonance c is decreased. Consequently, the DFG amplitude also decreases.

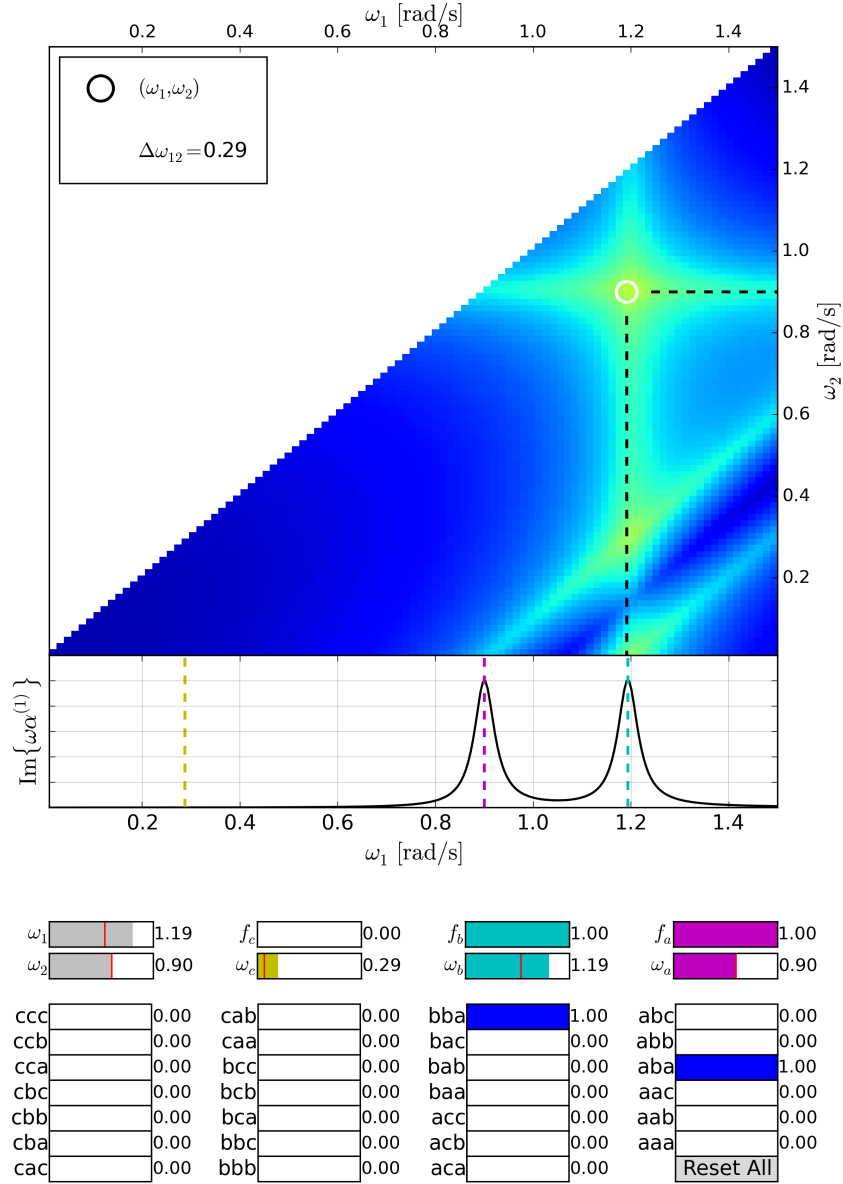


Figure 7.6: DFG from PNP model with three resonances (6). Compared to Fig. 7.5, the oscillator strength of resonance c is set to zero. The DFG response is now only possible when other coupling terms are active. Specifically, the terms aba and bba lead to enhanced DFG.

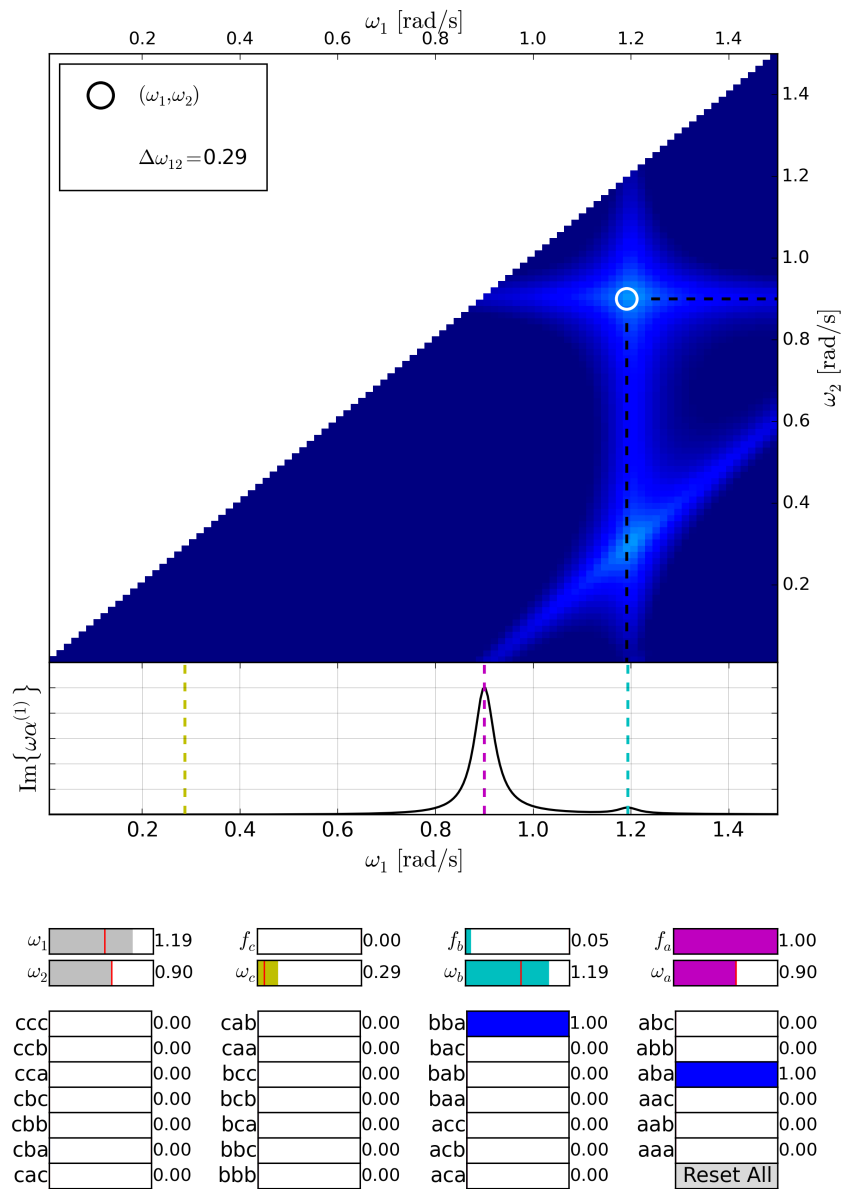


Figure 7.7: DFG from PNP model with three resonances (7). Compared to Fig. 7.6, the oscillator strength of resonance b is decreased. Consequently, the DFG amplitude also decreases.

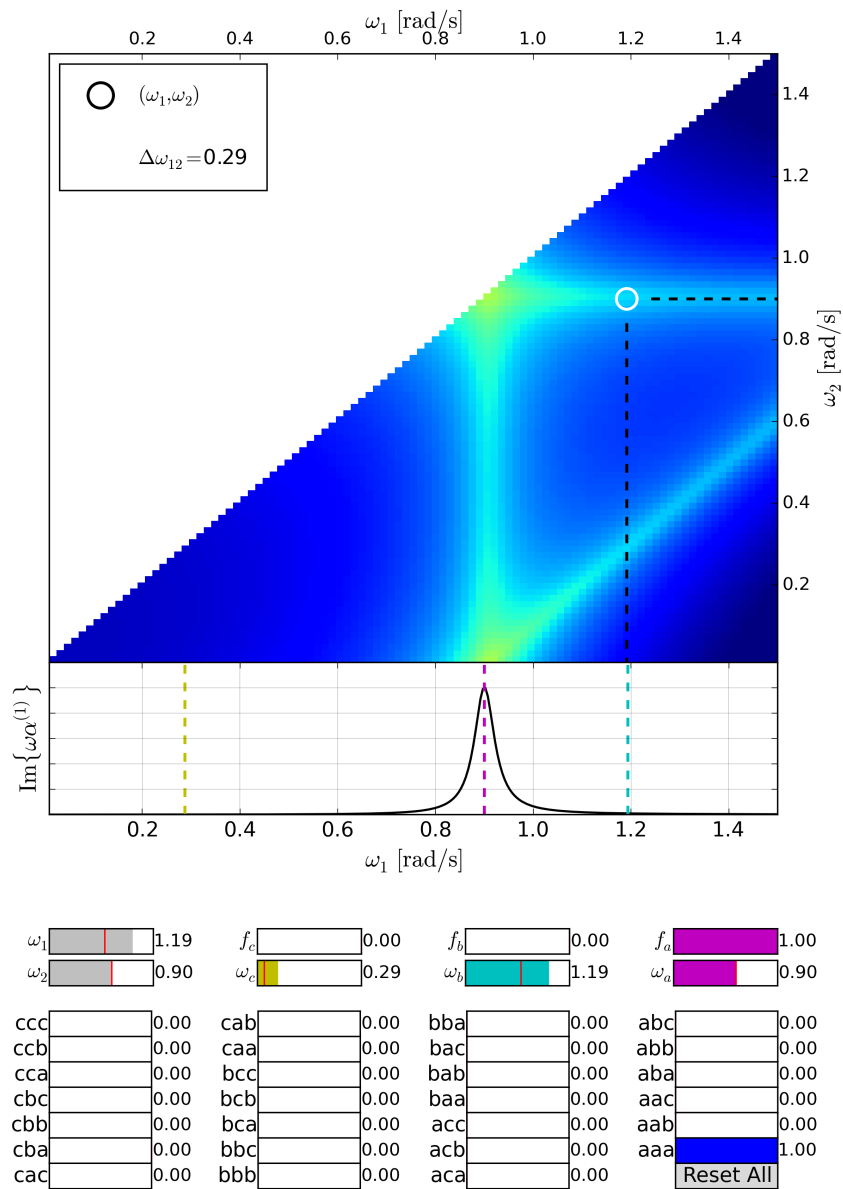


Figure 7.8: DFG from PNP model with three resonances (8). Compared to Fig. 7.7, the oscillator strength of resonance b is set to zero. The DFG response is now only possible when the coupling term aaa is active.

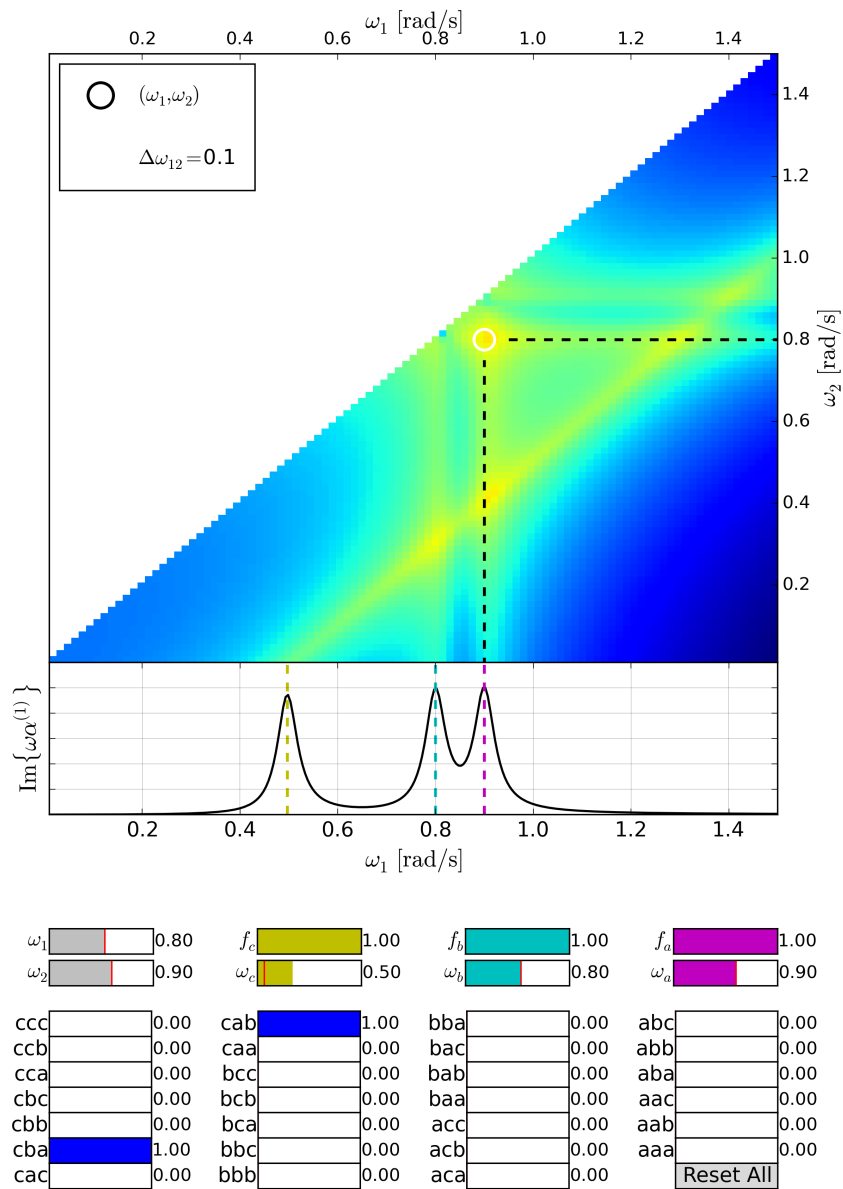


Figure 7.9: DFG from PNP model with three resonances (9). Compared to Fig. 7.1, the third resonance of the system is changed such that $\omega_c = 0.50$. The DFG amplitude is no longer maximized, since $\omega_c \neq \Delta\omega_{12}$.

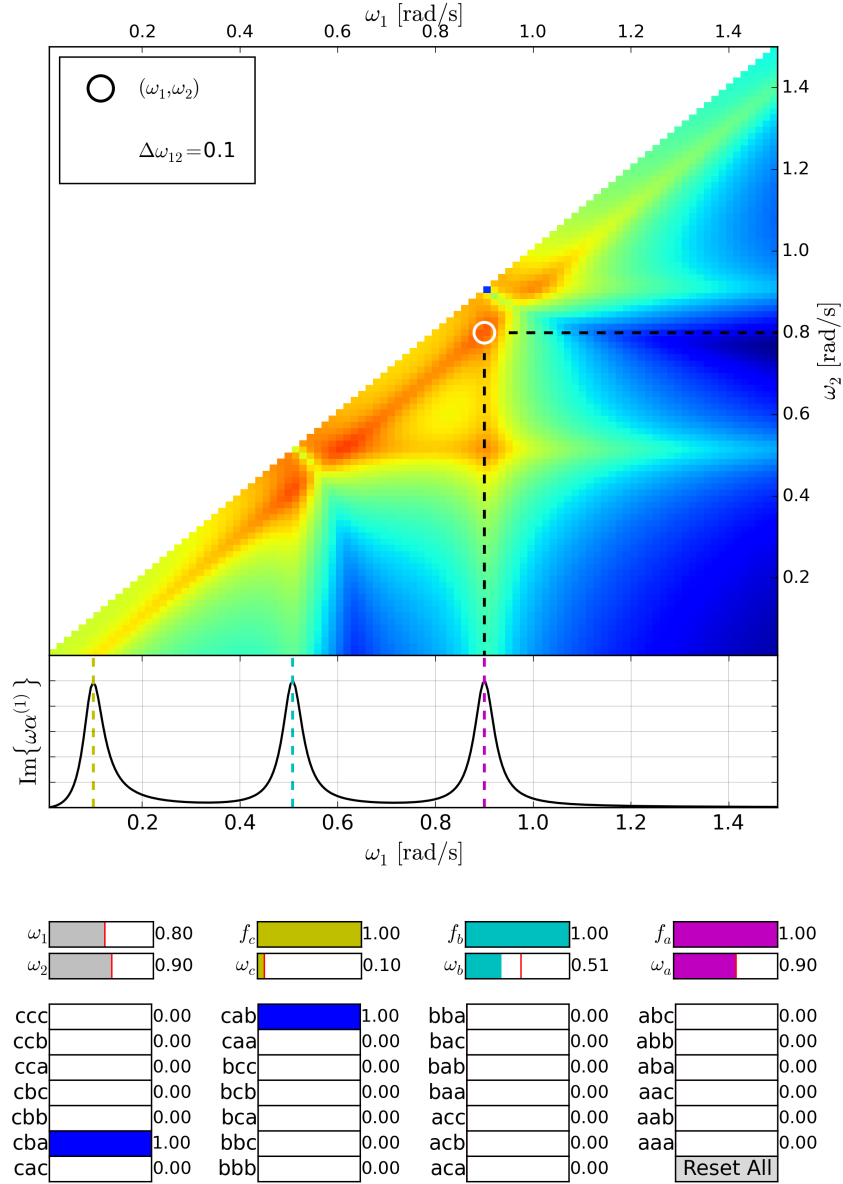


Figure 7.10: DFG from PNP model with three resonances (10). Compared to Fig. 7.1, the second resonance of the system is changed such that $\omega_b = 0.51$. The DFG amplitude is no longer maximized, since both resonances of the system do not coincide with both driving frequencies, i.e., $(\omega_a, \omega_b) \neq (\omega_1, \omega_2)$.

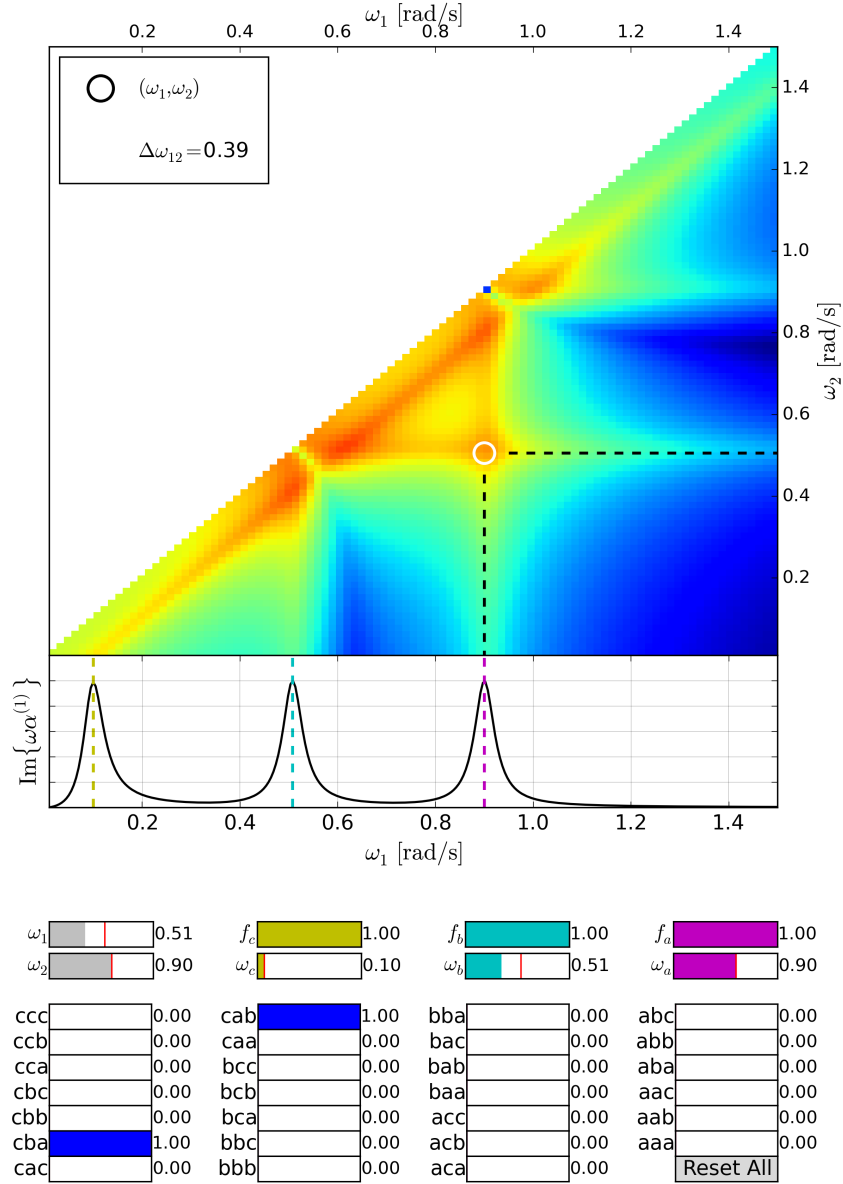


Figure 7.11: DFG from PNP model with three resonances (11). Compared to Fig. 7.10, the first driving frequency is changed such that $\omega_1 = 0.51$. Now two resonances of the system coincide with the driving frequencies, i.e., $(\omega_a, \omega_b) = (\omega_1, \omega_2)$, but DFG is still not maximized since $\omega_c \neq \Delta\omega_{12}$.

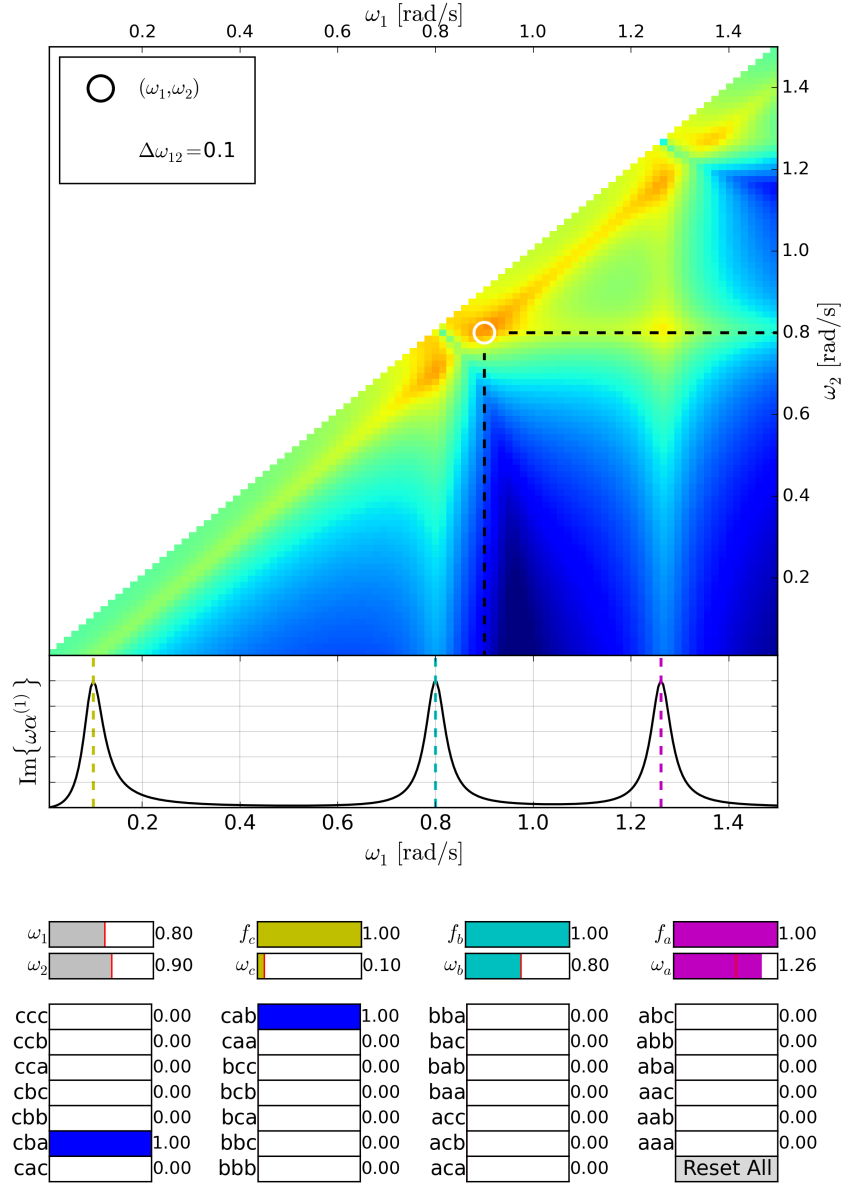


Figure 7.12: DFG from PNP model with three resonances (12). Compared to Fig. 7.1, the first resonance of the system is changed such that $\omega_a = 1.26$. The DFG amplitude is no longer maximized, since both resonances of the system do not coincide with both driving frequencies, i.e., $(\omega_a, \omega_b) \neq (\omega_1, \omega_2)$.

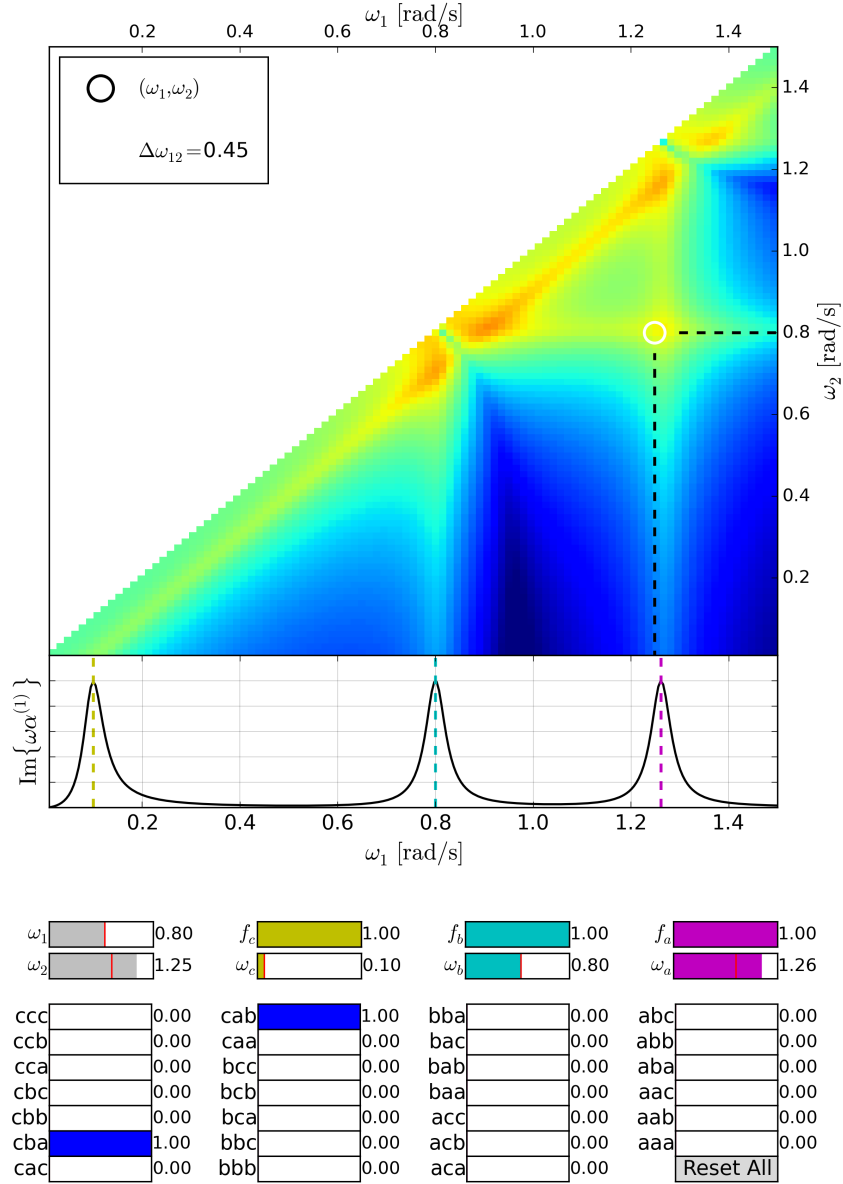


Figure 7.13: DFG from PNP model with three resonances (13). Compared to Fig. 7.12, the second driving frequency is changed such that $\omega_2 = 1.25$. Now two resonances of the system coincide (approximately) with the driving frequencies, i.e., $(\omega_a, \omega_b) = (\omega_1, \omega_2)$, but DFG is still not maximized since $\omega_c \neq \Delta\omega_{12}$.

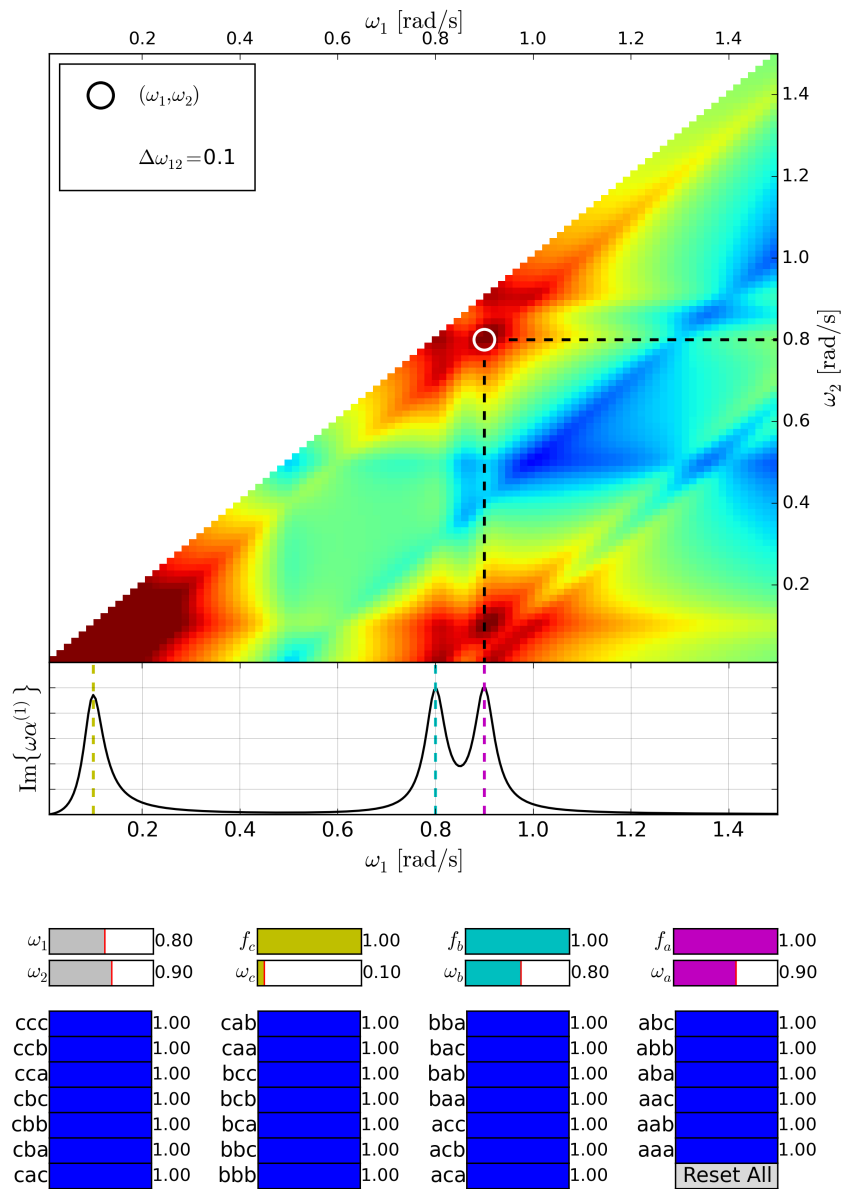


Figure 7.14: DFG from PNP model with three resonances (14). Compared to Fig. 7.1, all coupling terms are now active. When all coupling parameters are equal, the modal model reduces to the classical Miller’s rule.

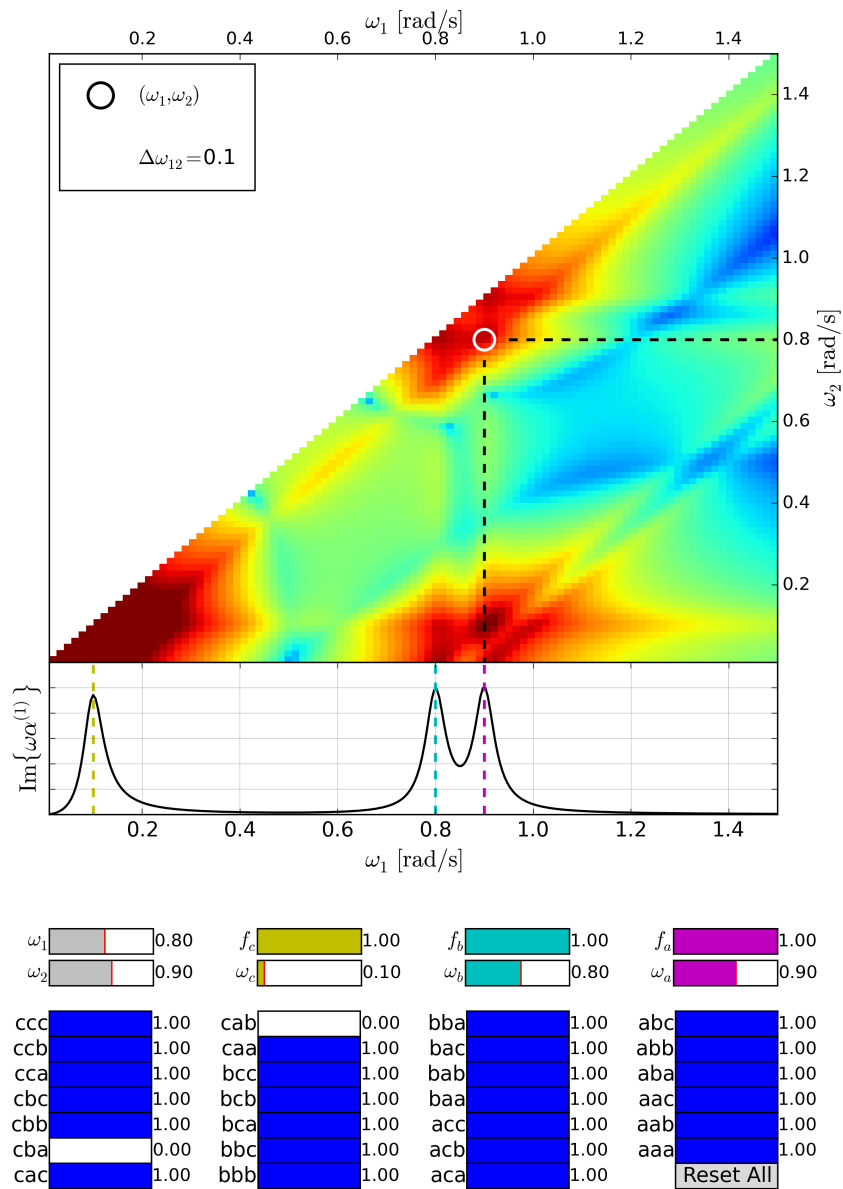


Figure 7.15: DFG from PNP model with three resonances (15). Compared to Fig. 7.14, the coupling terms cba and cab are deactivated. The DFG response decreases, indicating that these terms are responsible for significant DFG amplitude.

This modal model is a useful route towards understanding and optimizing the DFG response. If possible, a tri-resonant system should be designed and the coupling between all three modes should be maximized. Fortunately, of the many possible coupling terms, only a minimal number participate in the DFG response. Simple particles with three resonances do exist, for instance [104], although it may be difficult to engineer a low-frequency response that also allows the particle to be sufficiently small. Of course, it is also possible to obtain enhanced DFG from a doubly resonant system, although our analysis establishes that the amplitude of the response will necessarily be less than that of a tri-resonant system.

The resonant enhancement that this formalism suggests is also a characteristic of SHG, as Eq. (7.19) implies, and as Ref. [82] stated in their work. In fact, resonantly enhanced SHG has been observed in plasmonic systems, e.g., Ref. [105, 106, 107, 108, 109]. The resonant enhancement of other nonlinear phenomena has also been observed [110, 111]. This formalism for DFG reflects what is known about the behavior of other second-order response phenomena. Ultimately, the modal response model of Ref. [82], and our subsequent expression of a modified Miller's rule, is applicable to any system with resonant characteristics, not just plasmonic particles. Plasmonic characteristics enter through calculation of the linear polarizability and the microscopic details of the nonlinear coupling terms.

7.3 Driven DNA Damage with Plasmonic DFG

In the last section of this thesis, before the conclusion, we will try to tie together everything that was discussed in Part II by revisiting the study of DNA destruction from Chapter 5. Namely, we now wish to consider driving DNA towards destruction using a local plasmonic resonator, based on the scheme that was initially introduced.

The setup will be comprised of two driving fields at different frequencies that influence both a local, nonlinear PNP and a DNA strand. As per the model of the previous section, the PNP promotes DFG, which the DNA strand also experiences. Thus, the equation of motion of the n th base-pair of the DNA strand is:

$$m\ddot{y}_n = -U'(y_n) - W'(y_n, y_{n+1}) - W'(y_n, y_{n-1}) - m\gamma\dot{y}_n + \eta(t) + F_{\text{inc}}(t) + F_{\text{DFG}}(t) \quad (7.23)$$

where the incident AM field is

$$F_{\text{inc}}(t) = A_{\text{inc}} \cos(\omega_m t) \cos(\omega_c t) = \frac{A_{\text{inc}}}{2} [\cos(\omega_1 t) + \cos(\omega_2 t)] \quad (7.24)$$

and the DFG source, originating from a local PNP, is

$$F_{\text{DFG}}(t) = A_{\text{DFG}} \cos[(\omega_1 - \omega_2)t] \quad (7.25)$$

Note, if $F_{\text{DFG}}(t) = 0$ and $\omega_1 = \omega_2$, we have the same configuration as was investigated in Chapter 5.

First, we simulated the linear response of the system for a range of frequencies within the NIR window, $f^{\text{NIR}} \in [250 \text{ THz}, 400 \text{ THz}]$, for a setup that has no DFG signal. The amplitude-frequency response of AT and GC homogeneous sequences is shown below, for driving at a single frequency (i.e., $f_1 = f_2$).

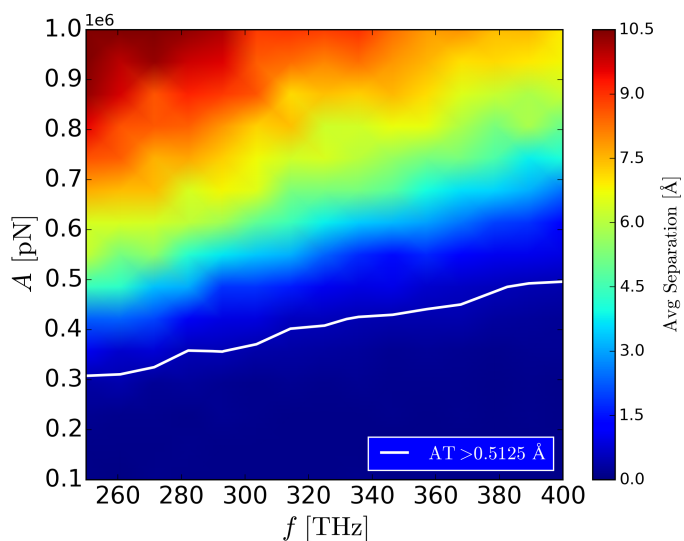


Figure 7.16: *Homogeneous AT sequence at high frequencies.* The intensity scale represents the average base-pair separation and the line indicates the boundary where the onset of damage occurs (average separation > 0.5125 Å).

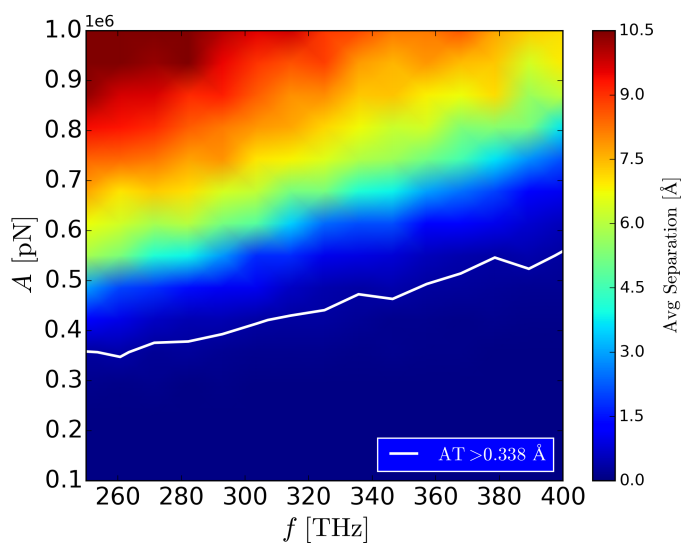


Figure 7.17: *Homogeneous GC sequence at high frequencies.* The intensity scale represents the average base-pair separation and the line indicates the boundary where the onset of damage occurs (average separation > 0.338 Å).

Fig. 7.16 & 7.17 show that the amplitude that causes DNA damage is incredibly high in this frequency range, with $A_{\max}^{\text{NIR}} > 3 \times 10^5 \text{pN}$. Within this region we chose two specific frequencies that would create a difference frequency of 1.5 THz, which is the destructive resonance of AT base-pairs: $f_1 = 375 \text{ THz}$ and $f_2 = 373.5 \text{ THz}$ (equivalent to $\lambda_1 \approx 0.799 \mu\text{m}$ and $\lambda_2 \approx 0.803 \mu\text{m}$). To see the effects of DFG on DNA damage with these driving frequencies, we simulated the response of single BPs substituted into homogeneous sequences, as in Chapter 5.

First, we simulated driving at these frequencies without DFG, i.e., for $F_{\text{inc}}(t) = \frac{A_{\text{inc}}}{2} [\cos(2\pi f_1 t) + \cos(2\pi f_2 t)]$ and $F_{\text{DFG}}(t) = 0$, where the driving amplitude was set to a value *below* the destructive threshold found in the previous figure, $A_{\text{inc}} = 3 \times 10^5 \text{ pN}$. This was in order to determine the bare response of BPs in the absence of DFG promoters. As in Chapter 5, we plot the normalized histogram of the occurrences when a given base-pair exceeds its damage threshold, shown in Fig. 7.18. As was expected, significant destruction did not occur for these values of amplitude and frequency.

Next we simulated the driving of DNA in the presence of DFG. We assumed that the response of this hypothetical particle was tailored to have optimal DFG at 1.5 THz. Based on the conclusions of the previous section, this would mean that the particle is resonant at $f_a = 375 \text{ THz}$, $f_b = 373.5 \text{ THz}$, and $f_c = 1.5 \text{ THz}$. Furthermore, we know that the threshold for driving at $f = 1.5 \text{ THz}$ is $A_{\text{thresh}}^{\text{THz}} \sim 120 \text{ pN}$, so we wish to simulate a DFG amplitude greater than this threshold. We calculate the histograms of base-pair separation for this full simulation in Fig. 7.13, where $f_1 = 375 \text{ THz}$, $f_2 = 373.5 \text{ THz}$, $|f_1 - f_2| = 1.5 \text{ THz}$, $A_{\text{inc}} = 3 \times 10^5 \text{ pN}$, and $A_{\text{DFG}} = 200 \text{ pN}$. Destructive behavior is observed.

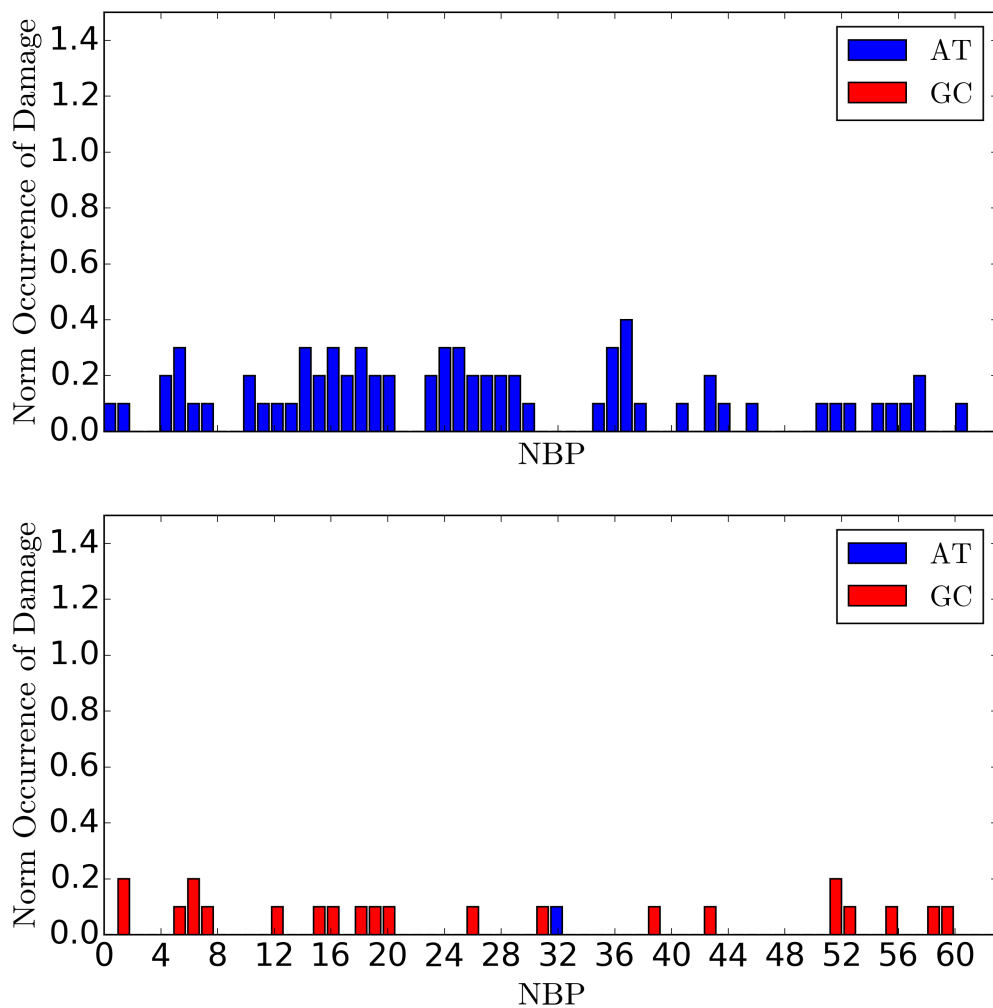


Figure 7.18: *Homogeneous sequence with one BP substitution: driving with no DFG* Driving at $A_{\text{inc}} = 3 \times 10^5$ pN and two high frequencies: 375 THz and 373.5 THz. The histograms represent the normalized number of occurrences when a given BP exceeds its damage threshold, where BP index is plotted on the horizontal axis. Upper plot: AT sequence with GC substitution at site 32. Lower plot: GC sequence with AT substitution at site 32.

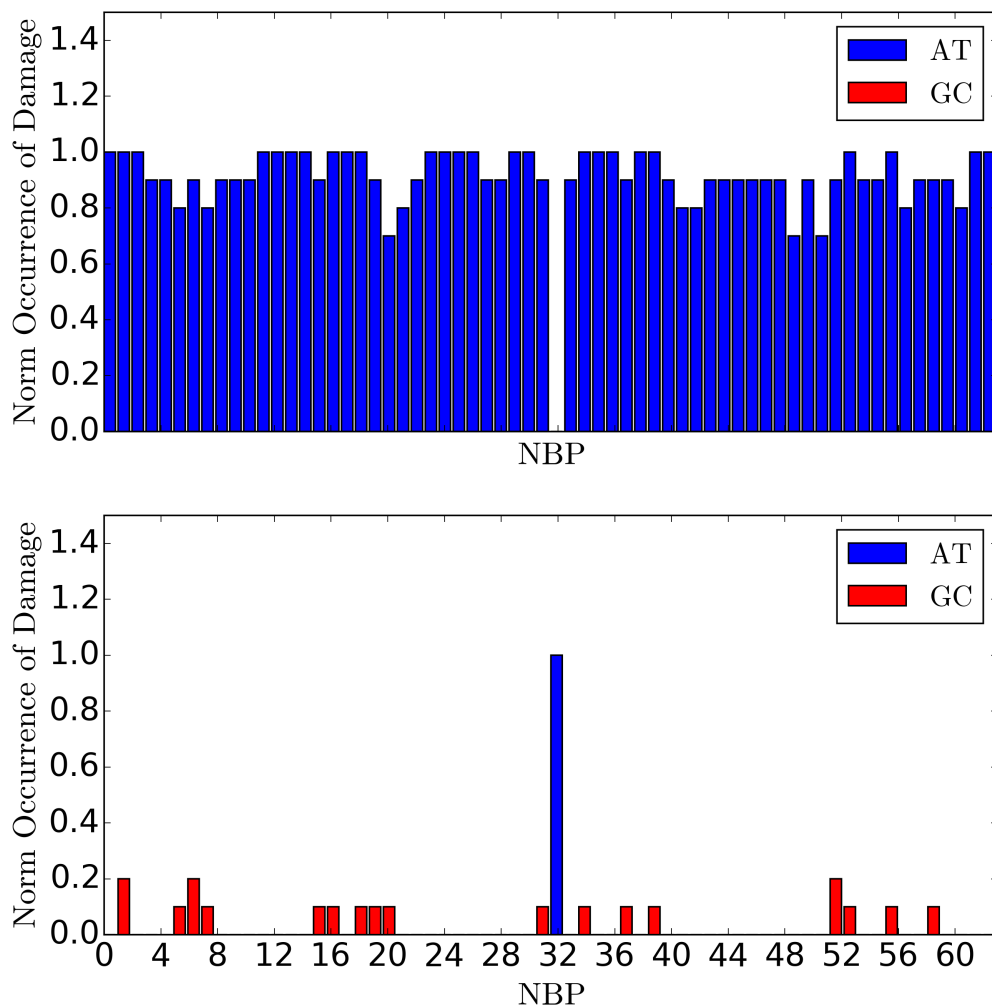


Figure 7.19: *Homogeneous sequence with one BP substitution: driving with DFG* Driving at $A_{\text{inc}} = 3 \times 10^5$ pN and $A_{\text{DFG}} = 200$ pN and two high frequencies: 375 THz and 373.5 THz. DFG occurs at 1.5 THz. The histograms represent the normalized number of occurrences when a given BP exceeds its damage threshold, where BP index is plotted on the horizontal axis. Upper plot: AT sequence with GC substitution at site 32. Lower plot: GC sequence with AT substitution at site 32.

Thus, we have demonstrated from raw simulation that it is possible, under an idealized configuration, to cause DNA damage at THz frequencies via DFG from an AM signal that uses an NIR carrier frequency. However, up to this point we have not said anything about the properties of the DFG source, other than that originates from a PNP, which produces the driving amplitude A_{DFG} . Now, we consider the strength of the nonlinearity that is necessary to produce this destructive behavior. Since second-order terms are proportional to the field strength squared, we can express $F_{\text{DFG}}(t)$ as:

$$F_{\text{DFG}}(t) = \left[\frac{A_{\text{inc}}}{2} \right]^2 \zeta_{\text{DFG}} \cos [(\omega_1 - \omega_2)t] \quad (7.26)$$

where ζ_{DFG} is the nonlinear coupling amplitude. Thus, $A_{\text{DFG}} = \left[\frac{A_{\text{inc}}}{2} \right]^2 \zeta_{\text{DFG}}$. The minimum nonlinear coupling amplitude that is necessary to cause damage at the difference-frequency, $\zeta_{\text{thresh}}^{\text{THz}}$, corresponds to the condition $A_{\text{DFG}} \geq A_{\text{thresh}}^{\text{THz}}$, where $A_{\text{thresh}}^{\text{THz}}$ is a quantity estimated through our simulation, as defined earlier in this section. Additionally, we wish to use incident fields that are smaller in amplitude than the destructive threshold for NIR radiation, $A_{\text{max}}^{\text{NIR}}$, lest the NIR radiation destroy the DNA at the expense of selectivity. Therefore, $A_{\text{inc}} \leq A_{\text{max}}^{\text{NIR}}$. Finally, we can relate these terms and solve for $\zeta_{\text{thresh}}^{\text{THz}}$:

$$\zeta_{\text{thresh}}^{\text{THz}} \geq \frac{A_{\text{thresh}}^{\text{THz}}}{\left[\frac{A_{\text{max}}^{\text{NIR}}}{2} \right]^2} \gtrsim 5.34 \times 10^{-9} \text{ pN}^{-1} \quad (7.27)$$

The parameter $\zeta_{\text{thresh}}^{\text{THz}}$ can be related to the DFG polarizability, $\alpha^{(2)}$, to estimate the requirements of a PNP that are necessary to facilitate destruction.

CHAPTER 8

Conclusion

In this chapter, we summarize the findings of this thesis with regards to nonlocal and nonlinear response phenomena. We then consider areas for additional investigation.



8.1 Summary of Work

In this thesis, we have examined nonlocal and nonlinear response models of plasmonic systems. In chapter 2, we introduced nonlocal models of plasmonic response, including the *ab initio* d-function formalism and the phenomenological hydrodynamic approximation. In chapter 3 we proposed a way of combining the d-function formalism and HDA to form an “extended d-function formalism.” We performed *ab initio* calculations of metallic slabs and demonstrated some scaling properties of this model, which we also argued could be used to predict nonlocal properties of subwavelength plasmonic nanostructures (e.g., metamaterials) based on effective medium arguments. In chapter 4, we introduced a method that enabled us to map the nonlocal properties of a plasmonic system onto a local, fictitious thin film using the d-function formalism. The film, which models the nonlocal response to linear order in q , provides a way to incorporate nonlocal physics into local calculation schemes, and can be utilized in existing FDTD simulation methods.

We also examined nonlinear models of response functions and tried to apply this to the analysis of difference-frequency generation from plasmonic systems, in the specific context of utilizing plasmonic DFG to create THz radiation *in vivo*. The goal of this endeavor was to selectively promote the destruction of specific DNA sequences within the human body.

In chapter 5, we first began by looking at the response of DNA to THz fields and tried to identify and understand regimes of destruction where the system was driven to a breaking point. We used a nonlinear oscillator model for double-stranded DNA, which incorporated inter- and intra-base-pair forces and thermal interactions, and we first drove the system with a sinusoidal force field to simulate monochromatic light. We found that, under certain combinations of driving amplitude and frequency, the system was driven to a regime of large BP separation, which we used as a proxy for damage. We also found that the region of amplitude-frequency parameter-space where such damage occurred was different for sequences composed of different BPs. Moreover, we found that we could selectively drive either AT or GC pairs within a heterogeneous sequence, allowing for the possibility of selective damage at the single base-pair level. Finally, our simulations of heterogeneous sequences also suggest that damage might be selective based on the ordering of BPs within a sequence.

In chapter 6, we introduced the nonlinear phenomenon of difference-frequency generation (DFG) as a means to enable THz signals to penetrate deeply into the body, with the goal of targeting DNA *in vivo*. We explained the concept that a local plasmonic constituent could be used to demodulate two high frequency signals into a signal at their difference-frequency. We presented the mathematical derivation of DFG and simulated the response of a classical anharmonic oscillator to demonstrate this process. Importantly, we introduced the concept of Miller’s rule and applied it to our simulation—Miller’s rule prescribes how to calculate the DFG response from

knowledge of the linear response of the system. In chapter 7 we extended the analogy of a simple anharmonic oscillator to plasmonic oscillators and proposed an effective Miller’s Rule for such systems. Thus, we demonstrated that it might be possible to express the DFG response of a plasmonic system in terms of its linear response. This tool would enable one to effectively estimate the magnitude of plasmonic DFG with knowledge of the linear response of a plasmonic system, which could be obtained from FDTD solvers, for instance. We emphasized the useful insights that such a relation would provide for optimization calculations, specifically the observation that DFG is maximized for a particle that exhibits 3 resonances: one at each driving frequency, and one at the difference-frequency.

Finally, we finished our investigation by conducting a model-based simulation of the response of a DNA sequence in the presence of a plasmonic-DFG promoter. Considering our proposed model for plasmonic-DFG, we simulated driving a heterogeneous sequence with two high-frequency signals and examined the parameter-space where destruction occurred. In the presence of two driving signals, the DNA strand was driven towards breaking for certain parameter values when DFG was present, but *not* when DFG was absent. Thus, we demonstrated a proof-of-concept for this scheme, albeit in an idealized environment.

8.2 Outlook and Future Work

We have shown that heuristic models of nonlocality (i.e., extensions of existing formalisms to new regimes of applicability) are useful for modeling the response phenomena of plasmonic systems. For instance, the extended d-function formalism adequately captures the nonlocal behavior of plasmonic response at moderate to high-q values. Thus, such extensions are a valid and useful program for studying nonlocality in nontrivial systems. If possible, *ab initio* calculations of structured plasmonic

systems, rather than planar slabs, should be undertaken to further demonstrate the validity of the extended d-function formalism.

We have also demonstrated that it is possible to map the complex physics of non-locality, specifically, the d-function formalism, into local response models, thereby incorporating the inherent quantum nature of plasmonic systems and enabling calculations using local computational schemes (e.g., FDTD). This was done with our thin-film mapping scheme. As a future endeavor, this scheme should be applied to other geometries and structures, perhaps leading to the discovery of novel response phenomena. Additionally, similar geometric mapping schemes should be identified for *multi-layer* or *gradient* films, which should be even more accurate.

In another area, our analysis of DNA damage offers many promising avenues for future research. Specifically, we showed that it is possible to selectively drive DNA towards destruction in certain regions of amplitude-frequency space. As a follow-up, one could consider whether designer signals could expand the destructive regime, i.e., whether it might be possible to destroy DNA at even lower amplitudes using combinations of different pulses or polarizations, for instance. Also, one could examine the sensitivity of the destructive dynamics to the model parameters used in simulation—different physical models have been proposed in the literature and may influence the parameter-space where damage is predicted to occur. Finally, one could investigate *specific* DNA sequences corresponding to *known biological entities*, in order to determine selectivity between real systems. Ultimately, we hope that this study will inform future projects which seek to target cellular destruction for therapeutic purposes.

Finally, we have also shown that the modal model of nonlinear response can be used as an effective tool to predict the characteristics of difference-frequency generation. To follow-up, simulations of plasmonic particles should be run in COMSOL

to confirm that a Miller-like relation holds between first-order and second-order polarizabilities. Informed by the modal model, one should be able to quickly optimize second-order responses by focusing only on relevant modal coupling terms, rather than the whole parameter-space. Designing subwavelength particles to exhibit desired resonances and modal-coupling terms will certainly be a challenge, but designer DFG (and other second-order response phenomena) will be yet another way to control light-matter interactions at the nanoscale for future novel applications.

BIBLIOGRAPHY

- [1] Y. Wang, E. Plummer, and K. Kempa, “Foundations of plasmonics,” *Advances in Physics* **60**, 799 (2011).
- [2] G. D. Mahan, *Many-particle physics* (Springer Science & Business Media, 2013).
- [3] J. Kong, A. Rose, C. Yang, X. Wu, J. Merlo, M. Burns, M. Naughton, and K. Kempa, “Hot electron plasmon-protected solar cell,” *Optics express* **23**, A1087 (2015).
- [4] J. B. Pendry, A. Holden, W. Stewart, and I. Youngs, “Extremely low frequency plasmons in metallic mesostructures,” *Physical review letters* **76**, 4773 (1996).
- [5] A. Alu and N. Engheta, “Plasmonic and metamaterial cloaking: physical mechanisms and potentials,” *Journal of Optics A: Pure and Applied Optics* **10**, 093002 (2008).
- [6] C. M. Watts, X. Liu, and W. J. Padilla, “Metamaterial electromagnetic wave absorbers,” *Advanced materials* **24**, OP98 (2012).
- [7] R. W. Ziolkowski, “Propagation in and scattering from a matched metamaterial having a zero index of refraction,” *Physical Review E* **70**, 046608 (2004).
- [8] N. Garcia, E. Ponizovskaya, and J. Q. Xiao, “Zero permittivity materials: Band gaps at the visible,” *Applied physics letters* **80**, 1120 (2002).
- [9] P. Drude, “Zur elektronentheorie der metalle,” *Annalen der Physik* **306**, 566 (1900).
- [10] F. Forstmann and R. R. Gerhardts, *Metal optics near the plasma frequency*, vol. 109 (Springer, 2006).
- [11] P. J. Feibelman, “Microscopic calculation of electromagnetic fields in refraction at a jellium-vacuum interface,” *Physical Review B* **12**, 1319 (1975).
- [12] P. J. Feibelman, “Surface electromagnetic fields,” *Progress in Surface Science* **12**, 287 (1982).
- [13] A. J. Shvonski, J. Kong, and K. Kempa, “Nonlocal extensions of the electromagnetic response of plasmonic and metamaterial structures,” *Physical Review B* **95**, 045149 (2017).
- [14] J. Kong, A. J. Shvonski, and K. Kempa, “Nonlocal response with local optics,” *Physical Review B* **97**, 165423 (2018).

- [15] R. W. Boyd, *Nonlinear optics* (Academic press, 2003).
- [16] M. A. Ordal, R. J. Bell, R. W. Alexander, L. L. Long, and M. R. Querry, "Optical properties of fourteen metals in the infrared and far infrared: Al, co, cu, au, fe, pb, mo, ni, pd, pt, ag, ti, v, and w.," *Applied optics* **24**, 4493 (1985).
- [17] A. D. Rakić, "Algorithm for the determination of intrinsic optical constants of metal films: application to aluminum," *Applied optics* **34**, 4755 (1995).
- [18] R. Ritchie, E. Arakawa, J. Cowan, and R. Hamm, "Surface-plasmon resonance effect in grating diffraction," *Physical Review Letters* **21**, 1530 (1968).
- [19] K.-D. Tsuei, E. Plummer, A. Liebsch, E. Pehlke, K. Kempa, and P. Bakshi, "The normal modes at the surface of simple metals," *Surface Science* **247**, 302 (1991).
- [20] R. D. Mattuck, *A guide to Feynman diagrams in the many-body problem* (Courier Corporation, 1976).
- [21] N. Lang and W. Kohn, "Theory of metal surfaces: charge density and surface energy," *Physical Review B* **1**, 4555 (1970).
- [22] K. Kempa and R. Gerhardtts, "Nonlocal effects in ellipsometry of metallic films on metals," *Surface Science* **150**, 157 (1985).
- [23] A. Liebsch, "Dynamical screening at simple-metal surfaces," *Physical Review B* **36**, 7378 (1987).
- [24] W. Plummer, K.-D. Tsuei, and B.-O. Kim, "The impact of the concept of a surface plasmon," *Nuclear Instruments and Methods in Physics Research Section B: Beam Interactions with Materials and Atoms* **96**, 448 (1995).
- [25] K.-D. Tsuei, E. Plummer, A. Liebsch, K. Kempa, and P. Bakshi, "Multipole plasmon modes at a metal surface," *Physical review letters* **64**, 44 (1990).
- [26] K. Kempa and W. Schaich, "Calculation of corrections to Fresnel optics from density response," *Physical Review B* **34**, 547 (1986).
- [27] K. Kempa, A. Liebsch, and W. Schaich, "Comparison of calculations of dynamical screening at jellium surfaces," *Physical Review B* **38**, 12645 (1988).
- [28] K. Kempa and W. Schaich, "Nonlocal corrections to Fresnel optics: Model calculations from first principles for flat jellium," *Physical Review B* **37**, 6711 (1988).
- [29] K. Kempa and W. Schaich, "Nonlocal corrections to Fresnel optics: Jellium-model calculations above the bulk-plasmon threshold," *Physical Review B* **39**, 13139 (1989).

- [30] A. Liebsch and W. Schaich, “Influence of a polarizable medium on the nonlocal optical response of a metal surface,” *Physical Review B* **52**, 14219 (1995).
- [31] K.-D. Tsuei, E. W. Plummer, and P. J. Feibelman, “Surface-plasmon dispersion in simple metals,” *Physical review letters* **63**, 2256 (1989).
- [32] K. Kempa and W. Schaich, “Calculation of corrections to Fresnel optics from density response,” *Physical Review B* **34**, 547 (1986).
- [33] K. Kempa, D. Broido, C. Beckwith, and J. Cen, “d-function approach to the electromagnetic response of semiconductor heterostructures,” *Physical Review B* **40**, 8385 (1989).
- [34] A. Liebsch, “Surface-plasmon dispersion and size dependence of Mie resonance: silver versus simple metals,” *Physical Review B* **48**, 11317 (1993).
- [35] D. R. Smith, S. Schultz, P. Markoš, and C. Soukoulis, “Determination of effective permittivity and permeability of metamaterials from reflection and transmission coefficients,” *Physical Review B* **65**, 195104 (2002).
- [36] A. Liebsch, *Electronic excitations at metal surfaces* (Springer Science & Business Media, 2013).
- [37] Y. Luo, A. Fernandez-Dominguez, A. Wiener, S. A. Maier, and J. Pendry, “Surface plasmons and nonlocality: a simple model,” *Physical review letters* **111**, 093901 (2013).
- [38] T. Reiners, C. Ellert, M. Schmidt, and H. Haberland, “Size dependence of the optical response of spherical sodium clusters,” *Physical review letters* **74**, 1558 (1995).
- [39] G. Bellisola and C. Sorio, “Infrared spectroscopy and microscopy in cancer research and diagnosis,” *American journal of cancer research* **2**, 1 (2012).
- [40] K. Jeong, Y.-M. Huh, S.-H. Kim, Y. Park, J.-H. Son, S. J. Oh, and J.-S. Suh, “Characterization of blood using terahertz waves,” *Journal of biomedical optics* **18**, 107008 (2013).
- [41] M. Peyrard, “Nonlinear dynamics and statistical physics of DNA,” *Nonlinearity* **17**, R1 (2004).
- [42] W. P. Roos and B. Kaina, “DNA damage-induced cell death by apoptosis,” *Trends in molecular medicine* **12**, 440 (2006).
- [43] L. V. Titova, A. K. Ayesheshim, A. Golubov, D. Fogen, R. Rodriguez-Juarez, F. A. Hegmann, and O. Kovalchuk, “Intense THz pulses cause H2AX phosphorylation and activate DNA damage response in human skin tissue,” *Biomedical optics express* **4**, 559 (2013).

- [44] K. Lewis, “Platforms for antibiotic discovery,” *Nature reviews Drug discovery* **12**, 371 (2013).
- [45] D. G. Murphy and J. P. Grummet, “Planning for the post-antibiotic era—why we must avoid TRUS-guided biopsy sampling,” *Nature Reviews Urology* **13**, 559 (2016).
- [46] R. Tapia-Rojo, J. J. Mazo, and F. Falo, “Thermal and mechanical properties of a DNA model with solvation barrier,” *Physical Review E* **82**, 031916 (2010).
- [47] J. R. Arias-Gonzalez, “Single-molecule portrait of DNA and RNA double helices,” *Integrative Biology* **6**, 904 (2014).
- [48] B. Alexandrov, V. Gelev, A. Bishop, A. Usheva, and K. Rasmussen, “DNA breathing dynamics in the presence of a terahertz field,” *Physics Letters A* **374**, 1214 (2010).
- [49] B. S. Alexandrov, Y. Fukuyo, M. Lange, N. Horikoshi, V. Gelev, K. Ø. Rasmussen, A. R. Bishop, and A. Usheva, “DNA breathing dynamics distinguish binding from nonbinding consensus sites for transcription factor YY1 in cells,” *Nucleic acids research* **40**, 10116 (2012).
- [50] E. S. Swanson, “Modeling DNA response to terahertz radiation,” *Physical Review E* **83**, 040901 (2011).
- [51] E. C. Friedberg, “DNA damage and repair,” *Nature* **421**, 436 (2003).
- [52] B. Alexandrov, N. K. Voulgarakis, K. Ø. Rasmussen, A. Usheva, and A. R. Bishop, “Pre-melting dynamics of DNA and its relation to specific functions,” *Journal of Physics: Condensed Matter* **21**, 034107 (2008).
- [53] T. Dauxois, M. Peyrard, and A. R. Bishop, “Entropy-driven DNA denaturation,” *Physical Review E* **47**, R44 (1993).
- [54] M. Peyrard and A. R. Bishop, “Statistical mechanics of a nonlinear model for DNA denaturation,” *Physical review letters* **62**, 2755 (1989).
- [55] T. Dauxois, M. Peyrard, and A. Bishop, “Dynamics and thermodynamics of a nonlinear model for DNA denaturation,” *Physical Review E* **47**, 684 (1993).
- [56] R. P. Sinha and D.-P. Häder, “UV-induced DNA damage and repair: a review,” *Photochemical & Photobiological Sciences* **1**, 225 (2002).
- [57] G. J. Wilmink and J. E. Grundt, “Invited review article: current state of research on biological effects of terahertz radiation,” *Journal of Infrared, Millimeter, and Terahertz Waves* **32**, 1074 (2011).

- [58] L. Zhao, Y.-H. Hao, and R.-Y. Peng, “Advances in the biological effects of terahertz wave radiation,” *Military Medical Research* **1**, 26 (2014).
- [59] A. E. Bergues-Pupo, J. M. Bergues, and F. Falo, “Modeling the interaction of DNA with alternating fields,” *Physical Review E* **87**, 022703 (2013).
- [60] A. Bergues-Pupo, J. Bergues, and F. Falo, “Unzipping of DNA under the influence of external fields,” *Physica A: Statistical Mechanics and its Applications* **396**, 99 (2014).
- [61] V. Franchini, S. De Sanctis, J. Marinaccio, A. De Amicis, E. Coluzzi, S. Di Cristofaro, F. Lista, E. Regalbuto, A. Doria, E. Giovenale, et al., “Study of the effects of 0.15 terahertz radiation on genome integrity of adult fibroblasts,” *Environmental and molecular mutagenesis* (2018).
- [62] A. A. Angeluts, A. B. Gapeyev, M. N. Esaulkov, O. G. Kosareva, S. N. Matyunin, M. M. Nazarov, T. N. Pashovkin, P. M. Solyankin, O. P. Cherkasova, and A. P. Shkurinov, “Study of terahertz-radiation-induced DNA damage in human blood leukocytes,” *Quantum Electronics* **44**, 247 (2014).
- [63] K.-T. Kim, J. Park, S. J. Jo, S. Jung, O. S. Kwon, G. P. Gallerano, W.-Y. Park, and G.-S. Park, “High-power femtosecond-terahertz pulse induces a wound response in mouse skin,” *Scientific reports* **3**, 2296 (2013).
- [64] H. Hintzsche, C. Jastrow, T. Kleine-Ostmann, H. Stopper, E. Schmid, and T. Schrader, “Terahertz radiation induces spindle disturbances in human-hamster hybrid cells,” *Radiation research* **175**, 569 (2011).
- [65] E. V. Demidova, T. N. Goryachkovskaya, T. K. Malup, S. V. Bannikova, A. I. Semenov, N. A. Vinokurov, N. A. Kolchanov, V. M. Popik, and S. E. Peltek, “Studying the non-thermal effects of terahertz radiation on *E. coli*/pKatG-GFP biosensor cells,” *Bioelectromagnetics* **34**, 15 (2013).
- [66] H. Hintzsche, C. Jastrow, T. Kleine-Ostmann, U. Kärst, T. Schrader, and H. Stopper, “Terahertz electromagnetic fields (0.106 THz) do not induce manifest genomic damage in vitro,” *PloS one* **7**, e46397 (2012).
- [67] A. Bogomazova, E. M. Vassina, T. Goryachkovskaya, V. Popik, A. Sokolov, N. Kolchanov, M. Lagarkova, S. Kiselev, and S. Peltek, “No DNA damage response and negligible genome-wide transcriptional changes in human embryonic stem cells exposed to terahertz radiation,” *Scientific reports* **5**, 7749 (2015).
- [68] N. Grønbech-Jensen and O. Farago, “A simple and effective Verlet-type algorithm for simulating Langevin dynamics,” *Molecular Physics* **111**, 983 (2013).
- [69] A. Cromer, “Stable solutions using the Euler approximation,” *American Journal of Physics* **49**, 455 (1981).

- [70] J. Butcher, “Runge-Kutta methods,” *Scholarpedia* **2**, 3147 (2007).
- [71] A. Brünger, C. L. Brooks III, and M. Karplus, “Stochastic boundary conditions for molecular dynamics simulations of ST2 water,” *Chemical physics letters* **105**, 495 (1984).
- [72] A. Fitzgerald, E. Berry, N. Zinov’ev, S. Homer-Vanniasinkam, R. Miles, J. Chamberlain, and M. Smith, “Catalogue of human tissue optical properties at terahertz frequencies,” *Journal of Biological Physics* **29**, 123 (2003).
- [73] URL https://en.wikipedia.org/wiki/Electromagnetic_absorption_by_water#/media/File:Absorption_spectrum_of_liquid_water.png.
- [74] URL <https://omlc.org/spectra/water/abs/index.html>.
- [75] P. H. Siegel, “Terahertz technology in biology and medicine,” *IEEE transactions on microwave theory and techniques* **52**, 2438 (2004).
- [76] E. Pickwell and V. Wallace, “Biomedical applications of terahertz technology,” *Journal of Physics D: Applied Physics* **39**, R301 (2006).
- [77] L. Ho, M. Pepper, and P. Taday, “Terahertz spectroscopy: Signatures and fingerprints,” *Nature Photonics* **2**, 541 (2008).
- [78] Y.-Y. Huang, A. C.-H. Chen, J. D. Carroll, and M. R. Hamblin, “Biphasic dose response in low level light therapy,” *Dose-response* **7**, dose (2009).
- [79] A. M. Smith, M. C. Mancini, and S. Nie, “Bioimaging: second window for in vivo imaging,” *Nature nanotechnology* **4**, 710 (2009).
- [80] S. Stolik, J. Delgado, A. Perez, and L. Anasagasti, “Measurement of the penetration depths of red and near infrared light in human “ex vivo” tissues,” *Journal of Photochemistry and Photobiology B: Biology* **57**, 90 (2000).
- [81] URL [http://emlab.utep.edu/ee5390em21/Lecture 2 -- Lorentz and Drude models.pdf](http://emlab.utep.edu/ee5390em21/Lecture%20--%20Lorentz%20and%20Drude%20models.pdf).
- [82] Y. Zeng, D. Dalvit, J. O’hara, and S. Trugman, “Modal analysis method to describe weak nonlinear effects in metamaterials,” *Physical Review B* **85**, 125107 (2012).
- [83] M. Kauranen and A. V. Zayats, “Nonlinear plasmonics,” *Nature Photonics* **6**, 737 (2012).
- [84] J. Butet and O. J. Martin, “Evaluation of the nonlinear response of plasmonic metasurfaces: Miller’s rule, nonlinear effective susceptibility method, and full-wave computation,” *JOSA B* **33**, A8 (2016).

- [85] J. Rudnick and E. Stern, “Second-harmonic radiation from metal surfaces,” *Physical Review B* **4**, 4274 (1971).
- [86] W. Schaich and A. Liebsch, “Nonretarded hydrodynamic-model calculation of second-harmonic generation at a metal surface,” *Physical Review B* **37**, 6187 (1988).
- [87] M. Corvi and W. Schaich, “Hydrodynamic-model calculation of second-harmonic generation at a metal surface,” *Physical Review B* **33**, 3688 (1986).
- [88] W. Schaich, “Second harmonic generation by periodically-structured metal surfaces,” *Physical Review B* **78**, 195416 (2008).
- [89] J. Sipe, V. So, M. Fukui, and G. Stegeman, “Analysis of second-harmonic generation at metal surfaces,” *Physical Review B* **21**, 4389 (1980).
- [90] J. A. Maytorena, W. L. Mochán, and B. S. Mendoza, “Hydrodynamic model for sum and difference frequency generation at metal surfaces,” *Physical Review B* **57**, 2580 (1998).
- [91] Y. Zeng, W. Hoyer, J. Liu, S. W. Koch, and J. V. Moloney, “Classical theory for second-harmonic generation from metallic nanoparticles,” *Physical Review B* **79**, 235109 (2009).
- [92] J. Petschulat, A. Chipouline, A. Tünnermann, T. Pertsch, C. Menzel, C. Rockstuhl, and F. Lederer, “Multipole nonlinearity of metamaterials,” *Physical Review A* **80**, 063828 (2009).
- [93] J. Petschulat, C. Menzel, A. Chipouline, C. Rockstuhl, A. Tünnermann, F. Lederer, and T. Pertsch, “Multipole approach to metamaterials,” *Physical Review A* **78**, 043811 (2008).
- [94] J. Petschulat, J. Yang, C. Menzel, C. Rockstuhl, A. Chipouline, P. Lalanne, A. Tünnermann, F. Lederer, and T. Pertsch, “Understanding the electric and magnetic response of isolated metaatoms by means of a multipolar field decomposition,” *Optics express* **18**, 14454 (2010).
- [95] O. Wolf, S. Campione, Y. Yang, and I. Brener, “Multipolar second harmonic generation in a symmetric nonlinear metamaterial,” *Scientific Reports* **7**, 8101 (2017).
- [96] G. D. Bernasconi, J. Butet, and O. J. Martin, “Mode analysis of second-harmonic generation in plasmonic nanostructures,” *JOSA B* **33**, 768 (2016).
- [97] A. G. de Beer and S. Roke, “Nonlinear Mie theory for second-harmonic and sum-frequency scattering,” *Physical Review B* **79**, 155420 (2009).

- [98] A. Capretti, C. Forestiere, L. Dal Negro, and G. Miano, “Full-wave analytical solution of second-harmonic generation in metal nanospheres,” *Plasmonics* **9**, 151 (2014).
- [99] A. Hille, M. Moferdt, C. Wolff, C. Matyssek, R. Rodríguez-Oliveros, C. Prohm, J. Niegemann, S. Grafström, L. M. Eng, and K. Busch, “Second harmonic generation from metal nano-particle resonators: Numerical analysis on the basis of the hydrodynamic drude model,” *The Journal of Physical Chemistry C* **120**, 1163 (2016).
- [100] J. I. Dadap, J. Shan, and T. F. Heinz, “Theory of optical second-harmonic generation from a sphere of centrosymmetric material: small-particle limit,” *JOSA B* **21**, 1328 (2004).
- [101] M. Finazzi, P. Biagioni, M. Celebrano, and L. Duo, “Selection rules for second-harmonic generation in nanoparticles,” *Physical Review B* **76**, 125414 (2007).
- [102] J. Butet, P.-F. Brevet, and O. J. Martin, “Optical second harmonic generation in plasmonic nanostructures: From fundamental principles to advanced applications,” *Acs Nano* **9**, 10545 (2015).
- [103] K. O’Brien, H. Suchowski, J. Rho, A. Salandrino, B. Kante, X. Yin, and X. Zhang, “Predicting nonlinear properties of metamaterials from the linear response,” *Nature materials* **14**, 379 (2015).
- [104] D. C. Tzarouchis, P. Ylä-Oijala, T. Ala-Nissila, and A. Sihvola, “Plasmonic properties and energy flow in rounded hexahedral and octahedral nanoparticles,” *JOSA B* **33**, 2626 (2016).
- [105] M.-L. Ren, S.-Y. Liu, B.-L. Wang, B.-Q. Chen, J. Li, and Z.-Y. Li, “Giant enhancement of second harmonic generation by engineering double plasmonic resonances at nanoscale,” *Optics Express* **22**, 28653 (2014).
- [106] K. Thyagarajan, S. Rivier, A. Lovera, and O. J. Martin, “Enhanced second-harmonic generation from double resonant plasmonic antennae,” *Optics express* **20**, 12860 (2012).
- [107] P. Ginzburg, A. Krasavin, Y. Sonnefraud, A. Murphy, R. J. Pollard, S. A. Maier, and A. V. Zayats, “Nonlinearly coupled localized plasmon resonances: Resonant second-harmonic generation,” *Physical Review B* **86**, 085422 (2012).
- [108] H. Linnenbank and S. Linden, “Second harmonic generation spectroscopy on second harmonic resonant plasmonic metamaterials,” *Optica* **2**, 698 (2015).
- [109] B. Metzger, L. Gui, J. Fuchs, D. Floess, M. Hentschel, and H. Giessen, “Strong enhancement of second harmonic emission by plasmonic resonances at the second harmonic wavelength,” *Nano letters* **15**, 3917 (2015).

- [110] M. Danckwerts and L. Novotny, “Optical frequency mixing at coupled gold nanoparticles,” *Physical Review Letters* **98**, 026104 (2007).
- [111] M. Hentschel, T. Utikal, H. Giessen, and M. Lippitz, “Quantitative modeling of the third harmonic emission spectrum of plasmonic nanoantennas,” *Nano letters* **12**, 3778 (2012).
- [112] D. Griffiths, *Introduction to Electrodynamics* (Prentice Hall, 1999), 3rd ed.
- [113] URL https://www.hit.ac.il/.upload/imported_files/file/Handasa/tikshoret/experiment_6-Frequency%20modulation.pdf.

APPENDICES

APPENDIX A

List of Physical Constants

$$\hbar = 6.58211957 \times 10^{-16} \text{ eVs} \quad \text{reduced Planck constant} \quad (\text{A.1})$$

$$c = 2.99792458 \times 10^8 \text{ m/s} \quad \text{speed of light} \quad (\text{A.2})$$

$$\epsilon_0 = 8.854 \times 10^{-12} \text{ C}^2/\text{Nm}^2 \quad \text{vacuum permittivity} \quad (\text{A.3})$$

$$\mu_0 = 4\pi \times 10^{-7} \text{ Tm/A} \quad \text{vacuum permeability} \quad (\text{A.4})$$

$$e = 1.602176634 \times 10^{-19} \text{ C} \quad \text{charge of electron} \quad (\text{A.5})$$

$$m_e = 0.5109 \text{ MeV}/c^2 \quad \text{mass of electron} \quad (\text{A.6})$$

$$r_s = 5.2917721067 \text{ \AA} \quad \text{Bohr radius} \quad (\text{A.7})$$

$$k_B = 1.38064852 \times 10^{-23} \text{ J/K} \quad \text{Boltzmann constant} \quad (\text{A.8})$$

APPENDIX B

Maxwell and Auxiliary Equations

Maxwell's equations in vacuum are [112]:

$$\nabla \cdot \mathbf{E} = \frac{\rho}{\epsilon_0} \qquad \text{Gauss's Law} \qquad (\text{B.1a})$$

$$\nabla \times \mathbf{E} = -\frac{\partial \mathbf{B}}{\partial t} \qquad \text{Faraday's law of induction} \qquad (\text{B.1b})$$

$$\nabla \cdot \mathbf{B} = 0 \qquad \text{Gauss's law for magnetism} \qquad (\text{B.1c})$$

$$\nabla \times \mathbf{B} = \mu_0 \mathbf{J} + \mu_0 \epsilon_0 \frac{\partial \mathbf{E}}{\partial t} \qquad \text{Ampère's law} \qquad (\text{B.1d})$$

Maxwell's equations in media are:

$$\nabla \cdot \mathbf{D} = \rho_f \qquad (\text{B.2a})$$

$$\nabla \times \mathbf{E} = -\frac{\partial \mathbf{B}}{\partial t} \qquad (\text{B.2b})$$

$$\nabla \cdot \mathbf{B} = 0 \qquad (\text{B.2c})$$

$$\nabla \times \mathbf{H} = \mathbf{J}_f + \frac{\partial \mathbf{D}}{\partial t} \qquad (\text{B.2d})$$

The electric auxiliary fields in linear media are:

$$\mathbf{D} = \epsilon_0 \mathbf{E} + \mathbf{P} \qquad (\text{B.3})$$

$$\mathbf{P} = \epsilon_0 \chi_e \mathbf{E} \qquad (\text{B.4})$$

$$\mathbf{D} = \epsilon \mathbf{E} \qquad (\text{B.5})$$

$$\epsilon = \epsilon_0 (1 + \chi_e) \qquad (\text{B.6})$$

The magnetic auxiliary fields in linear media are:

$$\mathbf{H} = \frac{1}{\mu_0} \mathbf{B} - \mathbf{M} \quad (\text{B.7})$$

$$\mathbf{M} = \chi_m \mathbf{H} \quad (\text{B.8})$$

$$\mathbf{H} = \frac{1}{\mu} \mathbf{B} \quad (\text{B.9})$$

$$\mathbf{H} = \frac{1}{\mu} \mathbf{B} \quad (\text{B.10})$$

$$\mu = \mu_0 (1 + \chi_m) \quad (\text{B.11})$$

APPENDIX C

Derivation of Surface Plasmon Condition

Starting from Fig. 4.2, we write the electric field on each side an interface (without an intermediate slab):

$$\vec{E}_1(\vec{r}, t) = \vec{E}_{1+}e^{i(\omega t - qx + k_1 z)} + \vec{E}_{1-}e^{i(\omega t - qx - k_1 z)} \quad (\text{C.1a})$$

$$\vec{E}_2(\vec{r}, t) = \vec{E}_{2+}e^{i(\omega t - qx + k_2 z)} \quad (\text{C.1b})$$

where $\vec{E}_{j\pm}$ is the electric field vector of the incoming (+) or outgoing (-) wave in the outside dielectric ($j = 1$) or metal ($j = 2$). The the respective wavevectors are $\vec{k}_{j\pm} = (q, \mp k_j)$, where $k_j = \sqrt{(\omega/c)^2 \epsilon_j - q^2}$ is the z-component and q is the in-plane component. The boundary conditions are D_z and E_x continuous:

$$D_z(0^-) = D_z(0^+) \quad (\text{C.2a})$$

$$E_x(0^-) = E_x(0^+) \quad (\text{C.2b})$$

which lead to the following relations:

$$\epsilon_1 E_{1iz} + \epsilon_1 E_{1rz} = \epsilon_2 E_{tz} \quad (\text{C.3a})$$

$$E_{1ix} - E_{1rx} = E_{tx} \quad (\text{C.3b})$$

Now we use Gauss's law, $\nabla \cdot \vec{E} = 0$ and $\nabla \cdot \vec{D} = 0$, evaluated at $(x, z) = (0, d)$:

$$\nabla \cdot \vec{E}_{1i} = qE_{1ix} - k_1 E_{1iz} = 0 \quad (\text{C.4a})$$

$$\nabla \cdot \vec{E}_{1r} = -qE_{rix} + k_1 E_{riz} = 0 \quad (\text{C.4b})$$

$$\nabla \cdot \vec{E}_t = qE_{tx} - k_2 E_{tz} = 0 \quad (\text{C.4c})$$

which result in the following relations:

$$E_{1ix} = \frac{k_1}{q} E_{1iz} \quad (\text{C.5a})$$

$$E_{1rx} = \frac{k_1}{q} E_{1rz} \quad (\text{C.5b})$$

$$E_{tx} = \frac{k_2}{q} E_{tz} \quad (\text{C.5c})$$

and

$$k_1 E_{1iz} - k_1 E_{1rz} = k_2 E_{tz} \quad (\text{C.6})$$

Using the definitions $r = E_{1rz}/E_{1iz}$ and $t = E_{tz}/E_{1iz}$, we have:

$$\epsilon_1 + \epsilon_1 r = \epsilon_2 t \quad (\text{C.7a})$$

$$k_1 - k_1 r = k_2 t \quad (\text{C.7b})$$

and can solve for r to obtain:

$$r = \frac{\epsilon_2 - \epsilon_1 \frac{k_2}{k_1}}{\epsilon_2 + \epsilon_1 \frac{k_2}{k_1}} \quad (\text{C.8})$$

Now, to find the SP condition, we find the poles of the reflection coefficient,

$$0 = \epsilon_2 + \epsilon_1 \frac{k_2}{k_1} \quad (\text{C.9})$$

which, with the relation $k_j = \sqrt{(\omega/c)^2 \epsilon_j - q^2}$, results in the SP condition:

$$q = \frac{\omega}{c} \sqrt{\frac{\epsilon_1 \epsilon_2}{\epsilon_1 + \epsilon_2}} \quad (\text{C.10})$$

APPENDIX D

Derivation of Reflection from Two Layers

Starting from Fig. 4.2, we again write the electric field in each region:

$$\vec{E}_1(\vec{r}, t) = \vec{E}_{1+}e^{i(\omega t - qx + k_1 z)} + \vec{E}_{1-}e^{i(\omega t - qx - k_1 z)} \quad (\text{D.1a})$$

$$\vec{E}_s(\vec{r}, t) = \vec{E}_{s+}e^{i(\omega t - qx + k_s z)} + \vec{E}_{s-}e^{i(\omega t - qx - k_s z)} \quad (\text{D.1b})$$

$$\vec{E}_2(\vec{r}, t) = \vec{E}_{2+}e^{i(\omega t - qx + k_2 z)} \quad (\text{D.1c})$$

where $\vec{E}_{j\pm}$ is the electric field vector of the incoming (+) or outgoing (-) wave in the outside dielectric ($j = 1$), surface layer ($j = s$), or metal ($j = 2$). The the respective wavevectors are $\vec{k}_{j\pm} = (q, \mp k_j)$, where $k_j = \sqrt{(\omega/c)^2 \epsilon_j - q^2}$ is the z-component and q is the in-plane component. The boundary conditions are D_z and E_x continuous:

$$D_z(0^-) = D_z(0^+) \quad (\text{D.2a})$$

$$D_z(d^-) = D_z(d^+) \quad (\text{D.2b})$$

$$E_x(0^-) = E_x(0^+) \quad (\text{D.2c})$$

$$E_x(d^-) = E_x(d^+) \quad (\text{D.2d})$$

which lead to the following relations:

$$\epsilon_1 E_{1iz} + \epsilon_1 E_{1rz} = \epsilon_s E_{siz} + \epsilon_s E_{srz} \quad (\text{D.3a})$$

$$\epsilon_s E_{siz} \exp[ik_s d] + \epsilon_s E_{srz} \exp[-ik_s d] = \epsilon_s E_{tz} \exp[ik_2 d] \quad (\text{D.3b})$$

$$E_{1ix} - E_{1rx} = E_{siox} - E_{srox} \quad (\text{D.3c})$$

$$E_{siox} \exp[ik_s d] - E_{srox} \exp[-ik_s d] = E_{tx} \exp[ik_2 d] \quad (\text{D.3d})$$

Now we use Gauss's law, $\nabla \cdot \vec{E} = 0$ and $\nabla \cdot \vec{D} = 0$, evaluated at $(x, z) = (0, d)$:

$$\nabla \cdot \vec{E}_{1i} = qE_{1ix} - k_1E_{1iz} = 0 \quad (\text{D.4a})$$

$$\nabla \cdot \vec{E}_{1r} = -qE_{rix} + k_1E_{riz} = 0 \quad (\text{D.4b})$$

$$\nabla \cdot \vec{E}_{si} = qE_{six} - k_sE_{siz} = 0 \quad (\text{D.4c})$$

$$\nabla \cdot \vec{E}_{sr} = -qE_{srx} + k_sE_{srz} = 0 \quad (\text{D.4d})$$

$$\nabla \cdot \vec{E}_t = qE_{tx} - k_2E_{tz} = 0 \quad (\text{D.4e})$$

which result in the following relations:

$$E_{1ix} = \frac{k_1}{q}E_{1iz} \quad (\text{D.5a})$$

$$E_{1rx} = \frac{k_1}{q}E_{1rz} \quad (\text{D.5b})$$

$$E_{six} = \frac{k_s}{q}E_{siz} \quad (\text{D.5c})$$

$$E_{srx} = \frac{k_s}{q}E_{srz} \quad (\text{D.5d})$$

$$E_{tx} = \frac{k_2}{q}E_{tz} \quad (\text{D.5e})$$

and

$$k_1E_{1iz} - k_1E_{1rz} = k_sE_{siz} - k_sE_{srz} \quad (\text{D.6a})$$

$$k_sE_{siz} \exp[ik_s d] - k_sE_{srx} \exp[-ik_s d] = k_2E_{tz} \exp[ik_2 d] \quad (\text{D.6b})$$

Our objective is to solve for $r_p = E_{1rz}/E_{1iz}$. The above relations can be formulated

into the following matrix equation:

$$\begin{bmatrix} 1 & -\frac{\varepsilon_s}{\varepsilon_1} & -\frac{\varepsilon_s}{\varepsilon_1} \\ 1 & \frac{k_s}{k_1} & -\frac{k_s}{k_1} \\ 0 & \left(\frac{\varepsilon_s}{\varepsilon_2} - \frac{k_s}{k_2}\right) e^{ik_s\Delta d} & \left(\frac{\varepsilon_s}{\varepsilon_2} + \frac{k_s}{k_2}\right) e^{-ik_s\Delta d} \end{bmatrix} \begin{bmatrix} \frac{E_{1rz}}{E_{1iz}} \\ \frac{E_{siz}}{E_{1iz}} \\ \frac{E_{srz}}{E_{1iz}} \end{bmatrix} = \begin{bmatrix} -1 \\ 1 \\ 0 \end{bmatrix} \quad (\text{D.7})$$

Solving for r_p , we obtain the following:

$$r_p = \frac{\begin{vmatrix} -1 & -\frac{\varepsilon_s}{\varepsilon_1} & -\frac{\varepsilon_s}{\varepsilon_1} \\ 1 & \frac{k_s}{k_1} & -\frac{k_s}{k_1} \\ 0 & \left(\frac{\varepsilon_s}{\varepsilon_2} - \frac{k_s}{k_2}\right) e^{ik_s\Delta d} & \left(\frac{\varepsilon_s}{\varepsilon_2} + \frac{k_s}{k_2}\right) e^{-ik_s\Delta d} \end{vmatrix}}{\begin{vmatrix} 1 & -\frac{\varepsilon_s}{\varepsilon_1} & -\frac{\varepsilon_s}{\varepsilon_1} \\ 1 & \frac{k_s}{k_1} & -\frac{k_s}{k_1} \\ 0 & \left(\frac{\varepsilon_s}{\varepsilon_2} - \frac{k_s}{k_2}\right) e^{ik_s\Delta d} & \left(\frac{\varepsilon_s}{\varepsilon_2} + \frac{k_s}{k_2}\right) e^{-ik_s\Delta d} \end{vmatrix}}, \quad (\text{D.8})$$

which reduces to:

$$r_p = \frac{\left(\varepsilon(\omega) - \varepsilon_1 \frac{k_2}{k_1}\right) \cos k_s \Delta d - i \left(\frac{\varepsilon_s k_2}{k_s} - \frac{\varepsilon_1 \varepsilon_2 k_s}{\varepsilon_s k_1}\right) \sin k_s \Delta d}{\left(\varepsilon(\omega) + \varepsilon_1 \frac{k_2}{k_1}\right) \cos k_s \Delta d - i \left(\frac{\varepsilon_s k_2}{k_s} + \frac{\varepsilon_1 \varepsilon_2 k_s}{\varepsilon_s k_1}\right) \sin k_s \Delta d}. \quad (\text{D.9})$$

In the limit of $k_s \Delta d \ll 1$, and with the identification of $\varepsilon_1 = \varepsilon_0$ and $\varepsilon_2 = \varepsilon(\omega)$, Eq. (D.9) reduces to that of Eq. (4.2) in the main text.

$$r_p^{TF} \approx \frac{\varepsilon(\omega) - \varepsilon_0 \frac{k_2}{k_1} - i \frac{\varepsilon(\omega) \varepsilon_0}{\varepsilon_s(\omega) k_1} q^2 \Delta d + i \alpha_-(\omega) \Delta d}{\varepsilon(\omega) + \varepsilon_0 \frac{k_2}{k_1} + i \frac{\varepsilon(\omega) \varepsilon_0}{\varepsilon_s(\omega) k_1} q^2 \Delta d - i \alpha_+(\omega) \Delta d} \quad (\text{D.10})$$

APPENDIX E

Simulations of mPBD Model at T=310 K

We investigated damage to a homogeneous AT sequence of 64 BPs at a temperature of T=310 K. Our approach is identical to Chapter 5.3 & 5.4. First, we performed a simulation without driving, in order to determine the time it takes for the system to thermalize. In Fig. E.1, we show the average energy of BPs over 10 trials, simulated for 10000 ps (note, this is twice as long as in Chapter 5.3). We compare results for T=310 K (red) and T=290 K (blue). As we found in Chapter 5.3, the system at T=290 K equilibrates on the order of 3000 ps, whereas it appears that the system at T=310 K does not come to equilibrium, even after 10000 ps. This behavior is unsurprising since T=310 K is very close to the melting transition. We note that additional work must be done to determine an appropriate thermalization time.

We then simulated the system with driving, for all points in the amplitude-frequency parameter space spanning $A \in [0 \text{ pN}, 300 \text{ pN}]$ and $f \in [1 \text{ THz}, 2 \text{ THz}]$. For each trial, we first allowed the system to thermalize for 10000 ps. The average separation of all BPs within a sequence, over 10 trials, is shown in Fig. E.2, and the boundary for damage onset is indicated by a solid white line. Compared to Fig. 5.10, the boundary of damage onset occurs at lower amplitude and it is broader in frequency. Additionally, many different “islands” of damage occur in this parameter space, which suggests that the system is near a transitional state. Importantly, these results show that selectivity is preserved at this higher temperature, since the boundary of damage onset and the average separation amplitude (color scale) exhibit amplitude and frequency dependent characteristics.

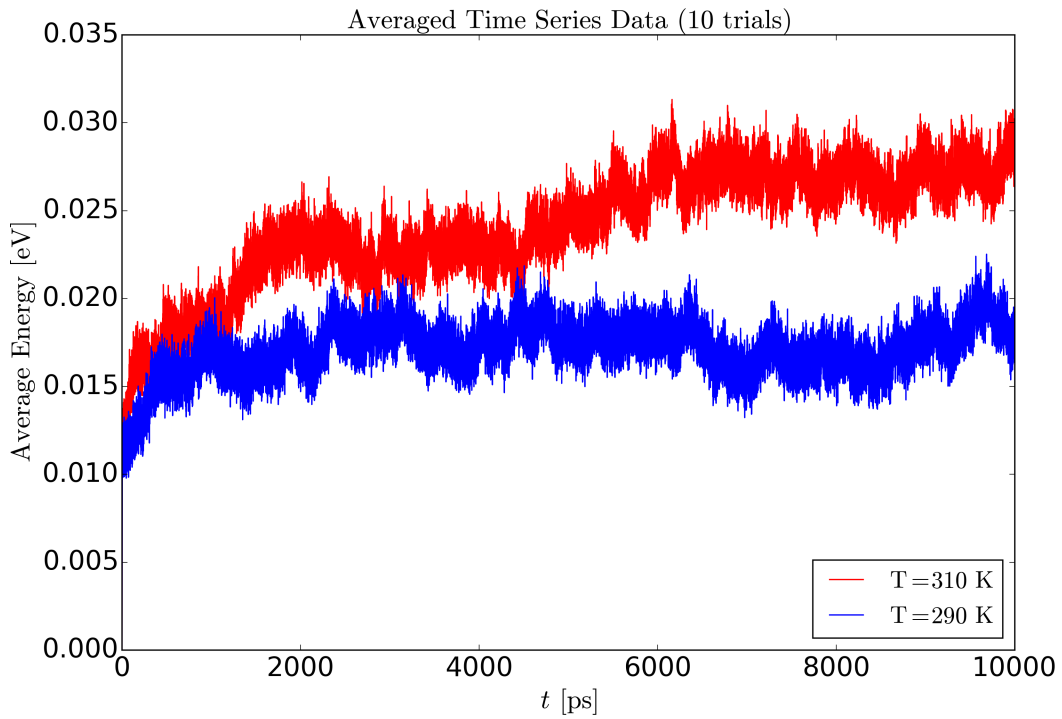


Figure E.1: *Average energy vs. simulation time: $T=310$ K vs. $T=290$ K* The simulation is run for 10000 ps and data are taken over 10 independent trials. The time-series data of the average energy, averaged over all 64 BPs and 10 trials, is shown for $T=310$ K (red) compared to $T=290$ K (blue).

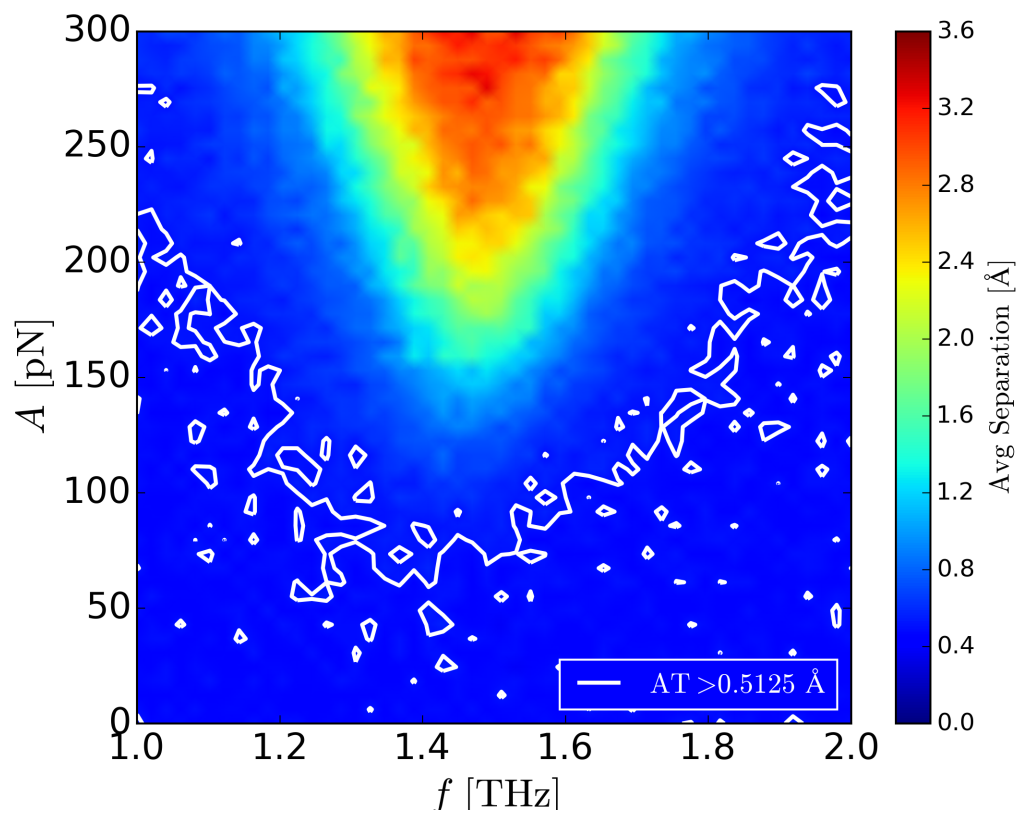


Figure E.2: Average base-pair separation for homogeneous AT sequence ($T=310 \text{ K}$). The intensity scale represents the average base-pair separation and the line indicates the boundary where the onset of damage occurs (average separation $> 0.5125 \text{ \AA}$).

APPENDIX F

Derivation of DFG from Frequency Modulated Signal

We start by deriving an expression, $S(t)$, for a frequency modulated signal, and then obtain the corresponding DFG terms from the expression of $S^2(t)$. Initially, we follow the outline and notation of Ref. [113]. For carrier frequency ω_c and modulation frequency ω_m :

$$S(t) = A \cos [\omega_c t + \beta \sin (\omega_m t)] \quad (\text{F.1})$$

where $\beta = k_f A_m / \omega_m$. We express $S(t)$ as a Fourier series:

$$\begin{aligned} S(t) &= \text{Re} \{A \exp [i (\omega_c t + \beta \sin (\omega_m t))]\} \\ &= \text{Re} \{A \exp [i \omega_c t] \exp [i \beta \sin (\omega_m t)]\} \end{aligned} \quad (\text{F.2})$$

where,

$$\exp \{[i \beta \sin (\omega_m t)]\} = \sum_{-\infty}^{\infty} C_n \exp [in \omega_m t] \quad (\text{F.3})$$

We can determine the Fourier coefficients, C_n :

$$C_n = \frac{\omega_m}{2\pi} \int_{-T_m/2}^{T_m/2} \exp [i \beta \sin (\omega_m t)] \exp [-in \omega_m t] dt \quad (\text{F.4})$$

where, the integration occurs over the full period, $T_m = 2\pi/\omega_m$. Now, with the substitution $\theta = \omega_m t$:

$$C_n = \frac{\omega_m}{2\pi} \int_{-\pi}^{\pi} \exp [i (\beta \sin (\theta) - n\theta)] d\theta \quad (\text{F.5})$$

which is the definition of a Bessel function. Therefore,

$$C_n = J_n(\beta) \tag{F.6}$$

which we can plug back into Eq. (F.2) to obtain

$$\begin{aligned} S(t) &= \text{Re} \left\{ A \exp [i\omega_c t] \sum_{-\infty}^{\infty} J_n(\beta) \exp [in\omega_m t] \right\} \\ &= A \sum_{-\infty}^{\infty} J_n(\beta) \cos [(\omega_c + n\omega_m) t] \end{aligned} \tag{F.7}$$

The previous derivation explicitly follows Ref. [113]. Now, we begin our original analysis and go on to calculate the components of $S^2(t)$. First, we further reduce $S(t)$, using the identity $J_{-n}(\beta) = (-1)^n J_n(\beta)$:

$$\begin{aligned} S(t) &= A J_0(\beta) \cos(\omega_c t) \\ &\quad + A \sum_{n=1}^{\infty} J_n(\beta) \cos [(\omega_c + n\omega_m) t] \\ &\quad + A \sum_{n=1}^{\infty} (-1)^n J_n(\beta) \cos [(\omega_c - n\omega_m) t] \end{aligned} \tag{F.8}$$

Grouping odd and even terms, we have:

$$\begin{aligned} S(t) &= A J_0(\beta) \cos(\omega_c t) \\ &\quad + A \sum_{n=\text{odd}}^{\infty} J_n(\beta) \{ \cos [(\omega_c + n\omega_m) t] - \cos [(\omega_c - n\omega_m) t] \} \\ &\quad + A \sum_{n=\text{even}}^{\infty} J_n(\beta) \{ \cos [(\omega_c + n\omega_m) t] + \cos [(\omega_c - n\omega_m) t] \} \end{aligned} \tag{F.9}$$

Using the identity $\cos(a \pm b) = \cos(a)\cos(b) \mp \sin(a)\sin(b)$, we have:

$$\begin{aligned}
S(t) = & AJ_0(\beta) \cos(\omega_c t) \\
& - 2A \sum_{n=\text{odd}}^{\infty} J_n(\beta) \sin(\omega_c t) \sin(n\omega_m t) \\
& + 2A \sum_{n=\text{even}}^{\infty} J_n(\beta) \cos(\omega_c t) \cos(n\omega_m t)
\end{aligned} \tag{F.10}$$

Ultimately, the frequency modulated signal can be expressed as a sum of three components, which are a signal at the original carrier frequency and two amplitude modulated signals. The DFG term arises from $S^2(t)$, which has many possible combinations of frequency components. This is a rather laborious derivation, but straightforward. We report the result, considering only terms that are *independent* of ω_c . From our previous definition in the Chapter, the DFG frequency is related to the modulation frequency by $\omega_{DFG} = 2\omega_m$, and the corresponding DFG term is:

$$S^2(t) = A^2 \sum_{|n-k|=1} [J_{2n-1}(\beta)J_{2k-1}(\beta) + J_{2n}(\beta)J_{2k}(\beta)] \cos(\omega_{DFG}t) \tag{F.11}$$

The DFG amplitude also has the following form in the limit of $\beta \ll 1$:

$$\begin{aligned}
A_{DFG} = & A^2 \sum_{|n-k|=1} [J_{2n-1}(\beta)J_{2k-1}(\beta) + J_{2n}(\beta)J_{2k}(\beta)] \\
\approx & A^2 [J_1(\beta)J_3(\beta) + J_2(\beta)J_4(\beta)]
\end{aligned} \tag{F.12}$$

Clearly, the amplitude of DFG from a frequency modulated signal is *less* than the amplitude from an amplitude modulated signal, since $J_{n>1}(\beta \ll 1) \ll 1$.